THE DEVELOPMENT OF NEXT-GENERATION ZEOLITE MATERIALS FOR THE REMEDIATION OF AQUEOUS NUCLEAR DECOMMISSIONING WASTE

by

JAMES LESLIE ARVID REED

A thesis submitted to the University of Birmingham for the degree of
DOCTOR OF PHILOSOPHY

School of Chemistry
College of Engineering and Physical Sciences
University of Birmingham
April 2024

ABSTRACT

In the nuclear industry, materials capable of selective adsorption of caesium-137 and strontium-90 are paramount in the processing of nuclear effluent. This work pioneers the partial interzeolite transformations of natural zeolites to enhance the ion-exchange properties, thus producing industrially viable materials from a cost effective, single-step process.

Firstly, a methodology has been developed enabling a controlled partial transformation from natural zeolites (mordenite and clinoptilolite) to zeolite P. This process has been applied to produce powdered and granular composite materials, suitable for a variety of applications. A high level of control is demonstrated, facilitating the production of composite materials with a desired blend of parent phase and zeolite P.

A series of batch ion-exchange experiments suggest partially transformed natural zeolites are promising materials for the abatement of caesium and strontium from nuclear waste streams: drastic improvements to the strontium capacity and rate of uptake are observed whilst the high caesium selectivity of the parent material is maintained. These findings are validated in flow experiments using active liquor, where granular composite materials outperformed both their respective parents and Mud Hills clinoptilolite in the removal of Cs-137 and Sr-90.

Furthermore, the combination of SEM, XCT and local, image-guided micro-diffraction experiments provide comprehensive characterisation of the granular composite materials. This allows for bulk macroscale mechanisms of transformations from a mordenite and a clinoptilolite to be postulated.

Finally, the superior ion-exchange properties of Mud Hills clinoptilolite, in comparison to other isostructural natural materials, is explored. A suite of characterisation techniques and adsorption studies allows for several theories to be presented, potentially streamlining the selection process for future ion-exchange materials, which is an integral part of the UK's decommissioning efforts.

ACKNOWLEDGEMENTS

I would firstly like to thank my supervisors Phoebe Allan, Joseph Hriljac and Thomas Carey for providing guidance throughout the duration of this work – your wide-ranging technical expertise was amazing to draw on and allowed me to develop such a diverse and interesting project. You also provided excellent opportunities throughout my studies. Personal highlights include four international trips, four exhausting Diamond visits, and a six-week placement in NNL's active facilities. Furthermore, I thank you for encouraging independent thinking and planning throughout. The freedom you granted has made me a far better researcher and unmeasurably prouder of my achievements.

I would also like to thank Sellafield Ltd for funding the work and NNL for providing both technical and personal advice through Tom Carey. I also thank Simon Kellet for guidance. Throughout, I was inspired by the potential real-world applicability of my work, and it was a pleasure to present to industry experts at regular intervals. I would like to thank Transcend, the consortium which my project was a part of. The conferences were always fun, engaging, and allowed me to develop a vast network of nuclear professionals. I've also made many friends through the programme, notably Lucas, Elanor, Tom, Sarah and Joe – I'll miss the open bars at Waste Management.

I would like to thank Neelam Fitzgerald, John Rawcliff and the rest of the M&A team at NNL's Preston Laboratory for accommodating me for six weeks, especially Neelam, who supervised throughout and did a lot of the hands-on work. It was my first taste of industry and working in an active laboratory; the experience has already proven invaluable for my career. Special thanks to Tom Carey for organising the active work and the Nuclear Decommissioning Authority for financial support through the Transcend active fund.

I thank Diamond Light Source, UK, for allowing me to perform numerous experiments in your world leading facilities, in addition to Phobe and Joe – without your wealth of synchrotron knowledge this would not have been possible. I also thank Andrew James, Sharif Ahmed and Hans Deyhle for providing technical support during, and after, the visits and Antony Nearchou for help running the *in-situ* experiments.

I would like to thank the 'old school' members of the Hriljac group for mentoring during the early stages of my work, particularly Daniel Parsons, Daniel Smith, and Antony Nearchou. More widely, I would like to thank the whole of 'Floor 5' (and others I've encountered in the department) - over the past 5 years. You made it a fun, and often hilarious, place to work. Whether it be Friday drinks, football, pool, darts, karaoke, bottomless brunch, cricket, parkrun, pub-crawls, or even trips to the zoo, you have made the last 5 years very enjoyable. Special thanks to Alex S, Beatrice, Rosie, Jeremy, Luke, Dan, Jake, Caitlin, Ezri, Emily, Jacob, Jaime, Amie, Rob, Yanfang, Harry and, of course, Alex Green.

I would also like to acknowledge Norman Day for assistance in running ICP-MS measurements. It didn't always work, but we always had a laugh, and we did end up getting lots of valuable data. Additionally, I thank Chris Stark for assisting in running, and often fixing, the ICP-MS. Furthermore, I would like to thank Javier Castells-Gil for help in the acquiring, analysing, and interoperating of XPDF data. For consistent, and often under-appreciated, excellence on the floor, I would like to thank Abbey Jarvis, who helped me throughout with everything lab based. I would also like to thank Adele Farrelly for saving me a 450-mile round trip by conducting some SEM-EDS measurements shortly after my departure. I thank Hamish Yeung for providing supervisor cover during Phoebe's maternity leave.

In the later years of this project, it has been gratifying to see success and receive significant interest from industry. I would like to thank Nick Bryan, Jasmine Sharp and Dylan Watmough from the Effluent, HALES and Environmental Chemistry team at NNL for conducting further trials of some of the most promising materials produced in this work.

Finally, I would like to thank my immediate family, notably my three parents: Mum, Dad and Fergus, for providing me with a good start in life, without which, this would have been impossible. Last, but by no means least, I give immeasurable thanks to Georgia, for providing unwavering support during the write-up phase and for generally being amazing.

TABLE OF CONTENTS

LIST OF ABBREVIATIONS

ARS	Acute Radiation Sickness
CBU	Composite Building Unit
CEC	Cation Exchange Capacity
DF	Decontamination Factor
DIAD	Dual Imaging and Diffraction
EARP	Enhanced Actinide Removal Plant
EDS	Energy Dispersive X-ray Spectroscopy
ED	Energy Dispersive
FID	Free Induction Decay
GDF	Geological Disposal Facility
HAL	Highly Active Liquor
HALES	Highly Active Liquor Evaporation and Storage
HLW	High-Level Waste
ICP	Inductively Coupled Plasma
ILW	Intermediate-Level Waste
IZA	International Zeolite Association
LDPE	Low Density Polyethylene
LLW	Low-Level Waste
MAS	Magic Angle Spinning
MS	Mass Spectrometry
MTO	Methanol to Olefin
NMR	Nuclear Magnetic Resonance
NNL	National Nuclear laboratory
OES	Optical Emission Spectroscopy
OSDA	Organic Structure Directing Agent
PDF	Pair Distribution Function
PP	Polypropylene
PPB	Parts Per Billion
PPM	Parts Per Million
PXRD	Powder X-ray Diffraction

RF	Radiofrequency
RIX	Rapid Ion-Exchange
SBU	Secondary Building Unit
SDA	Structure Directing Agent
SEM	Scanning Electron Microscopy
SIXEP	Site Ion Exchange Effluent Plant
VLLW	Very Low-Level Waste
WD	Wavelength Dispersive
WVP	Waste Vitrification Plant
XCT	X-ray Computed Tomography
XRF	X-ray Fluorescence

CHAPTER 1: INTRODUCTION

1.1 Nuclear Energy

Nuclear power provides around 10% of humanity's energy requirements and is currently produced in 30 countries[1]. Unlike fossil-fuel technologies, nuclear power doesn't release CO_2 into the atmosphere during operation, rendering it a 'green' source of energy. The energy density of nuclear fuel is also order of magnitudes greater than fossil fuel equivalents: one uranium pellet creates as much energy as approximately 900 kg of coal, 500 L of oil or 500 m^3 of natural gas[2]. Modern reactors typically contain upwards of 10 million fuel pellets, which are assembled in thousands of fuel rods[3]. The International Atomic Energy Agency estimate that nuclear power has prevented the release of 64 Gt of CO_2 since 1971, equivalent to 2 years' worth of global emissions[1]. Furthermore, the energy output is constant and predictable, unlike renewables such as wind and solar which rely on changeable weather. This makes it an attractive and vital technology for decarbonising the energy sector, which is paramount in achieving national and international carbon emission targets[1].

Nuclear energy is produced by nuclear fission whereby the nucleus of a large atom, such as uranium-235, splits into two smaller species, typically after bombardment from a neutron, and releases a large amount of energy[4]. As a result of this process, additional neutrons are emitted, which can cause the splitting of further nuclei, thus initiating a chain reaction (Figure 1.1)[4]. This phenomenon was first discovered in 1938 by Otto Hahn and Fritz Strassmann, who observed barium species after neutron bombardment of uranium nuclei[5]. Soon after, physicists Lise Meitner and Otto Frisch explained the nuclear processes involved and named the process[5]. Since its discovery, nuclear fission has been widely utilised worldwide for both the development of nuclear weapons and generation of nuclear power[4, 6].

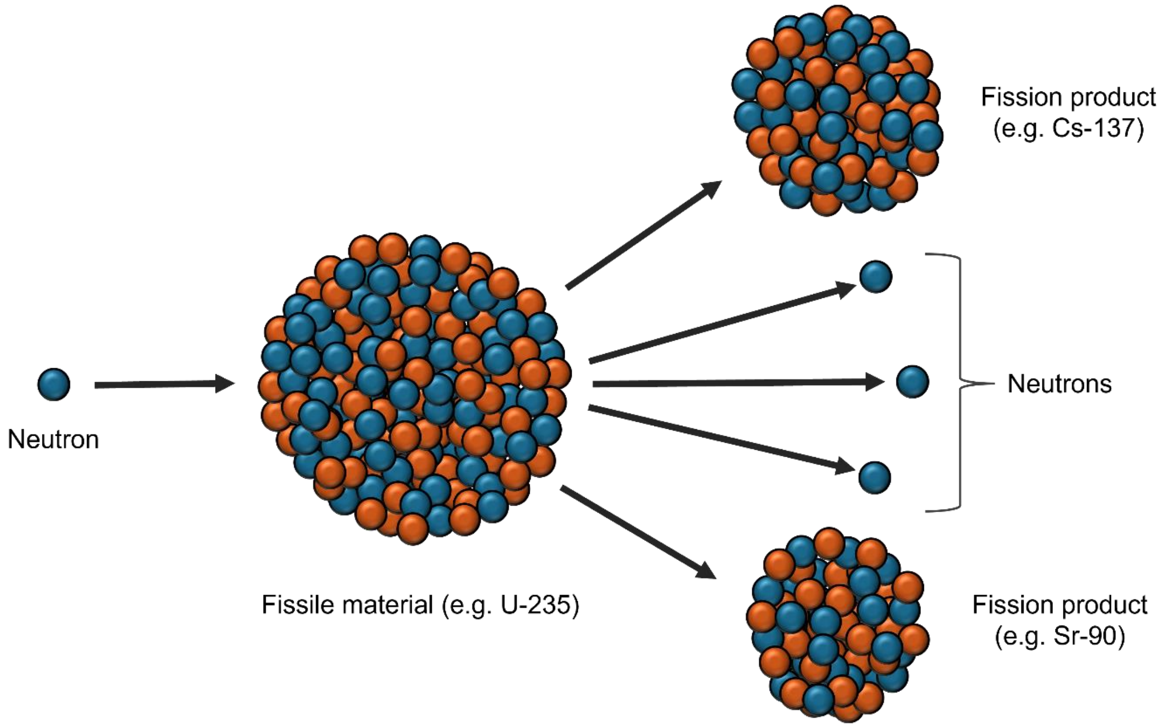

Figure 1.1. Nuclear fission.

The two smaller species produced by the splitting of a single nucleus are termed fission by-products[4]. These species are often radioactive, meaning they emit ionising radiation, and can damage the body's cells and proteins, including DNA. High levels of exposure over a short period of time can cause acute radiation sickness (ARS) or, if the dose is high enough, death[7]. Any exposure increases the probability of cell mutations, which can result in cancer[7]. The units of Becquerel (Bq) are used to measure the radiation emitted from a source, where 1 Bq is equal to one radioactive decay event per second[7]. Sieverts (Sv) is a unit of radiation which measures exposure in terms of effects on the human body; factors such as exposure locality, tissue type and route of exposure are considered[7].

1.1.1 Ionising Radiation

Three types of ionising radiation commonly associated with radionuclides are alpha, beta and gamma radiation. Alpha particles consist of two neutrons and two protons, which makes them the same as the helium nucleus, and are emitted by heavier radionuclides such as uranium. Whilst high in energy, alpha particles can only travel short distances because of their large mass. However, their double positive charge allows them to cause numerous ionisation events in a small distance. As alpha particles cannot penetrate human skin, the principal hazards arise through internal exposure such as inhalation, swallowing or injection[7].

Beta radiation consists of fast-moving electrons or positrons, generated *via* the decay of one of the nucleus' neutrons into a proton (emitting an electron, β^-), or a proton into a neutron (emitting a positron, β^+). They are less ionising than alpha particles, but can travel greater distances[7]. Consequently, external exposure to large amounts of beta radiation can cause tissue damage, although internal exposure through direct entry remains the most significant hazard.

Gamma decay is the emission of short-wavelength electromagnetic radiation from a high-energy, unstable radionuclide to a lower energy species. Unlike alpha and beta decay, the atomic structure of the parent nucleotide remains constant during this process[7]. Gamma radiation is the least ionising compared to alpha or beta, but can travel large distances through significant medium, including through the human body[7]. Protection against high-count gamma sources therefore requires extreme shielding measures, such as several inches of lead or a few feet of concrete[7].

Different radionuclides emit a variety of radiation types, often releasing multiple forms of radiation during their respective decay chain[8]. This includes the fission products of uranium-235, which cannot be individually predicted, but follow a statistical distribution according to mass number, with two peaks centred at 95 and 140 atomic mass units[4, 9]. Over 20 species are directly produced in varied quantities from the fission process[4, 9]. These fission products present the most significant challenge for the nuclear energy industry: the radioactive waste generated. This waste comes in many forms through the handling and processing of these fission fragments.

1.1.2 Nuclear Waste

Each country has its own guidelines and regulations in place regarding the characterisation, handling and disposal of nuclear waste, including the UK[10]. Nuclear waste is universally classified in three categories: high-level waste (HLW), intermediate-level waste (ILW) and low-level waste (LLW). HLW is the highest classification, generally consisting of the spent nuclear fuel itself; it generates significant quantities of heat and therefore requires cooling systems and robust shielding during storage. In the UK, spent nuclear fuel is stored in concentrated nitric acid prior to vitrification in the waste vitrification plant (WVP)[10]. Both the acidic solution and the glass produced is attributed HLW, in addition to some insoluble fission products. The UK's HLW inventory currently occupies 1470 m^3 and will be emitting 14,000,000 TBq of radiation in 2100[10].

ILW possesses lower levels of radioactivity than HLW but is not independently heat-generating. ILW can include materials such as ion-exchange resins, fuel cladding, concrete, graphite and sludges, all of which still require significant shielding. The UK is currently in possession of 496,000 m^3 of ILW which is forecast to produce 1,000,000 TBq in 2100[10].

In the UK, LLW is defined as any material which emits <4 GBq ton^{-1} α or <12 GBq ton^{-1} β/γ radiation[10]. The majority of LLW is comprised of building materials and soil from nuclear sites, although the waste can be extremely varied. The UK also contains a sub-category for the lowest risk waste: very low-level waste (VLLW)[10]. This material is able to be disposed of in a specialist landfill located near the village of Drigg, Cumbria[11]. 4,000,000 m^3 of LLW has been reported in the UK, however, this waste is only forecast to release 140 TBq in 2100[10]. A summary of the UK's nuclear waste stockpile by categorisation is presented in Figure 1.2, in addition to the forecast activity in 2100.

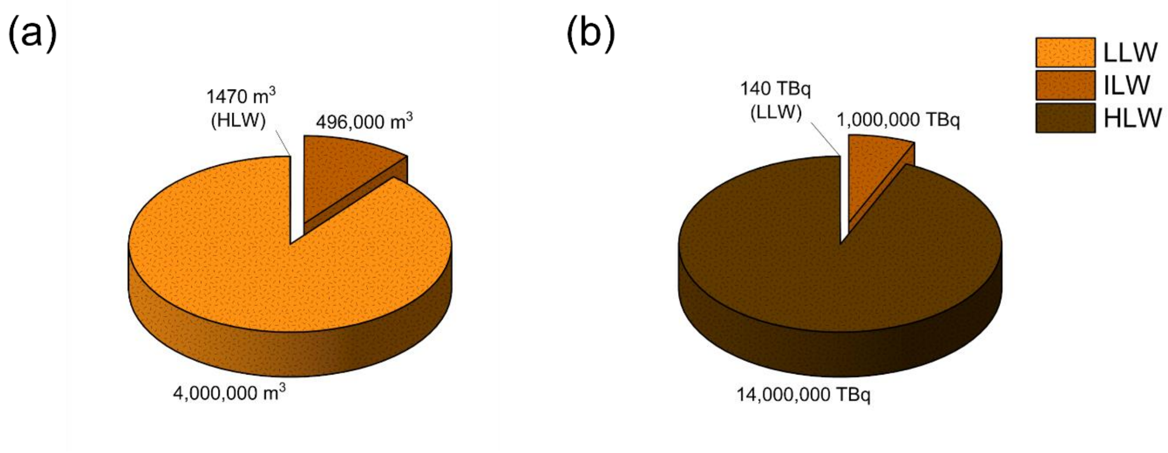

Figure 1.2. The UK's nuclear waste inventory. (a) by volume and (b) by forecast activity[10].

Currently, all forms of nuclear waste are housed above ground (or at near surface) on designated nuclear waste sites with sufficient shielding in place to protect personnel, the environment and the public[10]. Typically, LLW and ILW are deposited into metal canisters, which are subsequently backfilled with cement. Similarly, the HLW glass from the vitrification process is encapsulated in stainless steel canisters[10]. It is widely accepted among the nuclear community, however, that this is not a suitable long-term option, and that the material should be permanently disposed of in an underground repository, or in a Geological Disposal Facility (GDF). Suitable sites for a GDF must have appropriate geology and location, in addition to a consenting local community, which has proven a significant barrier to projects worldwide. In fact, zero waste has actually been stored in a GDF at time of writing; Finland have made the most progress, estimated to commence operation of the Onkalo repository in 2025[12].

To facilitate both intermediate, overground storage and long-term disposal in a GDF, the waste material must be in a consolidated, solid form to minimise risk of environmental release. Unfortunately, significant quantities of aqueous waste are produced during the nuclear fuel cycle from activities including spent-fuel processing, washing and de-canning[13]. Radionuclides present in these waste streams must be transferred into solid media to comply with medium- and long-term storage ambitions. Caesium-137 and strontium-90 are the two most pertinent species of concern; combined, they account for approximately 99% of medium-lived radioactivity and possess characteristics which render them particularly harmful to human life and the environment[4].

1.1.2.1 Caesium-137

Caesium-137 is a highly water soluble species with a 30 year half-life and a fission yield of 6.1% from U-235[9]. Its predominant mechanism of decay (95%) is through emission of beta negative (β^-) radiation (0.512 MeV) to an excited Ba-137 species, which promptly decays ($t_{1/2}$ = 2.55 minutes) through release of gamma radiation (0.662 MeV) to give a stable Ba-137 species (Figure 1.2)[8]. Alternatively, a direct decay pathway to stable Ba-137 is also possible through emission of higher energy β^- radiation, although this only occurs in 5% of cases (Figure 1.3)[8].

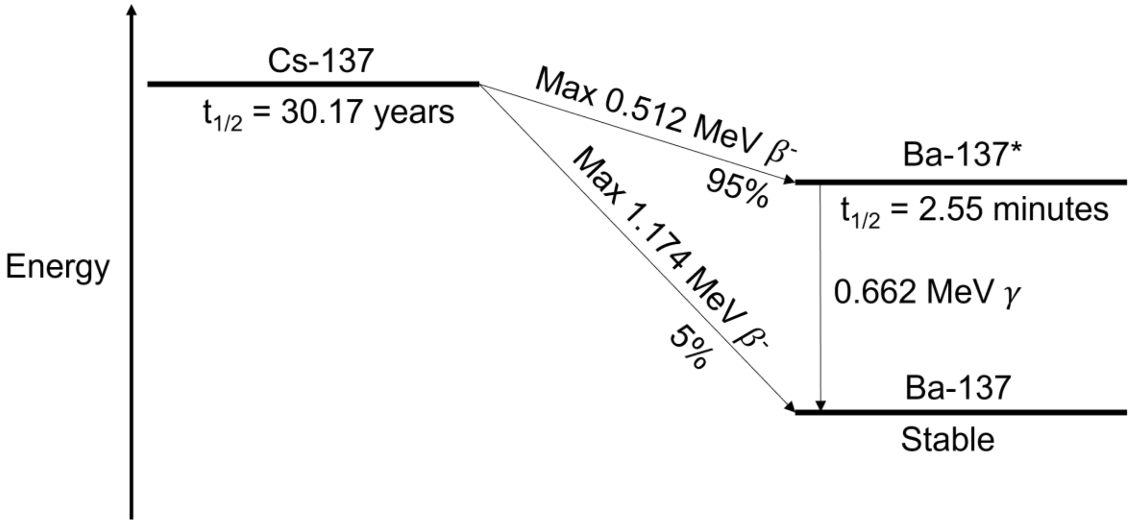

Figure 1.3. Decay pathway of Caesium-137[8].

The high water-solubility[14] and chemical likeness to potassium mean this species is also readily taken up by biological systems, whilst also having the ability to travel significant distances in groundwater if not contained. Therefore, abatement from aqueous waste streams is of utmost priority[15].

1.1.2.2 Strontium-90

Strontium-90 is also a highly water soluble species, with a half-life of 29 years and a fission yield of 5.7% from U-235[9]. Its sole decay pathway mechanism is through a double β^- emission, the first of which (0.546 MeV) forms Y-90, which subsequently decays to stable Zr-90 through a high energy (2.28 MeV) beta emission ($t_{1/2}$ = 64 hours) (Figure 1.4)[8].

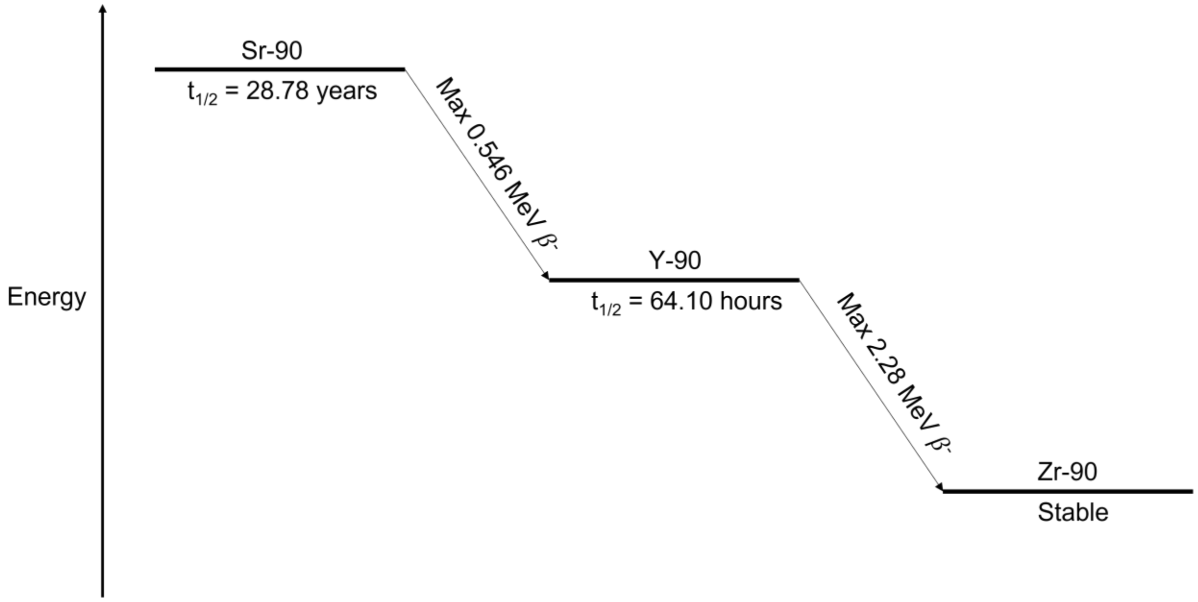

Figure 1.4. Decay pathway of strontium-90[8].

Analogous to caesium-137, strontium-90 is also highly soluble. Therefore, it is readily accepted in biological systems and can travel significant distances can travel large distances in groundwater if not contained. Additionally, due to its chemical likeness to calcium, strontium-90 can also accumulate in teeth and bones – adding further risk to human health[16, 17].

1.1.3 Processing of Nuclear Effluent

The processes used to treat nuclear effluent are dependent on the properties of the waste stream itself, with factors such as radioactivity, pH, solid content (quantity, phase, solubility, particle size), salt content and the radionuclides present needing to be considered. The aim of the treatment is to isolate the radionuclides into forms suitable for both medium- and long-term storage. Three processes used at the Sellafield site, UK, are evaporation, precipitation and ion-exchange. The Highly Active Liquor Evaporation and Storage (HALES) plant takes highly active acidic raffinate from spent fuel reprocessing plants and reduces the volume by a factor of 50 though evaporation, producing a highly active liquor (HAL). This HAL is subsequently vitrified in the Waste Vitrification Plant (WVP) to produce a stable, solid waste form[18].

Also at Sellafield, precipitation is utilised by the Enhanced Actinide Removal Plant (EARP), where sodium hydroxide is added to the iron-laden waste stream, initiating precipitation of a ferric floc[19]. Radioactive actinides are concurrently precipitated both directly and through co-precipitation, in addition to being adsorbed by the floc itself, thus enabling separation by filtration[19]. In EARP, sodium nickel hexacyanoferrate is also utilised as an ion-exchange material for extracting Cs-137 from solution. As the predominant method examined in this work, the ion-exchange process and its applicability in the remediation of aqueous nuclear decommissioning waste, is hereby discussed.

1.1.3.1 Ion-Exchange

Ion-exchange is a process where ions present in a solution exchange for other ions present in a solid material, such as a zeolite. This process is represented in Equation 1.1, where z_A and z_B represent the charges on species *A* and *B*; state symbols '*s*' and '*aq*' refer to the location of the ions (incorporation in the solid material and in the aqueous environment, respectively).

Equation 1.1: $$z_A B_{(s)}^{z_B^+} + z_B A_{(aq)}^{z_A^+} \leftrightarrow z_A B_{(aq)}^{z_B^+} + z_B A_{(s)}^{z_A^+}$$

The process is reversible, with the final position of equilibrium dependent on many factors including the species involved, sorbent characteristics and temperature. Zeolitic ion-exchange is utilised for the remediation of aqueous nuclear decommissioning waste at SIXEP, Sellafield, where radionuclides such as caesium-137 and strontium-90 are selectively exchanged for incumbent, non-hazardous cations, such as sodium.

1.1.3.2 The SIXEP Plant, Sellafield (UK)

Since the mid 1980's, the Site Ion Exchange Effluent Plant (SIXEP) has extracted caesium-137 and strontium-90 from approximately 4000 m^3 of effluent daily[20]. The plant utilises two 10 m^3 fixed bed columns of natural clinoptilolite zeolite in series, in which effluent is pumped though after filtration by a sand bed and pH adjustment (Figure 1.5)[20].

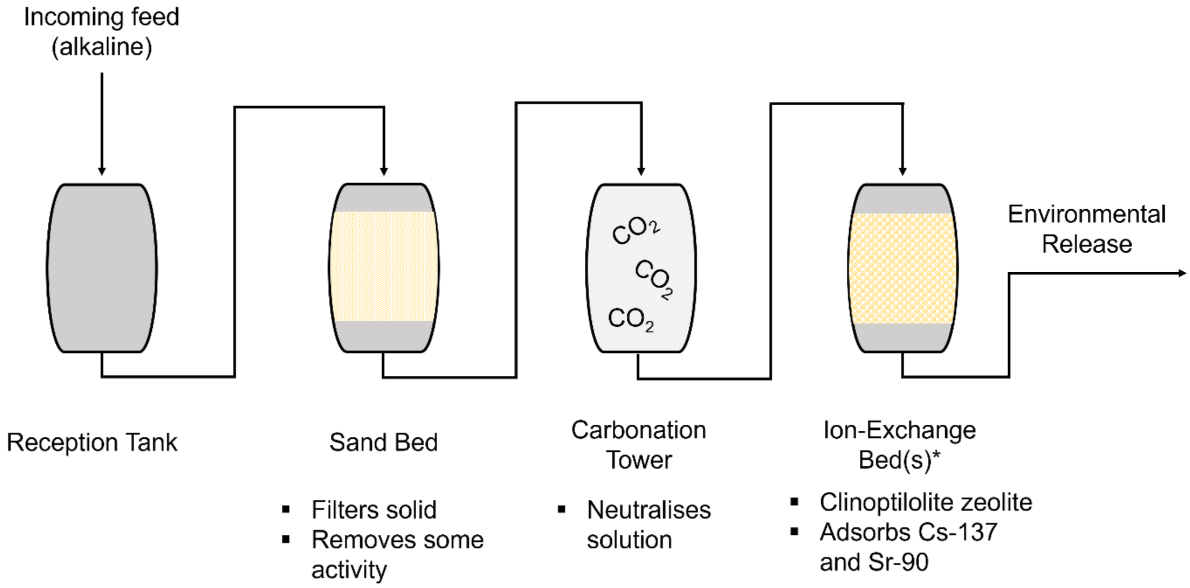

Figure 1.5. Schematic of the Site Ion Exchange Effluent Plant (SIXEP), located at the Sellafield site, UK[20]. *Only one ion-exchange bed is shown.

Activities of treated aqueous waste are sufficiently low to allow for environmental release into the Irish sea. When breakthrough is detected between the columns, operation ceases, the lag-bed is promoted and a replacement bed is installed[20]. Plant operation produces approximately 20 m^3 of spent ion-exchange material annually[21]. Interestingly, the ion-exchange material used, a clinoptilolite sourced from Mud Hills California, outperforms other clinoptilolites in its role as a dual ion-exchange material, particularly in its ability to sorb strontium. This is particularly significant as despite the strontium effluent concentration typically being an order of magnitude more dilute, it is often the first species to breakthrough. Whilst this property has been of great benefit to the nuclear industry, its origins are unclear. Unfortunately, the supply of this material is due to deplete in the mid-2030s, making it important that a replacement is identified in the coming years.

1.1.3.3 Aqueous Waste Produced from Nuclear Incidents

The vast majority of contaminated nuclear wastewater arises though routine waste processing. However, nuclear incidents can also produce significant quantities of aqueous waste requiring remediation. A notable example of this is the Fukushima Daiichi nuclear power plant, which was hit by a tsunami in 2011, flooding the plant and knocking out the reactor coolant system, resulting in the meltdown of three reactor cores[21, 22]. In attempt to cool the damaged reactors, large quantities of salt and fresh water were injected. Direct contact with molten nuclear fuel rendered these waters, which subsequently accumulated in reactor buildings and turbine halls, highly radioactive and in requirement of remediation[21].

Treatment of this aqueous waste is ongoing and has been achieved using several specially engineered treatment plants employing ion-exchange, co-precipitation and reverse osmosis processes. Zeolite chabazite, crystalline silicotitanates and hexacyanoferrates (CsTreat®) have all been deployed in fixed-bed columns for sequestration of caesium-137[21]. Strontium-90 has been removed through a combination of precipitation techniques and ion-exchange with a sodium titanate (SrTreat®)[21]. The remediation efforts at Fukushima have resulted in removal of all the radionuclides from the water, except for tritium and carbon-14, which were present at concentrations of 14 and 2% of the regulatory limits for drinking water, respectivly[23, 24]. Consequently, the discharge of treated water commenced in summer of 2023 and is expected to take approximately 30 years[23]. Similarly, after the Three Mile Island meltdown accident in 1979, caesium and strontium were extracted from waste effluent using fixed bed columns of synthetically produced chabazite and zeolite A, respectively[21].

Many nuclear sites worldwide are currently undergoing decommissioning; this will produce large quantities of nuclear effluent that will require treatment. The composition of this effluent is likely to be different, and remediation using established materials may not be possible. Specific to the UK, the supply of Mud Hills clinoptilolite is forecast to deplete in the 2030's, with no follow-on material yet identified. Therefore, it is paramount that research is conducted into alternative ion-exchange materials.

1.2 Zeolites

Zeolites are a class of porous aluminosilicates that have been deployed by the nuclear industry as an ion-exchange material for the removal of radionuclides from aqueous waste streams (1.1.3). More widely, zeolites are extensively deployed across a multitude of industrial processes encompassing catalysis, gas adsorption and other ion-exchange applications[25]. The fundamental building blocks of zeolites are silicon and aluminium tetrahedra, which themselves are comprised of Si /Al atoms each surrounded by four oxygen atoms. These units assemble to form three-dimensional macrostructures *via* corner-sharing tetrahedra, with most of these structures containing open channels or cages within the structure[25]. The presence of aluminium within the framework results in an overall negative charge, meaning cations are electrostatically bound within the internal channels and cages to maintain charge neutrality[25]. Water molecules occupy the remaining space inside the framework, resulting in the following general formula (for monocationic systems): $M^{n+}_{x/n}Al_xSi_{1-x}O_2{\cdot}zH_2O$, where n is the charge associated with cation M, x is the proportion of silicon substituted by aluminium, and z is the quantity of water molecules contained within each formula unit[25].

1.2.1 Zeolite Structures

Within the general structure, silicon and aluminium tetrahedra combine, forming larger aluminosilicate units including rings, chains and cages, which are termed secondary and tertiary building units[25]. These are capable of assembly in a large multitude of configurations to generate distinct zeolite structures (Figure 1.6). The largest building unit (or units) required to assemble the unit cell of a given framework is referred to as a composite building unit (CBU)[25]. For a more detailed discussion of zeolite structure assembly please refer to the review by Moshoeshoe[25]. At the time of writing, there are 251 unique zeolite structures reported in the International Zeolite Association (IZA) database[26], with more continuously being discovered[27]. Each of these unique frameworks are assigned a three-letter code for clarity; this nomenclature can originate from the natural mineral the structure was first found in (e.g., GIS - gismondine)[28], the location of discovery (e.g., MOR – discovered in Morden, Canada)[29] or the company that first synthesised it (e.g., LTA – Linde Type A)[30].

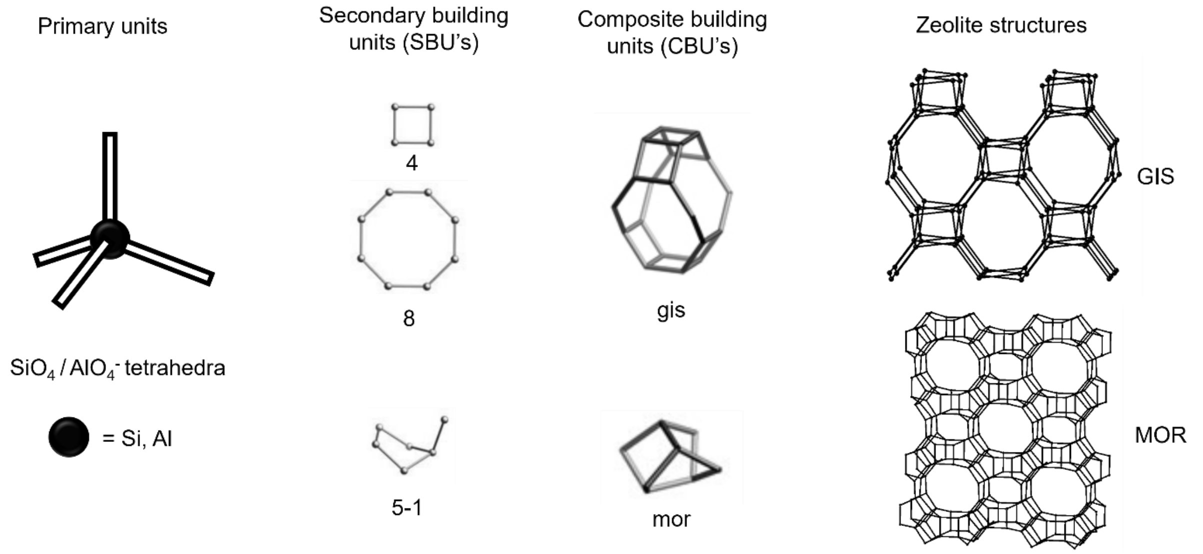

Figure 1.6. The building blocks of GIS and MOR zeolite frameworks[26]. In these 'chickenwire' depictions, vertices correspond to a single primary unit (SiO_4 or AlO_4^- tetrahedron).

Several factors contribute to the properties and thus the overall functionality of a zeolite, one of which being the geometries of the channels. In catalysis this is crucial; the organic species undergoing catalysis must be of suitable size to both enter the framework and undergo a reaction in the zeolites internal space, or microenvironment. This trait is often exploited by using catalyst with suitable apertures to either exclude certain reactants or restrict the release of a species until the correct product is formed[25, 31]. In ion-exchange applications, the size of the channels affects the affinity of the framework for a particular species due to both steric effects and the strength of electrostatic attractions[25].

Another property dictating the functionality of zeolite systems is the framework aluminium content, which is commonly reported as a Si/Al ratio. Each aluminium tetrahedron bears a net negative charge on the framework, which must be counterbalanced by cations residing within the structure. Therefore, the aluminium content is directly proportional to the cation exchange capacity (CEC) of any given zeolite. This is paramount in ion-exchange applications, where the increased CEC means more cations can be adsorbed by a unit mass. When considering the adsorption of divalent species, the aluminium distribution is also important, as they require two aluminium tetrahedra in proximity, or an aluminium pair, in order to adhere[32-34].

Both these effects are compounded when electrostatic interactions between framework and cation are considered; more aluminous, change-dense frameworks will exhibit greater affinity to cations possessing greater change density, whereas large, charge-diffuse species prefer adhesion to more siliceous frameworks[34]. In catalysis, the aluminium content and distribution can tune the Bronsted acidity of the framework and hence its catalytic functionality[25]. Different zeolite structures favour crystallisation at a particular aluminium content, although a range of Si/Al ratios are generally available, ranging from aluminium-free, charge-neutral frameworks[35] to structures with a Si/Al of 1[36]. Frameworks with equal amounts of silicon and aluminium (Si/Al = 1) are considered to have maximum aluminium content, as Al-O-Al linkages are generally forbidden. This is known as Lowenstein's rule[37], which can only be broken in high temperature syntheses for an extremely limited number of structures (e.g., aluminate sodalites[38]).

1.2.2 Zeolite Crystallisation and Synthesis

Zeolite crystallisation is complex, with processes such as dissolution, precipitation, polymerisation and depolymerisation all occurring simultaneously[39]. Whilst some of the intricacies are outside the scope of this monograph, the widely accepted general crystallisation pathway is discussed herein. The first step in the crystallisation of zeolites is the mixing of raw materials to form a hydrogel, the consistency of which can range from a transparent suspension to a thick gel[40]. Iterative hydrolysis reactions, catalysed by the OH^- mineraliser, produce silicic acid ($Si(OH)_4$) and aluminium equivalent monomers, which subsequently condense into oligomers[40]. These larger nanostructures are stabilised through coordination to cationic structure directing agents (SDAs) and further agglomerate into large-enough species to enable crystal growth. Subsequently, nascent aluminosilicate species diffuse to the surface and connect through condensation reactions, resulting in distinct zeolite crystals. All these stages of zeolite nucleation are reversible, often meaning the target framework structure is a metastable, kinetic product; this renders temperature and time as critical parameters in determining the structure of the crystalised species[39, 40].

Laboratory-scale synthesis of zeolites typically involves employing artificial sources of silica and alumina, a mineraliser, a structure directing agent (often a metal hydroxide species is employed to function as both a mineraliser and structure directing agent), and a solvent, which is usually water[41]. These components are thoroughly mixed to form a homogeneous gel prior to heating under autogenous pressure for a given period. This is generally achieved in an autoclave, although plastic bottles are often used where lower temperatures are required. Once finished, the solid zeolite is readily separated from the mother liquor[41]. A multitude of factors determine the zeolite structure crystalised, including the alkalinity, temperature, properties of the structure directing agent, and the concentration/composition of the precursor materials. Naturally, some species are simple to crystallise; others can be more difficult, requiring more specific conditions for significant yields.

1.2.3 Natural Zeolites

Zeolites can also be obtained from geological deposits, requiring the same ingredients as synthetic zeolite synthesis: a source of silica/alumina, a mineraliser, a structure directing agent and water. Natural zeolites crystallise over long time periods from aqueous volcanic matter when subjected to metamorphic conditions. The type of zeolite formed is dependent on a host of factors, chiefly the type of volcanic mater (e.g., magma or ash) and the composition of the water (e.g., alkalinity, ion content)[42]. Natural zeolites can be found worldwide, across all 7 continents; however only around 50 structures have been observed[43]. Furthermore, only three frameworks have had significant industrial relevance due to availability and adsorption properties: clinoptilolite, mordenite and chabazite[44, 45]. These natural analogues are cheap and available as industrially relevant granules for deployment in flow systems. These desirable properties result in the extraction of approximately 1 million tonnes of natural zeolites annually[44]. However, the lack of structural diversity, presence of impurities and significant variation between samples limits their usability.

1.2.4 Zeolite Structures Encountered in this Work

Of the 251 verified zeolite structures, only a handful are encountered as part of this work, namely mordenite (MOR), clinoptilolite (HEU), zeolite P (GIS) and chabazite (CHA). Herein, a brief overview of the structure, properties, and applications of these four frameworks is provided. For further information on any of these structures, or indeed any recognised zeolite framework, please refer to the International Zeolite Association (IZA) database[26].

1.2.4.1 Mordenite

Mordenite (MOR) is an abundant, naturally available zeolite which is also widely synthesised[29]. It adopts the orthorhombic *C m c m* space group with idealised unit cell parameters: $a = 18.256$ Å, $b = 20.534$ Å, $c = 7.542$ Å and $\propto = \beta = \gamma = 90°$[29, 46]. Cations reside in the 12- and 8-membered ring channels which run parallel to the *c* axis (Figure 1.7); however, diffusion between these channels is limited meaning the porosity is essentially one-dimensional[47]. Mordenite systems are extensively deployed as catalysts within chemical industry; even referred to as one of the 'big five' zeolites in catalysts, due to widespread use within the petrochemical industry, in addition to other areas such as the production of methylamine and disproportionation, and in trans-alkylation and hydroisomerisation reactions[48, 49]. Mordenite is also a good sorbent for both CO_2 and H_2[48], and shows promise as an ion-exchange material for removal of heavy metals such as lead[50] and copper[51, 52] from industrial effluents. Additionally, its comparatively siliceous framework and 12 and 8-membered ring channels render it an excellent caesium sorbent[34, 53-55].

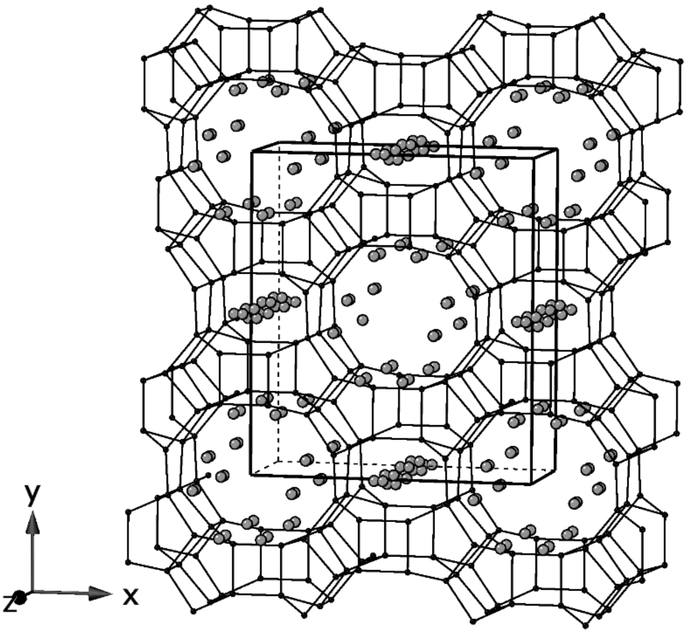

Figure 1.7. Crystal structure of Na-mordenite viewed down 12-ring channels running parallel to *c*-axis. The unit cell and location of sodium cations are displayed.

1.2.4.2 Clinoptilolite

Clinoptilolite (HEU) is the most abundant natural zeolite worldwide, with a structure belonging to the monoclinic *C 1 2/m 1* space group with idealised unit cell parameters: a = 17.523 *Å*, b = 17.644 *Å*, c = 7.401 Å, $\alpha = \gamma$ = 90° and β = 116.1°[46, 56, 57]. 10- and 8-membered ring channels run parallel to the *c*-axis, in addition to an 8-membered ring channel parallel to the *a*-axis (Figure 1.8)[46, 56]. These intersecting channels provide the structure with a three-dimensional pore system. The three-letter code 'HEU' originates from the mineral heulandite, to which clinoptilolite is isostructural[56]. This disparity in nomenclature originates historically; it is now accepted that heulandites have a more aluminous framework (Si/Al < 4) than clinoptilolites (Si/Al > 4)[56, 58]. Despite the high geological abundance of clinoptilolite, synthesis has generally proven difficult[59]. This has restricted applications to processes where natural clinoptilolite is suitable.

Naturally sourced clinoptilolite is inherently cheap as a result of its widespread abundance; this has led to its deployment in a variety of areas, including the agricultural sector, where it is added to livestock feed to improve heath[60-64] and as a soil additive where it aids water retention, nutrient delivery and pH control[65, 66]. It is also available as a dietary supplement to remove heavy metals from the body[67]. Additionally, the material is also deployed in water treatment, notably for the removal of ammonia[68, 69] and in the remediation of aqueous nuclear waste streams, particularly for the abatement of Cs-137[20, 53, 54, 70, 71]. Specific sources of clinoptilolite are even able to be deployed as dual ion-exchange materials which target both Cs-137 and Sr-90; a notable example of this is Mud Hills clinoptilolite, which has been utilised at the Sellafield site since the 1980's, remediating 100s of m^3 of effluent per day[20, 70].

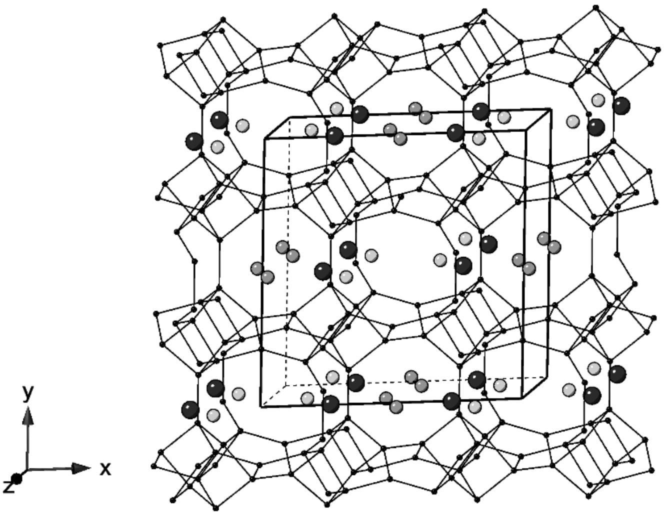

Figure 1.8. Crystal structure of clinoptilolite viewed down the *c*-axis. The unit cell and location of calcium (lightest), potassium (darkest) and sodium cations are displayed.

1.2.4.3 Zeolite P

Zeolite P (GIS) is a medium-pore zeolite adopting the tetragonal $I\,4_1/a\,m\,d$ space group with idealised unit cell parameters $a = b = 9.801$ Å, $c = 10.158$ Å and $\alpha = \beta = \gamma = 90°$[46]. Exchangeable cations reside in the 8-membered ring channels which run parallel to the *b*-axis. The code 'GIS' originates from gismondine, which was the first mineral discovered with this topology in 1817[28]. A widely observed isotypic structure of zeolite P, Na-P1, adopts the *I-4* space group (Figure 1.9). This structure generally has a higher framework aluminium content when compared to mordenite and clinoptilolite, meaning it has a higher cation exchange capacity (CEC). Synthesis methods for this structure are well established[72], with significant work undertaken on routes from unconventional, low-cost and environmentally friendly sources, such as coal fly ash[73, 74], clays[75] and even other zeolite materials[76-80]. Na-P2 is a polymorph of zeolite P which is comprised of alternating *dcc* chains misaligned by 15°[81, 82]. The structure has almost identical unit cell parameters to Na-P1 but does possess slightly smaller 8MR apertures[81, 82]. Zeolite P with maximum aluminium content (Si/Al of 1), also known as MAP, has been mass-produced for use as a detergent where it exchanges its intrapore sodium ions for calcium[36]. Studies have also shown zeolite P to be proficient at removing toxic[83] and radioactive[84] metals from solution in ion-exchange processes. The typically high aluminium content observed in these systems makes them especially suited for the sequestration of charge dense, multivalent species such as Sr^{2+}, due to the increased probability of 'aluminium pairs' and greater net negative charge associated with the zeolite framework[34, 76].

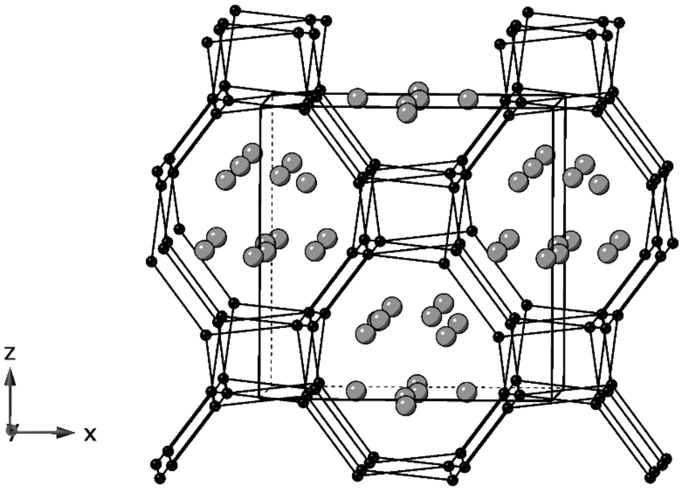

Figure 1.9. Crystal structure of Na-P1 viewed down 8-ring channels running parallel to *b*-axis. The unit cell and location of sodium cations are displayed.

1.2.4.4 Chabazite

The chabazite (CHA) framework belongs to the *R -3 m* space group with idealised unit cell parameters of: $a = b = 13.675$ Å , $c = 14.767$ Å , $\alpha = \beta = 90°$ and $\gamma = 120°$[46, 85]. Interconnecting 8-membered ring channels parallel to the *a*- and *b*-axis and 6-membered ring channels parallel to the *c*-axis grant the framework true three-dimensional porosity in which species can diffuse (Figure 1.10). Chabazite is found naturally and is also simple to prepare, hence its applications span the full range of zeolite science. Natural sources, such as Bowie, Arizona, fulfil low-cost uses, such as a soil and animal-feed additive, in addition to gas separation and ion-exchange applications, where it is particularly useful as an ammonium sorbent[86, 87]. Other natural chabazite sources have also been utilised in the aftermath of the Three Mile Island (1979) and Fukushima (2011) tragedies to remove Cs-137 from contaminated effluent - to which it shows excellent selectivity[21, 88-90]. Chabazite-based synthetic materials have also been shown to catalyse a host of industrially-relevant reactions, including the reduction of NO_x species[91], the dehydrogenation of ethane[92] and the methanol to olefin (MTO) process[93, 94].

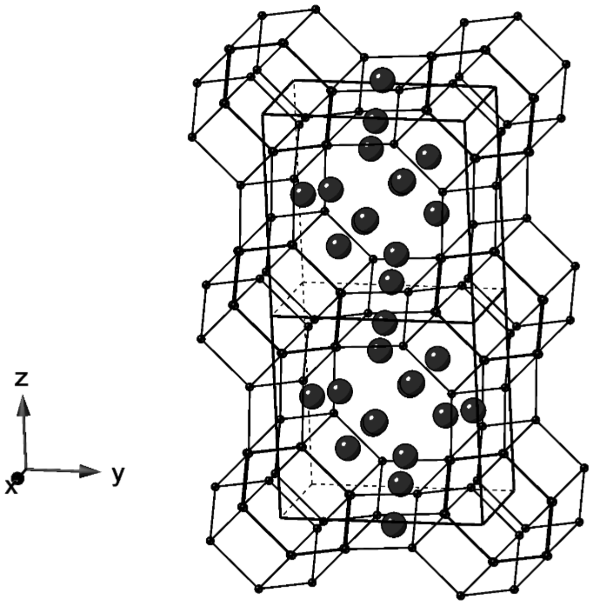

Figure 1.10. Crystal structure of K-chabazite viewed down the *a*-axis. The unit cell and location of potassium cations are displayed.

1.2.5 Zeotypes

To enhance the applicability zeolite structures, significant work has been undertaken investigating the synthesis and properties of zeotypes: materials which possess a zeolite-type framework but are comprised of different elemental motifs. Examples include silicon titanates, which are used extensively for selective sequestration of Cs-137 from nuclear waste streams[95, 96] and umbites, which are tin/ zirconium silicates which have demonstrated the potential to remove Cs-137 from nuclear effluent[97, 98]. Further discussion of the synthesis, properties, and applications of these zeotypes is beyond the scope of this work.

1.2.6 Modifications of Zeolites

The functionality, and therefore applicability, of zeolites is inherently limited by the number of readily available frameworks – hence, there remain promising applications to which we lack a suitable zeolitic material[99]. In work by Pophale[99], half a million zeolite structures with similar stabilities, topologies and geometrical and diffraction characteristics to known structures are highlighted – showcasing the vast disparity between the quantity of known and theoretical structures. This somewhat limited library of zeolite frameworks to select from has driven researchers to investigate novel synthesis methods capable of achieving a greater range of Si/Al ratios, and hence a wider-range of chemistries[100]. The most common method for attaining isostructural frameworks with varied aluminium content is through alteration of the mother liquor composition: higher Si/Al ratio gels can generate higher Si/Al ratio frameworks, and *vice versa*[100]. Additionally, the cation content in the synthesis mixture can steer the Si/Al ratio of the zeolite, as charge balance must be maintained. For example, the inclusion of large, tetrasubstituted ammonium species is common for obtaining high-silica zeolites[100].

While these methods, among others, have successfully expanded zeolite applications, each structure type seemingly remains bound to a range of Si/Al ratios, with mixtures outside of this range not resulting in crystallisation. Furthermore, the range of Si/Al ratios observed in natural zeolites is predetermined and often narrower than synthetic equivalents[29, 56, 85]. Rather than synthesising zeolites with desired framework compositions from the ground up, post-synthetic modifications can be undertaken on existing materials in an attempt to fine-tune their properties[100, 101]. Desilication and dealumination methods can alter the Si/Al ratio of the framework and cation-washing is used regularly to improve functionality. These post-synthetic treatments can also be performed on natural zeolites, expanding their scope for a range of applications.

1.2.6.1 Cation Washing

Cation washing entails exposure of the zeolite to a high concentration of a particular cation species (often sodium). This is normally achieved through use of a salt solution, with the aim of exchanging the cations within the zeolite so only a single pore species is present. This can create space within the structure, which aids intraframework diffusion, and removes species which exhibit a greater thermodynamic or kinetic barrier to exchange[102]. These washings, sometimes referred to as 'activation', are particularly useful when using natural zeolites, as several cationic species are often present within the channels. While this process does not change the zeolite framework itself, a significant improvement to both rate of uptake and capacity can be observed[102, 103]. Similarly, zeolites can be exchanged with protons to free up further pore space and generate acidic sites useful in catalytic processes[25, 102].

1.2.6.2 Dealumination

The dealumination of a zeolitic material entails the selective dissolution of aluminium species from the zeolite structure. This has direct effect on the framework charge-density and hence the adsorption characteristics. Additionally, the potential of mesopore formation can prove advantageous[25, 104]. One method of achieving zeolite dealumination is through acid leaching, where aluminium species are selectively dissolved (Figure 1.11)[100, 105, 106]. This process can be achieved with a variety of mineral and organic acids, typically at elevated temperature[100].

A second dealumination method is steaming, which involves exposure to gaseous water at elevated temperatures, thus hydrolysing Al-O bonds and reducing the framework aluminium content. Notably, this process is used in the manufacture of USY (ultra stable zeolite Y), which is employed industrially in catalytic cracking applications[107]. While dealumination is a useful tool to modify the properties of zeolites, particularly for catalysis applications, it is not without drawbacks. For example, significant dealumination can lead to a loss of crystallinity, or even framework collapse and loss of function.

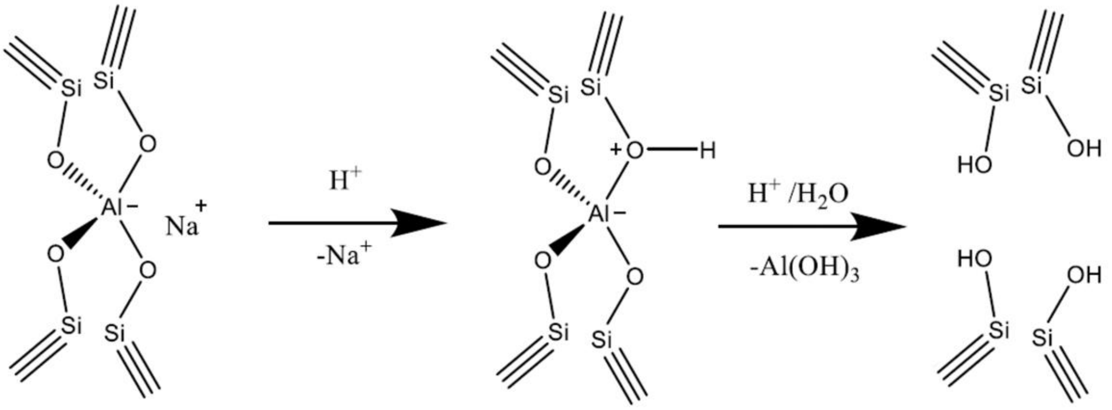

Figure 1.11. Zeolite dealumination by acidic leeching.

1.2.6.3 Desilication

Aqueous hydroxyl (OH^-) anions are capable of hydrolysing Si-O bonds at suitable temperatures. In zeolites, this can result in silicon-based species being selectively extracted from the framework: a process known as desilication, or alkaline leaching. Under these basic conditions, aluminium is also soluble as $Al(OH)_4^-$ [108]. However, the overall effect is net desilication, as silicate species are more readily dissolved[108, 109]. Desilication therefore produces a more aluminous material, which will inherently possess a greater capacity for intrapore cationic species, presuming the overall framework remains intact[110].

The process has also been widely explored as a methodology for the development of mesopores, allowing more zeolite exchange sites to be accessed[111-113]. As silicon tetrahedra adjacent to aluminium are less inert to hydroxyl attack, the degree of mesoporosity able to be developed is inherent of the initial aluminium content: too much aluminium will result in limited mesoporosity and too little can lead to a breakdown of overall structure[114].

1.2.7 Interzeolite Transformations

As discussed, different zeolite structures can possess inherently contrasting properties, and hence functionality. Transformation from one crystalline zeolite phase to another therefore provides means to alter the possible physical and chemical characteristics, influencing the processes it can perform. This process is known as interzeolite transformation (also referred to as interzeolite conversion[115]). Interzeolite transformations are as old as conventional zeolite synthesis; the first synthesised zeolite without a natural counterpart (KFI) was produced from an analcime (ANA) precursor by Barrer[116]. Transformation from parent into daughter phase is generally attained in basic media at elevated temperatures in the presence of an SDA. This method can be utilised to access certain zeolite structures in shorter timeframes and with greater control over framework composition[117, 118].

Despite a multitude of transformations being reported, there has been much debate on the underlying mechanism of conversion, particularly on the size of the pre-nucleation aluminosilicate nanoparts[115, 119-121]. Overall, a consensus on the size and role of nanoparts has not been reached. A brief overview of each of the mechanistic stages in interzeolite transformations (dissolution, nucleation and crystal growth) are discussed, in addition to an overview of typical SDAs, the use of natural zeolites as precursors and the formation of composite zeolites through partial interzeolite transformations.

1.2.7.1 Dissolution

Dissolution is the primary, and often rate-determining[122], step in an interzeolite transformation, where a mineralising agent (typically OH^-) depolymerises the solid parent zeolite *via* hydrolysis. Akin to zeolite desilication, silicon is preferentially extracted in the high pH (> 9) solutions utilised[108, 109]. The basic solutions are also capable of dissolving alumina species as $Al(OH)_4^-$, although to a lesser extent than silicon[108]. Considering this, a very high pH (> 13) is required to dissolve aluminous zeolites (Si/Al < 5). In addition to pH, the temperature is another key parameter in influencing the dissolution process; raising the temperature of transformation will both kinetically and thermodynamically aid zeolite solubility. The choice of SDA is also significant, with organic bases generally promoting slower dissolution to their inorganic counterparts, likely due to their reduced charge density and stability/ steric effects[123].

1.2.7.2 Nucleation

Nucleation is the initial ordering of dissolved species into an orientation representative of the subsequent crystalline solid. Nucleation occurs when the dissolved species reach the supersaturation threshold (where solute concentration exceeds solubility). Products from interzeolite transformations often consist of many small crystallites, indicating that nucleation is a quick process in these systems[124, 125]. The faster dissolution kinetics observed in interzeolite transformations provide a greater degree of supersaturation for nucleation, which is a key parameter in the determining the activation energy barriers (ΔG) of potential thermodynamic and kinetic pathways. This can provide a facile route to zeolite structures which are conventionally difficult to synthesise[126].

At time of writing there is no true consensus on the size of the aluminosilicate species directly involved in the nucleation process despite it being an incredibly active area of research over the last 15 years. Sano proposed that the transformation from low to high framework density zeolites *via* large aluminosilicate intermediates, such as cages or even CBUs, is due to parent-daughter structural similarities[127]. However, many observed transformations do not contain large, shared aluminosilicate units, demonstrating that these rules cannot apply to all systems[119, 128, 129]. Furthermore, these CBU fragments are derived as a 'block' from which the entire structure can be assembled and are unlikely to be completely intact in the solution post-dissolution. Instead, Suhendar postulated that the smaller, ring building units are the best predictor for a successful conversion: transformations between structures with 4 / 5 / 6 - membered rings in common are more likely to be achievable[119]. Furthermore, the Si/Al ratio of the parent zeolite and base concentration are also significant; more siliceous frameworks have a greater probability of yielding structures containing 5 MRs and increased base concentrations tend to generate structures with smaller ring sizes[119].

Additionally, studies have shown that nucleation in transformations with no shared structural units is often faster than amorphous equivalents and that nucleation rates are similar when there are in fact common structural units[130, 131]. However, work by Fichtner-Schmittler[132] found that matching lattice parameters in both parent material and daughter AEI/AFX frameworks were a pre-requisite for transformation, which could be an indication of larger nanoparts. From a general reactivity standpoint, smaller, acyclic oligomers are more likely to participate in the nucleation processes as they can readily expand their co-ordination beyond four, which is paramount for condensation reactions which proceed *via* an S_N2 pathway[133]. Furthermore, larger units are less likely to 'dock' in the required orientation and therefore more likely to re-dissolve[134]. Whatever the identity of the species participating in nucleation, the surface of the parent zeolite provides an ideal site for nucleation to occur, as the aluminous surface attracts a high concentration of SDAs[135]. This is particularly true when smaller, inorganic cations are deployed as SDAs.

1.2.7.3 Growth

The growth stage in an interzeolite transformation is an extension of the nucleation stage, whereby assembly continues *via* many reversible condensation reactions, akin to general zeolite synthesis (1.2.2). In contrast to nucleation, however, a lower degree of supersaturation is required; this renders the zeolite assembly autocatalytic[115]. Further, each condensation reaction releases hydroxyl anions, which increase supersaturation, and hence rate of growth. This results in sigmodal crystallisation curves, where the rate only decreases in the later stages of crystallisation due to the lack of aluminosilicate precursor availability (Figure 1.12). Aluminium yields are typically close to quantitative, as evidenced by very high Si/Al ratios in spent transformation solutions[122, 124]. Once these precursors are sufficiently consumed (no supersaturation), assembly will stop. From here, nucleation of another metastable phase is possible under certain conditions, as per Ostwald's rule of stages[39].

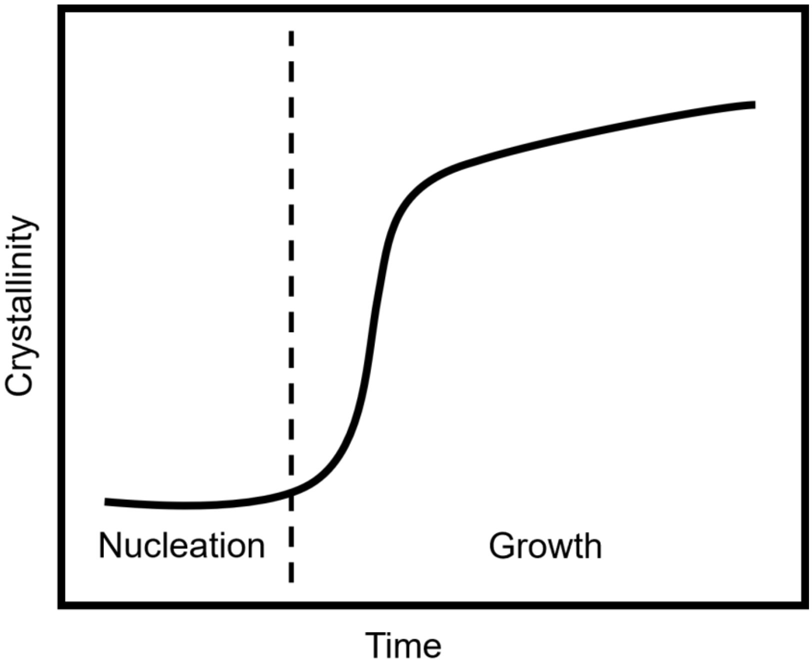

Figure 1.12. Rate of crystallisation in an interzeolite transformation. Dotted line indicates boundary between the nucleation and growth stages of interzeolite transformation.

1.2.7.4 Choice of SDA

The choice of SDA in an interzeolite transformation is paramount in determining whether a transformation will occur, and often what the resultant structure will be. Most transformations utilise SDAs that fall into one of two categories: a tetrasubstituted ammonium species or a metal cation. Tetrasubstituted ammonium species are large and charge-diffuse, favouring crystallisation of large-pore, silicious frameworks; this makes them well suited for generating materials for use in catalysis[136-139]. It is noteworthy that most detailed literature discussion on the finer mechanistic details of transformation have studied these systems which use organic structure directing agents (OSDAs), due to the extensive interest in the methodology to produce catalysts[115, 120, 137]. Furthermore, a vast quantity of potential SDAs are relatively accessible and can be used to dictate transformation product structure[120].

On the contrary, metal cations generally possess greater charge density, which leads to the formation of more aluminous structures, which are well suited to ion-exchange applications. Sodium is the most widely reported metal to fulfil this role[77-80, 140-143], although successful transformations have been achieved using other alkali[78, 141, 144] or alkali earth metals[141, 145, 146]. Metal hydroxides, most commonly sodium hydroxide, function as dual-purpose reagents by providing both the source of hydroxide ions and SDA. The use of sodium hydroxide is especially good for industry due to it being low cost and widely available. Due to the inherently smaller pool of metal cations available, there is less potential for generating structural diversity. However, choice of metal cation can still steer the transformation to a particular product[121, 144].

1.2.7.5 Interzeolite Transformations of Natural Zeolites

The widespread use of natural zeolites is limited by the number of frameworks available in sufficient quantity. Chemical modifications to improve the functionality would enable greater utilisation of these widely available natural resources. One way this can be attained is through an interzeolite transformation, which is readily achieved in caustic conditions. Generally, zeolite P structures are formed with a significantly increased cation capacity; this is consistent with the high charge density of the sodium SDA. Furthermore, transformation can be achieved at accessible temperatures (~ 100 °C), with sodium hydroxide as the sole reagent, thus rendering the process very cost-effective.

The transformation of clinoptilolites, the most abundant natural zeolite, into zeolite P is the topic of many studies[76-80, 147-149]. Transformation is typically achieved at 100 °C in > 2 M NaOH solutions, although temperatures as low as 80 °C[148] and reduced basicities[76] have been used. At least a doubling in the cation exchange capacity (CEC) is observed due to the crystallisation of the more aluminous zeolite P; de Fazio reported this could be further increased through the addition of aluminium sources into the transformation liqour[148]. In the context of remediation of aqueous nuclear decommissioning waste, Mimura reported caesium and strontium capacities of 234 and 161 mg g^{-1} respectively for the fully transformed pseudo-synthetic zeolite P material; this is significantly higher than for the parent clinoptilolite (180 mg g^{-1} caesium, 75 mg g^{-1} strontium)[76]. Similarly, Hong observed an approximate doubling of the strontium capacity (13 to 25 mg g^{-1}) of a mixed clinoptilolite-mordenite natural zeolite upon transformation to zeolite P[149]. In this case, however, there was no significant change to the caesium capacity[149]. Alternatively, fusion with NaOH has also proved an effective method in facilitating the transformation[77, 79]. The intense conditions used (550 °C) can result in a more complete conversion and a greater capacity, although the added complexity and elevated temperatures limit the scalability and hence industrial viability. Natural clinoptilolites can also be transformed to zeolite A with similar methodologies, although the addition of aluminium sources is required[150, 151].

Mordenite is another abundant natural zeolite; it has been observed on all 7 continents, often found collocated with clinoptilolite[80, 149, 152]. Studies examining the transformation behaviour of natural mordenite are limited to parent materials where clinoptilolite is the major component; nonetheless, analogous to clinoptilolite, zeolite P is crystalised at temperatures between 96 and 100 °C in caustic hydrothermal conditions[76, 80, 149].

Little work has been conducted investigating the macroscale mechanism of the interzeolite transformation of natural zeolites. Most studies have been conducted on fine powders, with little to no complementary imaging. Hong studied the transformation using both granular and powdered parent material, monitoring the reaction by SEM[149]. They observed the crystallisation of a new phase, presumed to be zeolite P, on the surface of the structurally decomposed parent[149]. This is consistent with interzeolite transformation nucleation theory (1.2.7.2), which states that crystallisation is preferred on the parent's surface as a result of the large quantity of SDAs attracted to the surface[135].

1.2.7.6 Composite Materials Through Interzeolite Transformation

The presence of two zeolitic structures within a material can be advantageous due to the combination of complementary characteristics. For example, physical mixtures of two zeolite structures can enhance the catalysis process across a host of industrially relevant reactions[153-155]. In ion-exchange systems, complementary sorbents are routinely used for different target species; for example in the aftermath of Fukushima, where a titanate material was used to extract strontium-90 in addition to a host of complementary caesium-137 sorbents[21]. It is conceivable that a single, tuneable, composite material could enhance performance and streamline material selection for these applications. Interzeolite transformations are well-suited to form these composites where there is significant overlap between dissolution of the parent phase and nucleation of the new phase; the transformation can then be 'quenched' at a given time to yield a preferred mixture of phases.

Formation of such composite zeolites for use as catalysis is an incredibly active area of research. Mendoza-Castro[156, 157] formed hybrid FAU/MFI and FAU/BEA zeolitic materials for catalytic applications using a carefully selected SDA which also acted as a surfactant. The prepared materials were mostly amorphous, comprised of building blocks from both zeolite systems. The interruption of the transformation at suitable times allowed for fine-tuning of the materials' properties[156, 157].

The development of such zeolite composites for ion-exchange applications is a far more underdeveloped area, currently limited to 'accidental' synthesis, as complete transformation to zeolite P is seen as desirable. The high sodium hydroxide concentrations deployed to completely convert the material accelerate the rate of dissolution to such an extent that complete framework breakdown of the parent material is achieved before growth of the new phase is detected[149]. Composite zeolites were formed *via* interzeolite transformation by Delaspozas[78], who slowed the rate of dissolution by pre-exchange with potassium and therefore unintentionally facilitating the formation of clinoptilolite/ zeolite P composites. The properties of these materials were not explored. In addition to the introduction of the newly-crystalised phase, partial transformation has potential to benefit the parent material *via* desilication and formation of mesopores.

1.3 Summary

Overall, there is a requirement to develop new ion-exchange materials to efficiently process nuclear effluent produced though both routine operations and decommissioning efforts. Zeolites have been extensively utilised by the nuclear industry for this purpose but are limited by the number of available framework types[21, 70]. One method to diversify natural zeolites is by means of transformation to zeolite P[76-80, 147-149]. This approach has been shown to significantly increase the cation exchange capacity, however, how the phase change affects the selectivity and kinetics of exchange has not been investigated. Furthermore, the potential of partial conversion, in particular how much control can be exerted on the process and the subsequent ion-exchange properties, is underexplored, in addition to the formation of granular analogues, which are capable of deployment in columns.

The aim of this work is to investigate the partial interzeolite transformation of natural zeolites as a means to enhance the ion-exchange proficiency for caesium and strontium, two species of particular relevance to the nuclear industry.

CHAPTER 2: EXPERIMENTAL

2.1 Characterisation

2.1.1 X-ray Diffraction

Diffraction experiments are the most important methods for determining the structure of crystalline solid materials. The diffraction, or scattering, of electromagnetic radiation occurs when it passes through apertures comparable in size to its radiation wavelength (λ); such is the case with spacings between planes of atoms in crystalline materials and X-rays[158]. To understand the principles of X-ray diffraction, a basic understanding of crystallography is required.

2.1.1.1 Basic Crystallography

A crystalline material consists of a repeating structure of molecules, atoms, or ions. The structure can be described by a unit cell, which is defined as the smallest three-dimensional unit from which the entire structure can be assembled. Unit cells are described by lattice constants corresponding to both the side lengths (a, b and c) and the corresponding angles between the sides (α, β and γ). α is the angle between sides b and c, β between a and c, and γ between a and b. Seven possible crystal systems exist, each with a different unit cell geometry (Table 2.1)[158-160].

Table 2.1. Unit cell geometries of the seven possible crystal systems.

Crystal system	Axes restrictions
Cubic	$a = b = c$, $\alpha = \beta = \gamma = 90°$
Tetragonal	$a = b \neq c$, $\alpha = \beta = \gamma = 90°$
Orthorhombic	$a \neq b \neq c$, $\alpha = \beta = \gamma = 90°$
Hexagonal	$a = b \neq c$, $\alpha = \beta = 90°$, $\gamma = 120°$
Trigonal	$a = b = c$, $\alpha = \beta = 90°$, $\gamma = 120°$
Monoclinic	$\alpha = \beta = 90°$
Triclinic	-

These 7 crystal systems produce 14 Bravais lattices, which are infinite arrays of fixed points, shown in the 19th century to be the only mathematical description of crystal lattices[160]. Another important concept is crystallographic point groups: a set of symmetry operations which can be applied to the atoms in a unit cell to generate an infinite lattice. Due to crystallographic limitations, there are only 32. Combining with a point group, a Bravais lattice produces a space group, which contains both the cell symmetry and the symmetry operations required to produce the infinitely extending lattice[160].

An alternative way to envisage crystal structures is by considering them assembled by parallel planes of atoms, known as lattice planes. These planes are separated by a distance, the interplane spacing (d_{hkl}), and are identified by Miller indices, which assume the format (*hkl*). In this description, *h, k and l* are the reciprocal of the fractional coordinates where the plane intersects the *a*, *b* and *c* axis of the unit cell, respectively[158-160]. Where a plane runs parallel to an axis, the appropriate Miller index is zero[158, 159]. In crystalline systems, the interplane spacing, d_{hkl}, is comparable to the wavelength of X-rays, which are therefore elastically scattered by the electrons present in solid structures[158-160]. This phenomenon underpins the concept of X-ray diffraction experiments.

2.1.1.2 Braggs Law

Considering the scattering of X-rays as a reflection between two parallel planes of atoms, separated by a distance *d* (Figure 2.1), then the angle of incidence, θ, at which constructive interference occurs can be derived. This relationship is commonly referred to as Bragg's Law (Equation 2.1).

$$\text{Equation 2.1:} \qquad n\lambda = 2dsin(\theta)$$

In a diffraction experiment, the diffraction maxima, or reflections, which occur upon satisfaction of Bragg's law, are determined through variation of the angle of incidence, θ. Each reflection arises from a set of lattice planes. Inspection of these maxima reveals the interplanar spacings present within a single lattice, facilitating detailed structural analysis. Two principal experiments are routinely performed: powder X-ray diffraction (PXRD) and single crystal X-ray diffraction.

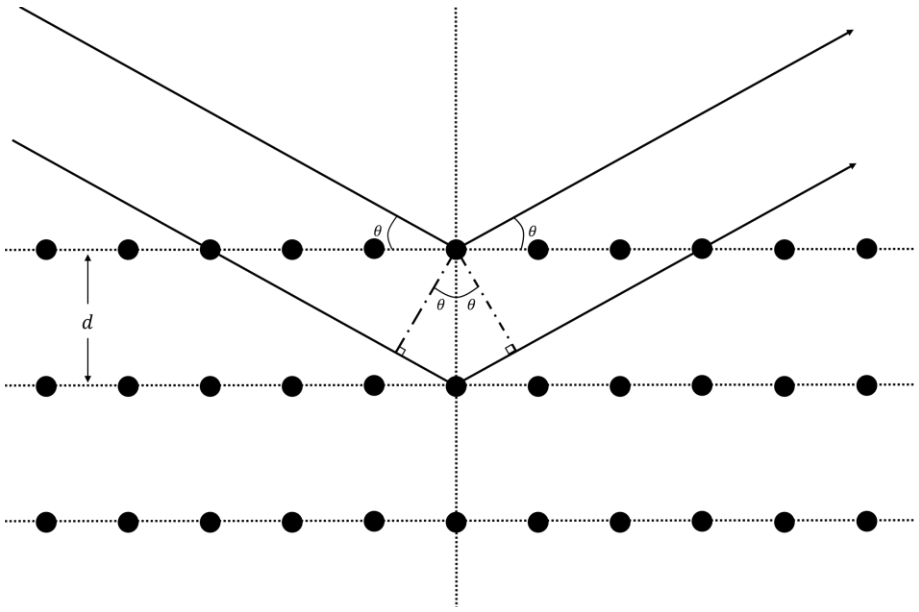

Figure 2.1. Schematic of the scattering of X-rays by two parallel planes of atoms.

2.1.1.3 Powder X-ray Diffraction

A powder, or polycrystalline, sample is comprised of a multitude of single crystallites arranged in a random distribution. Reflections will occur at angles where Bragg's law (2.1.1.2) is satisfied, but the X-rays will interact with each crystallite independently, meaning the beam is scattered in all directions. In older diffraction experiments, the diffracted radiation was observed on films, where a series of annular rings were observed; each ring is formed from contributions from many crystallites from a specific reflection (Figure 2.2)[161]. In more modern setups, a detector passes 'through' these rings by rotating around the sample in a circular manor. Diffraction intensity is then measured as a function of the detector angle, resulting in the more commonly interpreted diffraction pattern[160, 161].

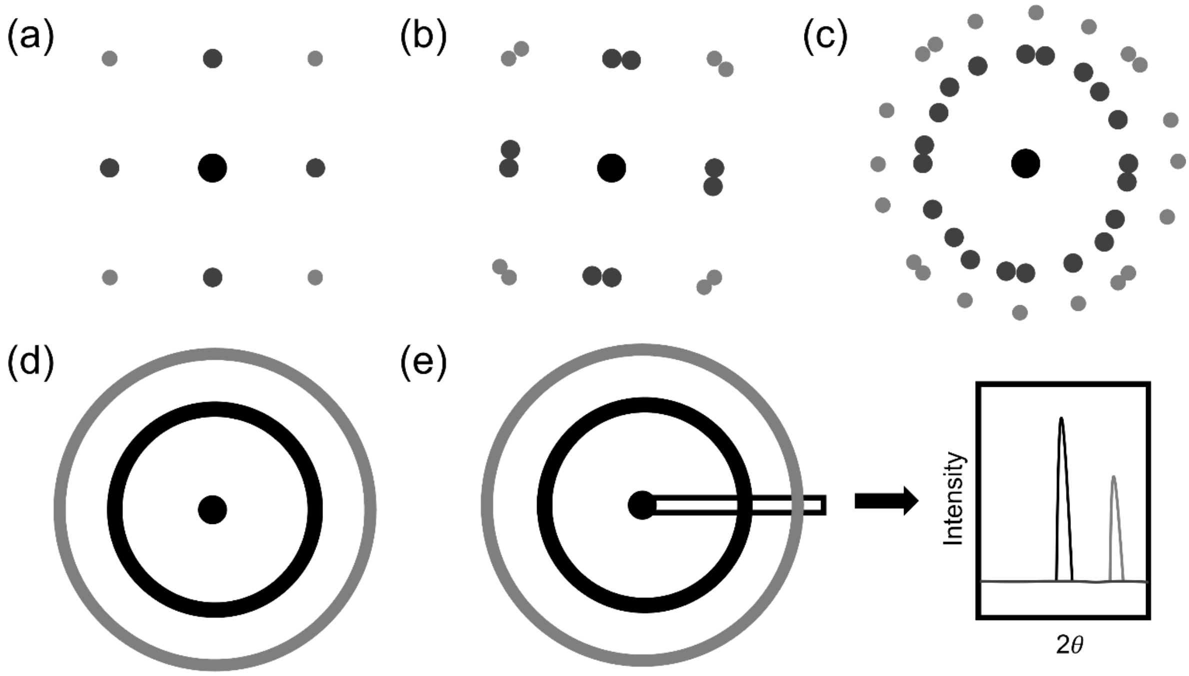

Figure 2.2. Formation of powder diffraction rings. (a) Example contribution from a single crystallite. (b) Example contribution from two crystallites in different orientations. (c) Example contribution from five crystallites in different orientations. (d) Powder diffraction rings. (e) Conversion of diffraction rings into PXRD pattern.

Each peak in the diffraction pattern corresponds to a set of lattice planes, often enabling facile phase identification. The intensity of reflections is proportional to the square of the structure factor, F_{hkl}[160]. This is proportional to the scattering power of the atoms comprising the material (f_{hkl}), where it is greatest for heavier atoms due to the increasing quantity of electrons[159, 160]. Where multiple phases are present within a given material, reflections from both phases are observed, with the intensities scaling with the fraction of each phase in the material. PXRD is therefore incredibly useful for determining the ratios of multiple phases within a material.

2.1.1.4 Rietveld Refinement

Developed in the late 1960's by Hugo Rietveld, a Rietveld refinement is a technique used in crystallography to determine the arrangement of atoms in a crystalline system from diffraction data[162, 163]. It involves calculating a theoretical pattern based on multiple parameters such as atomic positions, occupancies and thermal vibrations (terms to model the peak shape and background are also included). This model pattern is then compared to experimental data and parameters are repeatedly refined in order to minimise the disparities between the theoretical and observed patterns. An initial crystal model is required to begin the refinement – meaning prior knowledge or a crystallographic database is required. Multi-phase Rietveld refinements can also determine the relative weight fractions (W_f) where multiple crystalline phases are present.

2.1.1.5 Pair Distribution Function

The pair distribution function (PDF) is a mathematical function used in materials science to describe the probability of distances between atoms. It is particularly useful in the study of semi-crystalline or amorphous materials where conventional crystallographic methods are insufficient due to the lack of long-range order. Unlike conventional crystallography, both Bragg and diffuse (non-crystalline) scattering are considered[164].

To obtain the PDF, diffraction experiments are first performed on the material. The total scattering in *Q* space, *S(Q)*, is obtained, prior to being weighted by *Q* and levelled to generate *F(Q)*. *F(Q)* is then Fourier transformed with respect to *Q* to obtain *g(r)*, the PDF, which represents the probability of finding an atom at a particular distance, *r*, from another atom[164]. Interpretation of this probability distribution provides information on the local structure of the material. This is crucial in the identification and understanding of materials with no long-range order, such as glasses, or nanomaterials, where crystallographic domains are too small for conventional crystallographic techniques to be applied[164, 165]. For the Fourier transform to be as accurate as possible a large *Q*-range is required, meaning smaller wavelengths and higher scattering angles are preferable. Experimentally this is best achieved using synchrotron radiation and positioning the detector close to the sample[164].

2.1.2 X-ray Fluorescence Spectroscopy

X-ray fluorescence (XRF) spectroscopy is a widely used elemental analysis method which utilises characteristic X-rays emitted from atoms that have been bombarded with high-energy X-rays to quantitatively determine chemical composition[166]. Providing the energy of the incoming X-ray is sufficient, electrons are expelled from the given orbital, leaving a partially vacant core orbital, into which an electron from a higher energy level falls. This process emits an X-ray equal in energy to the difference in the two energy levels, characteristic of the elemental species. An XRF spectrum can be used to determine the presence/concentration of specific elements. The probability of this phenomena occurring is known as the fluorescence yield, ω, which increases with atomic number: boron has a fluorescence yield of 10^{-4} whereas uranium approaches 1[166]. The characteristic transitions are described with Seigbahn notation, where K, L and M describe the energy level in which the X-ray releasing electron relaxes into (s, p or d respectively), Greek letters (α, β etc.) portray how many shells higher that electron is coming from, and finally subscript numbers denote the subshell that the electron has come from (1 being the highest energy)[166]. For example, an electron relaxing from the highest energy 2p subshell into a vacancy in the 1s orbital is denoted Kα_1[166]. The K$\alpha_1$emission is shown in Figure 2.3, in addition to four other emissions.

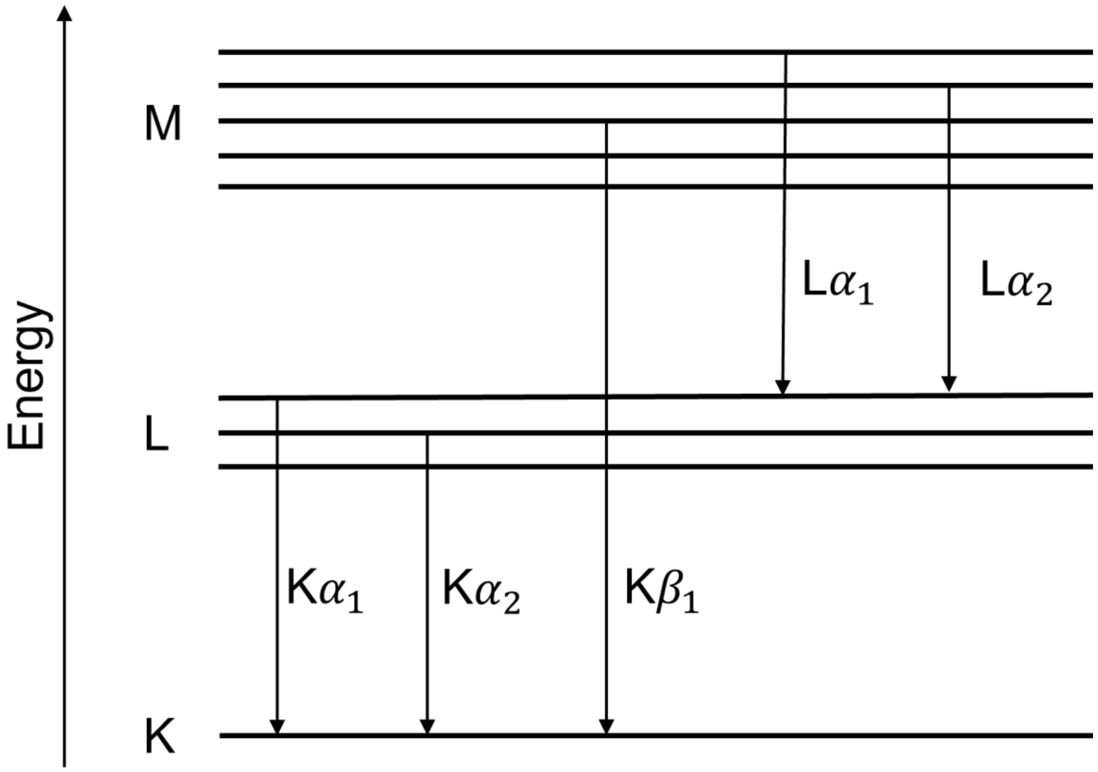

Figure 2.3. Atomic electronic transitions (Siegbahn notation).

XRF spectrometers, such as the Bruker S8 Tiger used in this work, are comprised of an X-ray source, a sample chamber, a detecting system and a data processing system. Two types of detector systems are used: wavelength dispersive XRF (WD-XRF) and energy dispersive XRF (ED-XRF). In WD-XRF, emitted X-rays are separated prior to detection by a series of dispersing crystals; geometrical manipulation of these crystals and the scintillation detector facilitate sequential measurement of emitted X-rays[166]. Energy-dispersive systems directly measure emitted X-rays using a semiconductor detector, which converts the X-ray into an electrical pulse with intensity proportional to its inherent energy[166].

Three methods of sample preparation are routinely used in XRF spectroscopy of solids: loose powder, pressed pellet or fused bead, where a closely packed, homogeneous sample with a flat surface is analysed. Loose powder is the least labour intensive, requiring only thorough grinding prior to analysis, however, significant void space remains present in the sample and the surface is not completely smooth, resulting in poorer data than the other two methods[166]. Pressed pellets involve mixing with an organic binder before compression of the sample in a die set; this gives a better representation of the sample than loose powder and is very useful in the detection of trace elements (ppm range)[166]. Fused beads possess near perfect homogeneity and are formed through by mixing some finely ground sample with a flux and exposure to elevated temperatures[166]. As the sample is significantly diluted during this process this method is somewhat unsuitable for the accurate determination of trace elements[166]. Qualitative analysis of XRF spectra is achieved through observation of elemental-specific emission lines, where the integrated intensity is proportional to the concentration.

2.1.3 Solution Elemental Analysis

2.1.3.1 Inductively Coupled Plasma Optical Emission Spectroscopy

Inductively coupled plasma optical emission spectroscopy (ICP-OES) is a widely used technique in analytical chemistry to determine concentrations of metal species in aqueous solutions. In operation, a liquid sample is introduced into the ~6000 °C plasma torch by means of a nebuliser. Upon entering the plasma, rapid evaporation of the aerosol droplets occurs leaving small solid particles, which subsequently atomise and ionise, resulting in a cloud of positively charged atoms and ions[167]. The high-energy environment generated by the plasma affords excited species, which subsequently relax, emitting light in the process; the intensity of this light at specific wavelengths is used to determine the elemental concentrations by direct comparison to solutions of known concentrations. ICP-OES is an excellent method for the determination of a large variety of trace metal concentrations routinely down to the low ppm range[167]. In subsequent chapters, ICP-OES is utilised for the determination of strontium concentrations in aqueous solutions.

2.1.3.2 Inductively Coupled Plasma Mass Spectrometry

Inductively coupled plasma mass spectrometry (ICP-MS) is distinguished from ICP-OES by its method of detection; the mass-to-charge ratio of ions generated in the plasma is measured using an in-built mass spectrometer[168]. ICP-MS has several advantages over ICP-OES, such as: greater sensitivity, lower limits of detection, less spectral interference, the ability to distinguish isotopes and greater elemental coverage[168]. This had led to extensive use in ultra-trace metal analysis and isotopic analysis, where ICP-OES is inadequate[168]. In subsequent chapters, ICP-MS is used for the determination of caesium concentrations. Caesium is very readily ionised and preferred emission lines are from atomic species; this results in very poor resolution when using ICP-OES.

2.1.4 Imaging Techniques

2.1.4.1 Scanning Electron Microscopy

The resolution of optical microscopes is inherently limited by the wavelength of light, which allows for a resolution of ~250 nm. Electrons have a much smaller wavelength than visible light (0.01 nm), facilitating a much higher resolution when used in microscopy[169]. This underpins scanning electron microscopy (SEM), a technique widely utilised to provide information on the topography of solid materials[169]. In SEM, electrons are produced by an electron gun and focused by a series of lenses before being projected in the sample. This highly focused beam scans the sample area, where three key interactions can occur: electron backscattering, secondary electron emission and the release of characteristic X-rays. Both backscattered electrons and secondary electrons are widely used to produce high resolution images of samples. Analogous to the process described in Section 2.1.2 in XRF analysis, electron bombardment may also ionise core electrons, resulting in an electron vacancy. The consequent filling of this vacancy by an electron from a higher energy orbital produces characteristic, element-specific X-rays, which can be interpreted to provide real space elemental mapping, termed energy dispersive X-ray spectroscopy (SEM-EDS)[169]. In subsequent chapters, SEM is used to assess the surface morphology of zeolitic materials and SEM-EDS is used for elemental analysis.

2.1.4.2 Computed Tomography

A material's ability to absorb X-rays is contingent on the electron density, which is directly linked to the material's density and elemental composition; the fraction of X-rays able to pass through a substance is dependent on these properties. Traditional X-ray imaging utilises this phenomenon to image bones inside the human body, as their denser structure absorbs a greater proportion of X-rays than surrounding tissue[170, 171]. In an X-ray computed tomography (XCT) experiment, X-rays are fired at the target from multiple directions; this is either achieved through rotation of the material or movement of the X-ray source. Each of these X-rays is attenuated by a varied degree dependent on the phases encountered; the resultant intensity is detected from every direction. This data is compiled and processed computationally to provide cross-sectional images of the material, which can be individually assessed or rendered into three-dimensional models[171]. In subsequent chapters, XCT measurements of granular zeolitic materials are performed at the K11 Dual Imaging and Diffraction (DIAD) beamline, Diamond Light Source, UK.

2.1.4.3 K11 DIAD at Diamond Light Source

The Dual Imaging and Diffraction (DIAD) beamline, located at Diamond Light Source, UK, enables users to perform full-field imaging/tomography and micro-diffraction experiments quasi-simultaneously[172]. An X-ray beam originating from the synchrotron storage ring is split into two: a monochromatic/pink beam is used for radiography and tomography, and a diffraction beam between 13 x 4 μm and 50 x 50 μm is used for collection of local diffraction data. One key feature is the ability to perform image-guided diffraction experiments in real-time according to imaging data. The ability to switch between imaging and diffraction modes quasi-simultaneously is only possible due to the unique optical arrangement[172]. In subsequent chapters, zeolitic materials are examined at K11 DIAD by mounting single granules on a rotation-enabled, fully controllable stage.

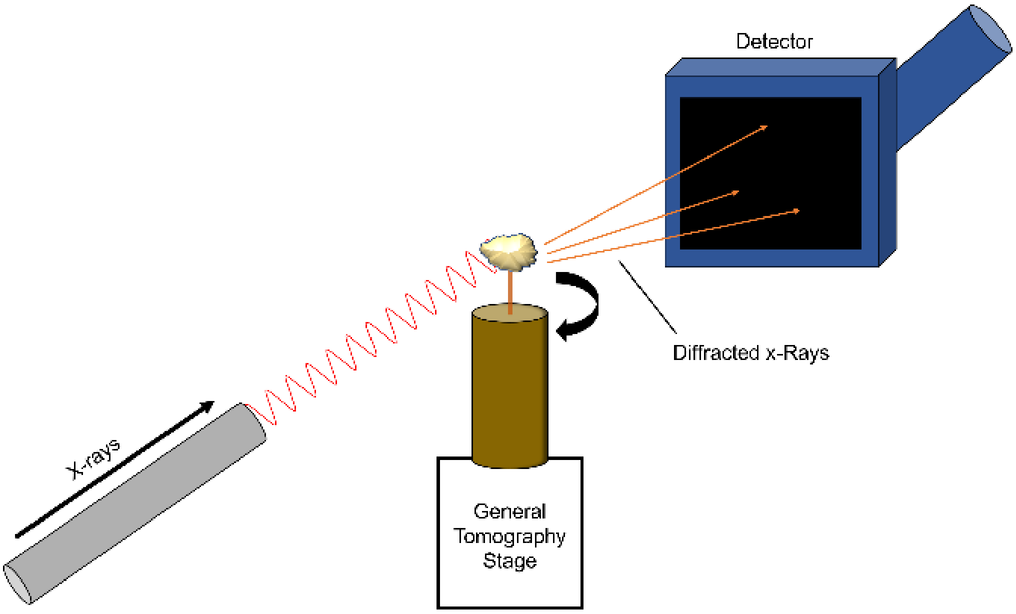

Figure 2.4. K11 DIAD experimental setup schematic.

2.1.5 Solid State NMR

Nuclear magnetic resonance (NMR) spectroscopy exploits the magnetic properties of atomic nuclei to provide information on the chemical environment of a particular atomic species. For a nucleus to be NMR active, it must possess angular momentum, or spin (*I*)[173]. This is true where the nuclei have either an odd number of protons, or neutrons, or an odd number of both. A nucleus with spin, *I*, will have *2I* + 1 possible orientations, which are degenerate in the absence of an external magnetic field. In an NMR experiment however, these spin active nuclei are placed in an external magnetic field, splitting the energy levels[173]. The distribution of these nuclei within these energy levels is then determined thermodynamically by the Boltzmann distribution[158], meaning lower energy levels are slightly more populated than higher energy levels. Next, a radiofrequency (RF) pulse at the Larmor frequency (the frequency at which nuclei precess around the magnetic field) is applied perpendicular to the magnetic field. Nuclei absorb this energy and are promoted from the lower energy state to the higher energy state, prior to relaxation back to the equilibrium, or Boltzmann, position. This produces a time-resolved NMR signal representing the free induction decay (FID), which is Fourier transformed to produce the

NMR spectrum[173]. Crucially, the time taken for the given nuclei to relax is dependent on the chemical environment, meaning the final spectrum provides information of all the chemical environments in the sample for the probed species[158, 173].

Most NMR experiments are conducted on liquid samples, with the compound of interest dissolved in an appropriate solvent. Rapid isotropic tumbling of the molecules minimises spectral broadening from effects including dipole-dipole interactions, chemical shift anisotropy and electric quadrupole interactions, which all have a dependence on $3\cos^2\theta - 1$. In solid samples, no such tumbling occurs, resulting in broad spectral lineshapes[158]. However, rapid rotation of the sample at the 'magic angle' of 54.74° with respect to the direction of the magnetic field introduces artificial motion and reduces peak broadening. This technique is termed magic angle spinning nuclear magnetic resonance (MAS-NMR) and is widely practiced for the study of solid materials, including natural minerals[174].

2.1.6 Radiometric Counting

2.1.6.1 Gamma Spectroscopy

Gamma radiation is released as part of the radioactive decay pathway of many radionuclides[175]. This occurs when an excited nucleon, typically produced as a result of alpha or beta decay, emits a photon of discrete energy, thus demoting the species to a lower energy state. In gamma spectroscopy, the energy and frequency of these photons is detected by either a scintillation- (e.g., NaI(Tl)) or semiconductor based detector. Detectors are heavily shielded to reduce background signal from the environment. As the emitted photons have discrete energy, species can readily be distinguished and concentrations accurately determined through integration of the spectral peaks[176]. In this work, gamma spectroscopy was used to determine the concentration of aqueous Cs-137.

2.1.6.2 Cherenkov Counting

When the velocity of a charged particle exceeds the speed of light in a medium, energy is lost by the particle as it retards to the speed of light in the form of electromagnetic radiation, typically in the violet-ultraviolet region. This phenomenon, named Cherenkov radiation, can be utilised to determine the concentration of high-energy beta emitters, such as Y-90[176]. In this work, Cherenkov counting was used to determine the concentration of Sr-90 though indirect measurement of beta radiation emitted by Y-90.

2.2. Adsorption Experiments

Adsorption refers to the process whereby an adsorbate adheres to an adsorbent. Weak van der Waals and dipole-dipole interactions can both contribute to the adhesion, in addition to stronger chemical bonding[158]. In this work, the adsorption of cationic species into zeolitic materials, *via* an ion-exchange process (1.1.1.4), is studied. Two principal methods in ion-exchange testing are batch and flow/column experiments, which are hereby discussed in turn.

2.2.1. Batch Adsorption Experiments

In batch experiments, a particular mass of adsorbent, such as a zeolite, is added to a solution with a particular concentration of adsorbate (Figure 2.5). Sometimes, agitation or heat is provided to drive the ion-exchange process. At the end of the experiment, the overall decontamination factor (DF) can be determined by dividing the initial concentration by the final concentration.

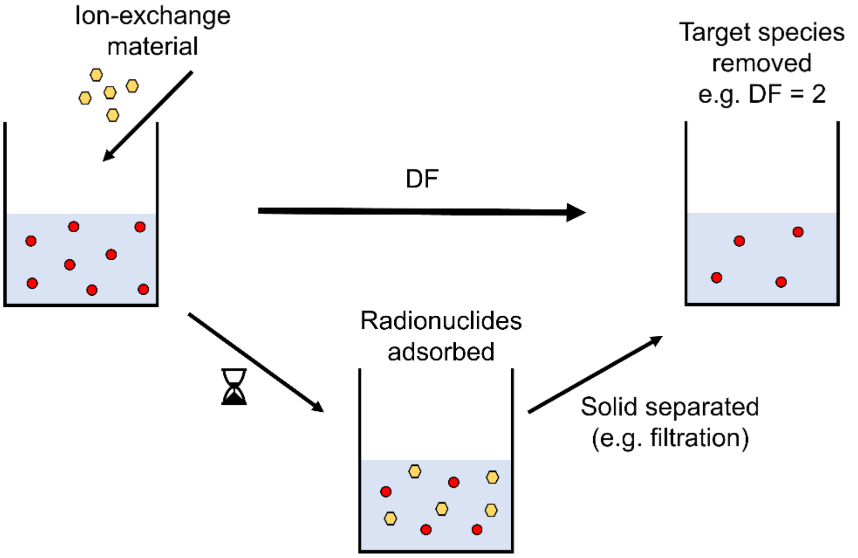

Figure 2.5. Schematic of a batch ion-exchange experiment.

When left to equilibrate, batch experiments can be utilised to determine the capacity of a material for a given adsorbate *via* adsorption isotherms[158]. Here, a range of adsorbate concentrations are utilised, with the equilibrium uptake (q_e) plotted as a function of the equilibrium concentration of solution (C_e). Adsorption isotherm models can then be fitted to the data. Models used in this work include the Langmuir, Freundlich, Temkin and Langmuir-Freundlich equilibrium adsorption isotherm models.

These batch adsorption experiments can also be kinetically resolved, where the adsorbate uptake (q_t) is plotted as a function of time. This provides valuable information about the rate of exchange, which is often crucial in industrial applications. Kinetic isotherm models can be fitted to the data. In this work the 2nd order kinetic and Elovich models are applied to kinetic data. A summary of all the isotherm models used in this work (both equilibrium and kinetic) is provided herein.

2.2.1.1 Langmuir Adsorption Model

The Langmuir adsorption model is a two-parameter isotherm model which assumes monolayer adsorption coverage and no sorbate-sorbate interactions. The rate of adsorption is assumed to be dependent on both the free space on the solids surface and the solution concentration, which gives rise to Equation 2.2[177]:

Equation 2.2: $$q_e = \frac{bC_e q_m}{1+bC_e}$$

Where q_e is the species uptake by the solid at equilibrium, C_e is the solution concentration at equilibrium, q_m is the sorption capacity, and b is a constant. Mathematical manipulation facilitates expression of the model in linear form (Equation 2.3), whereby linear regression can be applied to determine b and q_m:

Equation 2.3: $$\frac{C_e}{q_e} = \frac{1}{bq_m} + \frac{C_e}{q_m}$$

2.2.1.2 Freundlich Adsorption Model

The Freundlich adsorption model is a two-parameter isotherm model which assumes a heterogeneous surface, with an exponential distribution of active sites and energies. This gives rise to Equation 2.4, which can be manipulated into Equation 2.5 – facilitating the use of linear regression methods to determine parameters K_f and n, which represent the sorption capacity and a constant related to energy of sorption, respectively[177].

$$\text{Equation 2.4:} \quad q_e = K_f C_e^{1/n}$$

$$\text{Equation 2.5:} \quad \log(q_e) = \log(K_f) + \frac{1}{n}\log(C_e)$$

2.2.1.3 Temkin Adsorption Model

The Temkin adsorption model is a two-parameter isotherm model which takes into account adsorbate-adsorbate interactions; it is also assumed that ΔH decreases linearly as the number of available sites is reduced; this gives rise to Equation 2.6[177]:

$$\text{Equation 2.6:} \quad q_e = \frac{RT}{B_t} ln(A_t) + \frac{RT}{B_t}\ln(C_e)$$

Where R is the universal gas constant (8.314 J mol^{-1} K^{-1}), T is temperature (K), B_t is a Temkin constant (J mol^{-1}) and A_t is a Temkin isotherm constant. No rearrangement is required to determine parameters though linear regression methods.

2.2.1.4 Langmuir-Freundlich Adsorption Model

The Langmuir-Freundlich adsorption model is a three-parameter isotherm model which, as the name suggests, is a combination of the Langmuir and Freundlich adsorption models; it describes the distribution of adsorption energy over a heterogeneous surface (Equation 2.7)[177]:

$$\text{Equation 2.7:} \quad q_e = \frac{q_{max}(KC_e)^n}{1+(KC_e)^n}$$

At low levels of sorption, the model closely resembles the Freundlich model, whereas at higher adsorbate concentrations, the equation becomes the Langmuir model. q_{max} describes the maximum adsorbate concentration, *K* is an equilibrium constant, and *n* is a heterogeneous parameter with value between 0 and 1[177]. Non-linear regression methods are necessary to determine these parameters.

2.2.1.5 Pseudo 2nd Order Kinetic Model

This model is applied to kinetically resolved data and assumes the rate-limiting step to be chemisorption, with the adsorption rate dependent on the capacity of the material. The differential equation for the pseudo 2nd order kinetic model is shown below (Equation 2.8), where *k* is the 2nd order rate constant, q_e is the equilibrium sorption capacity and q_t is the sorption at a given time t[177].

$$\text{Equation 2.8:} \quad \frac{dq_t}{dt} = k(q_e - q_t)^2$$

Mathematical manipulation results in the pseudo 2nd order kinetic model being expressed in the following form (Equation 2.9), where a plot of $t/\,q_t$ as a function of time yields a linear plot from which the second-order rate constant (*k*) and the equilibrium adsorption capacity (q_e) can be readily determined.

$$\text{Equation 2.9:} \quad \frac{t}{q_t} = \frac{1}{kq_e^2} + \frac{t}{q_e}$$

2.2.1.6 Elovich Model

The Elovich model is closely related to the pseudo 2nd order kinetic model but assumes a heterogeneous sorbent surface. Surface deactivation phenomena therefore contribute to the reduction in sorption rate over time. The differential equation is shown (Equation 2.10), where α is the initial rate of adsorption, β is the desorption constant and q_t is the sorption at a given time, t[177].

$$\text{Equation 2.10:} \quad \frac{dq_t}{dt} = \alpha e^{-\beta q_t}$$

Integration, the application of boundary conditions and the assumption that $\alpha\beta t \gg t$, generates Equation 2.11. If a good fit is observed between the data and the model, a plot of q_t versus *ln(t)* yields a linear relationship, from which α and β can be readily derived.

Equation 2.11: $q_t = \frac{1}{\beta}\ln(\alpha\beta) + \frac{1}{\beta}\ln(t)$

2.2.2 Columnar Adsorption Experiments

While batch experiments are simple to conduct, many industrial processes operate using a columnar system, where solution is passed through a stationary bed of ion-exchange material (Figure 2.6). Columnar operation is preferred due the more efficient use of material and greater DF's. Put simply, an ion-exchange column can be regarded as a series of sequential batch experiments, where the DF's 'stack' accordingly, often resulting in high levels of remediation (Figure 2.6).

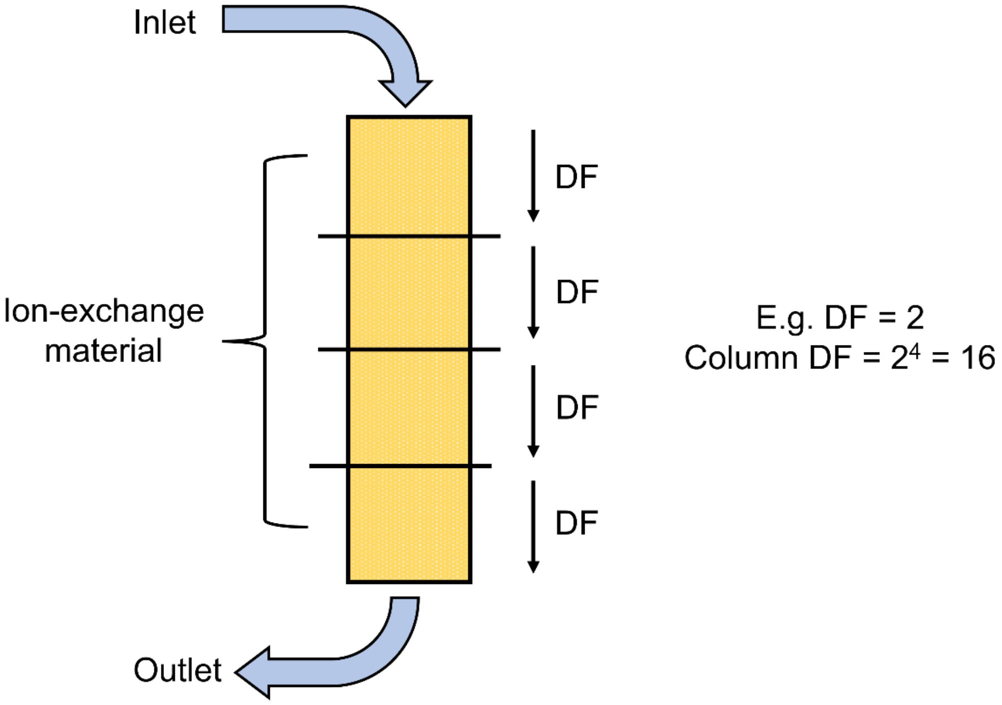

Figure 2.6. Schematic of a columnar ion-exchange setup.

In traditional column experiments, the adsorbate breakthrough is plotted as a function of volume (through column). Results from such columnar experiments are incredibly valuable, as the conditions can be tailored to mimic plant[70]; however, they require the ion-exchange material to be in granular form, are time consuming, and produce lots of waste.

2.2.2.1 The Rapid Ion Exchange (RIX) Method

To facilitate dynamic flow testing in a short timeframe, while simultaneously requiring less ion-exchange material and producing less waste, the Rapid Ion Exchange (RIX) method was developed by Sellafield Ltd and National Nuclear Laboratory (NNL). Here, a reservoir of solution is passed through a small quantity (e.g., 0.1 g) of ion-exchange material, prior to recirculation back into the reservoir (Figure 2.7). The concentration of the reservoir is then plotted as a function of volume (through column). A faster decrease in the rate of reservoir concentration indicates more adsorption is taking place and the loaded ion-exchange material is more proficient.

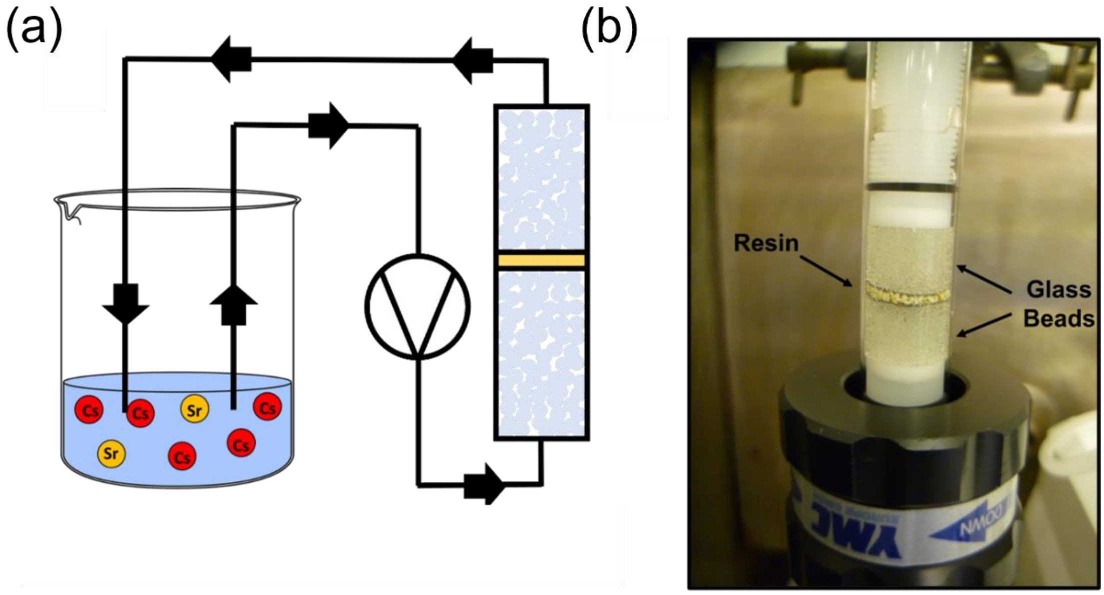

Figure 2.7. Rapid Ion Exchange (RIX). (a) Schematic. (b) Photograph.

In the RIX experiment, equal volumes of liquor are both extracted out of and extruded into the reservoir over any given time period. The concentrations of column output (C_{output}) and column input (C_{input}) can be linked using Equation 2.12, where α is the probability of sorption.

Equation 2.12: $C_{\mathrm{output}} = C_{\mathrm{input}} \times \alpha$

Considering this scenario, where a given volume is flown though the column (V_f) in a set time, the following equation (Equation 2.13) can be constructed, where C_x and $C_{x\text{-}1}$ are the final and initial concentration of the reservoir, which has associated volume (V_r):

Equation 2.13: $C_{\mathrm{x}} = \frac{(V_r - V_f)C_{x-1}}{V_r} + \frac{V_f(1-\alpha)C_{x-1}}{V_r}$

Considering the change in reservoir concentrations over a given time period, $\frac{dC}{dt}$, produces Equation 2.14.

Equation 2.14: $\frac{dC}{dt} = C_x - C_{x-1}$

Combining Equations 2.13 and 2.14 produces Equation 2.15, which provides a model for the reservoir concentration (C).

$$\frac{dC}{dt} = C_{x-1}(V_r - V_f\alpha - 1)$$

$$\int \frac{1}{C} dc = \int V_r - V\alpha - 1\, dt$$

Equation 2.15: $C = 100e^{\frac{-\alpha V_f t}{V_r}}$

This model does not account for the initial volume of water in the tubing, or the aliquots removed for analysis. Further, the initial concentration (t = 0) is given the arbitrary value of 100 for easy comparison to a reservoir concentration percentage curve. Furthermore, the probability of sorption, α, is expected to decrease as the reservoir concentration decreases, due to the reducing concentration of the column input liquor and the gradual loading of adsorbate onto the column. Therefore, we would not expect this model to fit any of our uptake curves; it is to be used only as a tool to estimate α for different materials at specific timepoints points in the experiment. A comparison of this model (using three sorption probabilities: α= 1, 0.5, 0.25) to adsorption data produced by a material developed in this work is displayed in Figure 2.8.

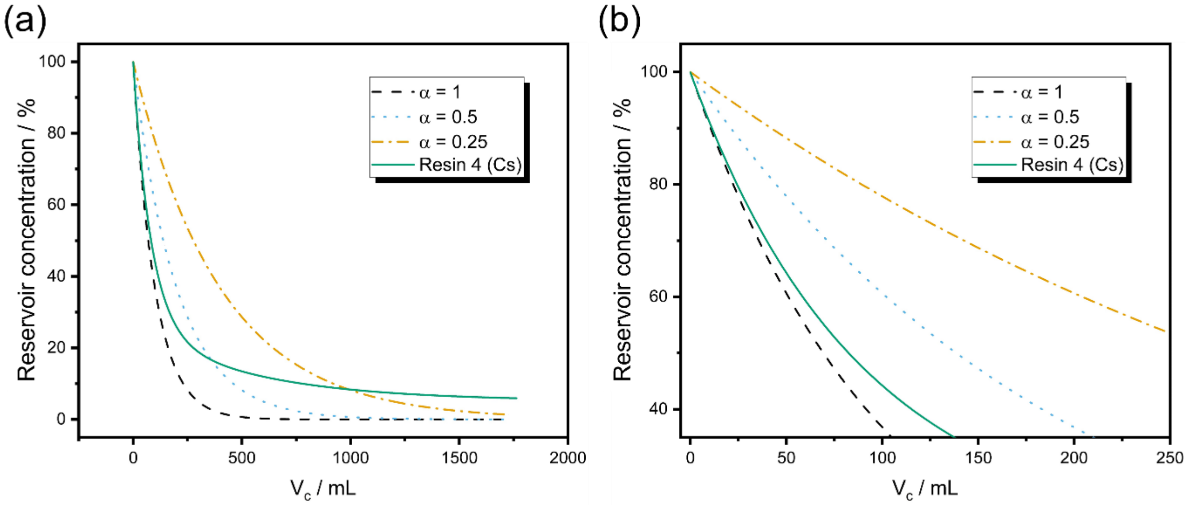

Figure 2.8. RIX model of reservoir concentration (Equation 2.15) using three adsorption probabilities (0.25, 0.5 and 1). Also displayed is some data collected from a material produced in this work. A flow rate of 10 mL minute^{-1} and a reservoir volume of 100 mL were used.

2.3 Experimental Details

2.3.1 Acquisition and Processing of Natural Materials

2.3.1.1 Mordenite

A raw mordenite material with ~ 1 cm granule size was sourced from Java, Indonesia. This material was crushed and sieved to desired particle size as appropriate: < 75 μm for powder transformations and 400-600 μm for granular work. Where stated, the raw material was subject to two washing steps: an extensive wash with distilled water (and subsequent drying at 60 °C) and a sodium wash, where 4 g of zeolite was added to a 40 mL 1 M NaCl solution (Fisher, 98%). After 24h of agitation, the remaining solid was washed with distilled water and left to dry at 60 °C for overnight.

2.3.1.2 Clinoptilolites

Four natural clinoptilolites were procured for use in this work: Mud Hills clinoptilolite (MH-HEU), Zeoclere-30 (MSI, Z-HEU)[178], Zeolitalia® (N-HEU) and Zeolite Clinoptilolite (Heiltropfen, S-HEU)[179]. MH-HEU is sourced from the Mojave Desert, California and is used at the SIXEP plant, Sellafield, for remediation of nuclear effluent. Z-HEU is sourced from South Africa and is commercially available as a swimming pool filter. N-HEU and S-HEU are sold as dietary supplements, originating from Slovakia and Norway, respectively. Both MH-HEU and Z-HEU were sourced as granular materials (400-600 μm and ~1 mm particle size, respectively), whereas N- and S-HEU were sourced as fine powders.

2.3.2 Hydrothermal Interzeolitic Transformations in Basic Media

0.667 g of raw zeolite material was added to a 60 mL polypropylene bottle charged with 23 mL NaOH solution (Alfa Aesar 98%, 0.2-1.2M) and heated at 100 °C for 24h. After cooling, the solid material was washed extensively with distilled water (until washings were pH neutral) and dried at 60 °C overnight.

2.3.3 Powder X-ray Diffraction (PXRD)

Powder diffraction patterns were measured on a Bruker D8 diffractometer (Cu source, λ = 1.5406 Å) or a Bruker D2 phase diffractometer (Co source, λ = 1.7926 Å). Data was acquired in flat-plane geometry using a θ-2θ configuration. Phases were identified using DIFFRAC.EVA and weight fractions determined though Rietveld refinement[162, 163] where appropriate using GSAS-ii[180].

2.3.3.1 Amorphous Content Determination

In order to determine the amorphous content of the clinoptilolites, approximately 17 Wt. % corundum (Fisher, >99 %) was added and thoroughly mixed (see Table 2.2). Phases were identified using DIFFRAC.EVA and measured weight fractions determined through Rietveld refinement[162, 163] using GSAS-ii[180].

Table 2.2. Masses corundum standard added to each of the four starting zeolites prior to collection of PXRD data.

Material	Mass zeolite / g	Mass corundum / g	Weight % corundum
MH-HEU	0.4955	0.1006	16.9
Z-HEU	0.5095	0.1025	16.7
N-HEU	0.5046	0.1109	18.0
S-HEU	0.5057	0.1049	17.2

Absolute weight fractions for a particular phase ($W_{x(\mathrm{absolute})}$) were determined using Equation 2.16. Subsequently, the total weight fraction of unknown material ($W_{(\mathrm{unknown})}$) were calculated using Equation 2.17. This is assumed to be equal to the total amorphous content of the material. Final weight fractions (W_f), excluding contributions from the corundum standard and considering amorphous contributions, were determined using Equation 2.18.

$$\text{Equation 2.16:}\quad \mathrm{W_{x(absolute)}} = \mathrm{W_{x(measured)}} \times \frac{\mathrm{W_{std(known)}}}{\mathrm{W_{std(measured)}}}$$

$$\text{Equation 2.17:}\quad \mathrm{W_{(amorphous)}} = 1 - \sum_{\mathrm{k=1}}^{\mathrm{n}} \mathrm{W_{k(absolute)}}$$

$$\text{Equation 2.18:}\quad \mathrm{W_f} = \frac{\mathrm{W_{x(absolute)}}}{\sum_{\mathrm{k=1}}^{\mathrm{n}} \mathrm{W_{k(absolute)}} + \mathrm{W_{(amorphous)}}}$$

2.3.4 X-ray Fluorescence (XRF)

A Bruker S8 TIGER WDXRF spectrometer was used for elemental analysis. Samples were run as pressed pellets formed under 7-8 tonnes of pressure with added inert wax binder (Spectroblend® 44 μm binder, 5:1 mass ratio). Pellets were analysed using an 8 mm mask and 18-minute data collection time. Kα1 emission line intensities were used to calculate elemental concentrations and subsequently molar ratios.

2.3.5 Energy Dispersive X-ray Spectroscopy

Samples were first pelletised using a load of 7-8 tonnes to ensure a flat surface for analysis. Elemental analysis was performed using energy dispersive X-ray (EDS) spectroscopy on an Oxford Instruments INCA micsF+ and xstream-2 system coupled to a Hitachi TM4000plus electron microscope. Six sites were analysed per sample with an average composition calculated.

2.3.6 ^{29}Si /^{27}Al NMR

Spectra were recorded on a Bruker Avance III 400 NMR spectrometer operating at a magnetic field strength of 9.4 T (^{1}H v_0 = 400 MHz) using a conventional Bruker 4mm low-γ HX double resonance probe. Powdered material was packed into a 4 mm ZrO_2 rotor and rotated at rates between 9 and 14 kHz at 54.74° with respect to the direction of the magnetic field. ^{29}Si Chemical shifts were reported in ppm relative to $Si(CH_3)_4$. In the case of ^{27}Al, chemical shifts were reported in ppm relative to $Al(NO_3)_3$ (1M) and measured using secondary reference of $Al(acac)_3$. Experiments were conducted at ambient temperatures with v_1 = 90 kHz and a recycle interval of 120 s.

2.3.7 Batch Ion-Exchange Scoping

Ion-exchange testing solutions of the following compositions were made up through dilution of ICP standards (Fisher): 10 ppm Cs, 50 ppm K; 10 ppm Sr, 50 ppm Ca. 0.03 g of relevant material was added to 15 mL of each solution and agitated for 24h on an orbital shaker before extraction of supernatant, which was subsequently passed through a 0.22 μm filter and acidified with 2% nitric acid (VWR, ultrapure).

The percentage uptake was calculated using Equation 2.19:

Equation 2.19: $$\text{Uptake (\%)} = \frac{\text{Initial concentration}-\text{Final concentration}}{\text{Initial concentration}} \times 100$$

2.3.8 Equilibrium Ion-Exchange of Caesium and Strontium

For caesium sorption studies, 15 mL of 50-1000 ppm Cs solution ($CsNO_3$, Alfa Aesar 99.8%) was dispensed into a polypropylene tube charged with 0.018 g zeolite material prior to agitation for 30 days at ambient temperature. Raw mordenite/clinoptilolite was Na-washed prior to addition to solution (2.3.15). Subsequent supernate was extracted, passed through a 0.22 μm filter, diluted in 2% nitric acid (VWR, ultrapure) and analysed by ICP-MS. For strontium sorption studies, a 10-500 ppm Sr solution ($Sr(NO_3)_2$, Fisher analytical reagent grade)) was added to a polypropylene tube charged with 0.018 g zeolite material prior to agitation for 30 days at ambient temperature. Raw mordenite/clinoptilolite was Na-washed prior to addition to solution. Subsequent supernate was extracted, passed through a 0.22 μm filter, diluted in 2% nitric acid (VWR, ultrapure) and analysed by ICP-OES. Each experiment was performed in triplicate with mean values reported. Freundlich, Temkin and Langmuir-Freundlich isotherm models were fitted to the data using a Levenberg Marquardt iteration algorithm until convergence was reached (Chi-Sqr tolerance value 1E-9). For further information regarding these models please refer to section 2.2.1.

2.3.9 Time-Resolved Ion-Exchange of Caesium and Strontium

For caesium sorption studies, a 250 ppm Cs solution was prepared ($CsNO_3$, Alfa Aesar 99.8%) and 250 mL dispensed into a 500 mL LDPE bottle prior to addition 0.3 g of zeolite material and rapid stirring. Raw mordenite/clinoptilolites were Na-washed prior to addition to solution (2.3.15). 1 mL aliquots were extracted at 2, 5, 15, 60 and 180 minutes, passed through a 0.22 μm filter and diluted appropriately in 2% nitric acid before analysis by ICP-MS. For strontium sorption studies, a 250 ppm Sr solution was prepared ($Sr(NO_3)_2$, Fisher analytical reagent grade) and 250 mL dispensed into a 500 mL LDPE bottle prior to addition 0.3 g zeolite material and rapid stirring. Raw mordenite was Na-washed prior to addition to solution. 1 mL aliquots were extracted at 2, 5, 15, 60, 180, 360 and 1440 minutes, passed through a 0.22 μm filter and diluted appropriately in 2% nitric acid before analysis by ICP-OES, using the emission peak at 460.73 nm. All experiments were performed in triplicate with mean uptakes reported. 2nd order kinetic and Elovich models were fitted to these points using a Levenberg Marquardt iteration algorithm until convergence was reached (Chi-Sqr tolerance value 1E-9). An arbitrary value of t = 100 (hours) was used for equilibrium estimations. For further information regarding these models please refer to section 2.2.1.

2.3.10 Scanning Electron Microscopy (SEM)

Images of powdered, crushed, or granular zeolites were captured on a Hitachi TM4000plus electron microscope using a beam energy of 5-15 keV.

2.3.11 X-ray Computed Tomography (XCT) and Local, Image-Guided Diffraction

X-ray imaging and diffraction were conducted on the Dual Imaging and Diffraction (DIAD) instrument at Diamond Light Source, UK[172]. The instrument's optical elements were configured to provide a pink imaging beam (low angle, Pt mirrors, 4 mm Al filter[172]) alongside a focused 25 x 25 µm monochromatic beam used for diffraction. Monochromatic light was produced by reflection through a double crystal monochromator equipped with Si (111) crystals. During the experiment the wavelength was calibrated at 0.5929 Å by observing points on Debye-Scherrer rings produced by a certified LaB6 powder[181]. Geometric instrument parameters were further refined in DAWN[182]. Local diffraction patterns were collected over 30 seconds. Tomograms consisted of 2500 projections over 180 degrees, with 20 flat and 20 dark frames taken at the start and the end of the tomography acquisition. Both diffraction and tomography data were processed using DAWN[182]. A long duration 7-slice diffraction tomography scan was conducted on a composite granule using 91 rotation steps over 360 degrees. Calculated, voxel-specific diffraction patterns had background subtracted prior to integration between Q values of 2.151-2.188 and 1.220-1.276 to obtain arbitrary intensities of both phases. These intensities are plotted as a function of real space to produce a 'phase map' of a single composite granule. For further information regarding calibration, specimen mounting, positioning and alignment, in addition to data analysis pipelines, please refer to appendices (A.1).

2.3.12 Single Granule *In-Situ* Ion-Exchange Experiments

Composite single granule mounted on a polyimide rod adhered to the interior of a borosilicate capillary. The granule was subsequently centred on the beam prior to addition of either 5000 ppm Cs solution ($CsNO_3$, Alfa Aesar 99.8%) or 5000 ppm caesium/strontium solution ($CsNO_3$, Alfa Aesar 99.8%; $Sr(NO_3)_2$, Fisher analytical reagent grade). This liquor was contained by the capillary throughout the experiment, ensuring constant exposure of the granule. Time-resolved diffraction patterns were collected at regions of interest in identical manor to described previously (2.3.11). These experiments were performed at K11 DIAD, Diamond Light Source, UK. Integrated intensities of key peaks were calculated using OriginPro.

2.3.13 Rapid Ion Exchange (RIX) Flow Studies

A 1 cm diameter column was loaded with 0.1 g ion-exchange material as slurry, surrounded (top and bottom) by 0.5 g 1 mm glass beads, separated by a stainless-steel mesh (Figure 2.7). Raw zeolite materials were subject to a sodium wash prior to loading, as per 2.3.15. The loaded column was connected to a peristaltic pump, operating at flow rate of ~10 mL min^{-1}. Ultrapure water flowed through the system for specific time intervals to accurately determine flow rate for each experiment. A simulant liquor was prepared to replicate the caesium (0.017 ppm) and strontium (0.0005 ppm) concentration expected in the SIXEP feed stream, similar to that reported previously[70]. An aqueous stock (pH 7-8) was prepared by spiking the solution with Sr-90 (37 Bq/ml) and Cs-137 (1000 Bq/ml) isotopic standards and adding inactive CsCl to prepare the desired concentration. Active simulant liquor was pumped through the column and recirculated back into the liquor reservoir (Figure 2.7).

At t = 0, 7, 15, 45, 90, 180 minutes, 1 mL aliquots were withdrawn from the reservoir and stored in glass vials for analysis. This procedure was performed in triplicate for each material. Cs-137 activity was determined by gamma spectroscopy on GMX-20190 and GMX-18190S N type spectrometers. Sr-90 activity was determined *via* Cherenkov counting on a TRI-CARB® Liquid Scintillation Analyser, Model 2700TR Series. Solution activities were reported as a percentage of starting activity (t = 0) and plotted as a function of volume (through column, V_c). A two-parameter exponential decay (Equation 2.20) function was fitted to these points using a Levenberg Marquardt iteration algorithm until convergence was reached (Chi-Sqr tolerance value 1E-9). This curve then represents all data for a single material.

Equation 2.20: $$y = y_0 + A_1 e^{-x/t_1} + A_2 e^{-x/t_2}$$

This method allows for dynamic flow testing in a short timeframe, requiring much smaller quantities of both ion-exchange material and solution in comparison to traditional column studies, resulting in reduced waste and costs. The probability of sorption (α) at a given volume can be estimated using Equation 2.21. For further information, including derivation, please refer to Section 2.2.2.1.

Equation 2.21: $$\alpha_v = \frac{V_r}{V_f t} \times ln\left(\frac{100}{C}\right)$$

2.3.14 Hydrothermal Breakdown of Clinoptilolite in Acidic Media

10 mL 6M HCl (Fisher, 37%) was added to 60 mL PP bottle charged with 0.5 mL of zeolitic material (sieved to < 75 μm particle size) prior to heating at 97 °C in a convection oven for one hour. The mixture was filtered and washed extensively with water until washings were pH neutral. The remaining solid media was then dried at 60 °C overnight in a convection oven.

2.3.15 Sodium Washing

1 g of ground, sieved zeolite (<75 μm) were added to a polypropylene (PP) bottle charged with 10 mL 1 M NaCl (Fisher, 98%). The mixture was then agitated on an orbital shaker for 24 hours at ambient

temperature before extraction of the solid material by Buchner filtration. The remaining solid was washed extensively with distilled water prior to drying overnight at 60 °C in a convection oven.

2.3.16 XPDF

Total scattering data were collected at the I15-1 XPDF Beamline at Diamond Light Source, U.K. Powder samples were loaded into borosilicate glass capillaries (1.5 mm outer diameter, 1.17 mm inner diameter) and spun perpendicularly to the beam to improve powder averaging during data collection. Total scattering data collection was carried out at an X-ray energy of 76.69 keV with two PerkinElmer area detectors using data collection times of 60 s, for XRD analysis, and for 300 s, for PDF analysis. The data were processed, and Fourier transformed using PDFGetX3 in the $0.5 < Q < 23$ Å^{-1} range to obtain the final Pair Distribution Function, $G(r)$.

2.3.17 Acidic Pre-Treatment of Clinoptilolites Prior to Transformation

1 g of ground, sieved zeolite (<75 μm) was added to a PP bottle charged with 10 mL 1 M HNO_3 (Fisher, 67 %). The mixture was then agitated on an orbital shaker for 24 hours at ambient temperature before extraction of the solid material by Buchner filtration. The remaining solid was washed extensively with distilled water until washings were pH neutral prior to drying overnight at 60 °C in a convection oven.

CHAPTER 3: ENHANCEMENT OF NATURAL MORDENITE THROUGH PARTIAL INTERZEOLITE TRANSFORMATIONS

3.1 Introduction

The decommissioning of nuclear sites worldwide will produce significant quantities of waste effluent, which must be treated to remove radioactive isotopes prior to environmental release. A key stage of this process is the removal of Cs-137 and Sr-90, which account for 99 % of medium-lived radioactivity within spent nuclear fuel. This is typically achieved by means of an ion-exchange material, such as zeolites[70], silicotitanates[95, 96] or hexacyanoferrates[183-185] (see 1.1.3 for further details). At Sellafield, Mud Hills clinoptilolite has performed well in the removal of caesium and strontium from waste effluent at SIXEP. However, its supply is due to deplete in the 2030's and removal rates may be insufficient when future waste streams are introduced (such as those arising through decommissioning operations). In addition to routine nuclear waste management, ion-exchange materials have been utilised to sequester a variety of aqueous cationic species in the aftermath of nuclear disasters such as those that took place in Three Mile Island (1979)[186], Chernobyl (1986)[187] and Fukushima (2011)[21, 188]. Therefore, it is paramount that alternative ion-exchange materials are explored to enable efficient processing of nuclear effluent, both saving public money and reducing the risk to life and the environment.

Nuclear effluent treatment plants often deploy two exchange materials, one to remove Cs-137 and the other to remove Sr-90 (e.g., ALPS plant, Fukushima[21]). However, the deployment of a material proficient in the uptake of both species is desirable, reducing the engineering complexity and associated research and development costs. At the SIXEP plant, Sellafield, a natural clinoptilolite zeolite, which is sourced from the Mud Hills region of California, has been used for over 30 years for the removal of both caesium and strontium. Unfortunately, other natural zeolites are not as proficient, particularly in their ability to adsorb strontium (Mud Hills clinoptilolite was in fact selected due to its unusually high affinity for strontium[70]) .

A striking example of this is mordenite (MOR topology), which is the second most abundant natural zeolite and well suited to the adsorption of caesium cations, but is a poor strontium sorbent (1.2.4.1)[34]. An interzeolite transformation of mordenite to a zeolite P (GIS) structure is readily attained in basic, hydrothermal conditions at elevated temperature and has been shown to enhance the strontium uptake in natural zeolites[76, 80, 149]. However, the generated zeolite P structure is poorly suited to selective caesium sorption[34]. Work in this chapter establishes the possibility of exploiting partial mordenite to zeolite-P transformations to produce composite zeolite materials capable of dual caesium and strontium abatement. Furthermore, if these systems could be tuned dependent on the composition of the waste stream, it would likely result in enhanced performance.

Firstly, the manufacturing route to these composite materials is established and the selectivity for caesium and strontium scoped in batch ion-exchange experiments. The methodology is then applied to granular materials, capable of deployment in flow systems. The generated composite morphologies are assessed through imaging and local micro-diffraction experiments. Finally, the ion-exchange properties are probed though *in-situ*, local diffraction studies and Rapid Ion Exchange (RIX) flow experiments using industrially relevant simulant liquor.

3.2 Results and Discussion

3.2.1 Characterisation of Raw Mordenite

Robust characterisation of the starting mordenite material is crucial to best understand the chemistry of any materials produced in this chapter. PXRD data and subsequent Rietveld refinement elucidate the presence of any impurities and their estimated abundances. In addition, XRF and SEM-EDS give elemental composition and SEM and XCT imaging provide insight into both the surface and internal morphology of mordenite granules.

3.2.1.1 PXRD Data and Rietveld Refinement

The PXRD pattern of the obtained mordenite material and subsequent Rietveld fitting is presented in Figure 3.1. Considering the material is naturally sourced, the fit is very good (wR = 4.89 %), with only minor differences in peak intensities between the collected data and the model. Reflections attributed to mordenite (87 %) and quartz (13 %) are both observed. Quartz (SiO_2) is the densest form of silica and is routinely found in natural mordenite deposits[152]. Its structural density and charge-neutral framework render quartz unable to participate in ion-exchange, although surface adsorption is still possible[189, 190]. Overall, these observations indicate a higher-grade mordenite has been sourced in comparison to other examples in literature, which often have significantly lower mordenite contents[76, 80, 149].

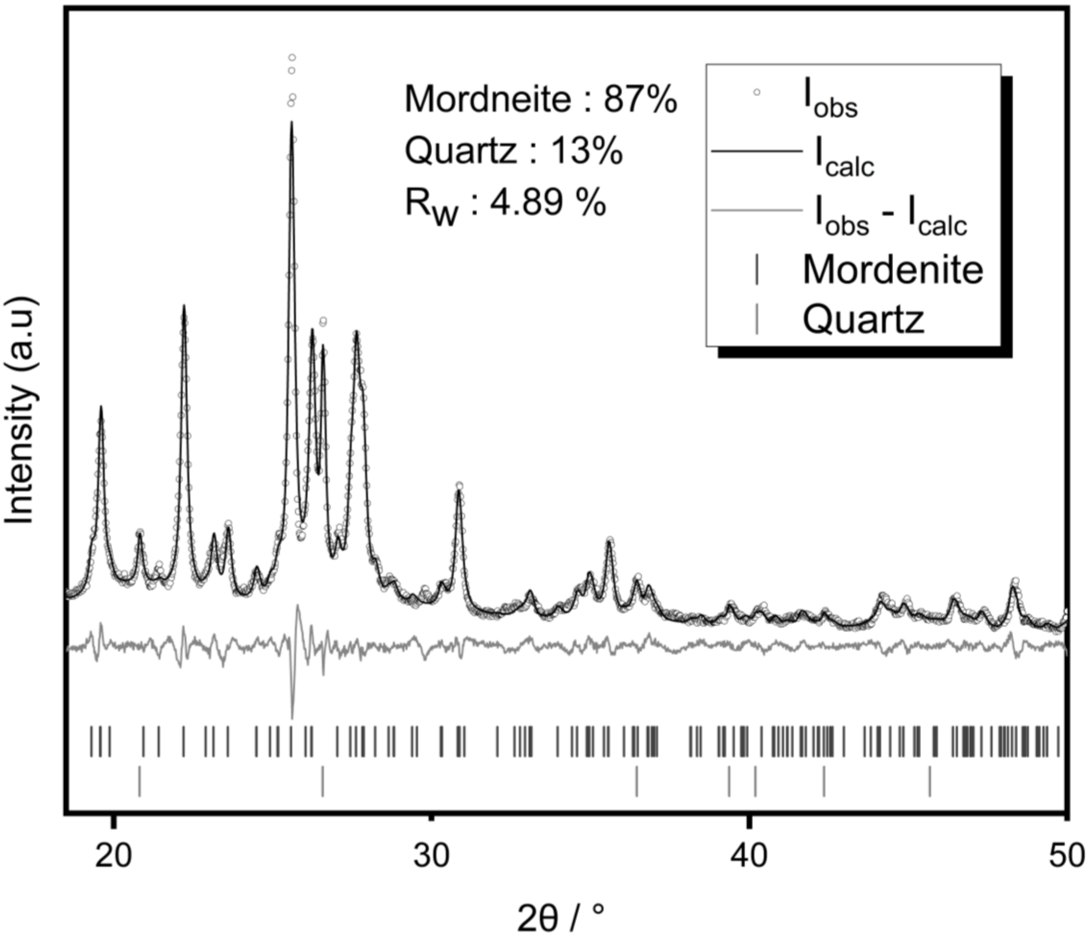

Figure 3.1. PXRD data and subsequent Rietveld refinement of the raw mordenite material (λ = 1.5406 Å).

3.2.1.2 Elemental Analysis

The framework aluminium content of a zeolite, often reported as the Si/Al ratio, dictates the framework charge, which can steer affinity to particular cationic species. The identity of the pore cations is also significant. Different cations are displaced by others in ion-exchange processes by varying degrees, dependent on the geometry and charge distribution of both the adsorbent and adsorbate. For a given material, these factors result in a selectivity series: the order of highest to lowest selectivity which is experimentally derived though an assortment of ion-exchange experiments. A reported selectivity series for a synthetic mordenite (Si/Al = 5.3) is as follows: Cs > K > NH_4 > Na > Ba > Sr > Ca > Li[191, 192]. Large, monovalent species are preferred due to the somewhat siliceous framework and limited diameter of side pockets (3.9 Å) lining the 12MR channels[191, 192]. Consequently, the identity of incumbent cations also influences the ion-exchange performance of a zeolite. Hence, materials are often pre-washed with a less strongly sorbed species. The Si/Al ratio of the raw mordenite material, determined through XRF and SEM-EDS analysis, is displayed in Table 3.1.

Table 3.1. Si/Al ratio of the raw mordenite material as determined by XRF and SEM-EDS.

XRF	**SEM-EDS**
4.7(1)	4.4(1)

This is comparable to work by Soetarji[193], who reported a Si/Al ratio of 4.6 for a natural mordenite material. In addition to the zeolite framework species (oxygen, silicon and aluminium), SEM-EDS analysis shows evidence for the presence of potassium, sodium, magnesium, calcium and iron. These cations are most likely located in zeolite framework channels or in an impurity not detected in the bulk diffraction pattern. Iron can also be present as $[Fe(H_2O)_6]^{3+}$ or Fe^{2+}, located in extraframework octahedral sites[194]. The abundance of each cation, in relation to aluminium, is presented in Table 3.2.

Table 3.2. Cationic content of raw mordenite material used in this work, as determined by SEM-EDS. [a]Iron is likely present as part of the zeolite framework, as opposed to as a charge-balancing, exchangeable cation.

Cation (X)	**X / Al**
Sodium	0.22(4)
Potassium	0.11(3)
Magnesium	0.07(2)
Calcium	0.20(4)
Iron[a]	0.07(2)

Sodium, which is the most abundant cation observed, is known to be a readily exchangeable species in zeolitic systems[70]. Calcium is the next most abundant cation and contributes over 40 % of the positive charge required to counterbalance the anionic framework charge. Both these species are low down in the mordenite selectivity series, so are expected to exchange readily. A significant quantity of potassium is also observed, which is less easily released from the framework due to the high selectivity of mordenite to potassium. This is demonstrated by Soetarji[193], who observed calcium preferentially leaving the framework over potassium in high molarity sodium solutions.

3.2.1.3 SEM and XCT Imaging

Imaging of the starting material allows the observation of any morphological changes arising from hydrothermal treatments discussed in future sections, which could have a meaningful impact on the adsorption chemistry. SEM imaging provides insight into the surface morphology and XCT enables the internal morphology to be assessed. A variety of images of granular mordenite (400 - 600 μm) are presented in Figure 3.2.

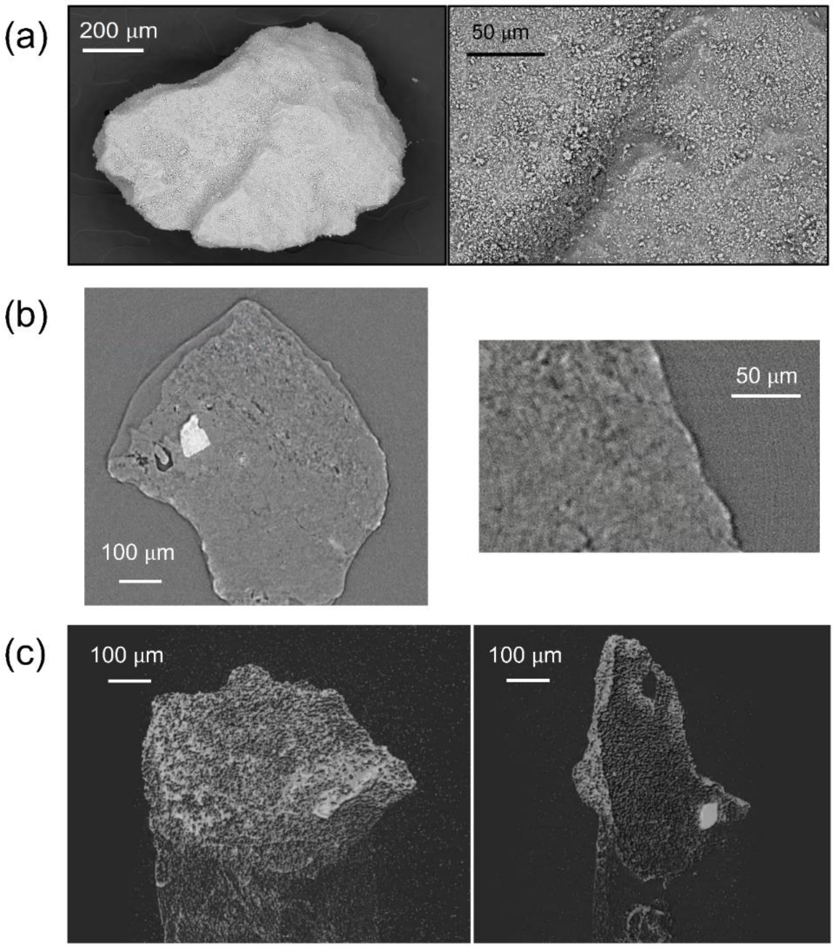

Figure 3.2. Images of a raw mordenite granule obtained from a variety of imaging techniques. (a) SEM, (b) XCT cross section, (c) XCT (dissected, 3D reconstruction).

The SEM images of the raw mordenite (Figure 3.2a) reveal the lightly contoured surface of the mordenite granules (left image), with a spattering of fine particles present on the surface (right image). The XCT images (Figure 3.2b) suggest a mostly smooth granule interior, although a domain of increased density is observed in the form of a lighter contrast spot. Considering the bulk diffraction pattern (3.2.1.1), it is reasonable to assume that this is a region of quartz. This moiety is also visible in the dissected, XCT 3D reconstruction (Figure 3.2c) represented by a lighter contrast area.

3.2.1.4 Local Micro-Diffraction

Local diffraction experiments were performed at the Dual Imaging and Diffraction beamline (DIAD, K11) at Diamond Light Source[172], UK. The beamline optics facilitate quasi-simultaneous imaging and micro-diffraction experiments; the 25 × 25 μm diffraction beam can be targeted at regions of interest within the imaged material. Two diffraction beam trajectories and recorded diffraction data are presented in Figure 3.3.

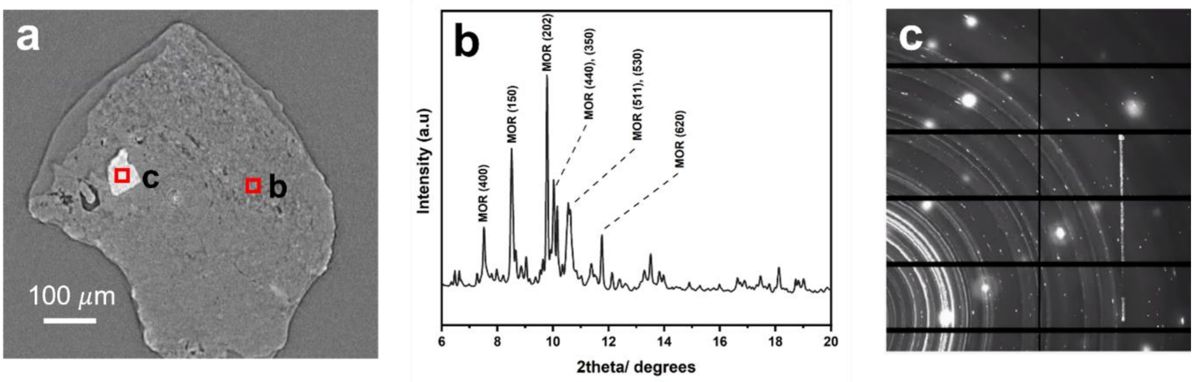

Figure 3.3. Local diffraction studies on raw mordenite material. (a) Diffraction beam trajectories superimposed on an XCT cross-sectional image. (b) Processed diffraction data obtained from diffraction beam trajectory b (λ = 0.5965 Å). (c) Raw diffraction data obtained from diffraction beam trajectory c.

Trajectory 'b' produced a pattern where the dominant reflections could be attributed to the mordenite structure, although secondary phases assigned to quartz, analcime and magnetite were also observed. Analcime and quartz were not observed in the laboratory diffraction data, although both structures are widely observed as impurities in zeolitic tuffs (analcime is in fact a zeolite itself)[195, 196]. It is unclear whether these phases were only observed by chance due to local distribution within the raw material or are now observable because of the greater signal-to-noise ratio achievable when utilising synchrotron radiation. Future work could look at the spatial distribution of phases within these materials.

Beam trajectory ‘c’ was targeted at a region of higher contrast within the cross-sectional XCT image (Figure 3.3a). The unprocessed diffraction data (Figure 3.3c) is comprised of bright spots, in addition to the diffraction cones that are routinely obtained from powdered crystalline samples. These spots originate from single-crystal material situated on the diffraction beam trajectory. In this case, they are presumed to be quartz due to its abundance and high-density structure.

3.2.2 Generation of Powder Composites

As observed in literature[76, 80, 149], basic hydrothermal treatment of the natural mordenite resulted in an interzeolite transformation to zeolite P. Further, the partial transformation of mordenite was achieved through the use of reduced solution basicity; eleven materials were generated from eleven NaOH concentrations between 0.20 and 0.70 M.

3.2.2.1 PXRD and Weight Fraction Estimations

The PXRD patterns corresponding to these materials are shown in Figure 3.4, in addition to the mordenite (Na-washed) and simulated patterns for mordenite and zeolite P. These patterns were analysed using the Rietveld method[162, 163] in order to estimate the weight fractions of mordenite, zeolite P and quartz (A.2). The estimated weight fractions are displayed in Table 3.3 and plotted as a function of solution basicity in Figure 3.5.

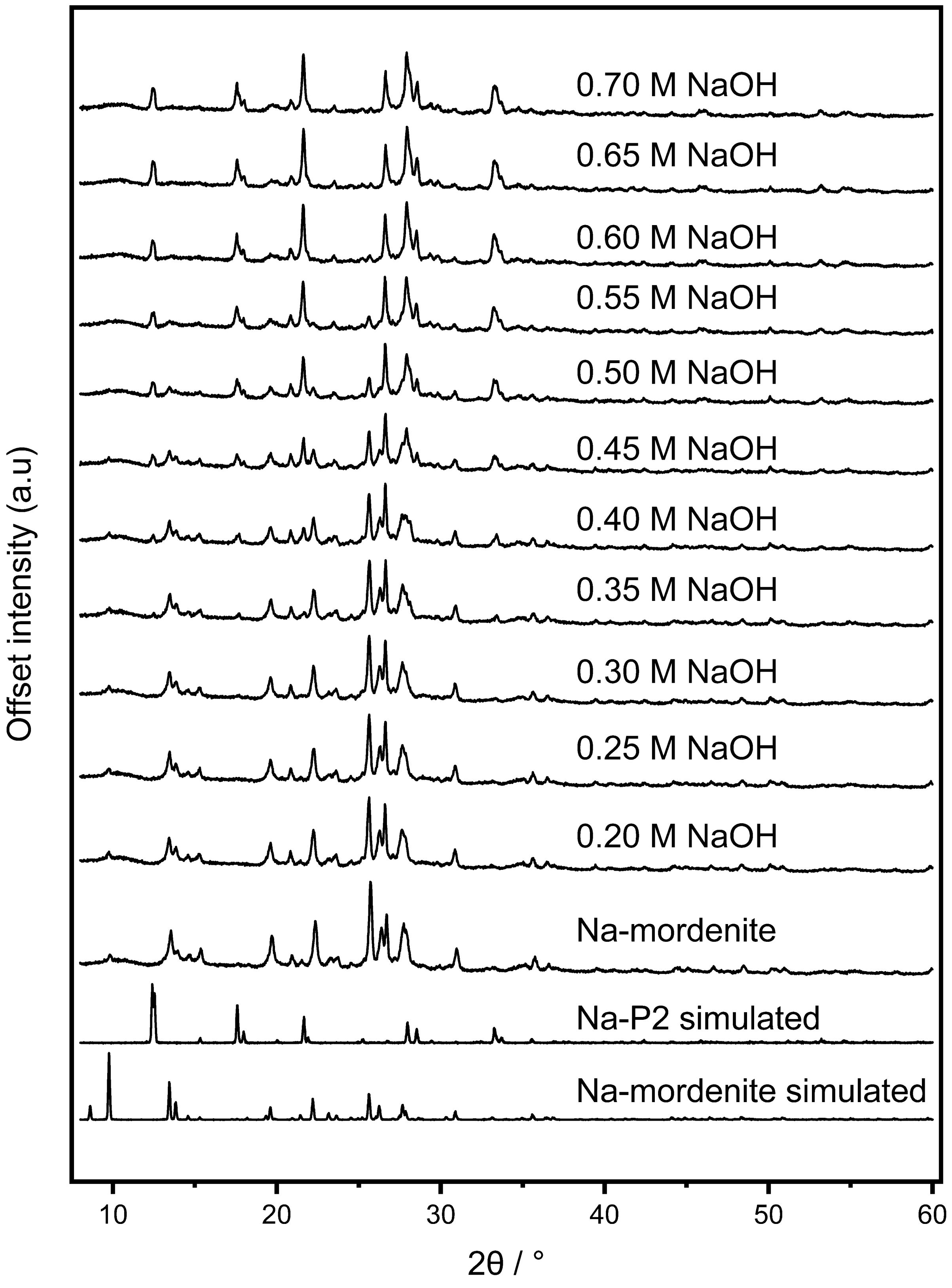

Figure 3.4. PXRD patterns of powdered mordenite material after hydrothermal treatment (0.20 – 0.70 M solutions). Simulated mordenite and zeolite P (Na-P2) patterns are also presented (λ = 1.5406 Å).

Table 3.3. Summary of estimated weight fractions of mordenite, zeolite P and quartz in the powdered composite materials. Values obtained though Rietveld refinement of PXRD data (A.2). Reported errors from GSAS-ii are < 1%.

NaOH concentration	Mordenite / %	Zeolite P / %	Quartz / %
0.20	92	0	8
0.25	93	0	7
0.30	95	0	5
0.35	84	6	10
0.40	76	14	11
0.45	61	29	10
0.50	32	56	12
0.55	25	65	11
0.60	15	74	11
0.65	0	94	6
0.70	0	93	7

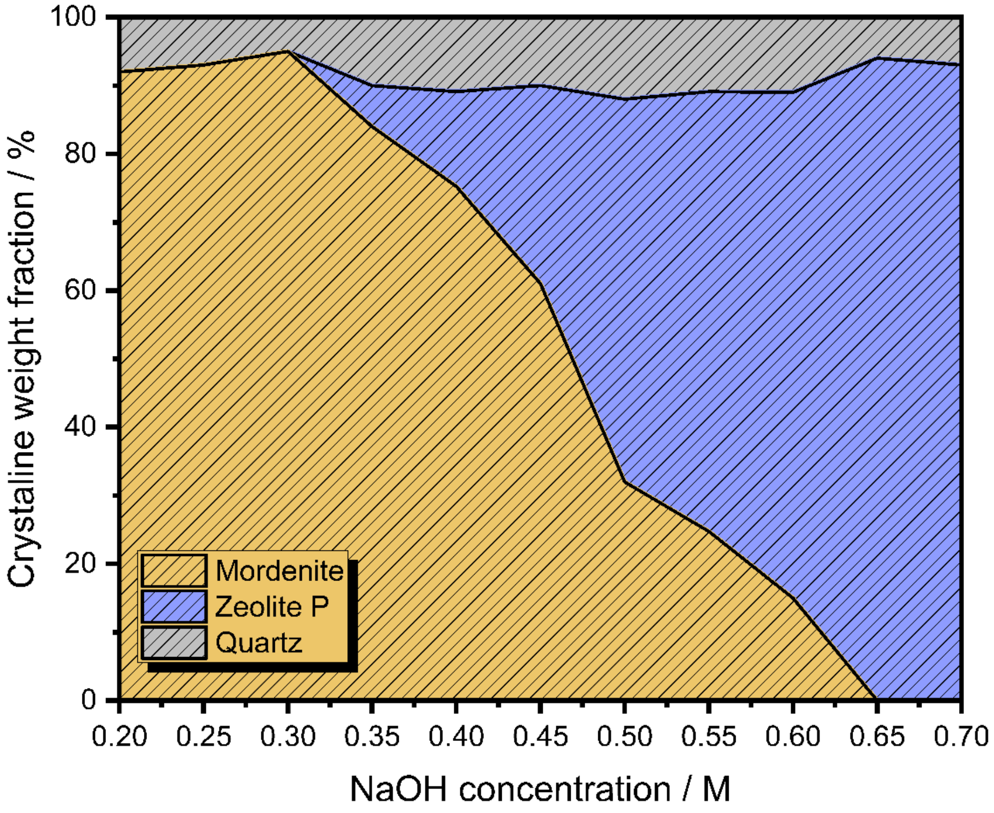

Figure 3.5. Crystaline weight fractions of mordenite, zeolite P and quartz as a function of solution basicity.

Growth of the zeolite P (GIS) phase was observed in concentrations > 0.30 M and increased steadily up to 0.65 M, where negligible quantities of mordenite remained. As expected, this was mirrored by the mordenite weight fractions, which decreased in NaOH concentrations > 0.30 M. An exceptional level of control over the ratios of mordenite and zeolite P in the composites is demonstrated over the full interconversion range. The weight fraction of quartz remained relatively constant regardless the degree of conversion. Although, it is possible they are slightly higher (~11 %) in materials with both mordenite and zeolite P present (0.35 – 0.60 M). An explanation for this is that the crystallinity of the zeolitic phases is lower within these materials. The sodium hydroxide concentrations used in this work are lower compared to literature examples[80, 149]. This facilitates concurrent crystallisation of zeolite P and mordenite dissolution, which subsequently allows for the generation of composite materials.

3.2.2.2 Si/Al Ratio

Additionally, Si/Al ratios of the eleven composite materials were determined though XRF spectroscopy. In NaOH concentrations > 0.30 M a steady reduction in the bulk Si/Al ratio of the materials was observed until 0.70 M, where a value of 2.5 was attained. This can be attributed to the nucleation of a more aluminous structure following parent dissolution; this is consistent with observations in litertaure[149]. It is highly likely that remaining mordenite in partially transformed materials is partially desilicated in comparison to the parent structure. The extent of this desilication can be estimated *via* the discrepancy observed between both observed, and 'theoretical', Si/Al ratios. The 'theoretical' Si/Al ratio is attained through a combination of XRF analysis of the 'end-members' (parent and fully converted mordenite) and relative weight fractions from Rietveld refinements (Table 3.3). In these estimations, it is assumed that the 'end-member' Si/Al ratios of 4.6 and 2.5, respectively, are unchanged throughout. Figure 3.6 displays the Si/Al ratios attained though XRF spectroscopy, the estimated Si/Al ratios, and the subsequent estimation of the mordenite Si/Al ratios. This analysis suggests an incremental decrease in mordenite Si/Al ratio of approximately 4.6 to 3.4 between 0.30 and 0.55 M NaOH solutions.

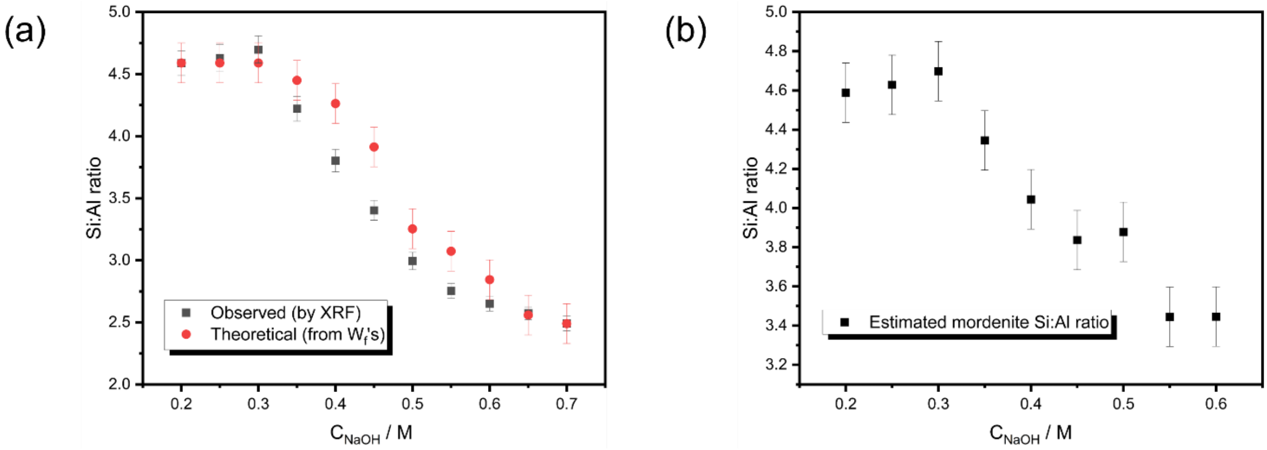

Figure 3.6. Si/Al ratios of the generated powdered composites. (a) Observed and theoretical Si /Al ratio, as determined by XRF analysis and calculated weight fractions, respectively. (b) Estimated mordenite Si/Al ratio, as determined from bulk elemental analysis by XRF and calculated weight fractions.

Strontium adsorption is more favourable by aluminous zeolite frameworks due to greater electrostatic attraction between he charge-dense aluminous framework and the divalent metal species, in addition to the greater likelihood of aluminium pairs[34]. Therefore, the nucleation of the zeolite P phase and the concurrent desilication of the parent should both improve the materials ability to adsorb strontium.

3.2.2.3 ^{29}Si NMR

In typical ^{29}Si NMR experiments, mordenite zeolites produce three major peaks, positioned at -100, -106 and -113 ppm[197, 198]. The -113 and -100 ppm peaks arise from silicon nuclei with zero and two aluminium atoms in the secondary coordination sphere, respectively[197, 198]. The remaining peak at -106 ppm is predominantly a result of silicon environments with one aluminium in the secondary coordination sphere, although contributions can also be associated to silanol moieties[197]. The significant overlap of these peaks, combined with contributions from defects, such as silanol groups and framework iron, make fitting peaks accurately to these datasets challenging. Synthetic zeolites generally possess more regular structures than their natural counterparts. Therefore, the peaks are often more distinguishable from each other[199]. Dependent on the Si/Al ratio of the zeolite framework, up to five peaks are generally observed (for silicon nuclei with between one and four aluminium species in the second coordination sphere)[200, 201].

^{29}Si NMR spectra of the mordenite precursor (Na-exchanged), a mordenite-zeolite P composite material and ‘fully converted’ zeolite P are presented in Figure 3.7. The composite material and the sample of zeolite P were prepared using NaOH concentrations of 0.50 and 0.70 M, respectively (32:56 and 0:93 MOR:GIS ratio). The spectrum produced by the parent mordenite resembles a broad hump between approximately -95 and -120 ppm. Peaks are visible at -102, -109 and -115 ppm and can be attributed to silicon environments with two, one and zero aluminium atoms in their secondary coordination sphere. This is typical for natural mordenite materials[197, 198]. A small peak is also observed at ~-95 ppm, which can be attributed to the presence of iron within the within the secondary coordination sphere[202]. Earlier PXRD and Rietveld analysis (3.2.2.1) showed quartz to be a significant impurity, with an approximate 16 Wt. %. The quartz signal generally resides at around -108 ppm and is therefore difficult to discern from the mordenite resonances[203].

Five distinct resonances are visible in the spectrum produced by the ‘fully converted’ zeolite P at chemical shifts of -88, -93, -98, -103 and -108 ppm (Figure 3.7). These shifts are assigned to Si(4Al), Si(3Al), Si(2Al), Si(1Al) and Si(0Al), respectively. This profile is expected for aluminous, synthetic zeolites and is comparable with spectrum presented by Delaspozas for zeolite P produced by interzeolite transformation[78]. Peak fitting to these resonances can be used to determine the peak area and hence estimate the Si/Al ratio to be 1.68 (Table 3.4). This is significantly lower than the Si/Al determined by XRF analysis, which suggests a value of approximately 2.5. Possible reasons for this discrepancy include significant interference from quartz peak or misassignment of resonances. For example, quartz could be responsible for the Si(0) peak at -108 ppm.

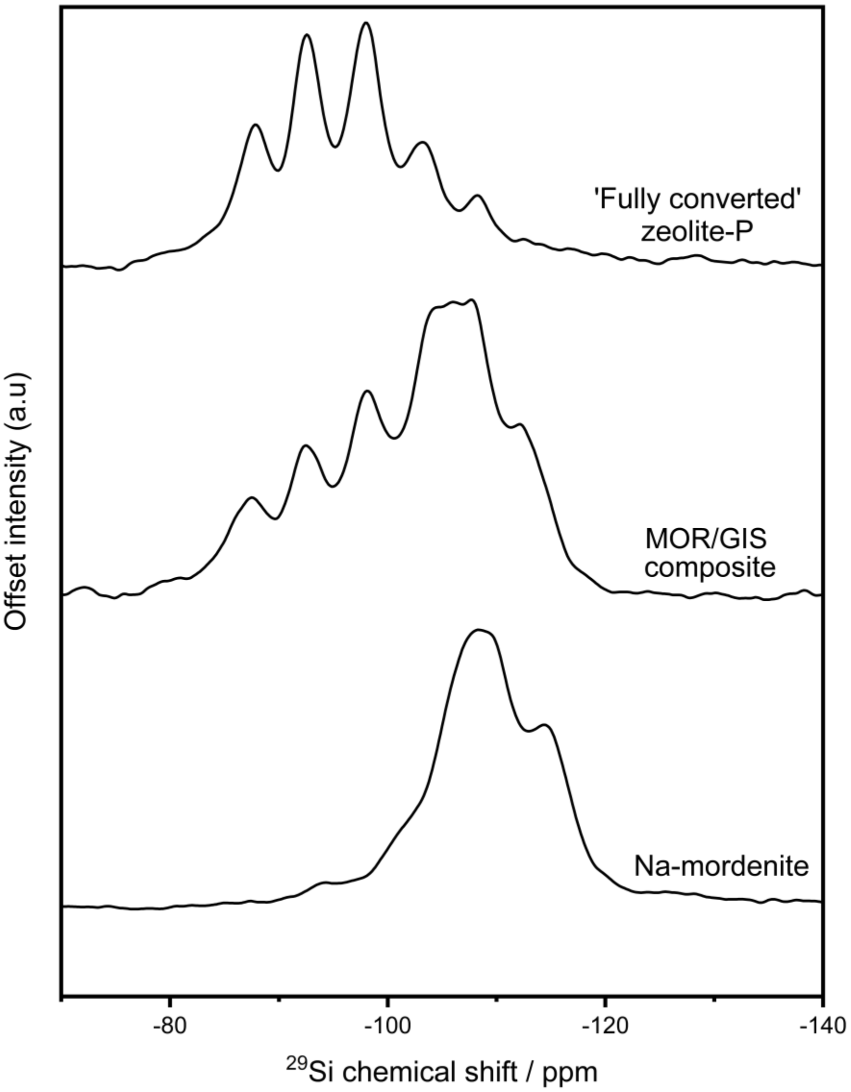

Figure 3.7. Solid state MAS ^{29}Si NMR spectra of the parent mordenite (Na-exchanged), a mordenite / zeolite P composite material (MOR/GIS) and a sample of 'fully converted' zeolite P.

Table 3.4. Chemical shifts and relative intensities of the five peaks observed in the 'fully converted' zeolite P ^{29}Si NMR spectrum. The peaks correspond to Si(4Al), Si(3Al), Si(2Al), Si(1Al) and Si(0Al) environments.

Peak	Chemical shift / ppm	Intensity / %
Si(4Al)	-88	11
Si(3Al)	-93	15
Si(2Al)	-98	24
Si(1Al)	-103	26
Si(0Al)	-108	24
		Si/Al = 1.68

As predicted, the NMR spectrum produced by the composite material (Figure 3.7) represents a superposition of the parent mordenite and 'fully converted' zeolite P spectra. Peaks at chemical shifts of -88, -93 and -98 ppm, attributed to zeolite P, are observable downfield of a broad, multi-peak region where the resonances from the parent mordenite overlap with the more shielded Si(1Al) and Si(0Al) silicon nuclei from zeolite P.

3.2.2.4 ^{27}Al NMR

The unfavorability of Al-O-Al linkages mean they are generally not observed in zeolite frameworks[37]. Therefore, framework aluminium, termed Al_{IV}, is a single resolvable environment, producing a peak at approximately 55 ppm – although this can vary with zeolite structure and framework composition[204]. Alternatively, aluminium in zeolites can exist with octahedral coordination geometry; this is termed extra-framework aluminium, or Al_{VI}. Extra-framework aluminium is located in intracrystalline spaces, is generally considered undesirable, and produces a resonance at approximately 0 ppm[204].

^{27}Al NMR spectra of the mordenite precursor (Na-exchanged), a mordenite-zeolite P composite material and ‘fully converted’ zeolite P are presented in Figure 3.8. The mordenite and zeolite P materials produced a single peak at 57 and 60 ppm, respectively. This is consistent with observations in literature[204]. The composite material appeared to produce a single, broader peak centred at approximately 59 ppm; this peak is a superposition of the resonances produced by both mordenite and zeolite P. A small peak at a chemical shift of approximately 3 ppm is observed in the spectra of all three materials, which can be attributed to the presence of extra-framework aluminium. The intensity of the resonance appears to decrease as a function of transformation extent. This potentially indicates the preferential dissolution of extra-framework aluminium during the transformation process, although the inherent increase in bulk aluminium content must also be considered.

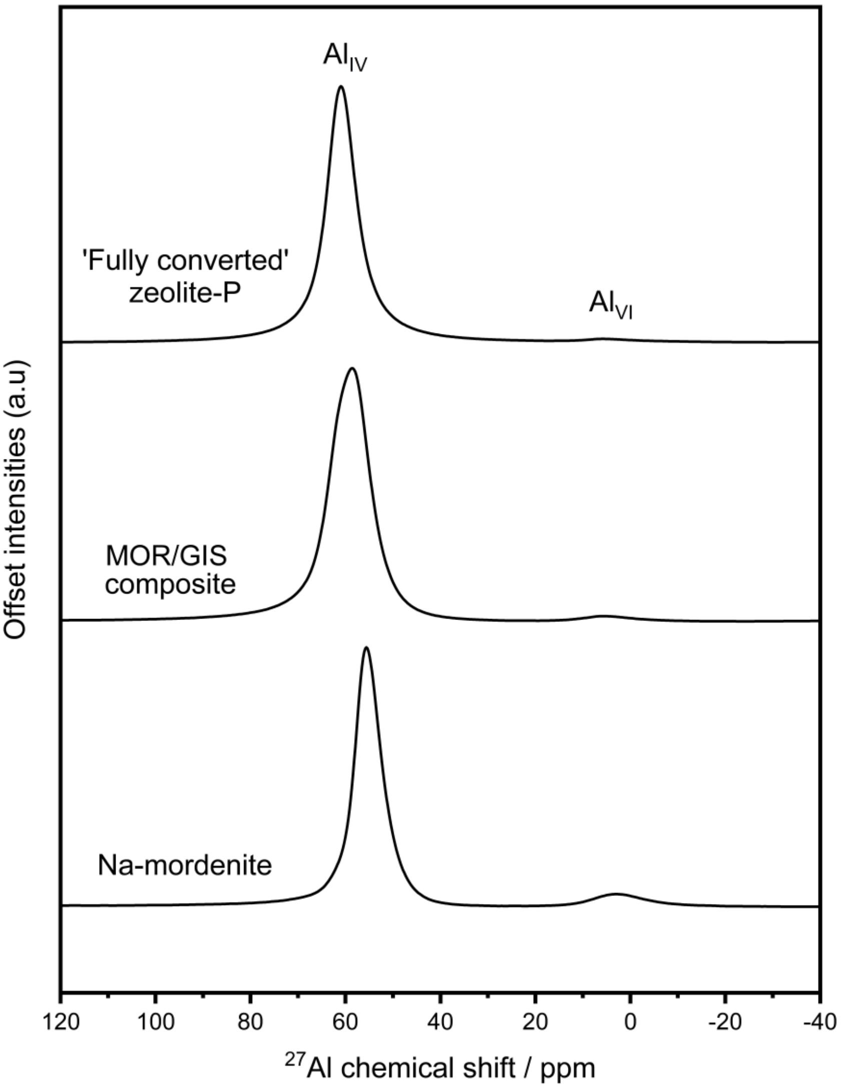

Figure 3.8. Solid state MAS ^{27}Al NMR spectra of the parent mordenite (Na-exchanged), a mordenite / zeolite P composite material (MOR/GIS) and a sample of 'fully converted' zeolite P. Peaks attributed to both tetrahedral (Al$_{IV}$) and octahedral (Al$_{VI}$) aluminium environments are annotated.

3.2.3 Batch Ion-Exchange Scoping

The elemental composition and topology of a zeolite framework dictate its affinity to a particular cationic species. Caesium is a large, monovalent ion which is most readily adsorbed by more siliceous frameworks[34]. Structures containing channels comprised of 8 membered rings are also reported to have excellent selectivity for caesium due to strong interactions between the large ion (3.6 Å) and the 3.6 – 4.1 Å cavity[34]. The natural mordenite precursor possesses both characteristics, in addition to 12-

ring channels, which facilitate rapid diffusion[34]. These factors should render the material an excellent caesium sorbent.

On the other hand, elemental analysis (3.2.2.2) suggests the nascent zeolite P has a much more aluminous framework (Si/Al = 2.5), which should be more tailored to the adsorption of strontium[34, 76]. Composite materials, containing significant quantities of both these complementary phases, could be promising ion-exchange materials for the simultaneous uptake of both caesium and strontium from aqueous nuclear decommissioning waste. This theory is scoped in a series is batch ion-exchange experiments, where caesium and strontium uptake are measured in the presence of excess potassium and calcium, respectively. These competitive ions, which are likely to be adsorbed in significant quantities, were selected for this study due to their chemical similarities to caesium and strontium, as opposed to their presence in a particular waste stream. Uptake data from these experiments is summarised in Figure 3.9.

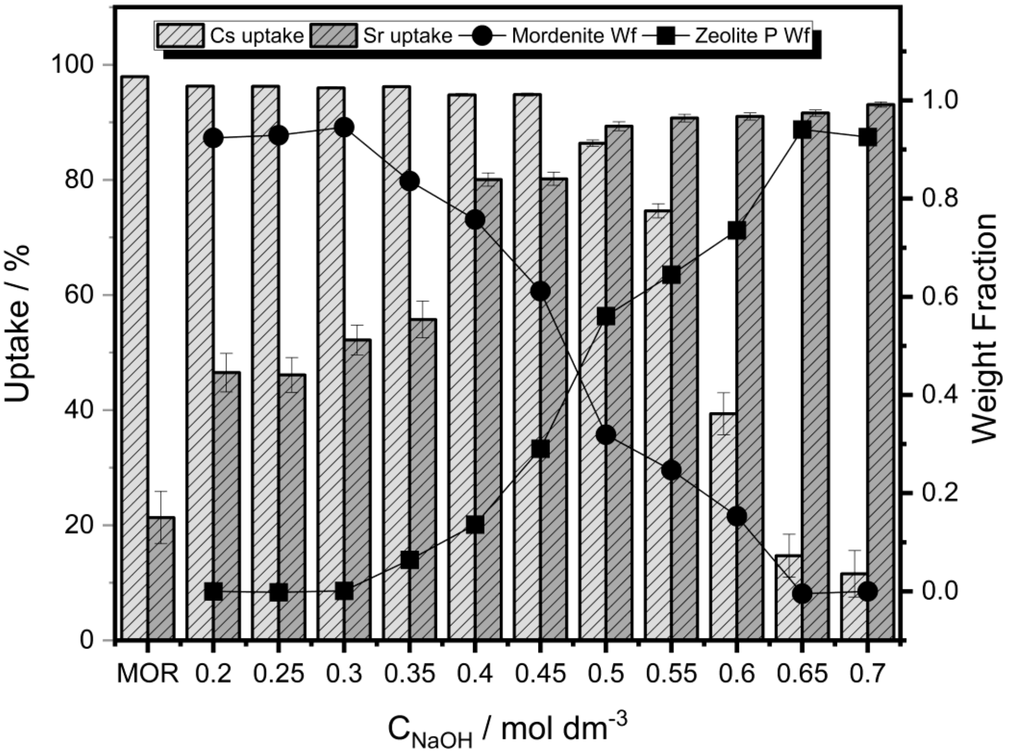

Figure 3.9. Uptake of caesium and strontium achieved by the powdered composites in scope batch trials. Estimated weight fractions of mordenite and zeolite P (Table 3.2) are also presented.

In line with its elemental and structural characteristics, the parent mordenite archives exceptional (> 96 %) caesium uptake. This high uptake is retained in composites containing more than 60 % mordenite (materials generated in up to 0.45 M NaOH). In more converted materials (> 0.45 M NaOH), caesium uptake decreased drastically, with the fully converted analogue displaying a caesium uptake of approximately 10 % in these conditions. The strontium uptake exhibited the opposite trend, with parent mordenite only removing about 20 %. This increased rapidly as a function of NaOH concentration up to 0.5 M and continues to rise to a maximum of 90 % in fully converted zeolite P material (0.70 M NaOH). Interestingly, strontium removal improved significantly in 0.20 and 0.25 M treatments when compared to parent mordenite, when no growth of zeolite P or change to Si/Al ratio was detected. This is possibly due to initial desilication of the mordenite material at the surface (prior to significant crystallisation of zeolite P), or dissolution of amorphous content within the parent material, to which conventional diffraction studies would be insensitive. Another possibility is the formation of mesopores, which would accelerate exchange[193].

The ratio of mordenite/ zeolite P within the powder composites was shown to tune the relative uptake of the two ions (Figure 3.9). This can be attributed to the fundamental zeolite characteristics of both phases: mordenite is comparably siliceous with favourable ring sizes for caesium adhesion and zeolite P possesses a greater density of aluminium, which increases favourability of strontium adsorption[34, 76]. The material formed using a 0.5 M treatment, containing an approximately 2:3 weight ratio MOR: GIS in the composite, displays optimal dual uptake from within these cation matrices (86 % Cs uptake, 89% Sr uptake). A 50:50 physical mixture of the starting mordenite (Na-exchanged) and 'fully converted' zeolite P (i.e. the material transformed in 0.7 M NaOH where no mordenite was observed in the XRD) were also analysed in equivalent conditions: 94 and 67 % of caesium and strontium were removed, respectively. Based on our data, a 50:50 composite material formed through hydrothermal conversion would be expected to remove approximately 90 % of caesium and 85 % of strontium. This increased strontium (and slight decrease in caesium) uptake is attributed to the aforementioned partial desilication of the parent mordenite (3.2.2.2), which occurs concurrently to the partial inter-zeolite transformation.

3.2.4 Equilibrium Adsorption Studies

A high capacity of an ion-exchange material is not necessarily a desirable property when used to remediate nuclear effluent, as materials are typically considered spent at very low adsorption levels (e.g., < 1%) due to exceptionally low breakthrough tolerance levels in column systems. Additionally, excessive adsorption of radionuclides like caesium and strontium would result in highly radioactive spent material, adding significant storage and processing considerations. Nonetheless, capacity is a fundamental property of ion-exchange materials and is hereby probed in attempt to determine how the properties differ in the parent material and composite or fully converted analogues.

3.2.4.1 Caesium Adsorption Isotherms

The maximum caesium adsorption capacity, $q_{\max}$, was determined through analysis of adsorption isotherms for the parent mordenite (Na-washed), a composite material (0.50 M NaOH, MOR:GIS ratio 32:56) and the fully converted zeolite P material (0.70 M NaOH) (Figure 3.10). Langmuir, Freundlich, Temkin and Langmuir-Freundlich isotherm models were fitted to the datasets; Langmuir-Freundlich consistently provided the best fit and was therefore used to determine capacity, $q_{\max}$. Langmuir-Freundlich fitting parameters are presented in Table 3.5. Fitting parameters of all models are available in the appendix (A.3).

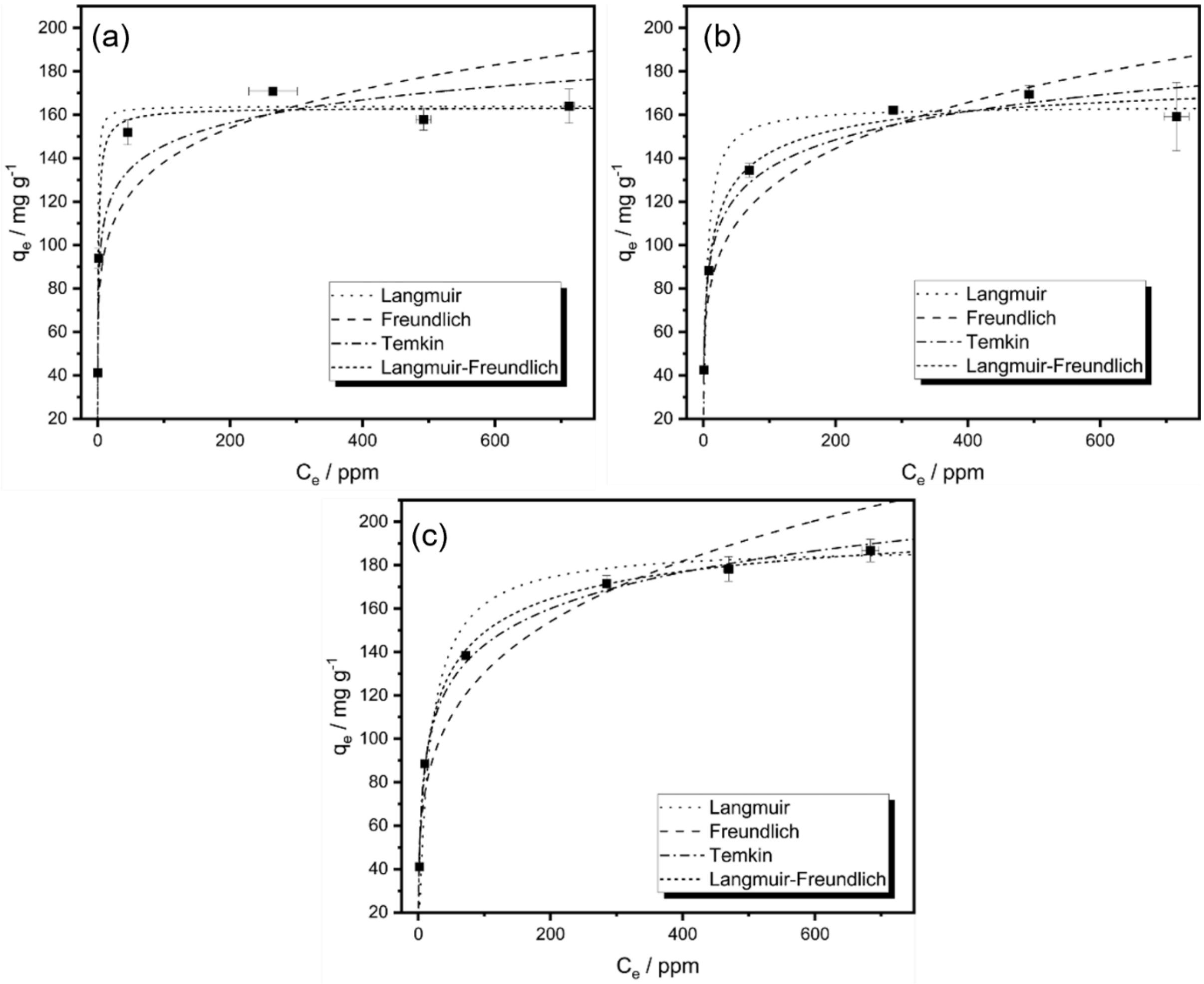

Figure 3.10. Caesium adsorption isotherms obtained through batch ion-exchange experiments. Freundlich, Temkin and Langmuir-Freundlich isotherm models have been applied to each dataset. (a) Parent mordenite (Na exchanged), (b) Composite zeolite (MOR:GIS ratio 32:56) and (c) Fully converted material (zeolite P).

Table 3.5. Langmuir-Freundlich caesium adsorption isotherm parameters for Na-exchanged mordenite (Na-MOR), MOR/GIS composite (32:56 MOR: GIS ratio) and 'fully converted' zeolite P.

	Langmuir-Freundlich			
Material	**q_{max} / mg g^{-1}**	***K***	***n***	**R^2**
Mordenite	164(4)	0.95(14)	0.87(17)	0.982
Composite	186(14)	0.32(5)	0.51(9)	0.984
Zeolite P	213(10)	0.20(2)	0.54(5)	0.997

The interzeolite transformation from parent mordenite to zeolite P, attained in a 0.70 M NaOH solution, results in an increase in caesium capacity from 164 to 213 mg g^{-1}. This is due to the highly aluminous zeolite P framework generated, as revealed by XRF spectroscopy (3.2.2.2). This is comparable to work by Mimura, where a caesium capacity of 234 mg g^{-1} was determined in pseudo-synthetic zeolite P[76]. An intermediate capacity of 186 mg g^{-1} was also shown by the composite material. This capacity increase in comparison to the parent material was likely achieved as a result of both crystallisation of the aluminous zeolite P phase and desilication of the mordenite parent (3.2.2.2). Additionally, the probable formation of mesopores in the material could be significant[193]. When examining the isotherm profiles, the parent mordenite adsorbs more caesium in lower concentration solutions ($C_e < 100$), in comparison to the composite and fully converted materials, which required higher solution concentrations to force the cations into the structure, despite their higher capacities. This indicates that caesium adsorption is more thermodynamically favourable into the mordenite material than the newly crystallised zeolite P. This is in agreement with the batch ion-exchange experiments (3.2.3) and expected due to the ideal diameter of the side pockets that line the 12MR channel in the mordenite structure (3.9 Å) [34, 191, 192].

3.2.4.2 Strontium Adsorption Isotherms

The maximum strontium adsorption capacities, q_{max}, were determined through analysis of adsorption isotherms for the parent mordenite (Na-washed), a composite material (0.50 M NaOH, MOR:GIS ratio 32:56) and the fully converted zeolite P material (0.70 M NaOH) (Figure 3.11). As with caesium adsorption isotherms (3.2.4.1), Langmuir, Freundlich, Temkin and Langmuir-Freundlich isotherm models were fitted to the datasets; Langmuir-Freundlich consistently provided the best fit and was therefore used to determine capacity, q_{max}. Langmuir-Freundlich fitting parameters are presented in Table 3.6. Fitting parameters of all models are available in the appendix (A.3).

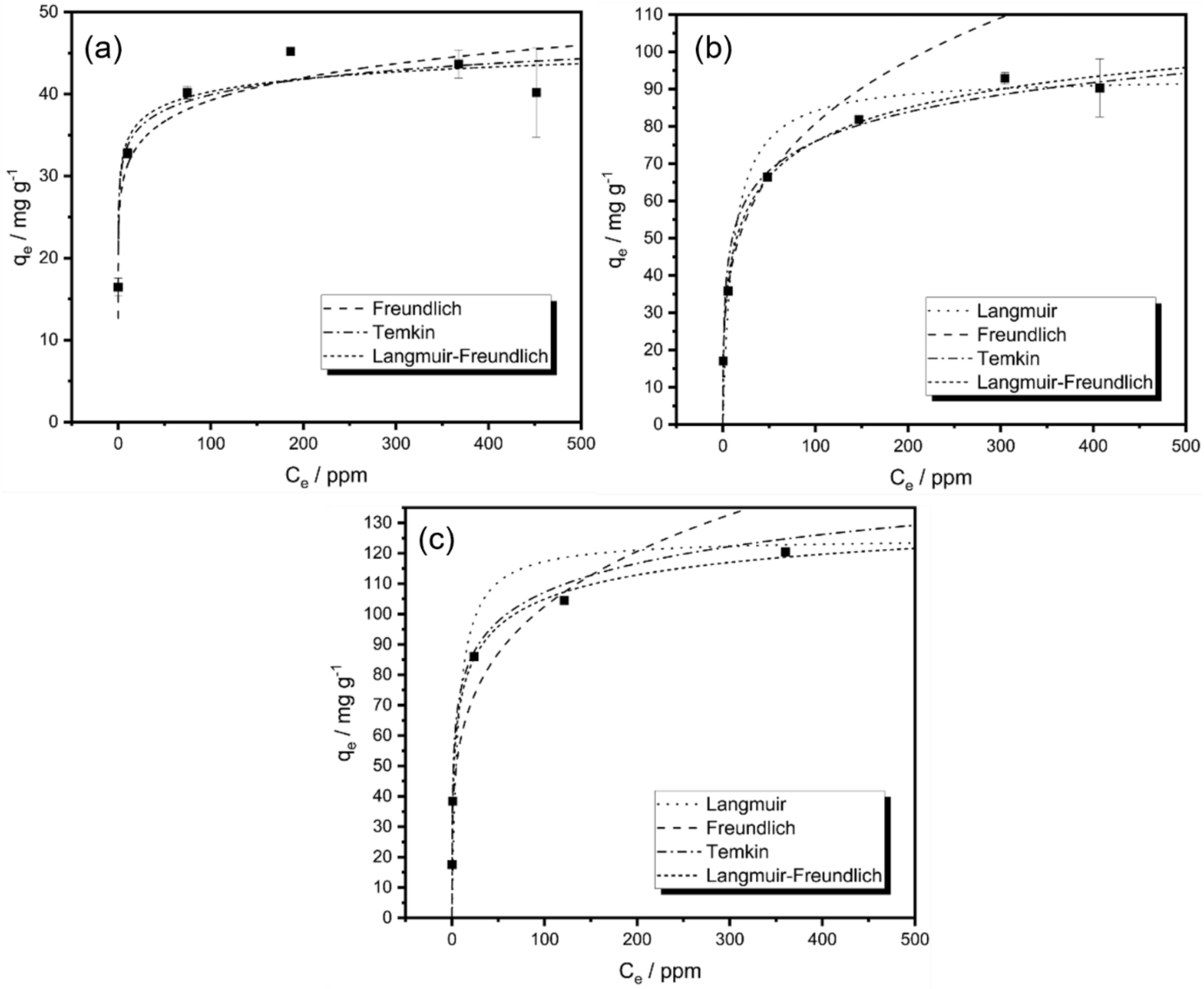

Figure 3.11. Strontium adsorption isotherms obtained through batch ion-exchange experiments. Freundlich, Temkin and Langmuir-Freundlich isotherm models have been applied to each dataset. The Langmuir isotherm model has also been applied where appropriate. (a) Parent mordenite (Na exchanged), (b) Composite zeolite (MOR:GIS ratio 32:56) and (c) Fully converted material (zeolite P).

Table 3.6. Langmuir-Freundlich strontium adsorption isotherm parameters for the parent mordenite (Na exchanged), composite zeolite (MOR:GIS ratio 32:56) and fully converted material (zeolite P).

	Langmuir-Freundlich			
Material	***q$_{max}$* / mg g^{-1}**	***K***	***n***	**R^2**
Mordenite	54(17)	1.0(8)	0.23(11)	0.923
Composite	130(22)	0.20(4)	0.42(8)	0.994
Zeolite P	146(15)	0.38(7)	0.42(6)	0.997

Full transformation from the parent mordenite to zeolite P (achieved in 0.70 M NaOH solution) saw an increase in strontium capacity from 54 to 146 mg g^{-1}, due to the increased concentration of aluminium pairs within the aluminous zeolite P framework. Mimura determined a capacity of 161 mg g^{-1} for a similarly developed material[76]. The composite material was calculated to have a strontium capacity of

130 mg g^{-1}. This drastic increase is a result of the nascent zeolite P framework, which is well-suited material for strontium adsorption due to its abundance of aluminium pairs[34].

3.2.4.3 Caesium and Strontium Capacity Discussion

Caesium adsorption isotherms (3.2.4.1) indicate an approximate 30 % increase in capacity upon transformation to zeolite P. Strontium capacity, however, increased by 170 % (3.2.4.2). All the determined capacity values are presented on a single axis in Figure 3.12. The straight line $y = 0.33\,x$, which represents a system capable of accommodating equal amounts of charge from both caesium and strontium (such as the parent mordenite), is also included in Figure 3.12. Materials residing below the line are capable of absorbing less strontium than the caesium capacity suggests. This is likely to be a result of limited 'aluminium pairs' within the framework, which strontium requires in order to adhere. Materials positioned above the line can absorb more strontium than their caesium capacities suggest; this can be attributed to a lack of suitable caesium sorption sites within the framework.

This analysis emphasises the vast quantities of strontium adsorption sites produced during the transformation process as a result of the formation of zeolite P. This strengthens the premise of producing bespoke exchange materials that can be tailored to a given waste stream, especially as the quantity of zeolite P generated is so readily controlled (3.2.2). Another factor affecting the strontium capacity of the composite material is the possibility of the parent mordenite itself gaining strontium adsorption sites during the partial transformation (due to desilication). Given the errors associated with the adsorption capacity values of the composite material, it is difficult to say with certainty whether this is the case. Further adsorption studies on purely desilicated material would be required to confirm this.

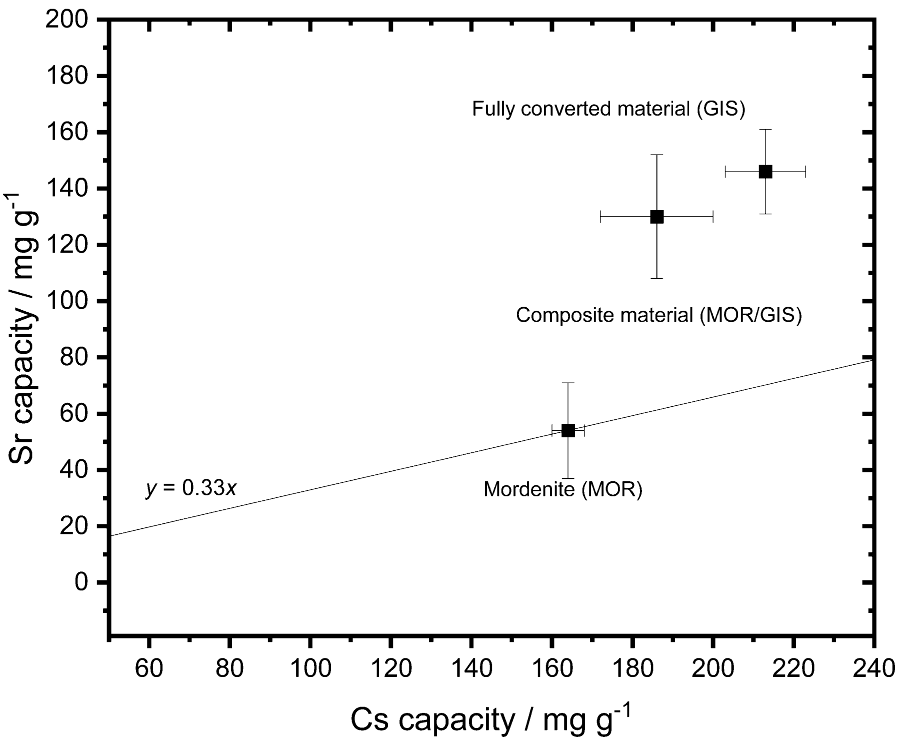

Figure 3.12. Caesium and strontium capacities (q_{max}) of mordenite, the composite material and the fully converted material, as determined from equilibrium adsorption isotherms. The straight line $y = 0.33x$ is plotted to depict region where equal quantities of charge from both caesium and strontium can be accommodated.

3.2.5 Kinetic Studies

Industrial ion-exchange is normally achieved through the deployment of fixed-bed columns, where effluent is pumped through a stationary phase of ion-exchange material[20, 95, 184, 185, 205]. Residence times of effluent in such columns can be as short as several minutes; it is therefore critical that the kinetics of exchange are suitably fast to ensure adequate remediation[20]. Here, batch ion-exchange experiments were performed to assess the rate of ion-exchange of both caesium and strontium in the parent mordenite (Na-washed), a composite material (0.50 M NaOH, MOR:GIS ratio 32:56) and the fully converted zeolite P material (0.70 M NaOH).

3.2.5.1 Rate of Caesium Uptake

Kinetic isotherms showing the adsorption of caesium by the parent mordenite (Na-washed), a composite material (0.50 M NaOH, MOR:GIS ratio 32:56) and the fully converted zeolite P material (0.70 M NaOH) are presented in Figure 3.13. The 2nd order kinetic model (2.2.1.5) has been applied each dataset, with excellent accordance shown ($R^2 > 0.99$). Qualitatively, equilibrium was reached, despite the short 3-hour experimental run time. Calculated isotherm parameters from the applied second order kinetic models are presented in Table 3.7, in addition to the estimated time required to reach 95 % of the equilibrium uptake.

The 2nd order rate constants (k) associated with the caesium uptake in mordenite, and the composite material were similar; the system took 3 and 5 minutes respectfully to reach 95 % of the derived equilibrium uptake. Furthermore, these $t_{95\%}$ values are within error of each other, suggesting no significant differences were observed experimentally. The fully converted zeolite P material reached 95 % of its equilibrium uptake in under a minute. As such, the reported rate constant is exceptionally high (40 g mg^{-1} h^{-1}), with a large associated error due to the gradient during the initial stages of the isotherm. Caesium adsorption is typically faster than strontium due to the small hydration sphere, which renders the cation more mobile than other species with larger hydration spheres, such as strontium[34]. In these experiments, the rapid rate of exchange of the parent mordenite can be attributed to the combination of twelve- and eight-ring channels. The 12-ring channels act as a 'molecular motorway', enabling rapid diffusion within the zeolite structure, whereas the 8-ring channels provide excellent cavities for adhesion[34].

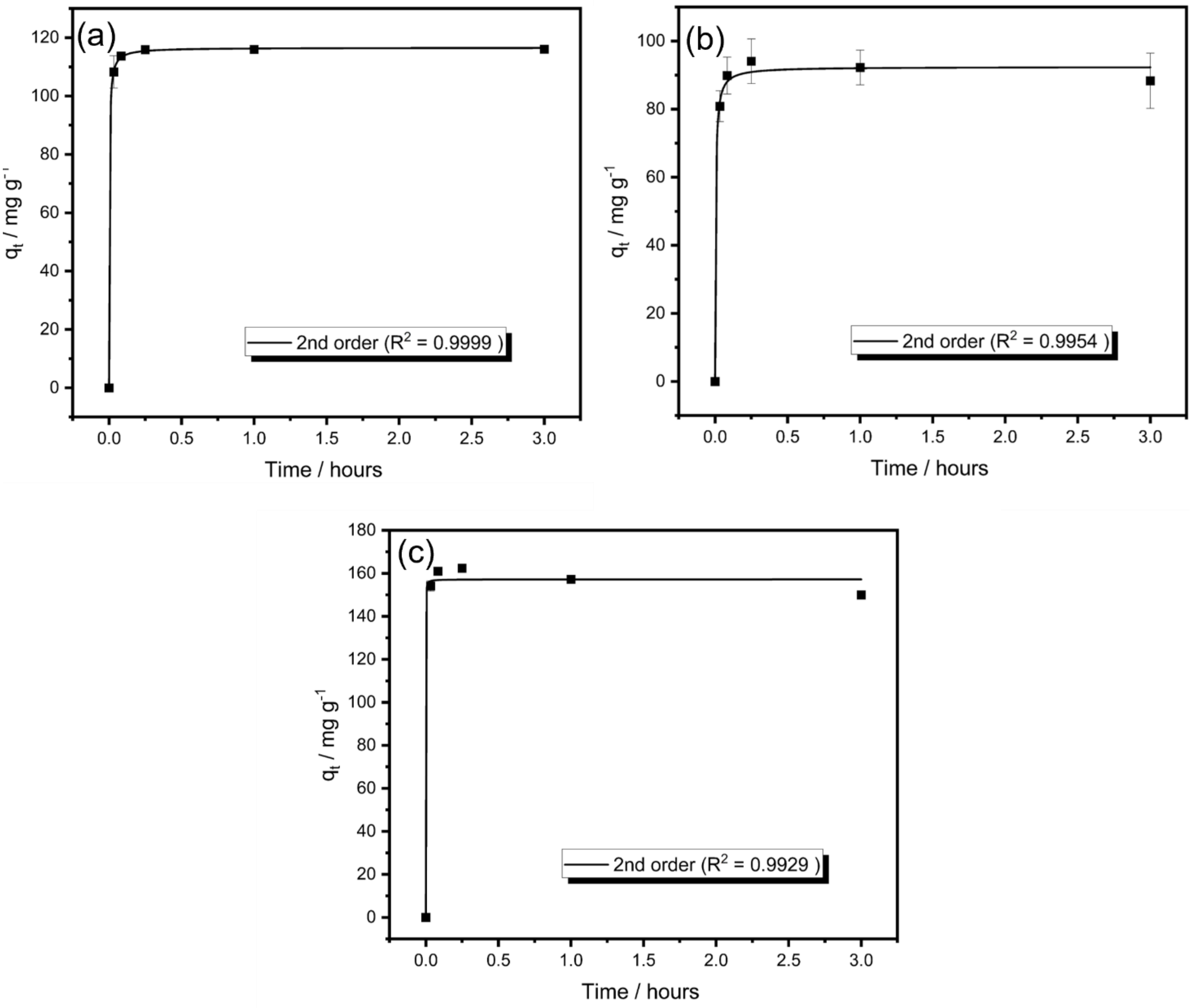

Figure 3.13. Kinetic isotherms showing the adsorption of caesium. (a) Na-exchanged parent mordenite, (b) 32:56 MOR:GIS composite material and (c) fully converted zeolite P material. The 2nd order kinetic model has been applied to each isotherm.

Table 3.7. 2nd order fitting parameters for caesium kinetic isotherms.

Material	**q_e/ mg g^{-1}**	**k / g mg^{-1} h^{-1}**	**R^2**	**$t_{(95\%)}$ / minutes**
Na-mordenite	117(1)	3.49(26)	0.9999	3(1)
MOR:GIS composite (32:56)	92(2)	2.61(97)	0.9954	5(3)
Fully converted zeolite P	157(3)	40(330)	0.9929	<1

3.2.5.2 Rate of Strontium Uptake

Kinetic isotherms showing the adsorption of strontium by the parent mordenite (Na-washed), a composite material (0.50 M NaOH, MOR:GIS ratio 32:56) and the fully converted zeolite P material

(0.70 M NaOH) are presented in Figure 3.14. Both Elovich and 2nd order kinetic isotherm models were fitted to the datasets (for more information on these models, see 2.2.1). Fits to both models are acceptable ($R^2 > 0.94$). However, the best fits are obtained using the Elovich model for the parent mordenite and the composite material, possibly due to the surface inhomogeneity of natural zeolites, whereas the 2nd order kinetic model provided the best fit to the dataset for fully converted zeolite P. Calculated isotherm parameters are shown in Table 3.8. Fits to the isotherm models not shown here are presented in Appendix A.4.

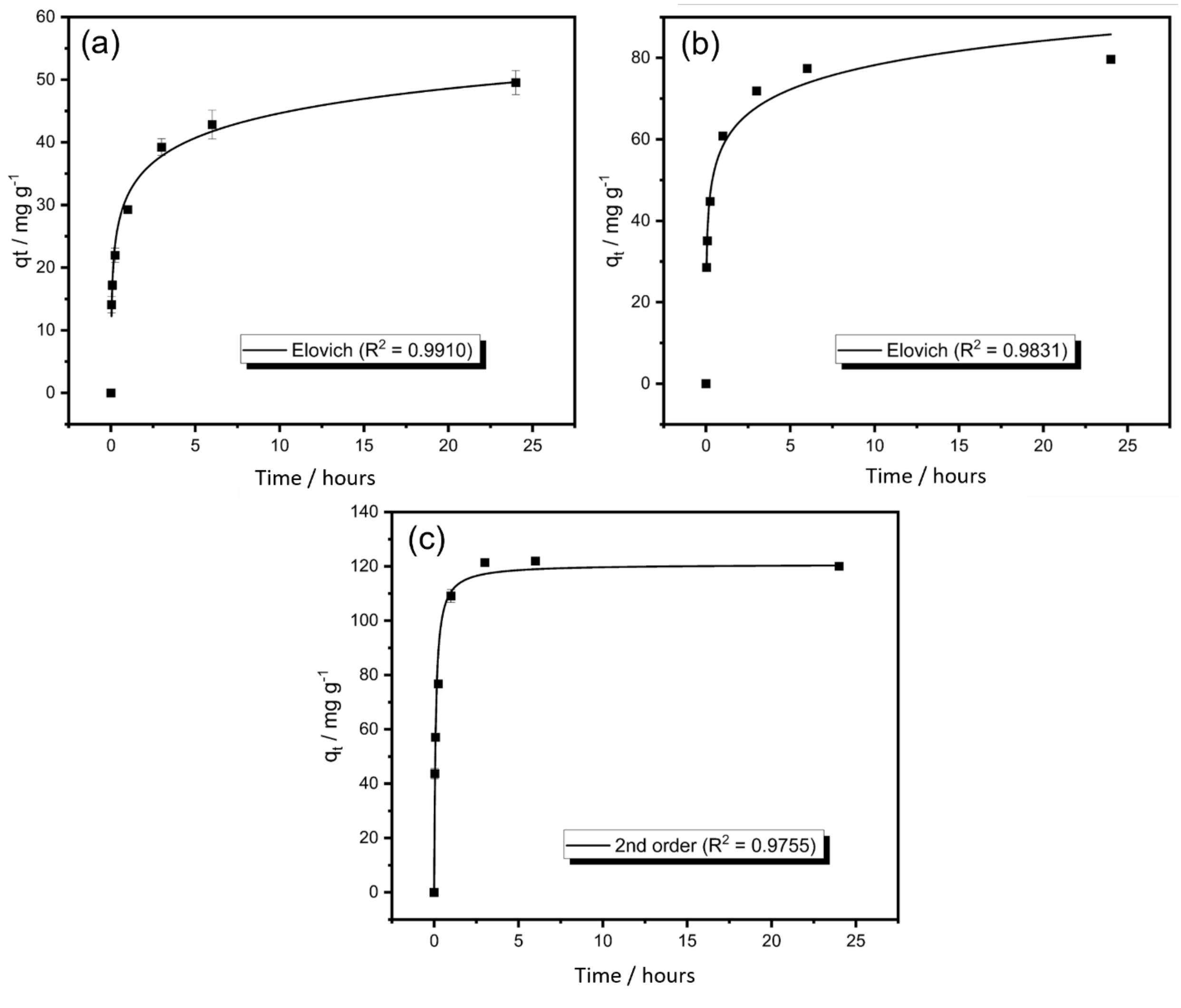

Figure 3.14. Kinetic isotherms showing the adsorption of strontium. (a) Na-exchanged parent mordenite, (b) 32:56 MOR:GIS composite material and (c) fully converted zeolite P material. The Elovich model is fitted to the parent mordenite and composite material datasets. The 2nd order kinetic model has been fitted to the dataset from the fully converted zeolite P.

Table 3.8. Elovich fitting parameters for strontium kinetic adsorption isotherms applied to the parent mordenite (Na-exchanged) and the composite material (MOR:GIS 32:56). 2nd order kinetic model fitting parameters for the strontium kinetic adsorption isotherm applied to the fully converted zeolite P material.

Material	α	β	**R^2**
Na-mordenite	3210000(2000000)	0.41(2)	0.9974
MOR:GIS composite (32:56)	7490(3260)	0.12(1)	0.9831
Material	**q_e / mg g^{-1}**	**k / g mg^{-1} h^{-1}**	**R^2**
Fully converted zeolite P	121(4)	0.09(2)	0.9755

In comparison to the rate of caesium adsorption, which reached equilibrium within a few minutes (3.2.5.1), the rate of strontium uptake is markedly slower, reaching equilibrium in multiple hours. The parent mordenite did not achieve equilibrium within the experimental timeframe of 24 hours. To more quantitatively compare rates of uptake between models, the estimated time to reach 95% equilibrium for each material has been calculated (Table 3.9). The sodium-exchanged parent mordenite material and the composite reached 95 % of equilibrium in 20 and 15 hours, respectively, and within calculated uncertainty. However, the model for the composite material does not fit particularly well at longer times, and therefore is likely to be underestimating the rate of exchange. The fully converted zeolite P material reaches 95 % of equilibrium after just two hours; suggesting the transformation has a positive effect on the rate of strontium uptake. This becomes further apparent when the significantly enhanced strontium capacities (highlighted in Section 3.2.4) are considered; the fully converted zeolite P can reach equilibrium faster than the parent mordenite with a far greater capacity. Similarly, the composite material reaches equilibrium more quickly than the parent, and also exhibits a sizeable increase in capacity. The dual improvement to rate and capacity equates to considerably more adsorption events in a given period of time, theoretically resulting to reduced breakthrough when deployed in industrial column systems. The origin of this increased rate of exchange can be attributed to the formation of a phase more suited to strontium adsorption, the probable generation of mesopores[193] and the increased surface area associated with the pseudo-synthetic zeolite P phase (3.2.7).

Table 3.9. Estimated time to 95% equilibrium loading determined from kinetic models.

Material	**Model**	**Time to 95% q_e / hours**
Na-mordenite	Elovich	20(12)
MOR:GIS composite (32:56)	Elovich	15(6)
Fully converted zeolite P	2nd order kinetic	2(1)

3.2.6 Formation of Granular Composites

Industrial ion-exchange processes often operate as dynamic flow systems, where effluent is pumped through a fixed bed of ion-exchange material[20, 95, 184, 185, 205]. To facilitate flow and prevent pressure discrepancies, granular material or beads are deployed (typically > 200 μm diameter). Previously discussed materials in this chapter have been in powder form and hence unsuitable for deployment in fixed-bed columns. Here, the possibility of generating more industrially relevant composite zeolite granules is explored.

Firstly, granular parent mordenite (400 – 600 μm) was attained though grinding and sieving of the raw material. Analogous to powdered material, basic hydrothermal treatment (0.70 -1.20 M NaOH) induced transformation to zeolite P, which could be similarly controlled through manipulation of the sodium hydroxide concentration. PXRD data of the generated materials, in addition to simulated patterns of mordenite and zeolite P, is displayed in Figure 3.15.

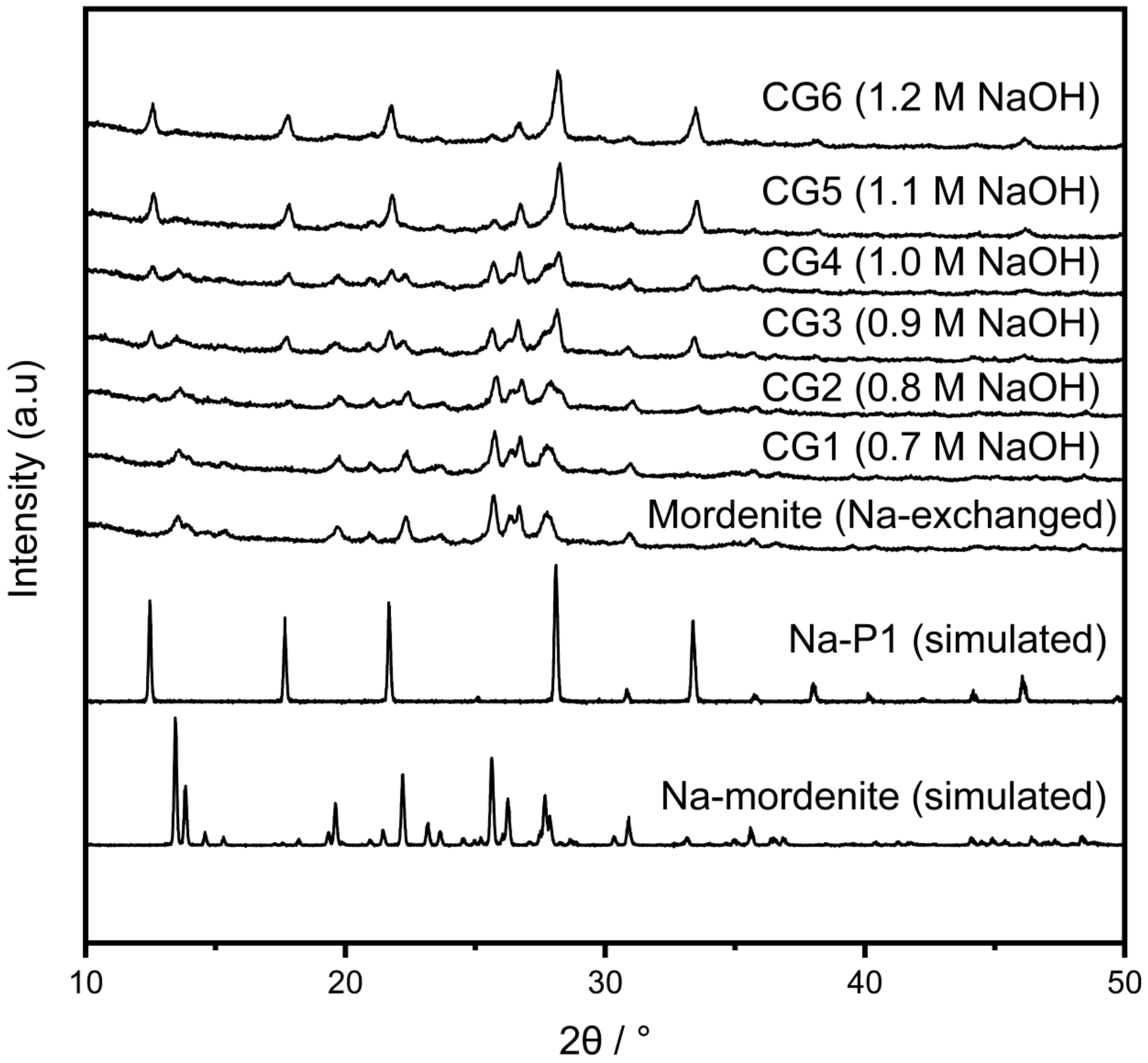

Figure 3.15. PXRD patterns of granular (400-600 μm) mordenite material after hydrothermal treatment (0.70 – 1.20 M solutions). Simulated mordenite and zeolite P (Na-P1) patterns are also presented (λ = 1.5406 Å).

Higher NaOH concentrations were required to facilitate transformation in comparison to previously discussed powdered transformations (3.2.2). This may be due to the reduced surface area, which would retard the kinetics of dissolution, which is often the rate-determining step in interzeolite transformations[115]. Phase fractions of these materials, as determined through Rietveld analysis[162, 163] (A.5), are presented in Table 3.10. Analogous to the generation of powdered composites, an excellent level of control was observed: the mordenite weight fraction decreased incrementally in more basic solutions (> 0.70 M NaOH) as zeolite P became more abundant. A granular composite with the desired blend of the complementary zeolitic phases can be generated.

In this work, the material obtained from hydrothermal treatment in the most concentrated NaOH solution, GC6, still contained 22 Wt. % mordenite. It is unclear whether fully transformed material is readily attained above this concentration, or if the granular nature somewhat restricts the dissolution of portions of the mordenite. Unlike in the powdered series, the zeolite P polymorph Na-P1 was exclusively produced. This is consistent with literature, which shows a preference for the formation of Na-P1 at higher basicity (> 0.7 M NaOH)[81].

Table 3.10. Estimated weight fractions of mordenite and zeolite P in granular composite materials generated in 0.70 to 1.20 M NaOH solutions. [a]Parent mordenite was subject to a sodium-wash prior to analysis.

Material	Treatment	Mordenite W_f	Zeolite P W_f
Mordenite	1.0 M NaCl[a]	0.92(1)	0.00(1)
CG1	0.70 M NaOH, 100 °C	0.91(2)	0.01(1)
CG2	0.80 M NaOH, 100 °C	0.85(1)	0.09(1)
CG3	0.90 M NaOH, 100 °C	0.62(1)	0.28(1)
CG4	1.0 M NaOH, 100 °C	0.57(1)	0.34(1)
CG5	1.10 M NaOH, 100 °C	0.25(1)	0.67(1)
CG6	1.20 M NaOH, 100 °C	0.22(6)	0.73(8)

Physically, all six composites remained granular after transformation. However, the structural integrity of the more transformed samples (e.g., GC6) was significantly worse than the parent mordenite. From an industrial perspective, this is undesirable due to the increased likelihood of fines production, which can lead to in-plant flow difficulties.

3.2.7 SEM Analysis of the Granular Composites

SEM imaging was deployed to examine the surface morphology of composite materials GC4 and GC5, both of which contain significant quantities of both mordenite and zeolite P (57:34 and 25:67 MOR:GIS ratios, respectively). SEM images of raw mordenite revealed a somewhat featureless exterior with only the presence of small fines (< 5 μm) on the surface (3.2.1.3). Equivalent imaging of GC4, a composite granule containing 57 and 34 Wt. % of mordenite and zeolite P, respectively, is displayed in Figure 3.16. Significant morphological differences are observed compared to the parent mordenite. Firstly, substantial cracking is seen. This is presumably a result of framework dissolution by NaOH and gives evidence of mesoporosity and a greater surface area. Secondly, spherical sub-particles of around 10 μm in diameter are shown to be populating the surface of the material. Considering the diffraction data, these are assumed to be polycrystalline zeolite P moieties.

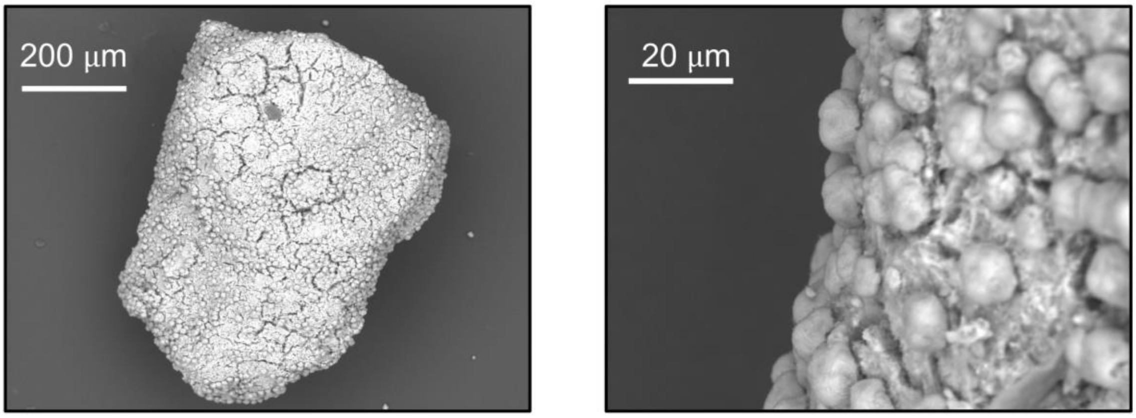

Figure 3.16. SEM images (15 keV) of a CG4 granule (57:34 MOR:GIS ratio).

SEM imaging of a granule of CG5, a composite comprised of 25 and 67 Wt. % of mordenite and zeolite P, respectively, is displayed in Figure 3.17. Analogous to CG4, spherical sub-particles populate the surface of the material. However, they have increased significantly in diameter to approximately 20 μm. Assuming the identity of these spheres to be zeolite P, this observation is in line with expectations, as CG5 contains significantly more zeolite P in comparison to CG4. Unlike CG4, no surface cracks are visible, although the abundance of the spherical sub-particles is obscuring the view to the surface.

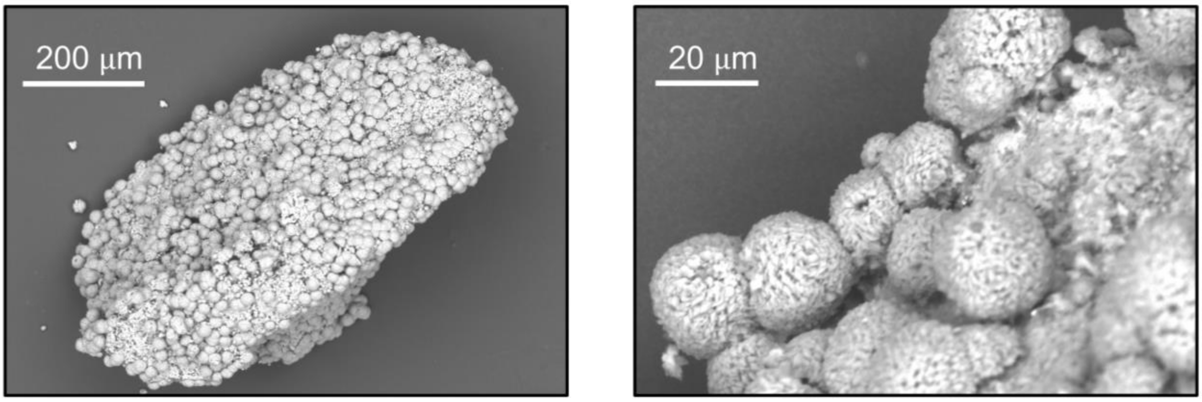

Figure 3.17. SEM images (15 keV) of a CG5 granule (25:67 MOR:GIS ratio).

3.2.8 XCT and Local, Image-Guided Diffraction Analysis of Composites

SEM imaging suggests the development of spherical analogues on the surface of the material as the transformation proceeds. However, the technique provides little information on the internal morphology of the materials, in particular what happens to the mordenite at high levels of conversions, such as in CG5. An understanding of both the surface and internal morphology of the composites is important, as it could have profound effect on the ion-exchange performance and industrial applicability of the material. Furthermore, up to this point, the structure of the nascent spherical moieties on the surface is assumed to be zeolite P. However, no conclusive evidence has been provided. To address both these points, the composite granules CG4 and CG5 were subject to XCT and local, image-guided diffraction experiments at the Dual Imaging and Diffraction (K11, DIAD) beamline at Diamond Light Source[172], UK.

3.2.8.1 Analysis of CG4

A cross-sectional image of CG4 (57:34 MOR:GIS ratio) obtained from tomography measurements is displayed in Figure 3.18. Additionally, powder diffraction patterns obtained from beam trajectories ‘b’ and ‘c’ are shown.

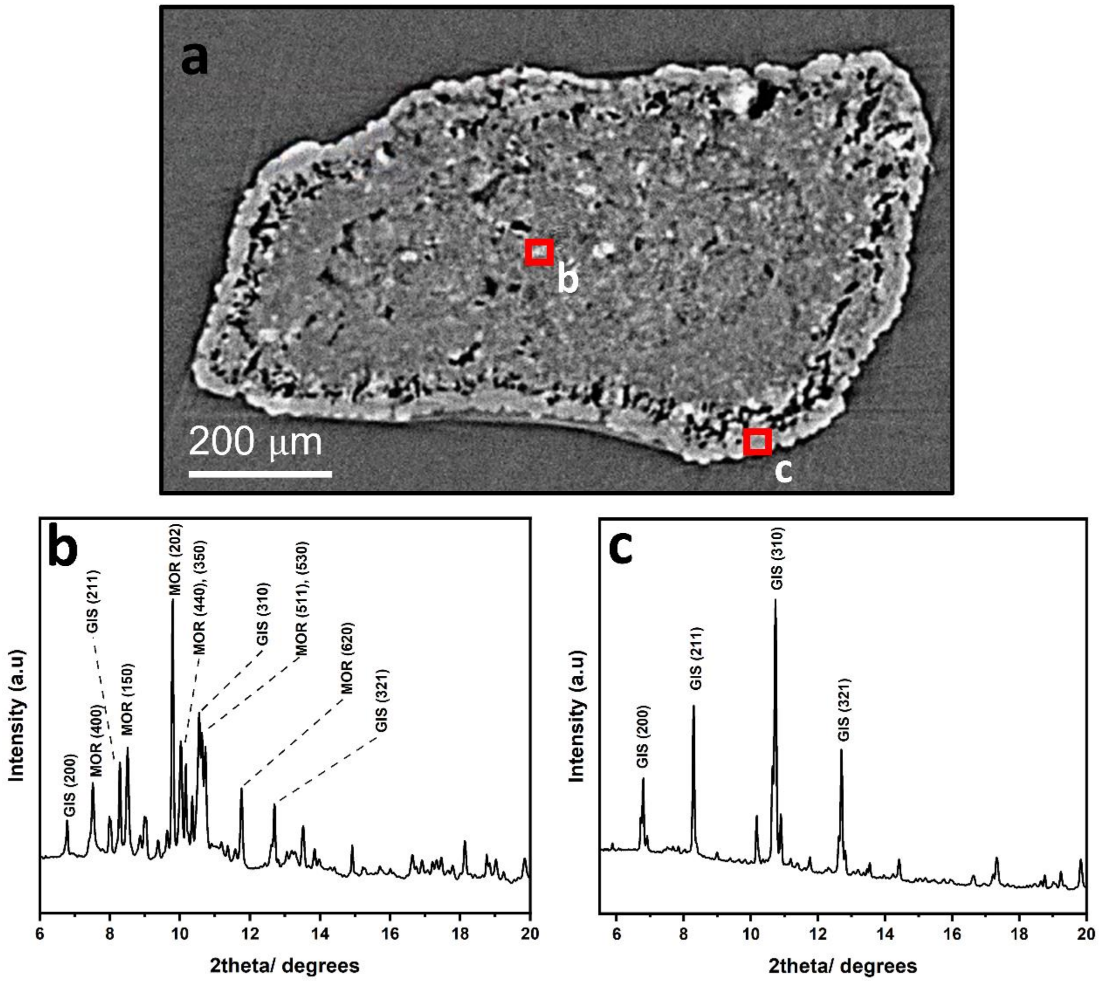

Figure 3.18. (a) Tomography cross-section of a CG4 granule with annotated diffraction beam trajectories, (b) Local PXRD pattern obtained from beam trajectory ‘b’. Key mordenite (MOR) and zeolite P (GIS) reflections are labelled. (c) Local PXRD pattern obtained from beam trajectory ‘c’. Key zeolite P (GIS) reflections are labelled.

The cross-sectional tomography image (3.18a) suggests the presence of two main phases in the granule: a lighter contrast ‘shell’ encapsulates the darker contrast interior of the granule. A distinct ‘void’ region is also present between the two phases, which is visible as an even darker contrast. Diffraction beam trajectory ‘b’ penetrates the centre of the granule and therefore travels through the outer shell, then the interior, before leaving through the outer shell. The diffraction pattern will therefore give a superposition of phases in both the outer shell and interior. Indeed, the diffraction pattern is comprised of significant Bragg peaks corresponding to both mordenite and zeolite P (Figure 3.18b). Beam trajectory ‘c’ was selected as it only penetrates the outer shell and therefore does not pass through the darker-contrast inner material. Diffraction data obtained from trajectory c (Figure

3.18c) confirms that zeolite P is the majority phase at the surface and is therefore the identity of the spherical moieties observed by SEM (3.2.7). Inspection of the zeolite P Bragg peaks reveals twinning shoulder peaks on the (200), (310) and (321) reflections. This suggests the presence of Na-P2, a zeolite P polymorph, in the shell of the composite material, in addition to Na-P1. Both P1 and P2 are comprised of identical building units; the only discrepancy is that in P2 *dcc* chains are alternating and are misaligned by a 15° rotation[81]. In this case, Na-P2 reflections are not observed in laboratory diffraction data (3.2.1.1). It is unclear whether this is due to local environments of Na-P2 or the difference in resolution between laboratory and synchrotron sources. Nonetheless, studies have shown the adsorption properties of the two polymorphs to be comparable[81], so any impact on the bulk ion-exchange properties is expected to be minimal.

Diffraction tomography data can be attained by collecting many diffraction patterns at different beam trajectories during staged sample rotation. This data is then spatially converted, resulting in a diffraction pattern for each 25 × 25 μm voxel in the scanning volume. Regions of these patterns corresponding to Bragg peaks for both mordenite and zeolite P are integrated and applied to a colour scale, thus providing a 'phase map' of a single granule of CG4 (Figure 3.19). This data reaffirms the core-shell model of the composite materials; the zeolite P shell is clearly observed in blue, surrounding the orange mordenite core.

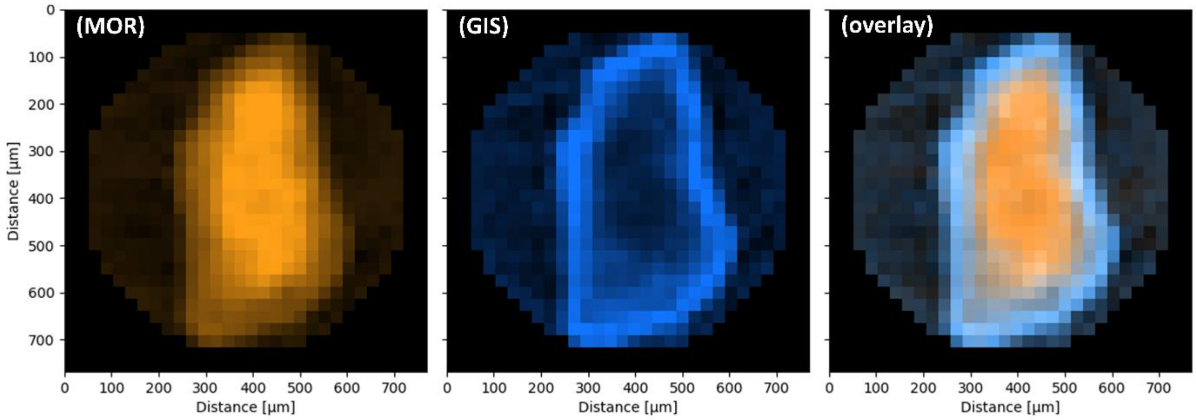

Figure 3.19. Spatially resolved diffraction tomography exhibiting phase distribution of mordenite and zeolite P phases in a granule of CG4.

3.2.8.2 Analysis of CG5

Tomography cross-sectional imaging of CG5, a composite granule comprised of 25 % mordenite and 34 % zeolite P, is displayed in Figure 3.20. Additionally, the diffraction pattern obtained from beam trajectory ‘b’ is shown.

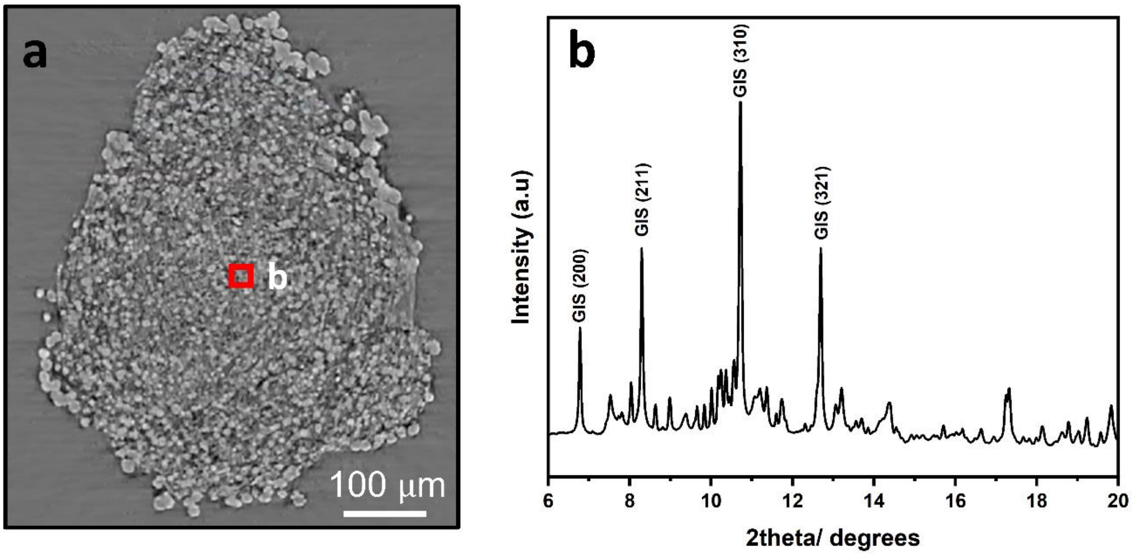

Figure 3.20. (a) Tomography cross-section of a CG5 granule with annotated diffraction beam trajectory ‘b’, (b) Local PXRD pattern obtained from beam trajectory ‘b’. Key zeolite P (GIS) reflections are labelled.

Significant morphological differences are observed in CG5 (Figure 3.20a). The large, spherical sub-particles observed by SEM can be seen on the exterior granule in tomography imaging, up to approximately 30 μm in diameter. Intrestingly, the interior also contains similar, albeit smaller, sub-particles of around 10 μm in diameter. Beam trajectory ‘b’ produces a diffraction pattern with zeolite P as the most abundant phase, although reflections attributed to mordenite and quartz are observed (A.6). Interestingly, no peaks for the Na-P2 structure are observed. This agrees with the bulk diffraction pattern (3.2.6).

3.2.8.3 Mechanism of Transformation

Drawing on the SEM, XCT and local diffraction data examined in this chapter, a macroscale mechanism of transformation can be proposed. Firstly, surface dissolution-crystallisation occurs, resulting in a zeolite P outer shell encapsulating a partially dissolved mordenite interior. The base then penetrates the outer shell, dissolving and recrystallising the interior into zeolite P. Containment by the nascent outer shell possibly aids this process by restricting diffusion of aluminosilicate nano particles into the bulk solution. A schematic of this process is depicted in Figure 3.21.

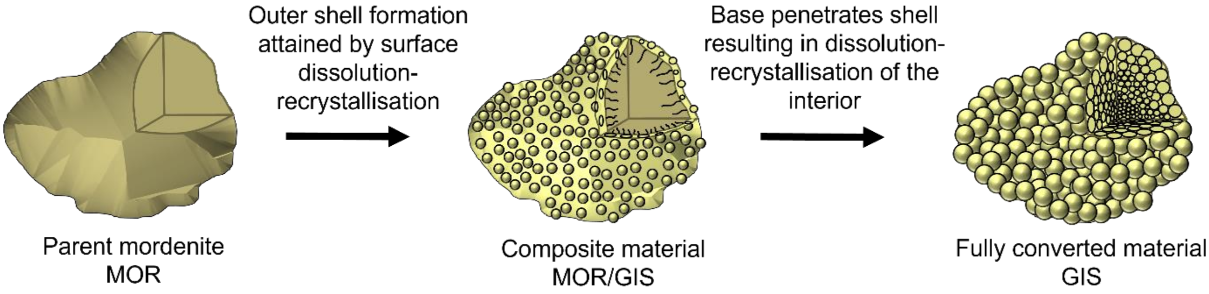

Figure 3.21. Proposed macroscale-mechanism of interzeolite transformation of the natural mordenite.

3.2.9 *In-Situ* Ion-Exchange at DIAD

Thus far, the caesium and strontium adsorption properties of the composite materials have been evaluated in bulk. However, the unique core-shell orientation of the two complementary zeolites raises questions regarding the functionality of both phases, especially the mordenite core. In particular, the individual exchange kinetics and selectivity for each discrete phase are unexplored. As the nascent zeolite P resides on the surface on the granules, exchange into these sites is expected to be immediate. However, the mordenite core appears to be somewhat protected from solution by the zeolite P shell. Determining the ion-exchange capability of the mordenite core will aid in understanding of the role of this phase within the composite zeolite systems. In this section, its ability to function as a discrete ion-exchange material, in addition to a zeolite P scaffold, is assessed through *in-situ* ion-exchange experiments supported with local, image-guided X-ray diffraction measurements.

Exchange of caesium into the mordenite framework exerts a change of space group from C2/m to C1[206]. This change in symmetry results in changes to the diffraction pattern; for example, the (130) reflection, which in no longer observed. Like the mordenite (130) reflection, the peak attributed to the zeolite P (200) reflection also decreases in intensity upon caesium incorporation. This, combined with local diffraction data, can be exploited to crudely 'track' the exchange of caesium within a single composite zeolite granule. The following section outlines the results from scoping experiments undertaken at K11 DIAD, Diamond Light Source, UK. Firstly, single composite CG4 granules are positioned in the beam and several pertinent 25 × 25 μm beam trajectories are identified. Concentrated (5000 ppm) caesium/strontium solution is then remotely injected into the cell prior to acquisition of local diffraction data from the pre-established diffraction beam trajectories. Despite not being relevant in the field of nuclear waste management, high caesium concentrations are required to observe the 'bulk' crystallographic changes associated with exchange.

3.2.9.1 CG4 Granule in 5000 ppm Caesium Solution

The radiograph of a positioned CG4 granule, annotated with three beam trajectories, is presented in Figure 3.22. Trajectory 1 penetrates the centre of the granule and hence receives diffraction contributions from both the zeolite P shell and all depths of the mordenite core. Similarly, trajectory 2 sees contributions from the zeolite P shell and the mordenite interior. However, as the beam trajectory is towards the exterior of the granule, mordenite Bragg peak contributions will be from the edge of the mordenite core. Diffraction beam trajectory 3 is located on the uppermost tip of the granule and was the best attempt at isolating the zeolite P shell; reflections attributed to zeolite P are by far the most abundant in the diffraction pattern. This information is summarised in Table 3.11.

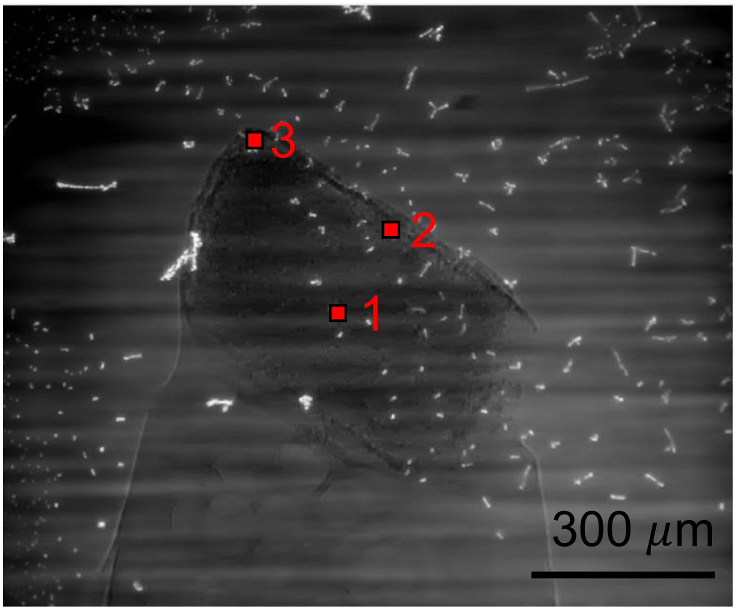

Figure 3.22. Radiograph of mounted CG4 granule annotated with diffraction beam trajectories (5000 ppm caesium experiment).

Table 3.11. Summary of diffraction beam trajectories utilised in *in-situ* ion-exchange experiments of CG4 (5000 ppm Cs solution).

Diffraction beam trajectory	Observable phases
1	Entire mordenite core, zeolite P shell.
2	Outer mordenite core, zeolite P shell.
3	Zeolite P shell.

A summary of diffraction data collected in this experiment (from all three beam trajectories) is displayed in Figure 3.23. Data collected prior and post solution infusion is presented, in addition to after exchange, which was deemed complete after approximately 150 minutes. Expectantly, peak positions did not change upon addition of the aqueous caesium solution as significant quantities of caesium are unable to enter in the framework in the short time period required to cycle through the points. However, the background in the region of interest (1.0 – 2.6 Q (Å^{-1})) is significantly greater after infusion of the caesium solution. This is due to the diffuse scattering contributions of the aqueous phase. This effect is most prominent in the diffraction data collected from diffraction beam trajectory 3 because of the inherently lower signal-to-noise ratio, which arises from the reduced amount of material the beam passes though.

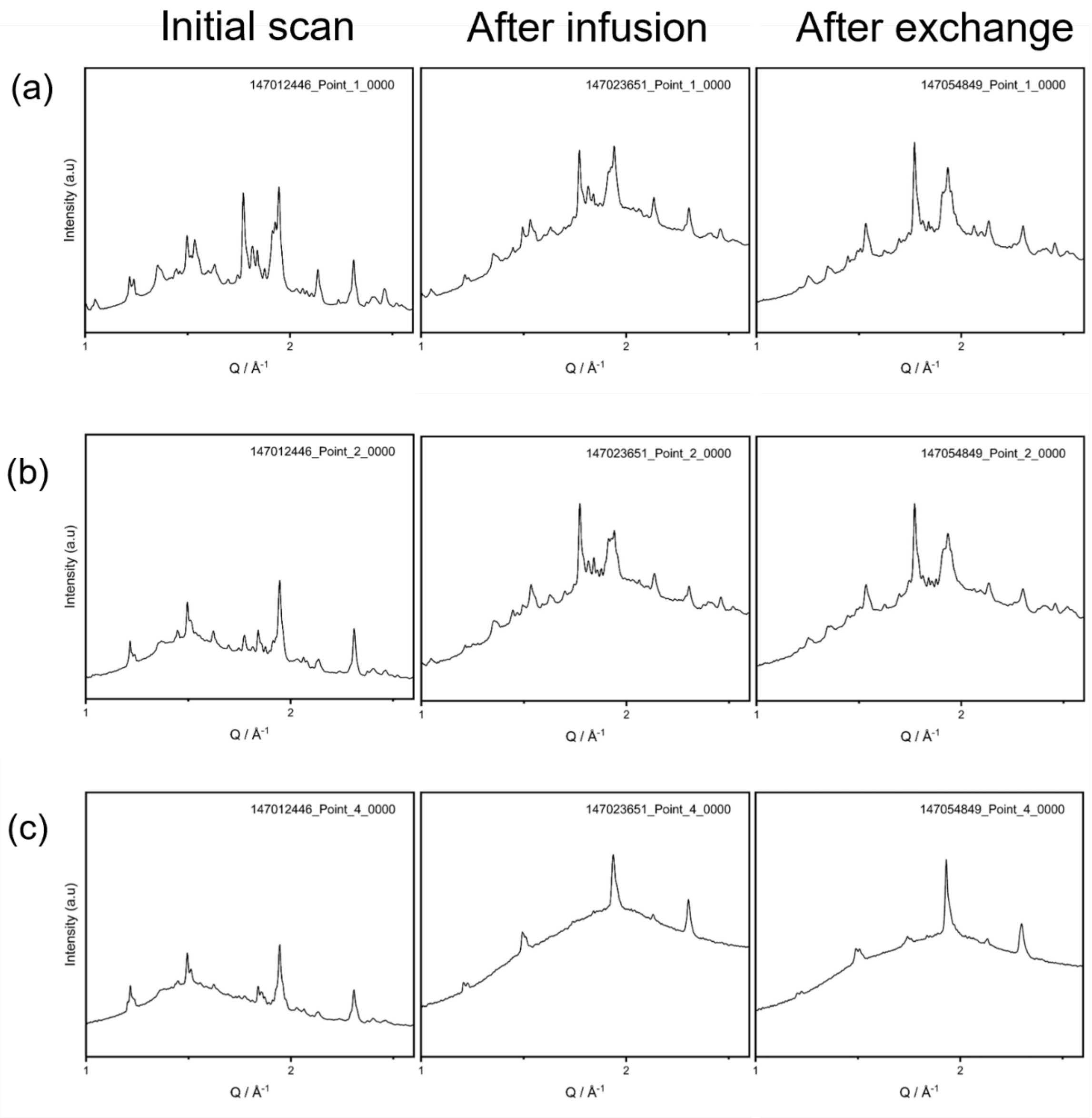

Figure 3.23. Overview of local PXRD patterns obtained from various beam trajectories after mounting, after infusion and after exchange (5000 ppm caesium experiment). (a) Patterns obtained from diffraction beam trajectory 1, (b) patterns obtained from diffraction beam trajectory 2, (c) patterns obtained from diffraction beam trajectory 3.

The Bragg peak attributed to the mordenite (130) reflection (~1.07 Q (Å^{-1})) decreases in intensity in diffraction data collected from beam trajectories 1 and 2 due to caesium incorporation within the framework channels. This is further highlighted in Figure 3.24. After ~150 minuites, the peak diminished to an extent that it is no longer discernable from the background for both trajectories. This suggests that the mordenite core retains the ability to function as an ion-exchanger after partial transformation and therefore that the nascent zeolite P shell is permeable to aqueous media.

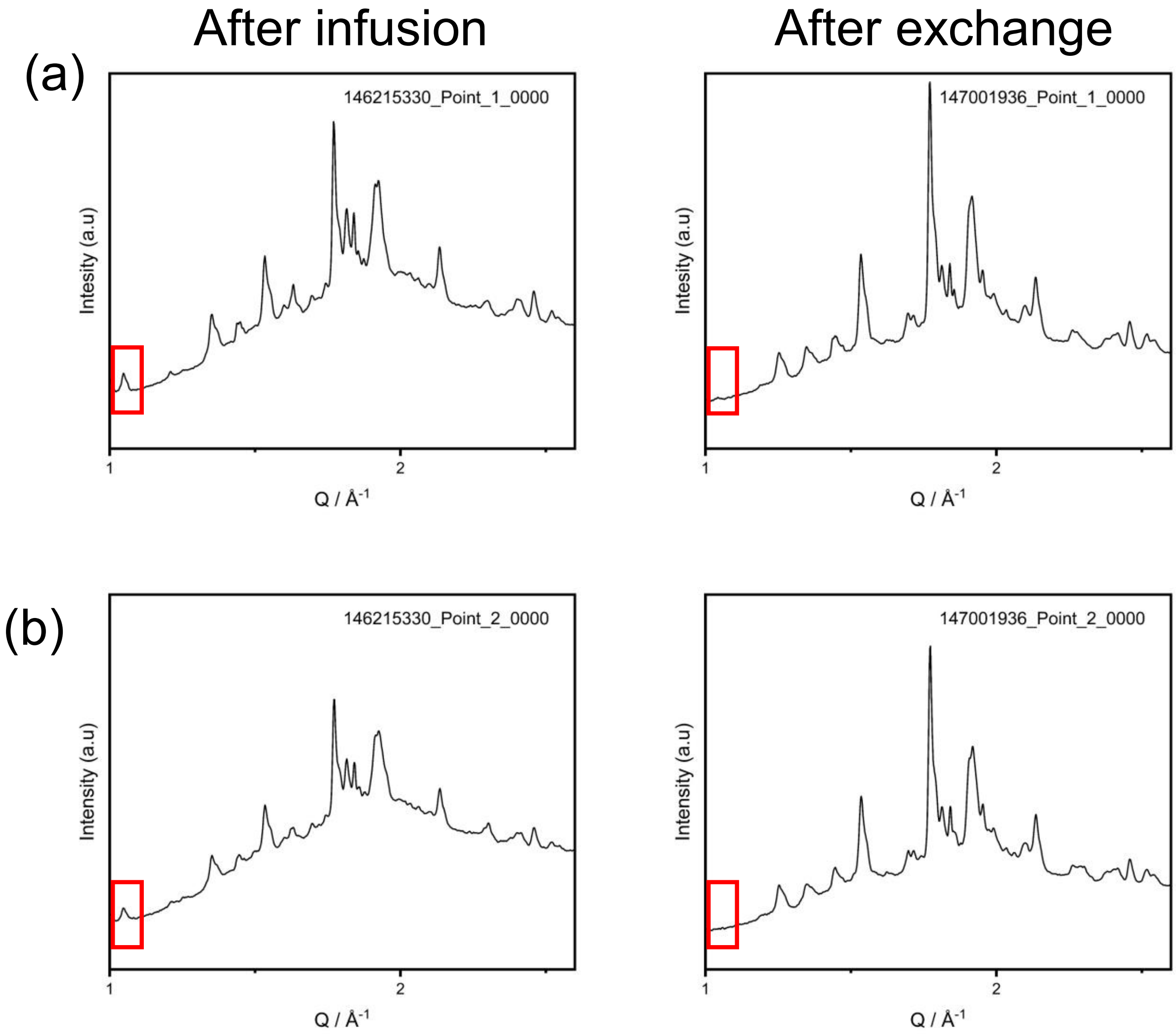

Figure 3.24. Local diffraction patterns highlighting the reduction in MOR (130) reflection intensity during the ion-exchange process (5000 ppm caesium experiment). (a) Patterns obtained from diffraction beam trajectory 1 and (b) patterns obtained from diffraction beam trajectory 2.

The diminishing intensity of the mordenite (130) Bragg peak, positioned at approximately 1.07 Q ($Å^{-1}$), indicates that the mordenite interior retains its functionality as an ion-exchanger. However, the rate of exchange is not discernible through observation of the final patterns. In order to qualitatively monitor the rate of exchange, the integrated intensity of the mordenite (130) reflection, for all diffraction patterns taken over the ~150 minute experiment, is plotted as a function of time (Figure 3.25). The intensity obtained from diffraction beam trajectory 1 decreases steadily to a value of about 5 % of the initial intensity after 150 minutes. The diffraction beam trajectory focused on the outer mordenite core (trajectory 2) saw a significantly faster reduction in the integrated peak intensity of the MOR (130) reflection. A value of around 5 % of the initial intensity is consistently achieved after approximately 30 minutes. Some patterns suggest that this minimum is reached after as little as 15 minutes. The observed initial, rapid decrease in intensity suggests that the outermost mordenite is accessible to the solution almost instantaneously. This indicates that the zeolite P shell is largely permeable, thus facilitating exposure of the aqueous solution with the mordenite core. The immediate decrease in intensity observed in data obtained from diffraction beam trajectory 1 also suggests that incorporation into the outer section of the mordenite core is essentially instantaneous.

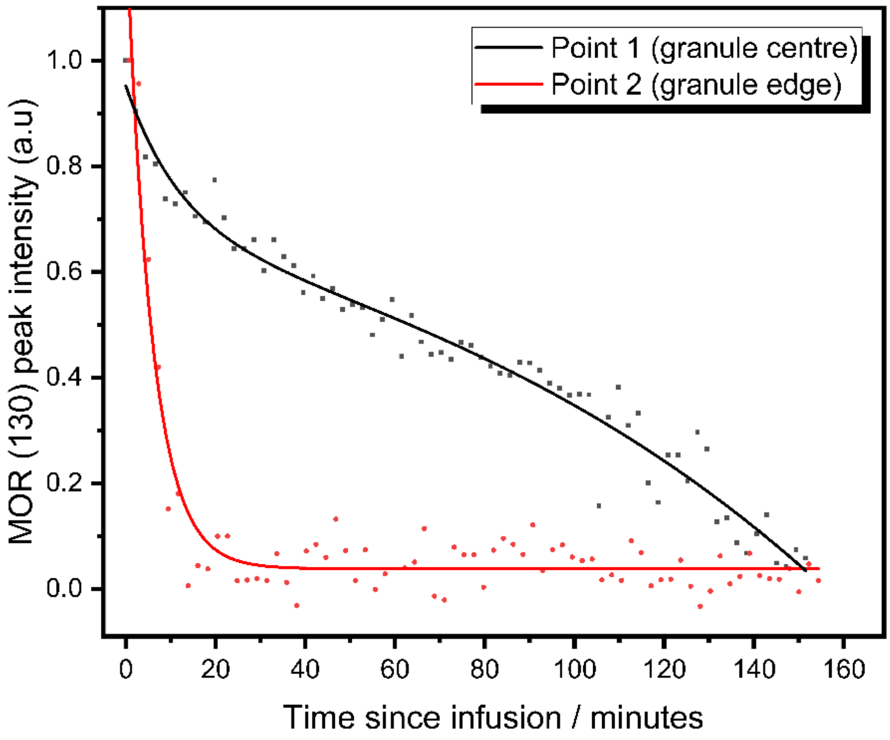

Figure 3.25. Mordenite (130) reflection intensity from two diffraction beam trajectories displayed as a function of time (5000 ppm caesium solution).

Diffraction data collected before and after caesium exchange for diffraction beam trajectory 3 shows a decrease in intensity of the zeolite P (200) reflection at 1.25 Q ($Å^{-1}$) (Figure 3.26). This is indicative of caesium exchange into the zeolite P outer shell. To aid in qualitatively assessing the rate of caesium adsorption by the zeolite P shell, the integrated peak intensity is plotted as a function of time in Figure 3.27.

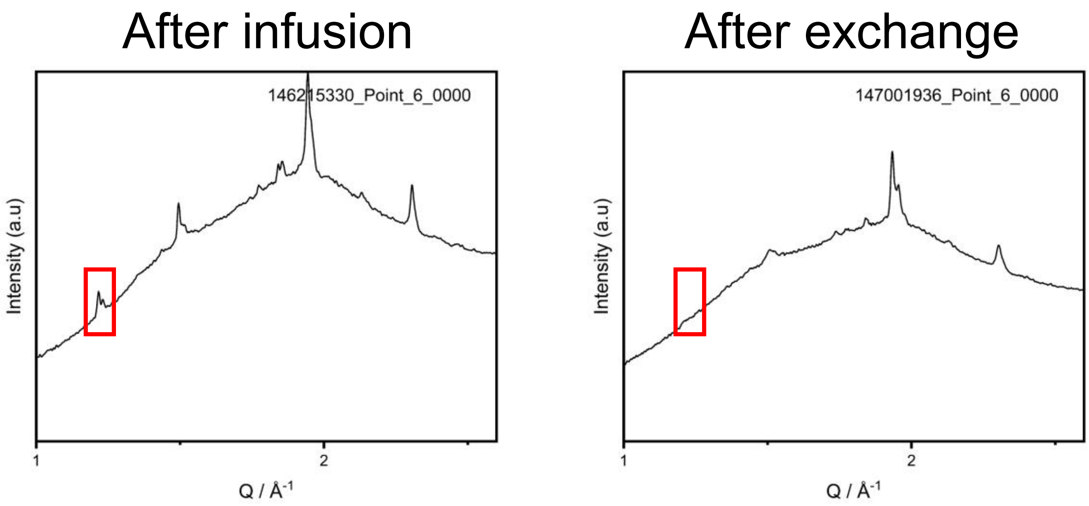

Figure 3.26. Local diffraction patterns highlighting the reduction in GIS (200) reflection intensity during the ion-exchange process (diffraction beam trajectory 3, 5000 ppm caesium experiment).

The reduction in integrated intensity of the GIS (200) Bragg peak is initially fast before slowly reducing over the course of the experiment. After 150 minutes, the intensity is still reducing, albeit slowly. This could be indicative of a faster rate of uptake of caesium in the mordenite core compared to the more exposed zeolite P shell. This is consistent with the inherent properties of the two phases: mordenite is a good caesium sorbent and zeolite P is more suited to adsorption of strontium[34]. Alternatively, the two zeolite phases may require differing quantities of caesium incorporation for a change in the bulk diffraction pattern to be observed.

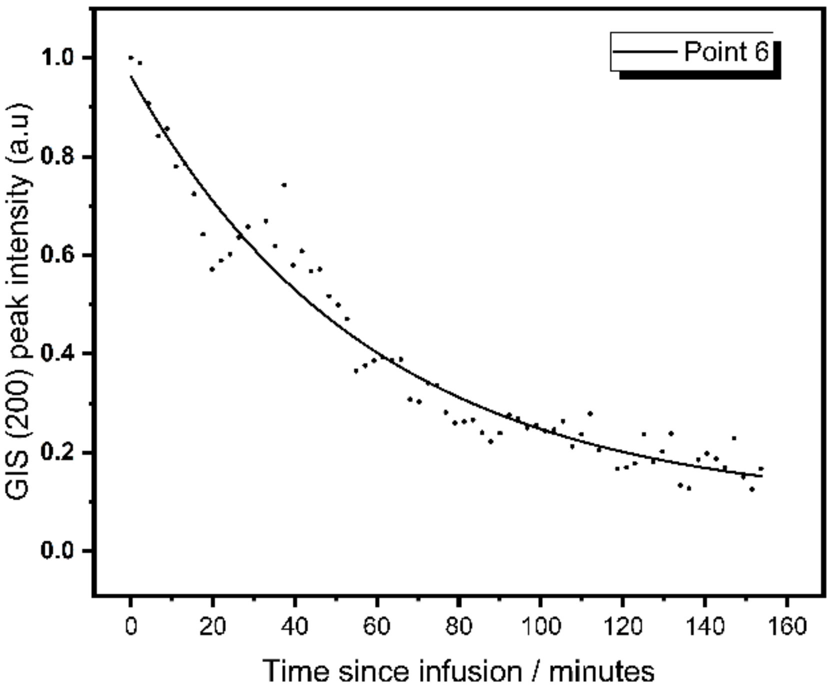

Figure 3.27. Zeolite P/ GIS (200) reflection intensity, obtained from diffraction beam trajectory 3, as a function of time (5000 ppm caesium experiment).

3.2.9.2 CG4 Granule in 5000 ppm Caesium and Strontium Solution

Unfortunately, the direct tracking of strontium within these systems through local diffraction measurements was not achieved in these scoping experiments. This was due to a combination of less significant discrepancies in the diffraction patterns, and the increased background as a result of the surrounding aqueous media. Nonetheless, a setup analogous to the sole caesium adsorption experiment (3.2.9.1), but using a solution matrix containing both caesium and strontium would shed light on how competitive strontium affects the caesium adsorption in both complementary zeolite phases. The radiograph of a positioned CG4 granule, annotated with three beam trajectories, is presented in Figure 3.28. Trajectory 1 penetrates the centre of the granule and hence receives diffraction contributions from both the zeolite P shell and all depths of the mordenite core. Trajectory 2 sees contributions from the zeolite P shell and the outer mordenite interior. Diffraction beam trajectory 4 was the best attempt at isolating the zeolite P shell and hence reflections attributed to zeolite P are by far the most abundant in the diffraction pattern. This information is summarised in Table 3.12.

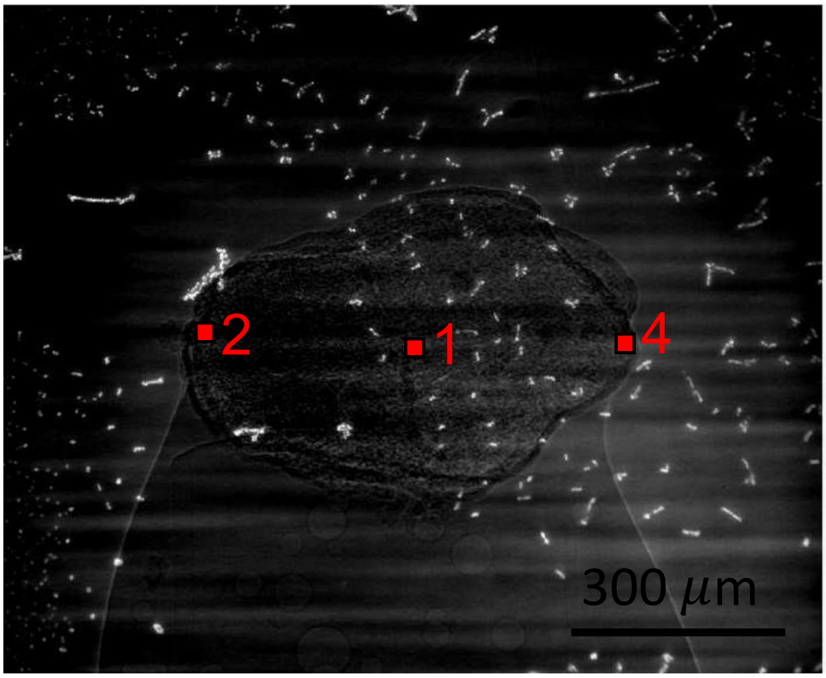

Figure 3.28. Radiograph of mounted CG4 granule annotated with diffraction beam trajectories (5000 ppm caesium/strontium experiment).

Table 3.12. Summary of diffraction beam trajectories utilised in *in-situ* ion-exchange experiments of CG4 (5000 ppm Cs solution).

Diffraction beam trajectory	**Observable phases**
1	Entire mordenite core, zeolite P shell.
2	Outer mordenite core, zeolite P shell.
4	Zeolite P shell.

A summary of diffraction data (pre- and post-infusion and after exchange) collected from beam trajectories 1, 2 and 4 is displayed in Figure 3.29. Analogous to the pure caesium exchange experiments, peak positions did not change upon addition of the aqueous solution, although a significant increase in background intensity increase was observed.

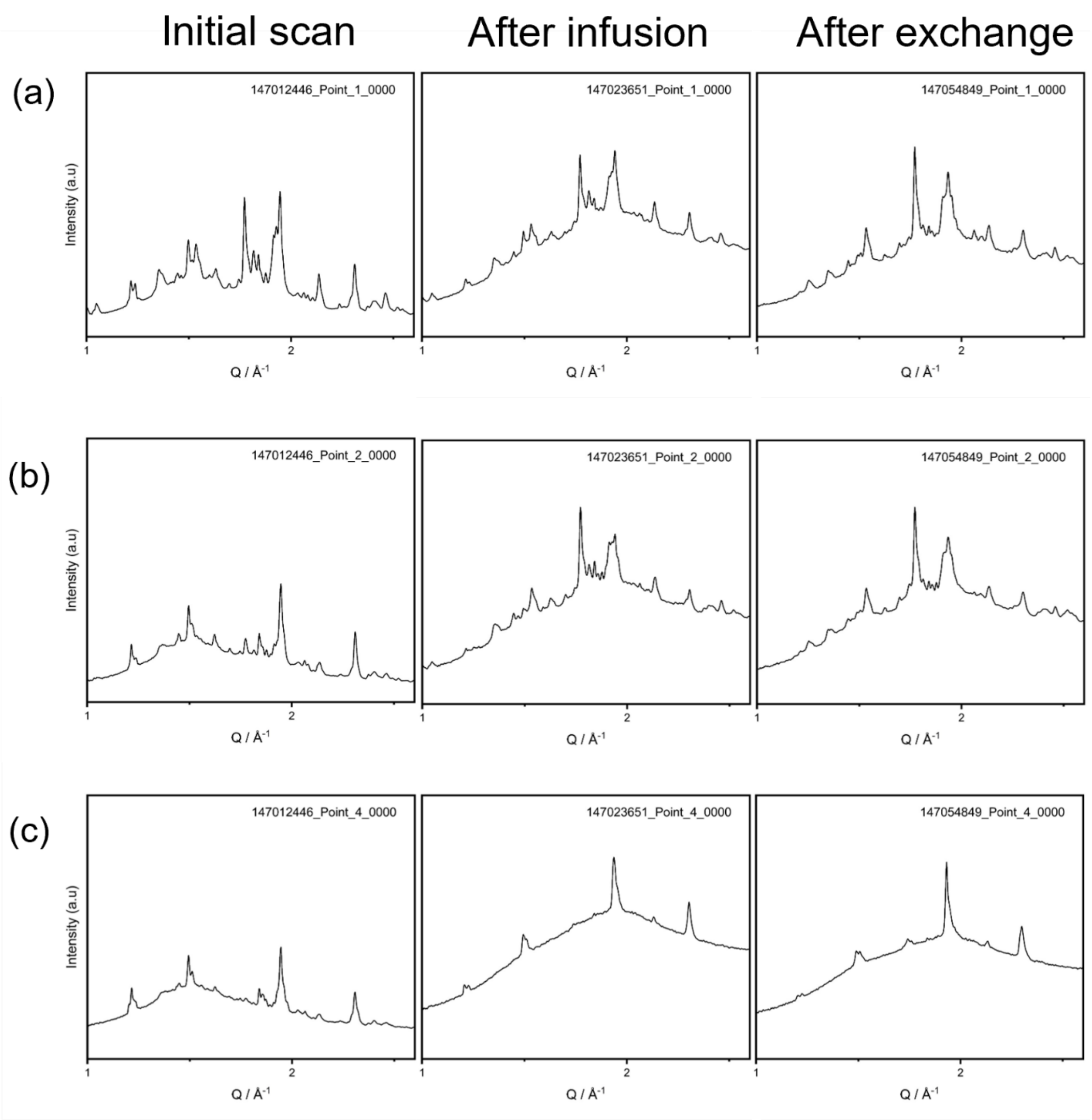

Figure 3.29. Overview of local PXRD patterns obtained from various beam trajectories after mounting, after infusion and after exchange (5000 ppm caesium/strontium experiment). (a) Patterns obtained from diffraction beam trajectory 1, (b) patterns obtained from diffraction beam trajectory 2, (c) patterns obtained from diffraction beam trajectory 4.

A reduction in the intensity of the mordenite (130) reflection (1.08 Q (Å^{-1})) is observed after exposure to the caesium and strontium solution (Figure 3.30). This can be attributed to uptake of caesium into the mordenite framework. After approximately 175 minutes the peak is significantly less prominent in patterns obtained from both diffraction beam trajectories 1 and 2, re-affirming that the mordenite core remains a functional ion-exchanger of caesium in these composite zeolite systems.

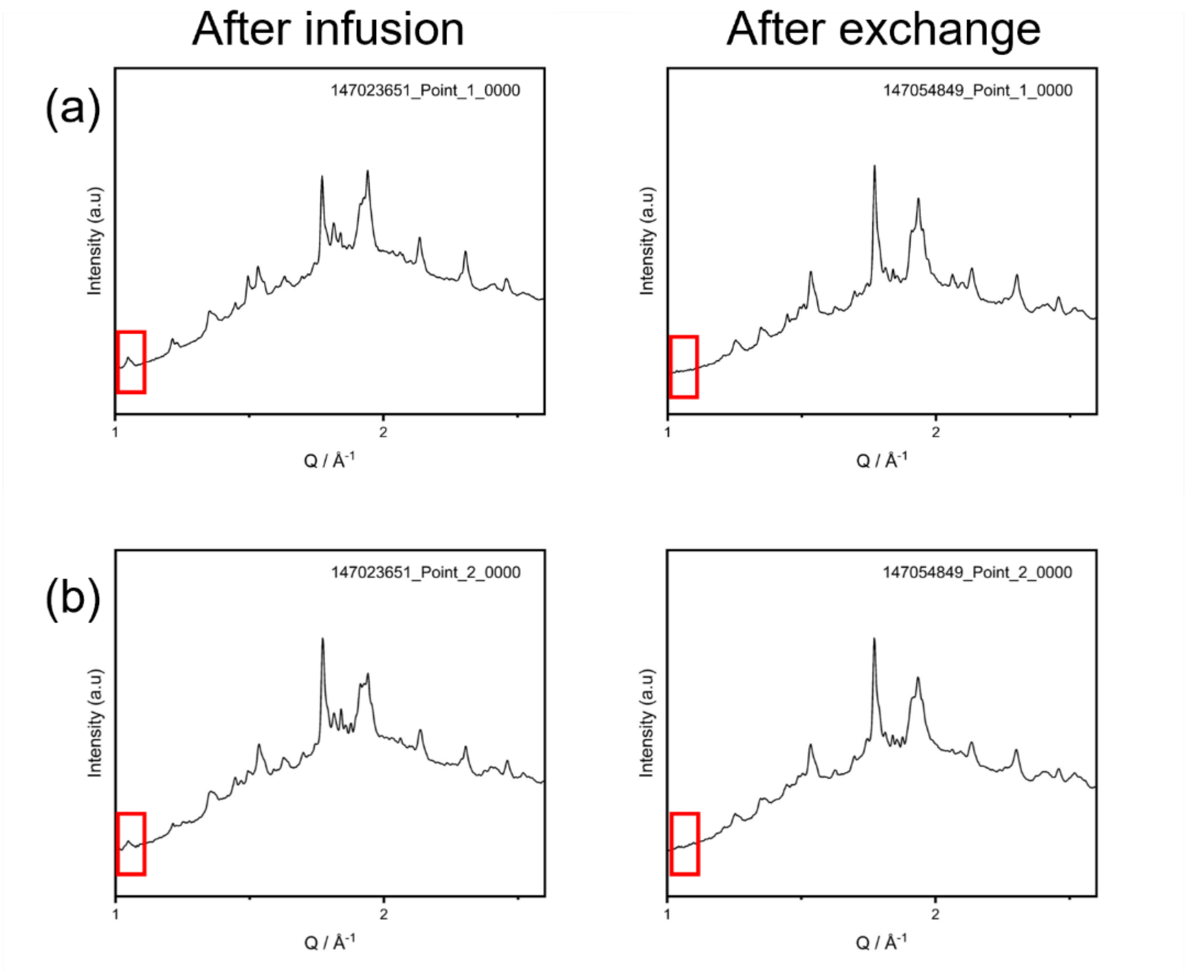

Figure 3.30. Local diffraction patterns highlighting the reduction in MOR (130) reflection intensity during the ion-exchange process (5000 ppm caesium/strontium experiment). (a) Patterns obtained from diffraction beam trajectory 1 and (b) patterns obtained from diffraction beam trajectory 2.

To provide qualitative information on the rate of exchange within the mordenite phase, the integrated peak intensity is plotted as a function of time (Figure 3.31). A steady reduction in the integrated peak intensity is observed from diffraction data obtained using beam trajectory 1. After ~175 minutes, the intensity is appoximatly 15 % of the starting value. This appears to be significantly higher than the post-exchange intensity observed in the equivalent experiment where only caesium is present in the added solution (3.2.9.1). This is likely due to the simultaneous adsorption of strontium into the mordenite framework.

Diffraction data collected from diffraction beam trajectory 2 showed an almost immediate reduction in the mordenite (130) peak intensity to approximately 30 % of its starting value. This corresponds to immediate caesium adsorption by the outer portion of the mordenite core. After this initial drop, which is achieved in the first 15 minutes, there is a slow decrease in peak intensity to approximately 25 % of its starting value (although there is significant variation associated with this value due to inconsistencies in integrated intensities). These observations re-affirm the 'instant' availability of the mordenite core to the metal-containing solution, and hence the permeability of the zeolite P shell. From the data obtained, it appears that the intensity of the mordenite (130) reflection from Point 1 is still decreasing significantly after 175 minutes. This could be a result of the solution penetrating further into the mordenite core, where caesium will exchange quicker than strontium due to its smaller hydrated radius. Conversely, the intensity of the peak from the Point 2 trajectory appears to be plateauing at a higher value ($\sim$ 0.2). This could be a result of significant strontium adsorption in the outer section of the mordenite core, which is more likely given the longer exposure time. It must be stated that further work is required to determine whether the disparities between relative intensities of the mordenite (130) reflections are statistically significant.

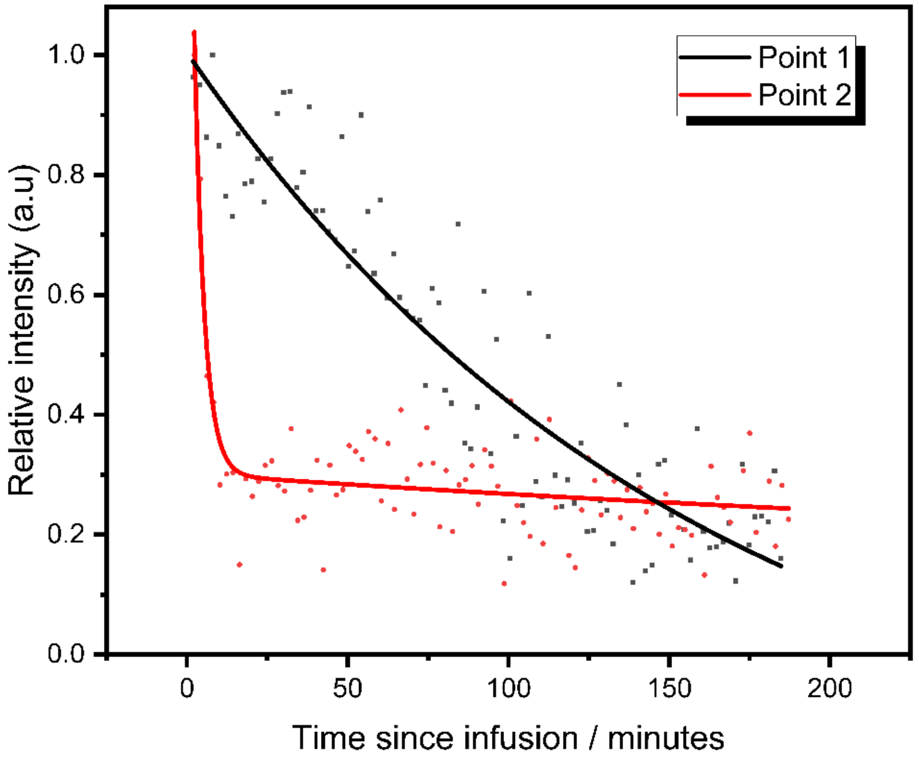

Figure 3.31. Mordenite (130) reflection intensity from two diffraction beam trajectories displayed as a function of time (5000 ppm caesium/strontium solution).

Local-diffraction data obtained using beam trajectory 4 shows a decrease in intensity of the zeolite P (200) reflection at 1.25 Q (Å^{-1}) (Figure 3.32). This corresponds to adsorption of caesium by the zeolite P outer shell. To further investigate the uptake, the integrated intensity of this Bragg peak is plotted as a function of time (Figure 3.33). An initial reduction in peak intensity to approximately 60 % of the initial intensity is observed in during the first 25 minutes of exchange. Subsequently, a small decrease in reflection intensity is observed; the peak retains approximately 55 % of its initial intensity after ~175 minutes. This is significantly higher than in the sole caesium exchange experiments, (3.2.9.1) where approximately 20 % zeolite P (200) peak intensity remained. This can be attributed to strontium adsorption in the outer shell of the composite granules.

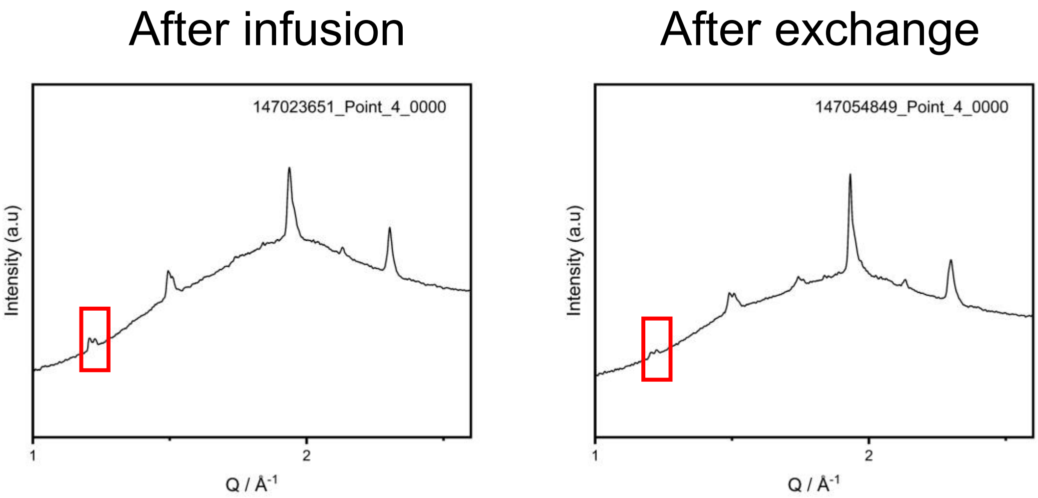

Figure 3.32. Local diffraction patterns highlighting the reduction in GIS (200) reflection intensity during the ion-exchange process (diffraction beam trajectory 4, 5000 ppm caesium/strontium experiment).

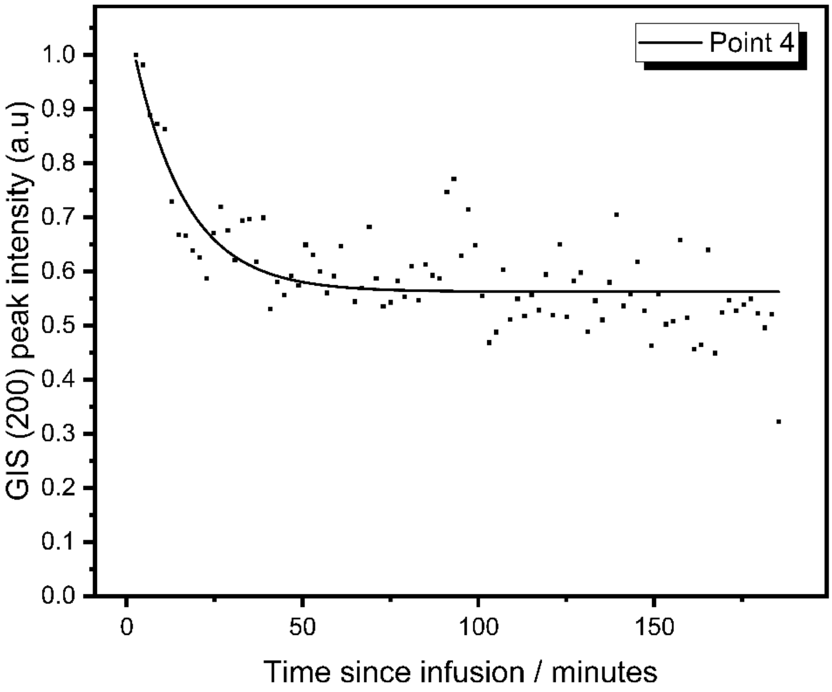

Figure 3.33. Zeolite P/ GIS (200) reflection intensity, obtained from diffraction beam trajectory 4, as a function of time (5000 ppm caesium/strontium experiment).

3.2.10 Rapid Ion Exchange (RIX) Experiments

Previous ion-exchange experiments (3.2.3, 3.2.4, 3.2.5 and 3.2.9) have proven useful in scoping the materials, providing information on the fundamental properties and the assessing the macroscopic adsorption behaviours of composite granular materials. However, the experimental setups used are not representative of the conditions observed in an industrial setting. Firstly, the caesium/strontium concentrations used have been orders of magnitude greater than is typical for an industrial feed stream. For example, effluent reaching the ion-exchange beds in the SIXEP plant routinely has a caesium concentration of around 17 ppb[70]. Strontium is even more dilute with a concentration of approximately 0.5 ppb observed[70]. This is compared to the concentrations > 10 ppm used previously in this chapter (3.2.3, 3.2.4, 3.2.5). The reduced abundance of strontium is in part due to coordination to hydrotalcite particles (> 1 μm), which are filtered by the sand beds upstream of the ion-exchange columns. Furthermore, industry typically operates using granular material in dynamic, flow systems, whereas the majority of the experiments conducted in this work have been on powdered samples in batch systems (for more information on the differences between flow and batch systems please refer to Section 2.2).

In order to best replicate the plant conditions and asses the performance of a material, full, active column trials have historically been conducted[70]. In these tests, approximately 5 g of granular ion-exchange material is packed into a column through which simulant effluent is passed through once prior to analysis. The breakthrough of radionuclides as a function of bed volumes is determined. As this methodology closely resembles the processes in SIXEP, excellent insight into a materials potential performance on plant is attained. However, these studies take several months to perform and produce significant quantities of active waste (both aqueous and solid). Consequently, they are very expensive to run and take up a meaningful quantity of limited active laboratory capacity.

The Rapid Ion Exchange (RIX) methodology (3.2.14), recently developed by Sellafield Ltd the National Nuclear Laboratory (NNL), facilitates dynamic flow testing in a very short timeframe and with significantly reduced costs and waste (in comparison to traditional column studies). An active simulant liquor is recirculated through a small bed (0.1 g) of ion-exchange material; the activity of the liquor reservoir is monitored as a function of volume (through column). Preliminary RIX experiments were conducted on CG2 and CG4, which had 85:9 and 57:34 MOR:GIS ratios by weight, in addition to the parent mordenite (Na-exchanged) and a sample of Mud Hills clinoptilolite, the material currently used at SIXEP. Uptake curves of both Cs-137 and Sr-90 for the four materials are displayed in Figure 3.34. Two-parameter exponential decay functions are also fitted to the datasets to aid comparison between materials (exponential parameters and fitting data are available in Appendix A.7).

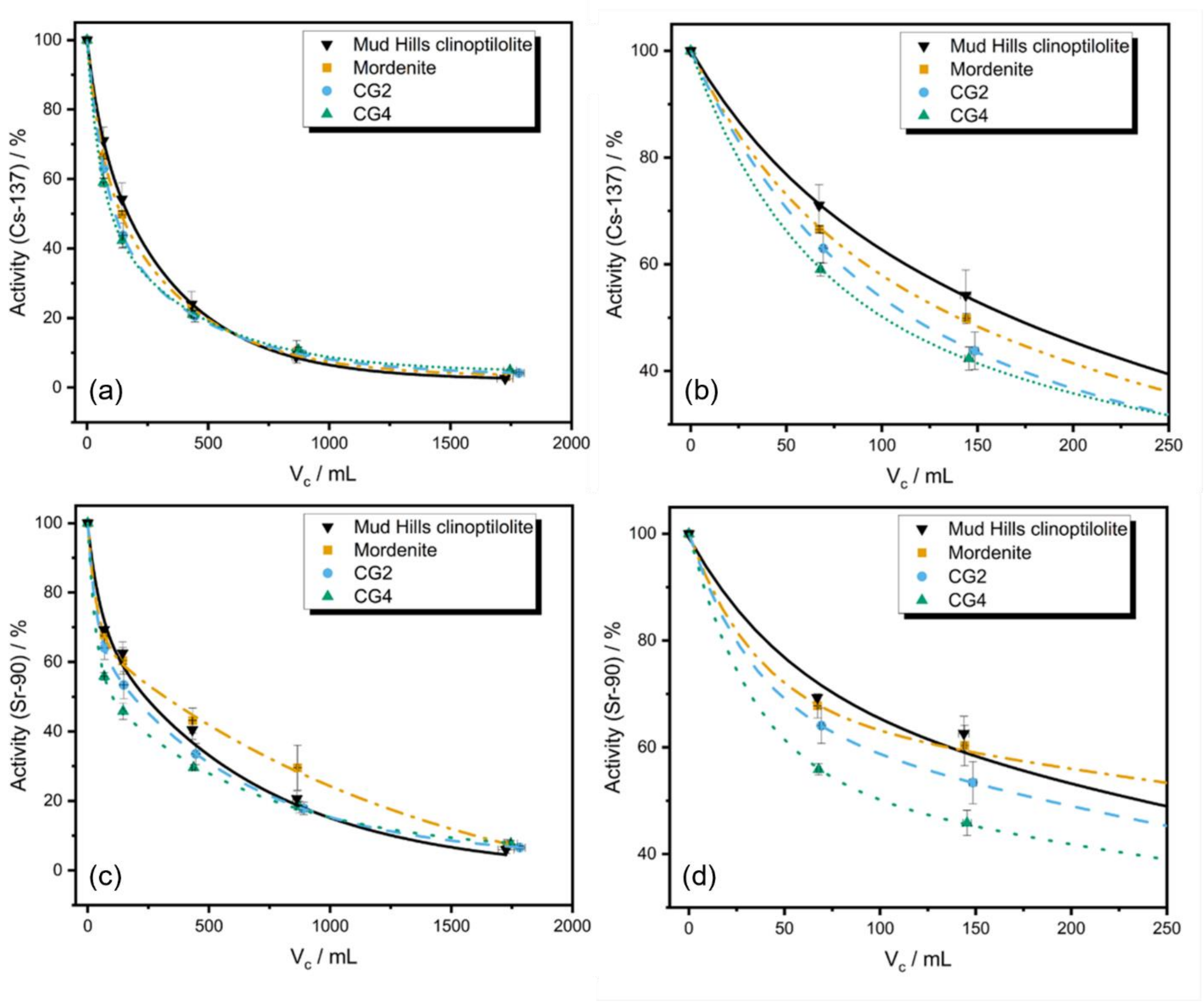

Figure 3.34. RIX uptake data for Mud Hills clinoptilolite, mordenite, CG2 and CG4. (a) Cs-137 activity throughout duration of experiment. (b) Cs-137 activity during initial stages of experiment (first 250 mL). (c) Sr-90 activity throughout duration of experiment. (d) Sr-90 activity during initial stages of experiment (first 250 mL).

The fit of two-parameter exponential decay functions to the caesium-137 uptake data are generally excellent ($R^2 > 0.993$, A.7). Fits to strontium-90 uptake data are also good ($R^2 > 0.98$, A.7). The slightly poorer fits to the strontium data potentially arise due to the greater variation of results associated with these datasets, likely due to the lower concentrations and contrasting counting methods.

The lower the activity at a given volume, V_C, the more radionuclides the ion-exchange material has adsorbed; steep curve gradients reaching lower activities faster are desirable. Mathematically, this is assessed by calculating the rate that the reservoir activity decreased after a given volume of active simulant, V_C, had passed through the material. However, as the experiment progresses, the radionuclides in the reservoir become more dilute as 'treated' simulant is re-circulated. This can be corrected for to give a probability of adsorption at a given volume, α, which is determined using Equation 2.21 (V_r = reservoir volume, V_f = flow rate, C = concentration of reservoir for a particular species, t = time). For further information regarding this equation, including its derivation, please refer to Section 2.2.2.1. A summary of adsorption probabilities for all materials at V_C = 50, 300 and 1500 mL is provided in Table 3.13.

Table 3.13. Adsorption probability (α_v) of Cs-137 and Sr-90 by Mud Hills clinoptilolite, parent mordenite, CG2 and CG4 after 50, 300 and 1500 mL of solution pass through in RIX experiments.

	Cs-137			**Sr-90**		
Material	α_{50}	α_{300}	α_{1500}	α_{50}	α_{300}	α_{1500}
Mud Hills clinoptilolite	0.53	0.36	0.23	0.53	0.26	0.18
Mordenite	0.63	0.38	0.21	0.60	0.23	0.14
CG2 (85:9 MOR:GIS ratio)	0.70	0.42	0.20	0.74	0.29	0.16
CG4 (57:34 MORGIS ratio)	0.83	0.42	0.19	0.98	0.34	0.16

Both natural zeolites tested in these experiments, namely Mud Hills clinoptilolite and the parent mordenite, display very similar caesium-137 uptake curves (Figure 3.34a). This agrees with earlier exchange experiments using powdered material, where the parent mordenite displayed good caesium-sorption properties (3.2.3, 3.2.4 and 3.2.5). The slightly faster initial uptake of caesium-137 in mordenite compared to Mud Hills clinoptilolite might reflect the enhanced ionic diffusion through the larger 12 membered ring channels, which are not found in clinoptilolite. Composite materials CG2 and

CG4 both exhibited faster uptake of caesium-137 compared to the naturally sourced materials. This is reflected in higher α_{50} values (0.70 and 0.83 vs 0.53 and 0.63, for CG2, CG4, Mud Hills clinoptilolite and mordenite, respectively). This increased rate of uptake is unlikely to originate from enhanced ionic diffusion in the nascent zeolite P, given that the GIS framework contains relatively narrow 8- and 4-MR units. Alternatively, this could reflect an enhanced diffusion through the bulk structure thanks to desilication and the presence of a more porous composite[193]. Further, an increase in surface area is also likely as a result of the spherical moieties on the surface of the granules (3.2.7).

Initially, the uptake of strontium-90 is faster in the mordenite material than for Mud Hills clinoptilolite (Figure 3.34d); this is reflected in α_{50} values of 0.60 and 0.53, respectively. However, after approximately 150 mL throughput, the rate of uptake for the mordenite significantly reduces and remains lower than for Mud Hills clinoptilolite throughout the rest of the experiment. Composites CG2 and CG4 showed significantly enhanced uptake of strontium-90 at low volumes in comparison to Mud Hills clinoptilolite and the parent mordenite (Figure 3.34c, Figure 3.34d). This is likely to originate from both the enhanced strontium capacity, revealed through adsorption isotherms (3.2.4), and the increased surface area and porosity, as observed in SEM (3.2.7) and XCT images (3.2.8). This facilitates easier access of ions to surface sorption sites, an effect likely to be more significant for the more hydrated strontium ion when compared to caesium. The composite materials continue to exhibit increased uptake of strontium at all throughput volumes used in these experiments (in comparison to the parent mordenite). After approximately 1000 mL of throughput, the uptake from Mud Hills clinoptilolite surpasses the uptake of the composites. This perhaps marks the point at which most surface absorption sites are occupied and diffusion through zeolite channels becomes the limiting factor. At this point, the small 8-ring channels observed in zeolite P may slow ion diffusion, despite having a higher capacity. It is also noteworthy that the uptake curves for strontium-90 remain further from equilibrium compared to the caesium-137 analogues at the end of the experiment. This can be attributed to the slower movement of the large, hydrated, divalent strontium cation and is consistent with kinetic studies (3.2.5) and literature[34].

3.3 Conclusion

The affordability, availability and deployment-ready morphology of natural zeolites are desirable properties for ion-exchange materials. However, few framework topologies are naturally abundant in significant enough quantities to be utilised. This has led to an overreliance on particular natural sources, with restricted routes to tailor functionality. In the nuclear industry, mordenite would typically not be considered as a dual caesium/strontium adsorption material due to its poorer selectivity for strontium. This chapter has highlighted the potential of interzeolite transformations as a means to enhance the ability to adsorb strontium whilst maintaining the ability to capture caesium effectively.

Firstly, the use of low (< 1 M) sodium hydroxide concentrations have been shown to be an effective method of retarding parent mordenite dissolution kinetics, facilitating the straightforward and cost-effective formation of composite zeolite systems. Furthermore, a high degree of control over the phase ratios is exhibited, potentially allowing for the ion-exchange properties to be tuned to a given waste stream (given the contrasting properties of the mordenite and zeolite P frameworks). These complementary ion-exchange behaviours of the mordenite and zeolite P phases were clearly observed in scoping batch experiments (3.2.3).

Adsorption isotherms were also utilised to gauge how the caesium and strontium capacity varied in both partially and fully transformed materials (3.2.4). Caesium capacity increased by 13 % upon 63 % conversion, with complete transformation increasing caesium capacity by 30 %. The change in strontium capacity was far more significant; increases of 140 and 170 % were observed from partial and full transformations, respectively. Likewise, kinetic studies (3.2.5) suggest strontium equilibrium is reached in a shorter timeframe for both partially and fully converted materials. Therefore, these generated materials both possess a higher capacity for strontium and reach equilibrium faster, compared to parent mordenite. This means significantly more adsorption events in a given timeframe, which translates to more effective removal when deployed in a column system. When all the ion-exchange experiments are considered, it is apparent that caesium is thermodynamically more preferred to adsorb into the mordenite framework and strontium into zeolite P. This is expected based on underlying framework structures and composition[34, 191, 192].

Granular composite zeolites, suitable for deployment in fixed bed columns, were developed using an identical methodology to powder composites, with similarly exquisite levels control over phase ratios exhibited (3.2.6). A core-shell structure of these granular composites was determined through SEM, XCT and local, image-guided diffraction studies (3.2.7, 3.2.8). A smaller diameter mordenite core was observed in more transformed analogues, indicating both the ratio of phases and granule morphology can be simultaneously controlled through synthesis solution basicity. This suggests the following mechanism of formation: dissolution of mordenite and subsequent crystallisation of zeolite P on the existing granule surface, followed by base penetration and internal dissolution-crystallisation.

Also discussed in this chapter were the scoping *in-situ* ion-exchange experiments, which demonstrated the ability to track caesium in bi-phasic composite zeolite granules and determine the permeability of the zeolite P shell, which readily allows solution access to the mordenite core (3.2.9). Lastly, RIX experiments indicate that the partial transformation process produces composite zeolite materials which surpass the currently deployed material, Mud Hills clinoptilolite, in its ability to remediate caesium and strontium from nuclear waste effluent (3.2.10).

Beyond nuclear waste management, the species selectivity is crucial to many industrial applications of zeolites, including gas absorption, catalysis and other ion-exchange processes. The methodology highlighted in this chapter, which produces tuneable, composite zeolites, may prove useful in developing materials for applications where there are multiple species of interest. Such examples where the complementary characteristics of phases may prove advantageous include water purification, multi-gas absorbers[207, 208], multi-molecular separation[209] and multi-process catalysts[210]. A summary of key findings from this chapter are displayed in Table 3.14.

Table 3.14. Summary of key findings from this chapter.

Section	Key findings
Generation of powder composites (3.2.2)	▪ A lower NaOH concentration facilitates composite formation. ▪ Concurrent mordenite desilication is observed during transformation. ▪ Ratios of phases can readily be controlled though manipulation of NaOH concentration.
Batch ion-exchange scoping (3.2.3)	▪ Ratio of zeolitic phases has profound effect on the uptake of caesium and strontium.
Adsorption studies (3.2.4)	▪ Small increase in caesium capacity upon transformation. ▪ Drastic increase in strontium capacity upon transformation.
Kinetic studies (3.2.5)	▪ Strontium equilibrium reached faster upon transformation.
Formation of granular composites (3.2.6)	▪ Granular analogues can be formed with control over ratios of both zeolite phases.
SEM, XCT and local diffraction studies (3.2.7, 3.2.8)	▪ Granular composite materials possess a core-shell structure, with a nascent zeolite P shell encapsulating a mordenite core.
In-situ ion-exchange at DIAD (3.2.9)	▪ Caesium adsorption can be locally monitored through local, image-guided X-ray diffraction techniques. ▪ Zeolite P shell is permeable to solution, allowing instantaneous access to mordenite core, which

	remains capable of participating in ion-exchange processes.
Rapid Ion Exchange experiments (3.2.10)	▪ Composite materials appear to be superior to Mud Hills clinoptilolite for sequestration of caesium/strontium solutions.

CHAPTER 4: ENHANCEMENT OF NATURAL CLINOPTILOLITES THROUGH PARTIAL INTERZEOLITE TRANSFORMATIONS

4.1 Introduction

Exploring the potential of alternative ion-exchange materials is paramount to enabling efficient processing of nuclear effluent due to potential changes in future feed streams and the imminent depletion of current material stockpiles, such as Mud Hills clinoptilolite, which is utilised at SIXEP, Sellafield[20, 70]. Caesium-137 and strontium-90 are two key target species, accounting for approximately 99 % of medium-lived radioactivity in spent nuclear fuel, in addition to posing significant risk to life and the environment (1.1)[4]. The simultaneous sorption of both these radionuclides by a single material is desirable, streamlining the process and complying with existing infrastructure at Sellafield.

In Chapter 3, the ability of a natural mordenite to sorb caesium and strontium was enhanced utilising a partial transformation to zeolite P. In this chapter, the applicability of this method to the world's most abundant natural zeolite, clinoptilolite, is explored, in attempt to expand the toolbox of viable materials for nuclear effluent remediation. Clinoptilolites are globally distributed[56, 57], with tuffs found on every continent; furthermore, they are utilised across many industrial applications, including ion-exchange[20, 68-70], as a soil additive[65, 66], and as dietary supplements for both animals[60, 62-64] and humans[67]. The clinoptilolite structure typically has a Si/Al ratio of approximately 5, containing 10- and 8-membered ring (MR) channels which accommodate framework cations[56]. Similarly to mordenite, these properties give the material excellent selectivity towards caesium[34, 53-55, 71]. To utilise this abundant natural resource for the dual-uptake of both caesium-137 and strontium-90, it is important to improve strontium affinity.

Basic, hydrothermal transformations of clinoptilolites into zeolite P are well reported[76-80, 147-149]. The conversion to a more aluminous framework generally results in at least a doubling in exchange capacity for strontium[76, 149]. These studies have, however, generally utilised high concentrations of NaOH (> 2M) to facilitate complete transformations to Na-P. In this chapter, reduced NaOH concentrations are deployed to generate powdered and granular composite materials from three parent clinoptilolites. Kinetic and equilibrium adsorption isotherms investigate the rate of uptake and the exchange capacity for both caesium and strontium. Additionally, batch and flow ion-exchange experiments are performed to probe the potential effectiveness in an industrial setting. Micro-diffraction and XCT imaging techniques are combined to assess the morphology of the granular composites produced.

4.2 Results and Discussion

4.2.1 Overview of Starting Materials

Characterisation of the parent clinoptilolites is important to best understand the properties of the materials generated in this chapter. Herein, a brief overview of the geological impurities detected by powder X-ray diffraction is presented. Additionally, the Si/Al ratio and incumbent cationic species, determined through XRF and SEM-EDS, respectively, are discussed.

4.2.1.1 PXRD Data

The PXRD patterns produced by the three starting materials are displayed in Figure 4.1, in addition to a simulated pattern for clinoptilolite. Generally, the major reflections can be attributed to the clinoptilolite framework. However, due to the natural nature of the materials, impurities are present as a result of the local geological environment.

Z-HEU contains cristobalite and feldspar, whereas reflections attributed to feldspar, quartz and mica are observed in N- and S-HEU. Estimated weight fractions determined through Rietveld refinements (5.2.1) are presented in Table 4.1. All three materials are comparable in purity and contain impurities expected in natural zeolites.

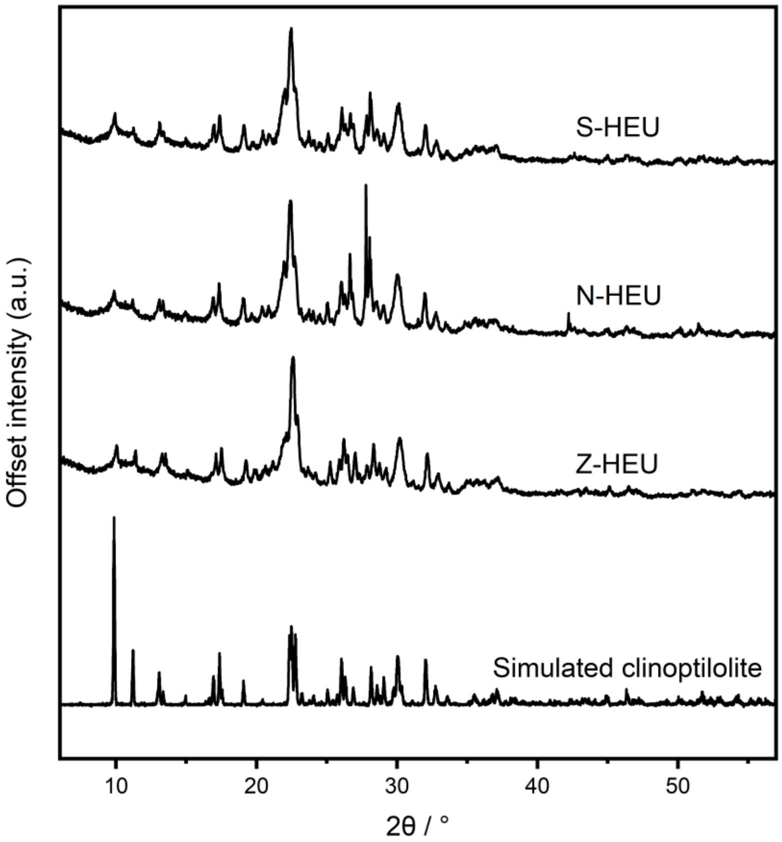

Figure 4.1. PXRD patterns of starting natural clinoptilolite zeolites. A simulated clinoptilolite pattern is also presented (λ = 1.5406 Å).

Table 4.1. Summary of parent clinoptilolite compositions, as determined by Rietveld refinement (5.2.1.5).

Material	Composition
Z-HEU	Clinoptilolite (67 %), feldspar (13 %), cristobalite (12 %)
N-HEU	Clinoptilolite (72 %), feldspar (25 %), quartz (2 %), mica (<1 %)
S-HEU	Clinoptilolite (67 %), feldspar (29 %), quartz (4 %), mica (<1 %)

4.2.1.2 Elemental Analysis

The elemental composition of a zeolite is integral to its properties, and hence potential applications. For example, the Si/Al ratio determines the framework charge, which can steer the affinity to a particular species for ion-exchange applications. In the context of caesium/strontium abatement from aqueous waste streams, a more aluminous framework would exhibit a greater affinity towards strontium cations. This is a result of the stronger electrostatic attraction between the charge dense, divalent, species and the greater net negative charge associated with the framework, in addition to the increased probability of aluminium pairs, which are a necessity for strontium adsorption[34]. The cations residing in the framework's channels, the incumbent cations, are also significant, as different species are displaced by others by varying degrees, dependent on factors including the geometry and charge distribution of both adsorbent and adsorbate. For clinoptilolite, a cation selectivity series is reported as follows: Cs > K > Sr > Ca > Mg > Na, where sodium is the most favourable cation to be displaced in an ion-exchange process[211]. The Si/Al ratios and cationic species in the three materials, determined by XRF and SEM-EDS respectfully, is presented in Table 4.2.

Table 4.2. Si/Al ratios of the raw clinoptilolite materials, as determined by XRF and SEM-EDS. Additionally, the cationic species observed by SEM-EDS are presented.

Material	Si/Al (XRF)	Si/Al (SEM-EDS)	Cationic species* in order of abundance (SEM-EDS)
Z-HEU	4.7(1)	4.72(8)	K, Na, Mg, Ca
N-HEU	5.0(1)	5.01(9)	K, Ca, Mg, Na
S-HEU	5.0(1)	4.95(5)	K, Ca, Mg, Na

Both N- and S-HEU have Si/Al ratios of 5, whereas Z-HEU is slightly more aluminous, with a Si/Al of 4.7. This suggests that Z-HEU may possess a slightly higher cationic exchange capacity and affinity for strontium, particularly as siliceous impurities (e.g., cristobalite) will inflate the observed Si/Al ratio above the framework composition (5.2.3.1). Additionally, Z-HEU contains significantly more sodium, a readily released metal from clinoptilolite, than N- and S-HEU (5.2.3.2). N- and S-HEU also contain significantly more calcium, a divalent species which is slow to exchange due to its large hydration sphere[34]. However, > 50 % of this incumbent calcium is released during sodium washing (5.2.3.2). As alluded to, a more comprehensive characterisation of these raw clinoptilolites is discussed in Chapter 5.

4.2.2 Generation of Powder Composites

Consistent with literature[76-80, 147-149], and analogous to work presented in Chapter 3, the basic hydrothermal treatment of all three natural clinoptilolites produced zeolite P through an interzeolite transformation. Furthermore, partial transformation was readily achieved through the use of reduced solution basicity, which retards dissolution and facilitates concurrent crystallisation of zeolite P. NaOH concentrations between 0.2 – 0.5 M were used with all three clinoptilolite parent materials, with the weight fractions of detected phases estimated through Rietveld analysis[162, 163] of the PXRD patterns (A.8-10). The data corresponding to each material is hereby discussed in turn.

4.2.2.1 Z-HEU

PXRD patterns of Z-HEU samples exposed to NaOH solutions (0.2 – 0.5 M) at 100 °C for 24h, are displayed in Figure 4.2, in addition to simulated patterns for clinoptilolite, Na-P1 and Na-P2 (two polymorphs of zeolite P).

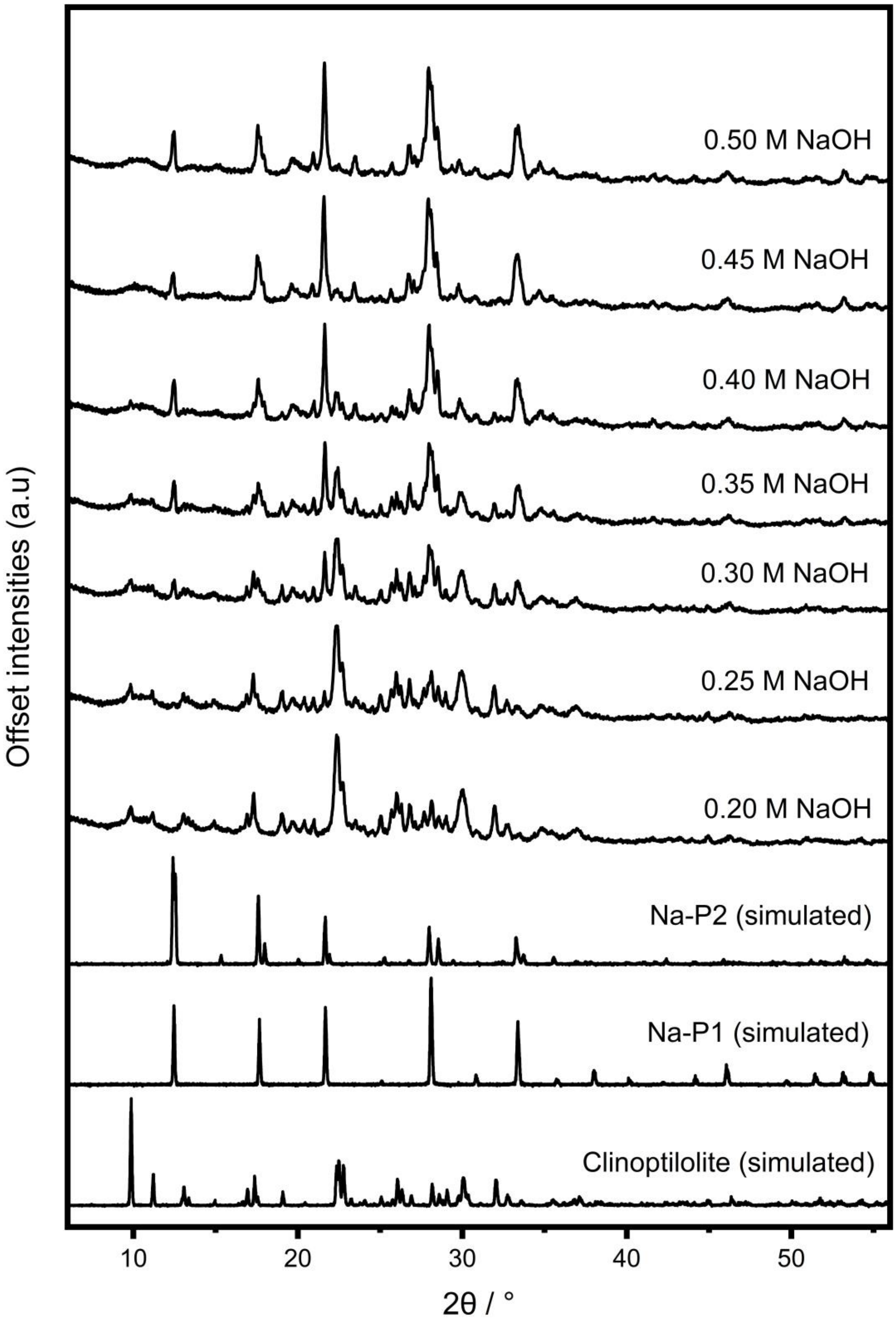

Figure 4.2. PXRD patterns of powdered clinoptilolite (Z-HEU) materials after hydrothermal treatment (0.20 – 0.50 M solutions). Simulated mordenite and zeolite P (Na-P1 and Na-P2) patterns are also presented (λ = 1.5406 Å).

Qualitatively, diffraction patterns from lower molarity treatments have the more intense clinoptilolite reflections, whereas zeolite P reflections are most intense in materials generated in higher molarity solutions. The presence of shoulder peaks on either side of the Na-P1 peaks indicates the presence of Na-P2, an Na-P1-like polymorph of zeolite P with slightly smaller 8MR apertures[81, 82]. The weight fractions of these phases are presented as a function of time in Figure 4.3.

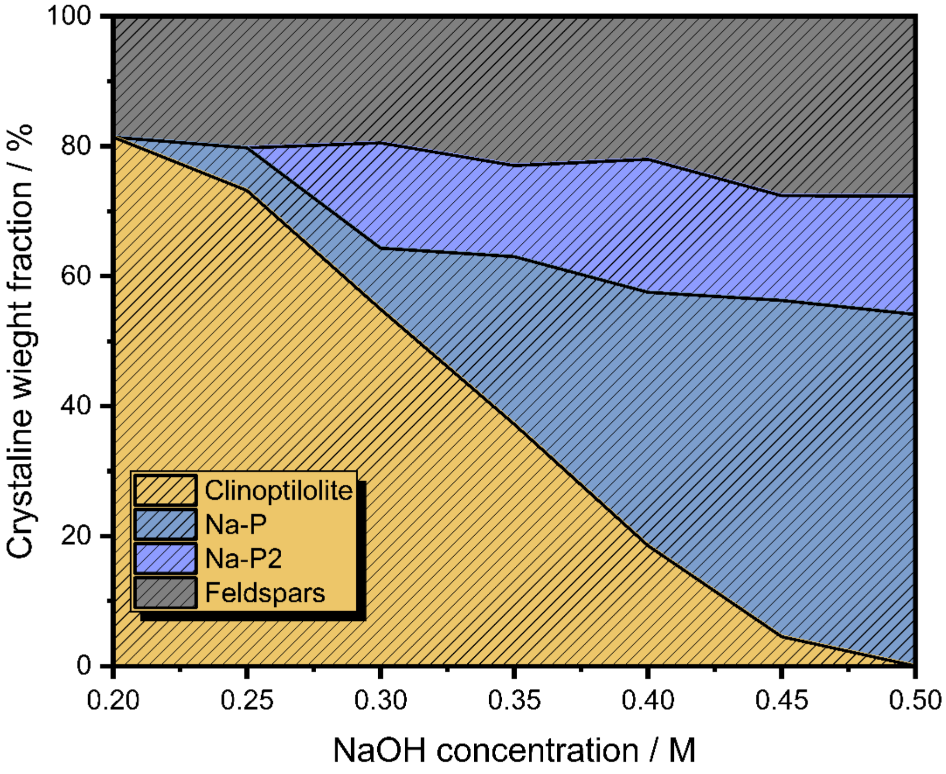

Figure 4.3. Estimated weight fractions of clinoptilolite, zeolite P (Na-P1 and Na-P2) and feldspars in hydrothermally treated Z-HEU.

Transformation from clinoptilolite to zeolite P was observed in concentrations greater than 0.25 M. Expectantly, as the solution basicity increased, more clinoptilolite was converted to zeolite P; this resulted in a range of composites with incremental quantities of the zeolite phases. Full conversion, indicated by a 0 % clinoptilolite weight fraction, was achieved using a 0.50 M NaOH solution. The data also suggests that both polymorphs of zeolite P, Na-P1 and Na-P2, crystalise in significant quantities. The weight fraction of the feldspar impurity remains somewhat constant at all degrees of transformation, suggesting it is somewhat inert to dissolution under these conditions. This is in contrast to cristobalite, which is solubilised in all treatment concentrations. This is expected in solutions of this basicity at elevated temperture[212].

4.2.2.2 N-HEU

PXRD patterns of N-HEU samples hydrothermally treated in NaOH solutions (0.2 – 0.5 M) at 100 °C for 24h are displayed in Figure 4.4. Simulated patterns of clinoptilolite, Na-P1 and Na-P2 are also presented.

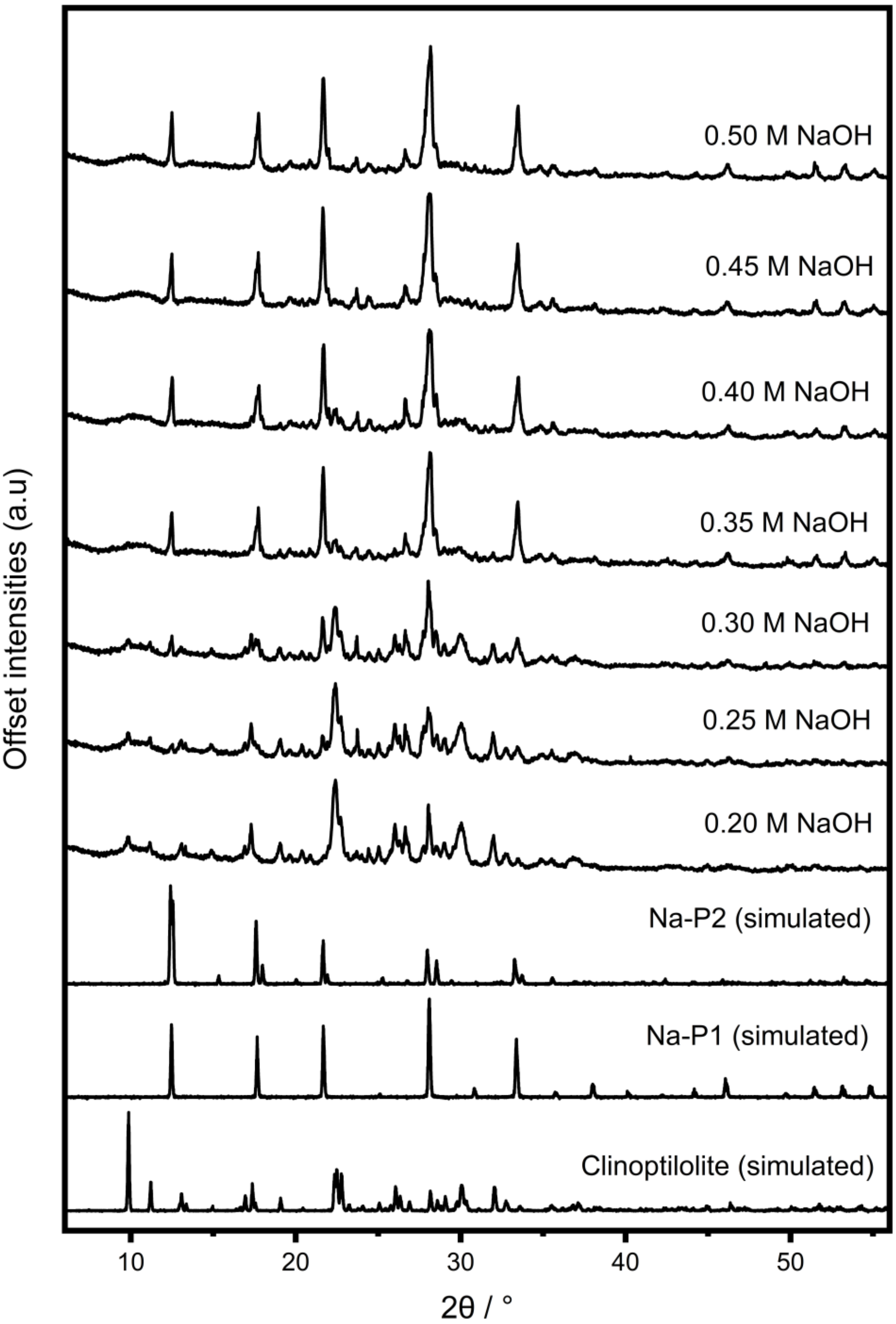

Figure 4.4. PXRD patterns of powdered clinoptilolite (N-HEU) materials after hydrothermal treatment (0.20 – 0.50 M solutions). Simulated mordenite and zeolite P (Na-P1 and Na-P2) patterns are also presented (λ = 1.5406 Å).

In parallel to diffraction patterns obtained from materials produced by Z-HEU (4.2.2.1), higher molarities produced patterns with more intense zeolite P peaks. On the contrary, lower molarities produced materials with higher intensity clinoptilolite reflections. The estimated weight fractions are presented as a function of solution basicity in Figure 4.5.

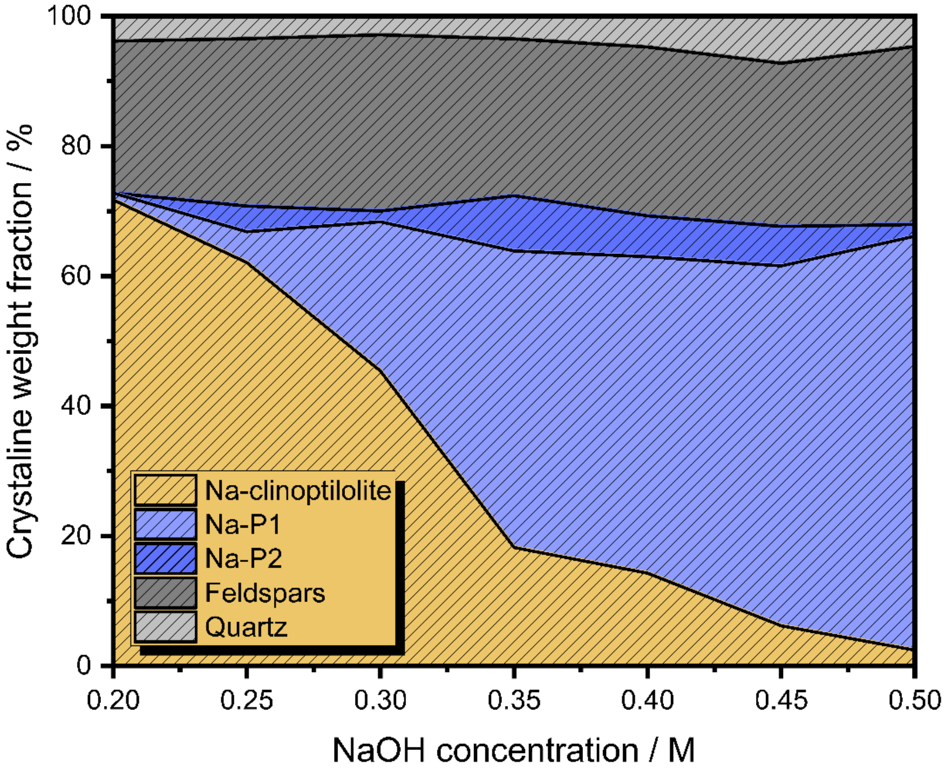

Figure 4.5. Estimated weight fractions of clinoptilolite, zeolite P (Na-P1 and Na-P2), feldspar and quartz in hydrothermally treated N-HEU.

Transformation from clinoptilolite to zeolite P was observed in solutions greater than 0.25 M NaOH solutions. Analogous to Z-HEU, higher NaOH concentrations resulted in conversion of more clinoptilolite to zeolite P, resulting in a series of composite materials with incremental proportions both zeolite phases. In the 0.50 M solution, negligible quantities of the clinoptilolite are present, suggesting that the transformation is complete. Na-P1 was more abundant in the composites than Na-P2, although observable quantities of Na-P2 are present when using between 0.25 and 0.50 M NaOH solutions. Weight fractions of feldspar and quartz remain somewhat constant throughout the transformation, suggesting a degree of inertness towards dissolution under these conditions.

4.2.2.3 S-HEU

PXRD patterns of S-HEU samples exposed to NaOH solutions (0.2 – 0.5 M) at 100 °C for 24h are displayed in Figure 4.6. Simulated patterns for clinoptilolite, Na-P1 and Na-P2 are also presented.

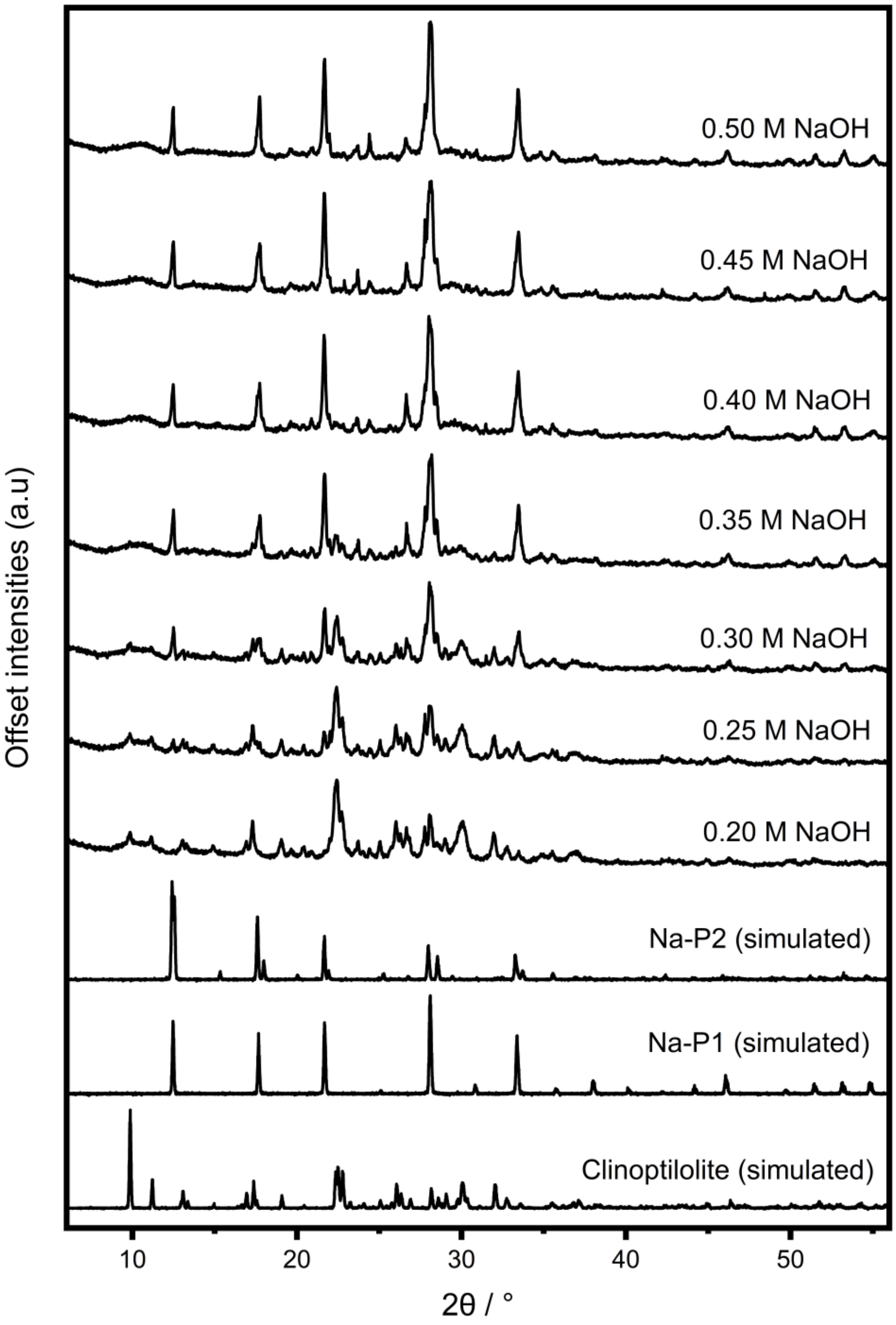

Figure 4.6. PXRD patterns of powdered clinoptilolite (S-HEU) materials after hydrothermal treatment (0.20 – 0.50 M solutions). Simulated mordenite and zeolite P (Na-P1 and Na-P2) patterns are also presented (λ = 1.5406 Å).

Expectantly, higher molarities produced patterns with more intense zeolite P peaks. On the contrary, lower molarities produced materials with higher intensity clinoptilolite reflections. The estimated weight fractions are presented as a function of solution basicity in Figure 4.7.

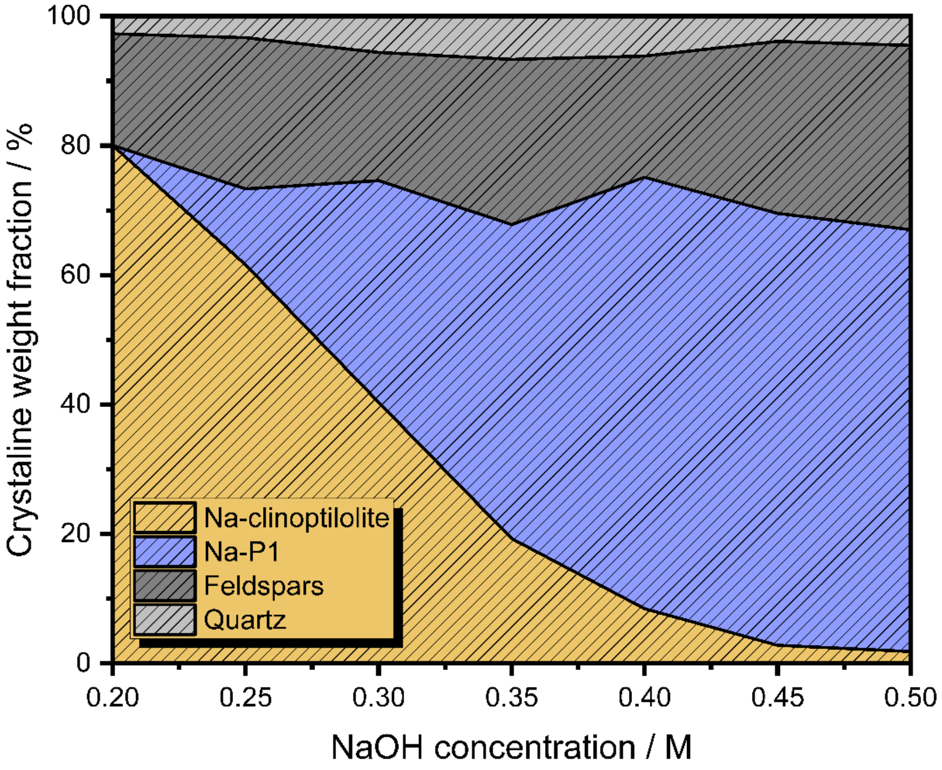

Figure 4.7. Estimated weight fractions of clinoptilolite, zeolite P (Na-P1 and Na-P2), feldspar and quartz in hydrothermally treated S-HEU.

Zeolite P crystallisation was observed in NaOH concentrations at 0.25 M and greater. Akin to Z-HEU and N-HEU (4.2.2.1, 4.2.2.2), more zeolite P and less clinoptilolite were observed as concentration increased, producing a range of composite materials with incremental ratios of both phases. The weight fraction of clinoptilolite is negligible after treatment in the 0.50 M solution, suggesting that the transformation is complete.

Na-P1 is the dominant zeolite P polymorph crystalised, with negligible quantities of Na-P2 detected. It is possible that the lack of observed Na-P2 is due to the limited quality of the diffraction data and complexity of the system (e.g., overlap with feldspar reflections from minerals such as albite). The estimated weight fractions of feldspar and quartz remain somewhat constant at all NaOH concentrations, suggesting a level of inertness to dissolution in these conditions.

4.2.2.4 Transformation Summary

A series of zeolite composite materials, with incremental ratios of clinoptilolite and zeolite P, were successfully generated from each of the three natural clinoptilolite parent materials. This demonstrates that the control achieved in the mordenite to zeolite P transformation (Chapter 3) is transferable to natural clinoptilolites. In contrast to the granular mordenite transformation discussed in Chapter 3, lower NaOH concentrations were required to facilitate transformation; full conversion was achieved in 0.5 M solution for all three clinoptilolites whereas 0.65 M was required for the mordenite (3.2.2.1). This is consistent with work by Sudo[213], which showed that natural mordenite materials are more resistant to chemical treatment, including NaOH.

Na-P2, a polymorph of zeolite P comprised of alternating *dcc* chains misaligned by 15°[82], was crystalised in approximately equal quantities to Na-P1 in composites generated from Z-HEU. Smaller quantities were also observed in materials produced from N-HEU. The structure of Na-P2 is very similar to Na-P1, with nearly identical unit cell parameters, but with slightly smaller 8MR apertures[81, 82]. The effect of these on the ion-exchange properties are not well documented. However, gas adsorption experiments by Oleksiak showed very similar performances by both polymorphs[81]. It is reported that Na-P2 is preferentially formed over P1 in less concentrated hydroxide solutions and from more siliceous mother liquors[81]. This is consistent with this work, where no co-crystallisation was observed in the granular mordenite transformations (Chapter 3), where more basic conditions were required, and presumably a more aluminous mother liquor is generated from dissolution. In the case of clinoptilolite transformations, the reduced NaOH concentrations and more siliceous materials may facilitate crystallisation of NaP2. Quantities of quartz and feldspars remained somewhat constant regardless of NaOH concentration, suggesting that these impurity phases are largely not broken down by the hydroxide species and therefore will not contribute to either the growth solution or the subsequent crystalised zeolite. Feldspars are readily decomposed in caustic solutions in temperatures greater than 150 °C[214-216], so their inert nature in these milder conditions is unsurprising. Further, the rate of quartz dissolution is reported to vary significantly as a function of NaOH concentration[217]. It is therefore conceivable that quartz is undergoing dissolution in these conditions, but at a rate too slow to observe a reduction in weight fraction.

4.2.2.5 Si/Al Ratio of the Composites

The Si/Al ratio of a zeolitic material is crucial in determining the materials' characteristics, particularly its ability so sorb cationic species (Section 1.2). The Si/Al ratio of the composite materials derived from all three natural zeolite precursors is displayed in Figure 4.8. More aluminous materials are produced upon increasing basicity until a Si/Al ratio of ~2.5 is reached in 0.45 and 0.50 M NaOH solutions; this correlates to a 'complete' transformation where negligible quantities of clinoptilolite remain. The reduction in silicon content arises from the crystallisation of the more aluminous zeolite P phase[78], in addition to possible desilication of the parent materials[108, 109], as observed in Chapter 3 (3.2.2.2).

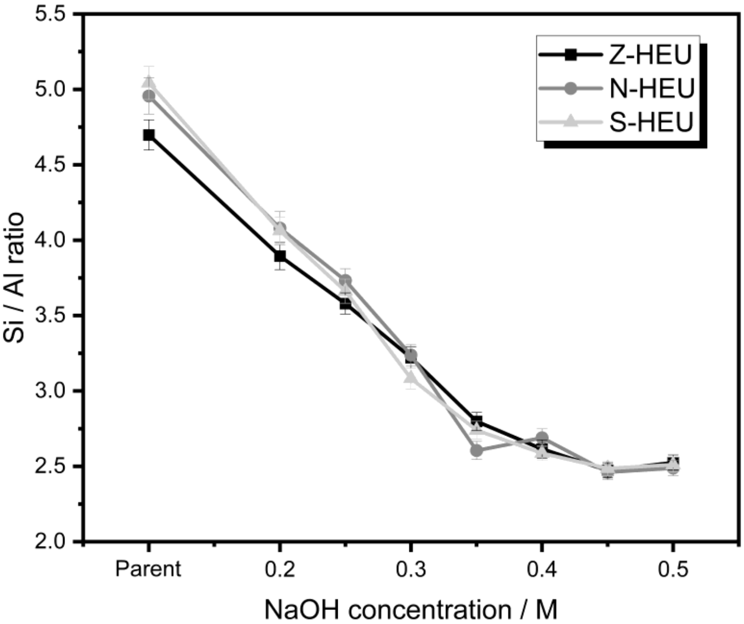

Figure 4.8. Si/Al ratios of the generated powdered composites, as determined by XRF.

The extent of parent clinoptilolite framework desilication can be estimated by calculating theoretical Si/Al ratios for each composite based off determined weight fractions and an assumed zeolite P Si/Al ratio of 2.5. These estimated theoretical values are plotted alongside observed ratios obtained by XRF in Figure 4.9. The theoretical values are consistently higher than the observed, indicating that significant desilication of the parent clinoptilolites has occurred. This is consistent with materials generated from all three parent clinoptilolites and must be considered when interpreting ion-exchange results.

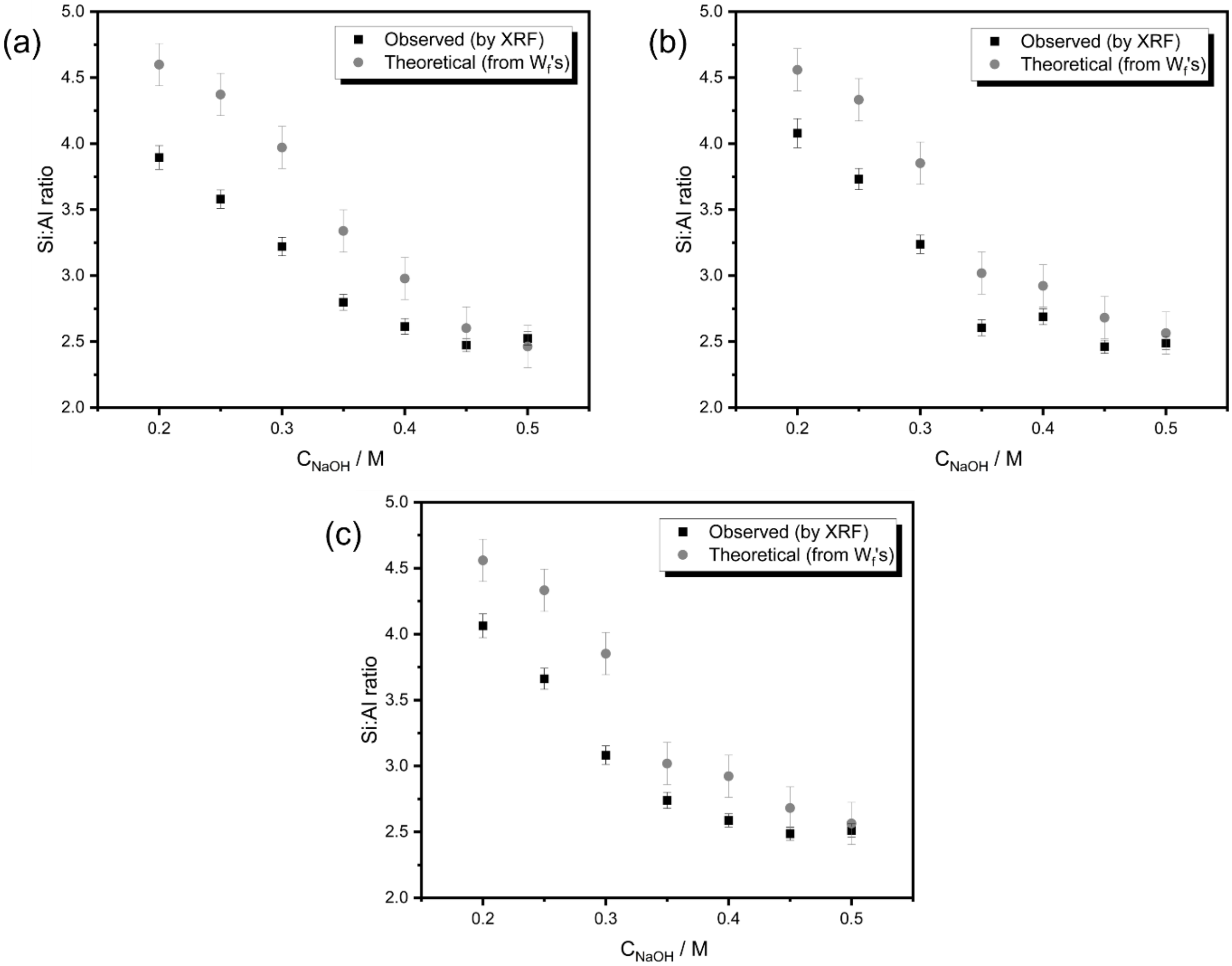

Figure 4.9. Theoretical Si/Al ratio of powdered composite materials, as determined through combination of XRF data and estimated weight fractions. Observed Si/Al ratios are also displayed for comparison. (a) Z-HEU, (b) N-HEU and (c) S-HEU.

4.2.3 Batch Ion-Exchange Testing

To scope the effect of the partial interzeolite transformations on the ion-exchange selectivity for caesium and strontium, batch ion-exchange studies were performed using 10 ppm solutions of caesium/strontium spiked with 50 ppm of competitive cation. Potassium was used as a caesium competitor and calcium as a strontium competitor due to their inherent chemical similarities. It is important to note that these experiments are not representative of industry conditions, where effluents contain a complicated matrix of cationic species and radionuclide levels far more dilute than 10 ppm[20, 70, 187]. Instead, they are used to quickly assess changes in selectivity induced by the transformation. The results for each series of composites are hereby discussed in turn.

4.2.3.1 Composites Generated from Z-HEU

The respective uptakes of caesium and strontium achieved by materials derived from Z-HEU are summarised in Figure 4.10. Additionally, the uptake data for the sodium-exchanged parent material and the weight fractions of both zeolitic phases (4.2.2) are presented.

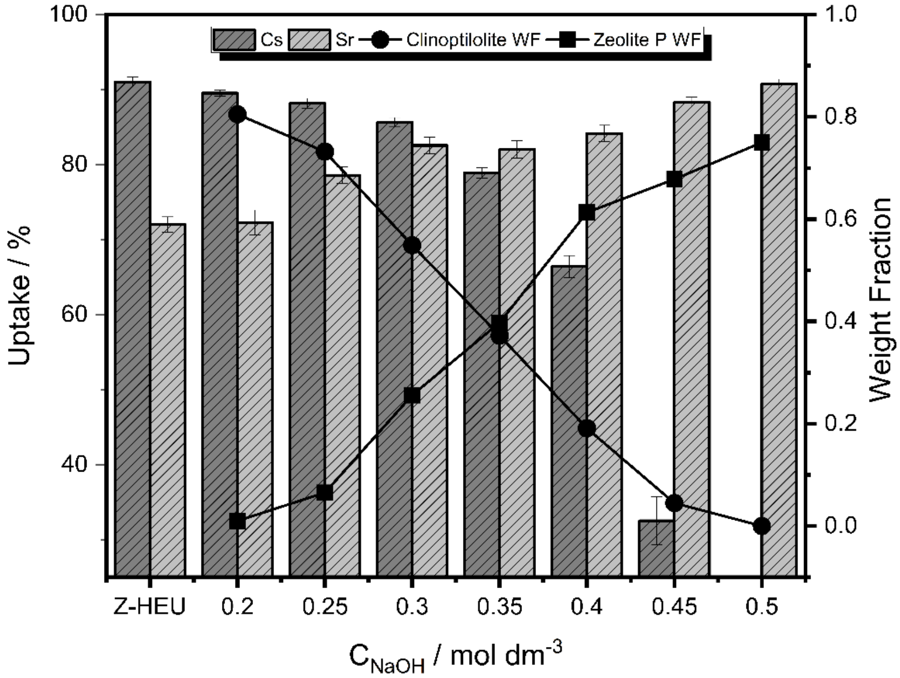

Figure 4.10. Uptake of caesium and strontium achieved by the powdered composites derived from Z-HEU in scope batch trials. Estimated weight fractions of clinoptilolite and zeolite P are also presented.

The sodium-exchanged, parent material exhibited a high caesium removal rate of 90 %, but a lower strontium uptake of approximately 70 %. In lower concentration NaOH solutions (0.20 – 0.25 M), an increase in strontium uptake is observed (up to 77%) and caesium uptake remains at approximately 90%. This can be attributed to generation of a small quantity of zeolite P, which favours strontium because of its more aluminous framework, in addition to the desilication of the parent material (Section 4.2.2.5). As the transformation solution basicity further increases, and the composites are comprised of greater fractions of zeolite P, caesium affinity decreases; this is most significant in concentrations 0.45 and 0.50 M, where very little clinoptilolite remains. On the contrary, strontium uptake increases steadily with basicity. Composites generated from 0.30 and 0.35 M NaOH solutions displayed optimal dual-uptake in these conditions (> 79 % for both caesium and strontium); this corresponds to materials comprised of between 35 – 65% clinoptilolite and 20 – 50% zeolite P.

4.2.3.2 Composites Generated from N-HEU

The respective uptakes of caesium and strontium achieved by materials derived from N-HEU are summarised in Figure 4.11, in addition to uptake data for the sodium-exchanged parent material and the respective zeolitic weight fractions (4.2.2).

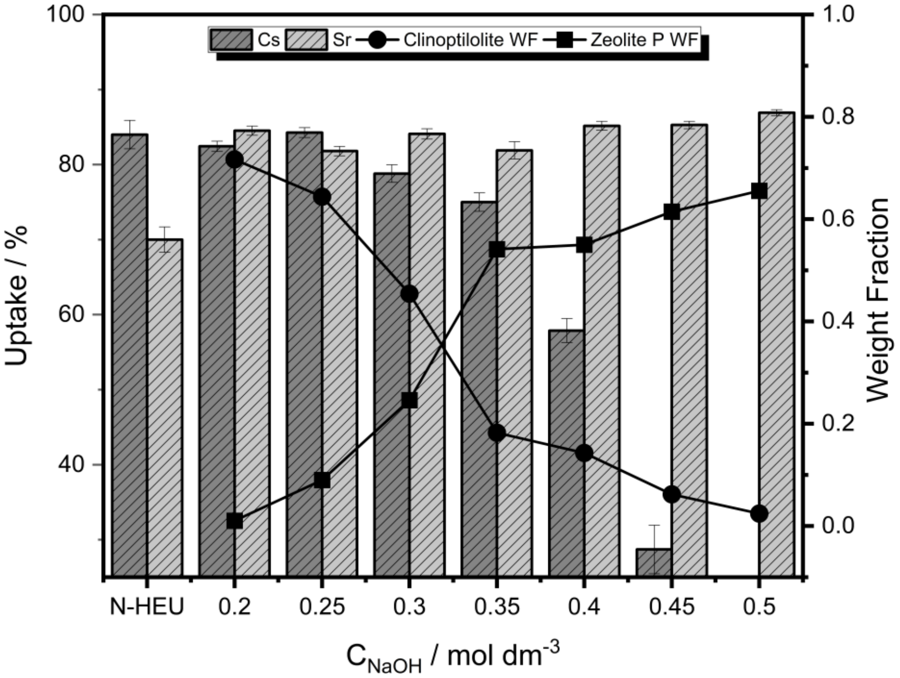

Figure 4.11. Uptake of caesium and strontium achieved by the powdered composites derived from N-HEU in scope batch trials. Estimated weight fractions of clinoptilolite and zeolite P are also presented.

Similarly to Z-HEU, Na-exchanged N-HEU exhibited a greater uptake of caesium compared to strontium (84 and 70 %, respectively). The trend in caesium uptakes with respect to solution basicity is also very similar; less transformed composites retained caesium affinity but when the resultant clinoptilolite weight fraction is below ~20 %, significantly reduced uptake is observed. Strontium uptake is greater than 80 % for all the composites, even when the material was formed in the 0.20 M NaOH solution – presumably a result of parent framework desilication (Section 4.2.2.5). A small increase in strontium uptake is observed from composites which contain negligible quantities of clinoptilolite (0.45 – 0.5 M NaOH). The optimal dual uptake materials, in these conditions, were the composites produced using

0.20 and 0.25 M NaOH solutions, which displayed an uptake of greater than 80 % for both species. This corresponds to materials comprised of < 15 Wt. % zeolite P.

4.2.3.3 Composites Generated from S-HEU

The respective uptakes of caesium and strontium achieved by materials derived from S-HEU are summarised in Figure 4.12, in addition to uptake data for the sodium-exchanged parent material and the weight fractions of clinoptilolite and zeolite P (4.2.2).

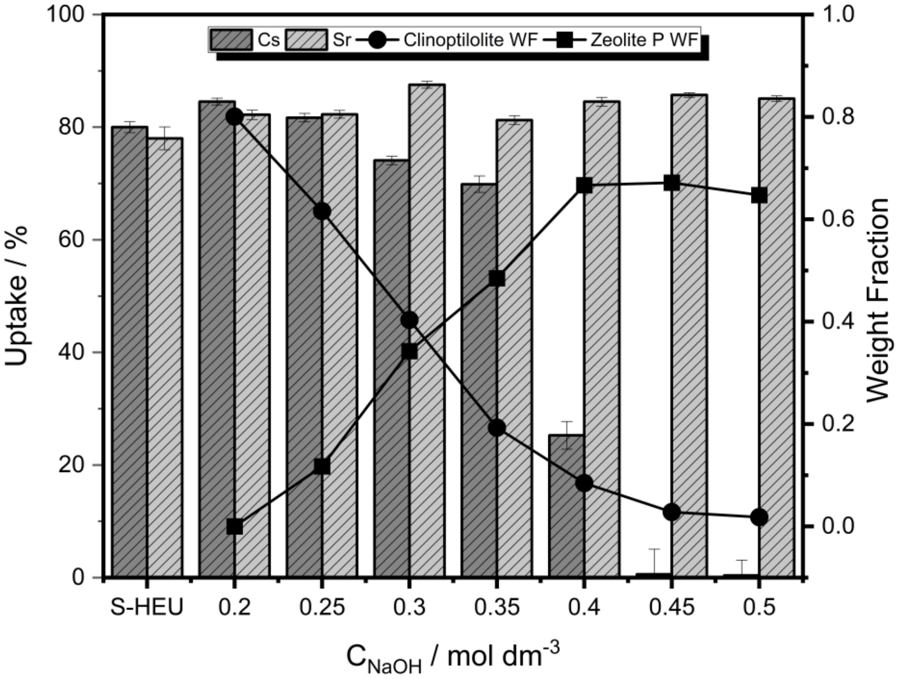

Figure 4.12. Uptake of caesium and strontium achieved by the powdered composites derived from Z-HEU in scope batch trials. Estimated weight fractions of clinoptilolite and zeolite P are also presented.

Parent S-HEU, pre-exchanged with sodium, removed about 80 % of both caesium and strontium from solution in these conditions. 0.20 and 0.25 M NaOH solutions afforded composites mostly consisting of a partially desilicated clinoptilolite framework, with small quantities (> 10 Wt. %) of zeolite P; these materials showed small increases in both caesium and strontium uptake to ~85%. Further increasing the solution basicity steadily decreases the caesium uptake, until 0.40 M where the removal rate is greatly decreased to < 30 %. This is a result of the small quantities of parent clinoptilolite remaining present in the material. Strontium uptake remained high (> 80 %), regardless of the composition of the composite, suggesting no gain in material performance as a result of the transformation (under these conditions).

4.2.3.4 Batch Ion-Exchange Testing of Composite Materials Summary

Overall, parent clinoptilolites displayed > 80 % uptake of caesium in excess potassium, demonstrating good selectivity for caesium over potassium. After transformation, the subsequent zeolite P removed negligible quantities of caesium, showing a poor selectivity for caesium over potassium in these conditions. The opposite trend is observed with strontium adsorption: the nascent zeolite P phase shows exceptional selectivity for strontium over calcium, in these conditions. Varied effectiveness of composite materials were observed across the three starting materials, despite the equally impressive control over respective weight fractions of zeolitic phases. Akin to the partial transformation of mordenite (Section 3.2.2.1), composites derived from Z-HEU displayed increasing strontium uptakes in more basic solutions. Caesium uptakes remained high in low NaOH concentrations, but diminished greatly in composites where the transformation was almost ‘complete’. Similar trends were observed in composites derived from N-HEU, albeit with less prominent disparities (largely due to the respective uptakes of caesium and strontium of the parent material). These datasets demonstrate the effect of the relative ratios of the zeolitic phases, which are closely controlled though manipulation of the solution basicity, on the ion-exchange properties of the materials, thus providing a method to generate tailor-made materials suitable for remediation of specific waste streams. Composites generated from S-HEU did not perform significantly better compared to the sodium-washed parent for sorption of either cation; this is largely due to the high quantities of strontium removed by the parent.

Considering the batch ion-exchange data and the industrial requirement for granular materials, the bulk of this chapter will now focus on materials generated from Z-HEU, as it was procured in granular form and displays the greatest improvement in strontium uptake. N- and S-HEU were procured as fine powders, limiting the development of granular materials for experimentation in industrially relevant flow systems. A post synthetic pelleting process could be deployed on powdered composites, although this adds complication to the process and is outside the scope of this work.

4.2.4 Equilibrium Adsorption Studies

A high-capacity ion-exchange material is not necessarily desirable when used to remediate nuclear effluent. This is because materials are considered spent at low adsorption levels (< 1 %) due to low breakthrough tolerances. Nonetheless, capacity is an important property of ion-exchange materials. Here, the caesium and strontium capacities are determined through adsorption isotherms to assess how the properties of a composite and fully converted material differ to the parent material, Z-HEU.

4.2.4.1 Caesium Adsorption Isotherms

Adsorption isotherms were applied to the caesium adsorption data obtained from three materials: the Z-HEU parent, a clinoptilolite/zeolite P composite material (37:40 HEU:GIS, 0.35 M NaOH solution) and a fully converted zeolite P analogue (0.50 M NaOH solution) (Figure 4.13).

Langmuir, Freundlich, Temkin and Langmuir-Freundlich isotherm models were fitted to the datasets; Langmuir-Freundlich consistently provided the best fit and was therefore used to determine capacity, $q_{\max}$. Langmuir-Freundlich fitting parameters are presented in Table 4.3. Fitting parameters of all models are available in the appendix (A.11).

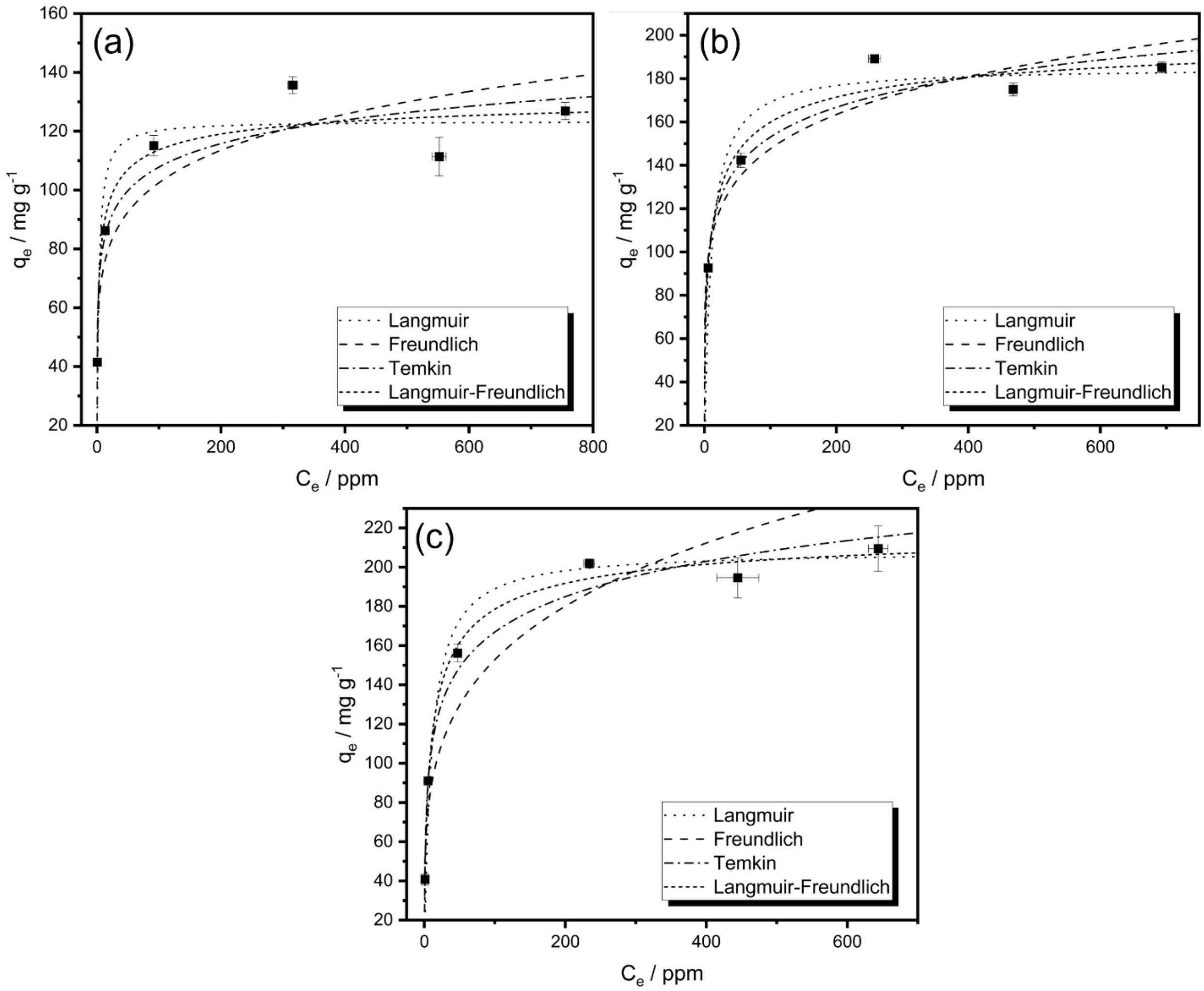

Figure 4.13. Caesium adsorption isotherms obtained through batch ion-exchange experiments. Langmuir, Freundlich, Temkin and Langmuir-Freundlich isotherm models have been applied to each dataset. (a) Parent clinoptilolite, Z-HEU (Na exchanged), (b) Composite zeolite (HEU:GIS ratio 37:40) and (c) Fully converted material (zeolite P).

Table 4.3. Langmuir-Freundlich caesium adsorption isotherm parameters for parent clinoptilolite, Z-HEU (Na exchanged), composite zeolite (HEU:GIS ratio 37:40) and fully converted material (zeolite P).

	Langmuir-Freundlich			
Material	**q_{max} / mg g^{-1}**	**K**	**n**	**R^2**
Z-HEU (parent, Na-washed)	136(20)	0.6(2)	0.5(2)	0.933
Composite (37:40 HEU:GIS)	207(39)	0.3(1)	0.5(3)	0.956
Zeolite P (fully converted)	223(13)	0.24(4)	0.61(9)	0.993

An impressive increase in caesium capacity from 136 to 223 mg g^{-1} was attained from full transformation to zeolite P (0.50 M NaOH). This can be attributed to the formation of the highly aluminous zeolite P phase, as revealed though elemental analysis (4.2.2.5). This is comparable to work by Mimura, where a caesium capacity of 234 mg g^{-1} was determined in pseudo-synthetic zeolite P[76]. The composite material (37:40 HEU:GIS) displayed a capacity of 207 mg g^{-1}. This significant increase in comparison to the parent clinoptilolite can be attributed to both crystallisation of the aluminium-rich zeolite P phase and concurrent desilication (and potential development of mesopores) in the parent material, as evidenced by elemental analysis (4.2.2.5).

4.2.4.2 Strontium Adsorption Isotherms

The maximum strontium adsorption capacities, $q_{\max}$, were determined through analysis of adsorption isotherms for the parent clinoptilolite (Na-washed), a composite material (HEU:GIS ratio 37:40, 0.35 M NaOH) and the fully converted zeolite P material (0.50 M NaOH) (Figure 4.14).

Analogous to caesium equilibrium adsorption experiments, Freundlich, Temkin and Langmuir-Freundlich isotherm models were fitted to the datasets. Additionally, the Langmuir isotherm was fitted to the dataset for the fully converted material. The Langmuir-Freundlich model provided a good fit in all three systems and was therefore used to determine capacity, $q_{\max}$. The Langmuir-Freundlich fitting parameters are presented in Table 4.4, with fitting parameters of all other fitting models available in the appendices (A.11). Fits are good to the composite and zeolite P adsorption data ($R^2 > 0.96$); however, the fit to the data from the parent Z-HEU is poor ($R^2 = 0.827$). Despite this, the derived capacity value of 30 mg g^{-1} appears sensible.

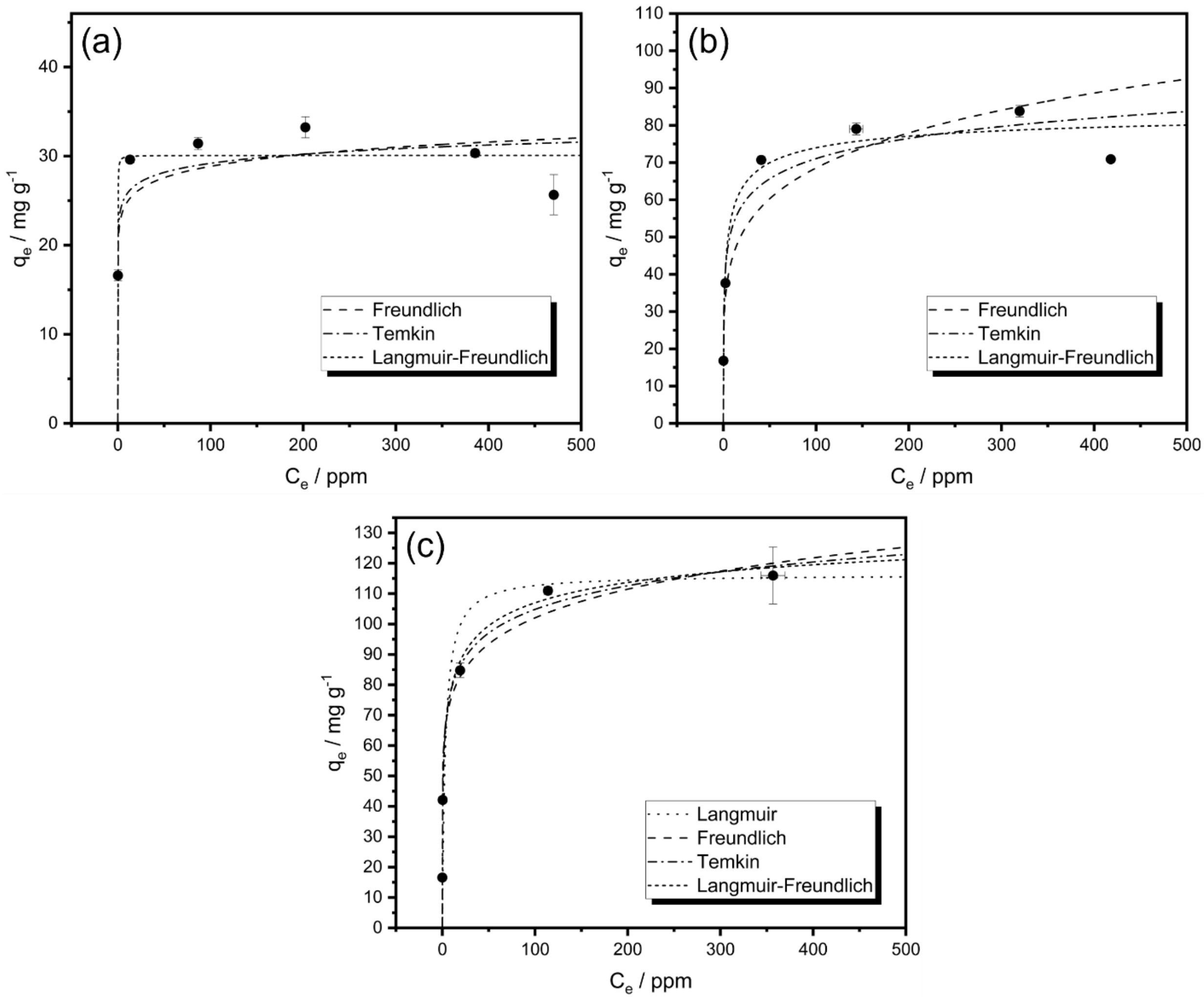

Figure 4.14. Strontium adsorption isotherms obtained through batch ion-exchange experiments. Where appropriate, Langmuir, Freundlich, Temkin and Langmuir-Freundlich isotherm models have been applied to each dataset. (a) Parent clinoptilolite, Z-HEU (Na exchanged), (b) Composite zeolite (HEU:GIS ratio 37:40) and (c) Fully converted material (zeolite P).

Table 4.4. Langmuir-Freundlich strontium adsorption isotherm parameters for parent clinoptilolite, Z-HEU (Na exchanged), composite zeolite (HEU:GIS ratio 37:40) and fully converted material (zeolite P).

	Langmuir-Freundlich			
Material	***q_{max}* / mg g^{-1}**	**K**	**n**	**R^2**
Z-HEU (parent, Na-washed)	30(2)	17(300)	1(7)	0.827
Composite (37:40 HEU:GIS)	86(12)	0.6(3)	0.5(2)	0.961
Zeolite P (fully converted)	145(15)	0.52(11)	0.37(6)	0.994

Full transformation from the parent clinoptilolite into zeolite P saw a remarkable increase in the strontium capacity, from 30 to 145 mg g^{-1}. This is comparable to work by Mimura[76], who reported a capacity of 161 mg g^{-1} for a zeolite P material produced *via* interzeolite transformation of a natural zeolite. This drastic increase can be attributed to an increased probability of aluminium pairs in the nascent zeolite P, as evidenced through elemental analysis (4.2.2.5). The composite material was determined to possess a strontium capacity of 86 mg g^{-1}. It is likely that this increase in capacity is due to a combination of the aluminous zeolite P, in addition to desilication of the parent clinoptilolite (4.2.2.5).

4.2.4.3 Caesium and Strontium Capacity Discussion

Adsorption isotherms (4.2.4.1) indicate an approximate 60 % increase in caesium capacity upon transformation to zeolite P. The strontium capacity, however, increased by 400 % (4.2.4.2). Partial transformation similarly increased the capacity, albeit to a slightly lesser extent. All capacity values are presented on a single axis in Figure 4.15, in addition to the straight line $y = 0.33x$, which represents a system capable of accommodating an equal quantity of charge from both caesium and strontium. Materials below the line are capable of adsorbing less strontium than the caesium capacity suggests, due to a lack of suitable strontium adsorption sites. On the contrary, materials positioned above the line can adsorb more strontium that their caesium capacities suggest, due to a deficit of appropriate caesium adsorption sites.

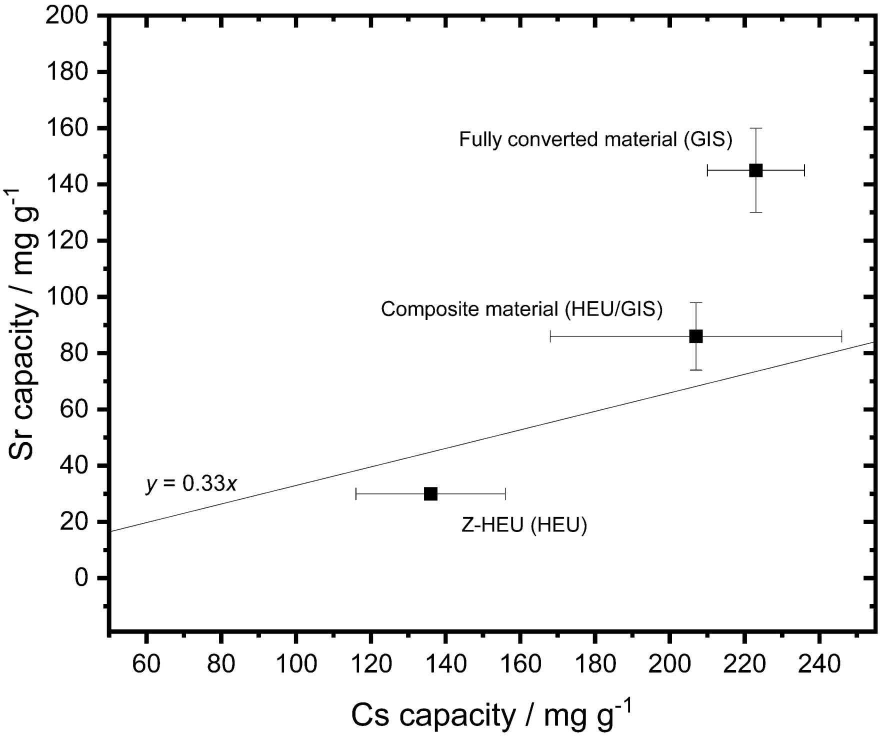

Figure 4.15. Caesium and strontium capacities (q_{max}) of parent clinoptilolite (Z-HEU, Na-exchanged), the composite material and the fully converted material, as determined from equilibrium adsorption isotherms. The straight line $y = 0.33x$ is plotted to depict the region where equal quantities of charge from both caesium and strontium can be accommodated.

This analysis shows the vast quantities of strontium adsorption sites produced as a result of the transformation to zeolite P: the parent material, Z-HEU, is deficient of strontium sites whereas both partially and fully converted materials are rich in strontium sites. These observations are consistent with data presented in Chapter 3 (3.2.4.3), where analogous transformations and adsorption experiments were performed on a natural mordenite. These results strengthen the premise of tuning ion-exchange materials to a given waste stream and demonstrate the applicability of this enhancement method to the most abundant natural zeolite: clinoptilolite.

4.2.5 Kinetic Adsorption Isotherms

In addition to the capacity and selectivity of an ion-exchange material, the rate of exchange is crucial, particularly in industrial flow systems, where residence times can be as short as a few minutes[20].

Herein, kinetic isotherms are plotted for the uptake of caesium and strontium for three materials: sodium-exchanged Z-HEU, in addition to composites generated from 0.35 and 0.50 M NaOH transformation solutions, which correspond to an approximately 37:40 HEU:GIS composite and a 'fully converted' material, respectively (Section 4.2.2.1). These experiments should aid in determining the effect, if any, of the extent of transformation on the kinetics of ion-exchange.

4.2.5.1 Rate of Caesium Exchange

Kinetic isotherms depicting the adsorption of caesium by Z-HEU, a composite material (0.35 M NaOH, 37:40 HEU:GIS ratio) and a 'fully converted' material are displayed in Figure 4.16. Second order kinetic models (2.2.1.5) are fitted to the datasets, with determined parameters, in addition to the estimated time to reach 95 % of the equilibrium uptake, presented in Table 4.5.

Fits to the second order kinetic model are excellent, with coefficients of determination (R^2) very close to unity. The rate of caesium exchange is rapid for all three materials, with equilibrium quantitatively reached in under 30 minutes. The treated materials did, however, exhibit faster rates of uptake compared to the Na-exchanged parent material; 2nd order rate constants of 1.76 and 6.69 g mg^{-1} h^{-1} for the composite and 'fully converted' materials, respectively, compared to value 1.12 g mg^{-1} h^{-1} for Z-HEU, confirm this. This equates to 95% of equilibrium uptake being achieved in 9, 4 and 1 minute(s) for Z-HEU, the composite material and the 'fully converted' material, respectively. This noticeable increase in rate suggests that the newly-crystalised zeolite P is capable of more rapid exchange than the clinoptilolite precursor; it is unclear whether this is an effect of the zeolite P framework, the micro-morphology/surface area of the pseudo-synthetic zeolite, or the desilication/framework breakdown of the parent clinoptilolite (for the composite material). The true origin of the increase in rate of caesium sorption is likely a combination of these factors. In agreement with observations in Section 4.2.4.1, where the transformation markedly increased the caesium capacity, greater equilibrium loadings were observed for composite and 'fully converted' materials in comparison to the parent Z-HEU.

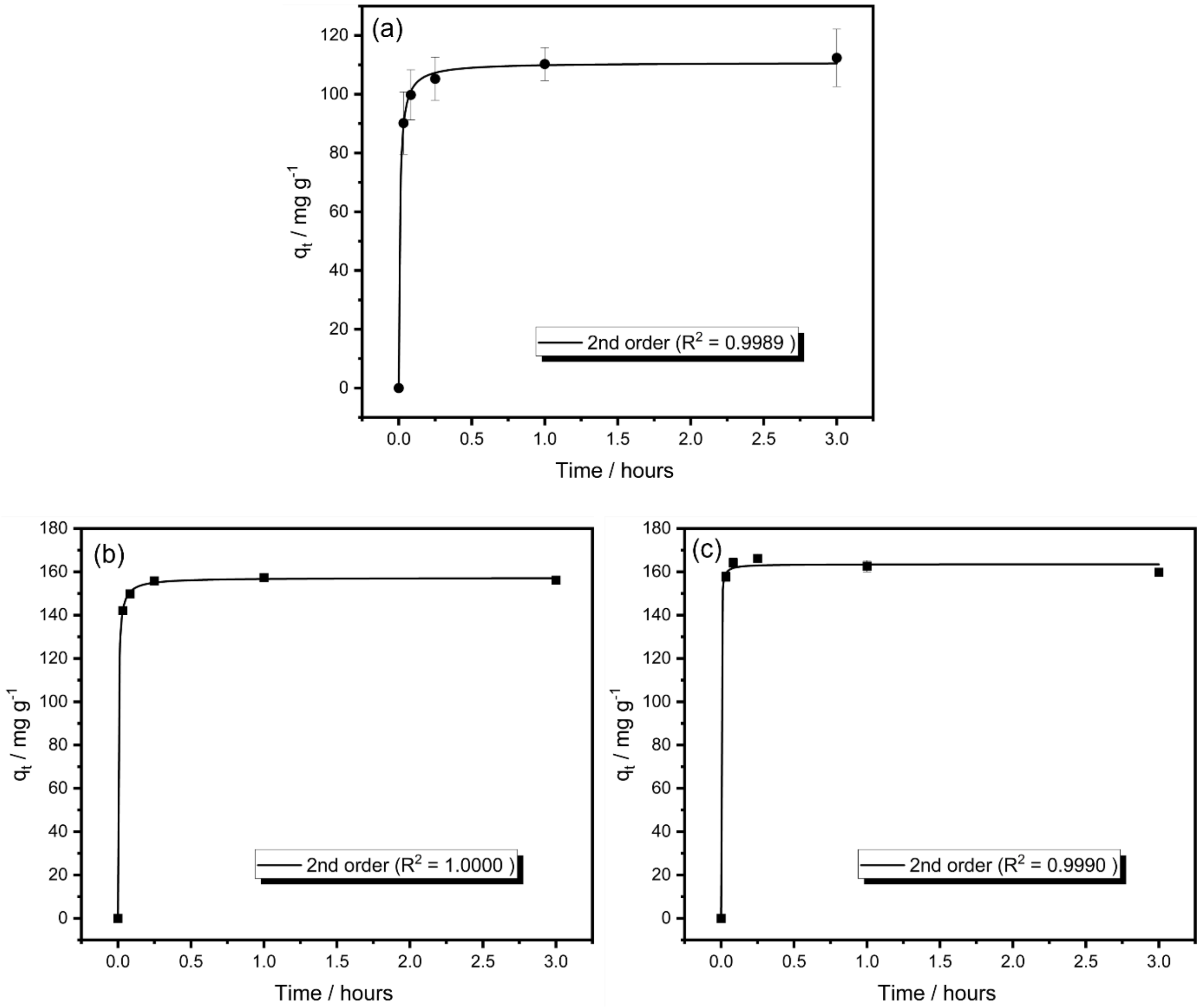

Figure 4.16. Kinetic isotherms showing the adsorption of caesium. (a) Na-exchanged parent clinoptilolite (Z-HEU), (b) 37:40 HEU:GIS composite material and (c) fully converted zeolite P material. The 2nd order kinetic model has been applied to each isotherm.

Table 4.5. 2nd order fitting parameters for caesium kinetic isotherms.

Material	**q_e / mg g^{-1}**	**k / g mg^{-1} h^{-1}**	**R^2**	**$t_{(95\%)}$ / minutes**
Z-HEU	111(1)	1.12(13)	0.9989	9(4)
Composite	157(1)	1.76(13)	1.0000	4(2)
‘Fully converted’	164(2)	6.69(550)	0.9990	1(1)

The improvement in the rate of caesium exchange would, in theory, transpose to elongated breakthrough times in a column setting, thus reducing the frequency of bed changes. While this can only be seen as a positive, strontium is often the first breakthrough species due to its large hydration sphere, which retards exchange[34]; investigation into the rate of strontium exchange is therefore paramount.

4.2.5.2 Rate of Strontium Exchange

Kinetic isotherms showing the adsorption of strontium by Z-HEU, a composite (0.35 M NaOH, 37:40 HEU:GIS ratio) and a ‘fully converted’ material are displayed in Figure 4.17. The data obtained from Z-HEU is fitted to the Elovich model, whereas isotherms from the composite and fully converted material are fitted to the 2nd order model, as these fits best represent the data ($R^2 > 0.98$). Parameters of both Elovich and 2nd order fits to all datasets are displayed in Table 4.6; for further information on the models themselves please refer to Section 2.2.

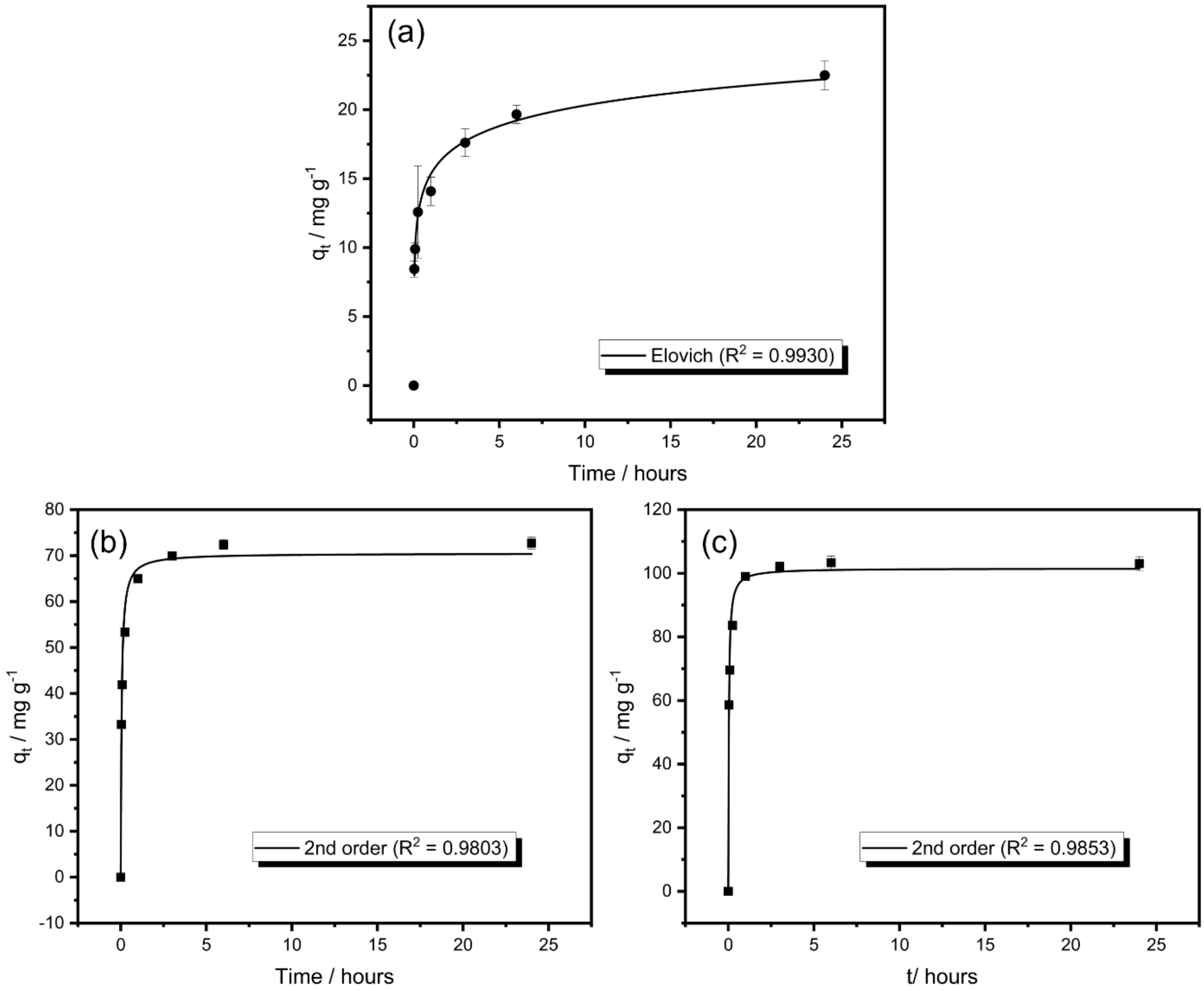

Figure 4.17. Kinetic isotherms showing the adsorption of strontium. (a) Na-exchanged parent clinoptilolite (Z-HEU), (b) 37:40 HEU:GIS composite material and (c) fully converted zeolite P material. The Elovich model is fitted to the parent clinoptilolite dataset. The 2nd order kinetic model has been fitted to the datasets from the composite and fully converted materials.

Table 4.6. 2nd order and Elovich fitting parameters for strontium kinetic isotherms. *Isotherms are depicted in Figure 4.17.

2nd order kinetic model				
Material	q_e **/ mg g^{-1}**	k **/ g mg^{-1} h^{-1}**	**R^2**	$t_{(95\%)}$ **/ minutes**
Z-HEU	18.9(14)	0.70(32)	0.8756	86(63)
Composite (37:40 HEU:GIS)*	70.5(19)	0.28(5)	0.9803	58(26)
'Fully converted'*	101.5(22)	0.32(5)	0.9853	35(15)
Elovich model				
Material	α	β	**R^2**	$t_{(95\%)}$ **/ hours**
Z-HEU*	2625	0.46(3)	0.9930	56(17)
Composite (37:40 HEU:GIS)	71072	0.16(2)	0.9676	13(14)
'Fully converted'	2×10^7	0.14(3)	0.9654	10(3)

The incorporation of strontium into these structures is visibly slower than for caesium in equivalent conditions; equilibrium takes several hours to reach for transformed materials and is not even reached after 24 hours for Z-HEU. This is confirmed by estimated times to reach 95% of equilibrium: according to the best fitting models, Z-HEU does not reach 95% of equilibrium loading until at least 39 hours, whereas the composite and 'fully converted' material reach this point in around 60 and 35 minutes, respectively. This is consistent with the requirement that strontium must shed a portion of its significant aqueous shell to fit inside the zeolite pores[34].

The Elovich model suggests far longer timeframes are required to reach 95 % of equilibrium in comparison to the 2nd order kinetic model. In the case of the composite and fully converted material, the fit is poor (A.12) and inappropriate for estimating the equilibrium loading. The model fits the data well in the case of Z-HEU, although, as equilibrium was not reached in the experiment timeframe, it is unclear how well the model would fit at longer time intervals, so the reported $t_{95\%}$ value of 56 hours should be considered an estimate. The 2nd order kinetic model provides a very poor fit to the data for Z-HEU (A.12).

Overall, an exceptional increase in the rate of strontium sorption, for both the composite and the fully converted material, is observed. This is a vital observation when considering the industrial relevance, as strontium is often the breakthrough species in the SIXEP plant. The enhancement becomes more impressive when considered in conjunction with the drastically improved capacity (4.2.4.2); both the composite and fully converted material adsorb significantly more strontium and reach equilibrium faster. In these rate experiments, the composite material sorbs over 4 times the quantity of strontium within the first few hours of exchange.

4.2.6. Generation of Granular Composites

Industrial ion-exchange processes typically operate in dynamic flow systems, where effluent is pumped though a fixed bed of a given material[20, 95, 184, 185, 205]. Granular materials (typically > 200 μm diameter) are required to facilitate flow and prevent pressure discrepancies. The work presented in this chapter has previously been limited to powdered materials, which are unsuitable for deployment in industrial column environments without further processing. Despite the fundamental findings from the powder experiments (e.g., transformation control, improved capacity, and enhanced kinetics) remaining valid, concept column trials are required to further gauge potential industrial usage. Thus, demonstrating the formation of granular composite materials from a natural clinoptilolite precursor would be a significant step in showing the wide-ranging, industrial applicability of the discussed partial transformation methodology. As Z-HEU is the only parent clinoptilolite in granular form, work in this section is limited to its transformation to zeolite P.

Firstly, granular Z-HEU (400 – 600 μm) was obtained through appropriate grinding and sieving of the raw material. Analogous to powdered transformations (4.2.2), basic hydrothermal treatment (0.25 – 0.50 M NaOH) induced transformation to zeolite P, which could be similarly controlled through manipulation of the sodium hydroxide concentration. PXRD patterns obtained from these generated materials is presented in Figure 4.18, in addition to simulated patterns for clinoptilolite, Na-P1 and a 50:50 mixture of both these phases.

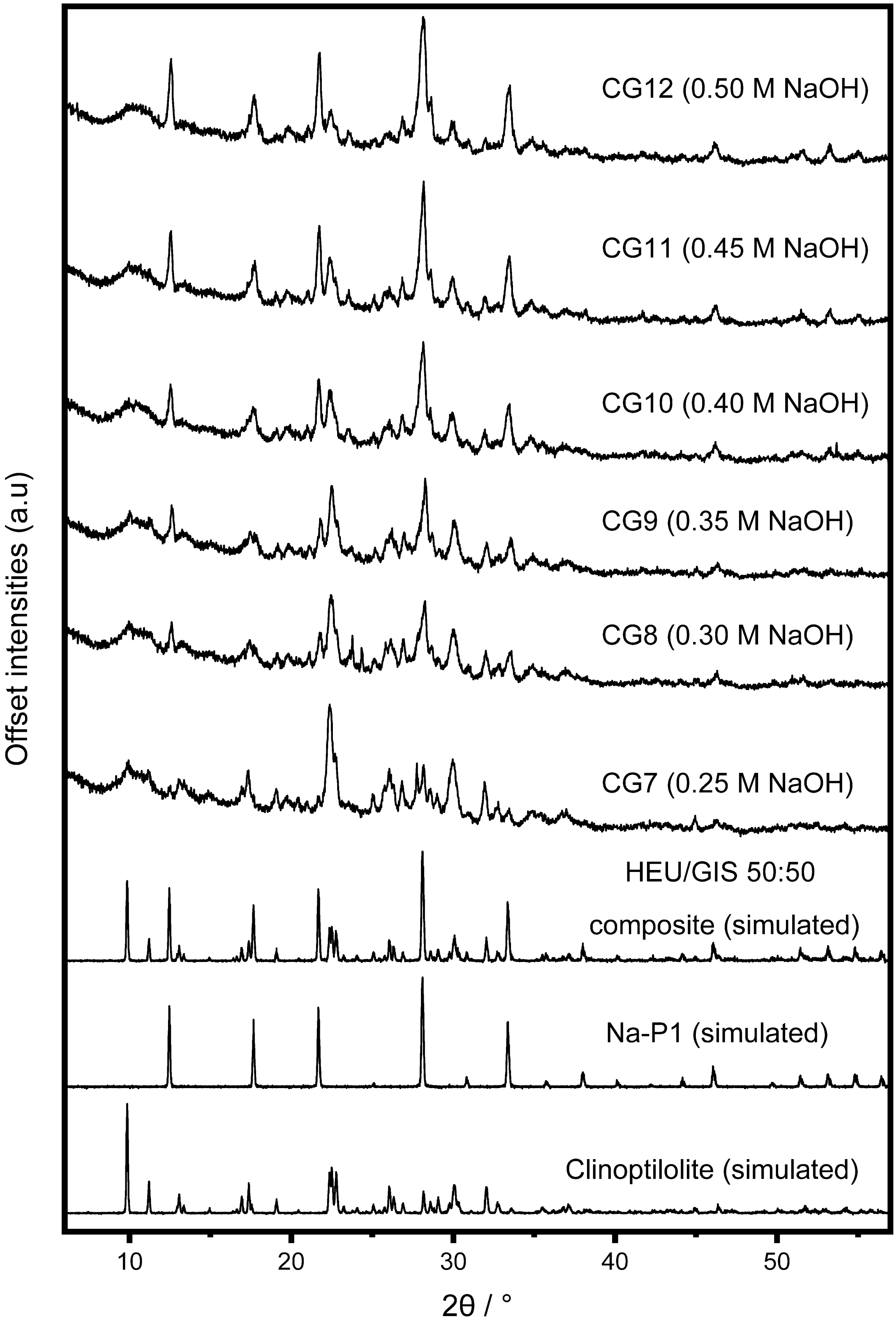

Figure 4.18. PXRD patterns of granular (400-600 μm) Z-HEU clinoptilolite material after hydrothermal treatment (0.25 – 0.50 M solutions). Simulated clinoptilolite and zeolite P (Na-P1) patterns are also presented (λ = 1.5406 Å).

The relative weight fractions of clinoptilolite and zeolite P within these materials are estimated through Rietveld analysis[162, 163] (A.13). The results from this analysis are presented in Table 4.7.

Table 4.7. Estimated weight fractions of clinoptilolite and zeolite P in granular composite materials generated in 0.25 to 0.50 M NaOH solutions.

Material	Treatment	HEU weight fraction	GIS weight fraction
Z-HEU	1.0 M NaCl	0.83(1)	-
CG7	0.25 M NaOH, 100 ℃	0.82(1)	0.04(1)
CG8	0.30 M NaOH, 100 ℃	0.58(1)	0.17(1)
CG9	0.35 M NaOH, 100 ℃	0.59(1)	0.22(1)
CG10	0.40 M NaOH, 100 ℃	0.42(1)	0.37(1)
CG11	0.45 M NaOH, 100 ℃	0.35(1)	0.45(1)
CG12	0.50 M NaOH, 100 ℃	0.18(1)	0.59(1)

Small quantities of zeolite P are observed in the material generated with 0.25 M NaOH solution (CG7). The quantity of zeolite P increased steadily with solution basicity - a desired blend of clinoptilolite/zeolite P phases could be achieved through manipulation of the NaOH concentration. Presumably, the increased pH accelerates parent dissolution and allows for more growth of zeolite P in the 24 h synthesis timeframe. Similar NaOH concentrations were required to initiate transformation to zeolite P when compared to the powdered transformations (4.2.2), indicating the rate of dissolution is comparable in both powdered and granular transformations. This is unexpected, and in direct contrast to the formation of granular mordenite/zeolite P composites (3.2.6), where more basic solutions were required to induce transformation. Materials formed in more concentrated solutions (e.g., CG12, 0.50 M NaOH) still contained a significant quantity of clinoptilolite, indicating a slower transformation compared to powders at higher concentrations.

Physically, all six granular composites remained intact after the partial transformation. However, the structural integrity of the more transformed materials (e.g., CG12) was significantly worse than the parent Z-HEU. This is undesirable from an industrial perspective, as increased friability increases likelihood of fines production, which can lead to in-plant flow difficulties.

4.2.7 SEM, XCT and Local Diffraction Studies

Scanning Electron Microscopy (SEM) imaging was deployed to examine how the surface morphology changes during the transformation process. X-ray Computed Tomography (XCT) data facilitates the generation of cross-sectional images of single granules, thus providing information on the internal morphology. This grants insight into the macroscale mechanism of transformation, providing a greater understanding of these systems and how they can be beneficial from an industrial perspective. Both these techniques were applied to the parent Z-HEU material, in addition to CG10 and CG12, which have HEU:GIS phase ratios of 42:37 and 18:59, respectively. Additionally, local, image-guided micro-diffraction studies were undertaken in attempt to distinguish phases within the materials. Both the tomograms and local, micro-diffraction patterns were recorded using the beamline K11-DIAD, located at Diamond Light Source[172], UK.

4.2.7.1 SEM, XCT and Local Diffraction Studies of Parent Z-HEU

SEM and an XCT cross section of the parent clinoptilolite, Z-HEU, are presented in Figure 4.19, in addition to a local diffraction pattern obtained using diffraction beam trajectory ‘a’. SEM imaging (Figure 4.19a) reveals a mostly featureless exterior, with only the presence of small fines on the surface. This is analogous to the parent mordenite material from Chapter 3 (3.2.1.3), which is expected as both materials are naturally sourced.

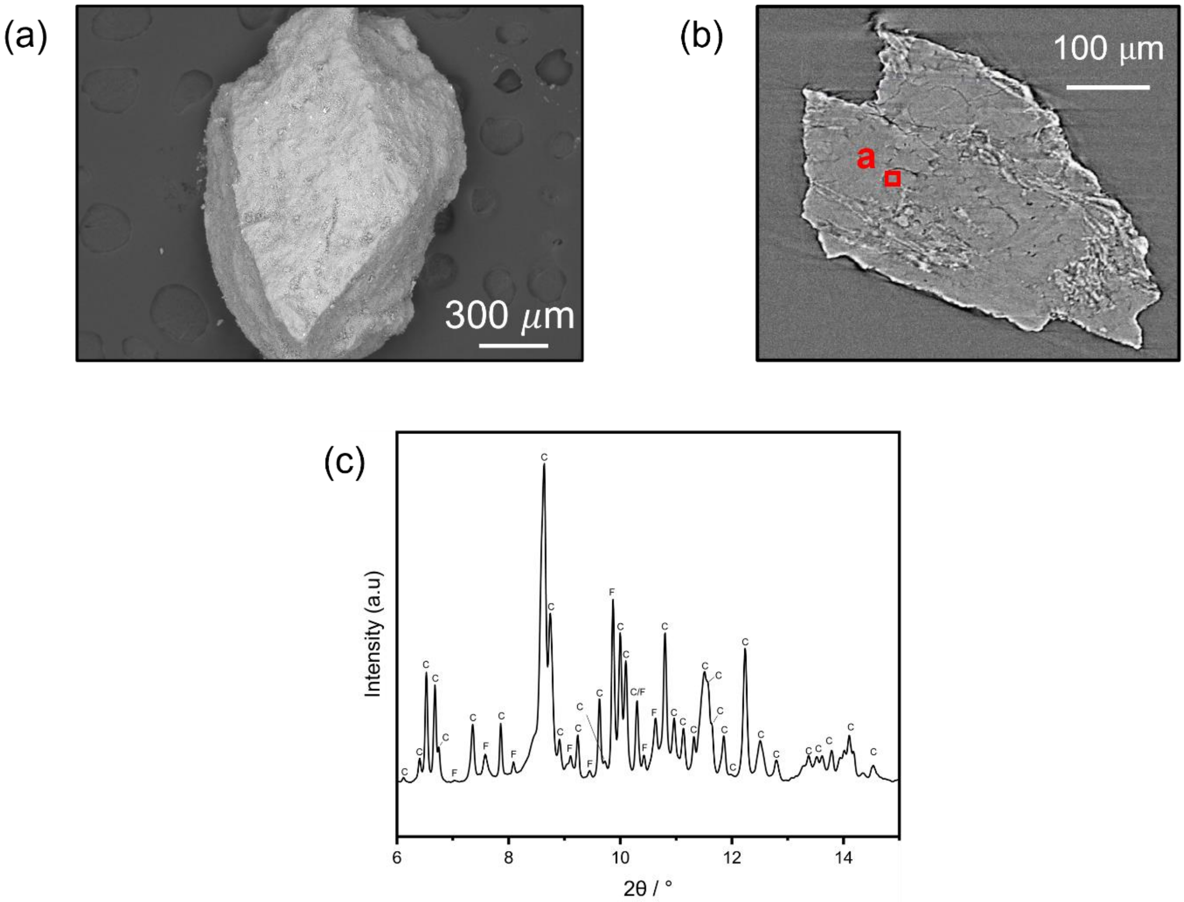

Figure 4.19. Imaging and local diffraction data obtained from a Z-HEU granule. (a) SEM image (15 keV). (b) Cross-sectional tomogram (diffraction beam trajectory ‘a’ is also displayed). (c) Local PXRD pattern obtained from beam trajectory ‘a’. Clinoptilolite (C) and feldspar (F) reflections are labelled.

Tomography cross-sectional imaging of the activated parent clinoptilolite (Figure 4.19b) reveals little contrast throughout the material, indicating a mostly consistent density and limited internal porosity. Again, this is comparable to the tomogram attained from the natural mordenite material in Chapter 3 (3.2.1.3). Unsurprisingly, diffraction data obtained using beam trajectory ‘a’ (Figure 4.19c) showed clinoptilolite as the dominant phase, with smaller quantities of feldspar observed. This is consistent with laboratory PXRD data (4.2.2.1).

4.2.7.2 SEM, XCT and Local Diffraction Studies of CG10

CG10 was formed in a 0.40M NaOH solution and is comprised of estimated phase ratios 42:37 clinoptilolite to zeolite P. SEM images of a CG10 granule are presented in Figure 4.20. A significant change in surface morphology in comparison to the parent clinoptilolite is observed. From first appearances (Figure 4.20a), the surface appears rougher, indicating an increased surface area. Small cracks are also observed, indicating the possibility of mesoporosity. Closer inspection (Figure 4.20b) reveals the presence of star-shaped moieties, with an approximate diameter of 10 μm, on the surface of the granule. Based on the diffraction data, these are assumed to be zeolite P. Furthermore, Huo[218] demonstrated that both spherical and star-shaped zeolite P morphologies were accessible through manipulation of the mother liquor chemistry. The differences in morphologies demonstrated in this work presumably arises from the varying rates of silicon and aluminium leaching from the mordenite and clinoptilolite frameworks during the transformation process.

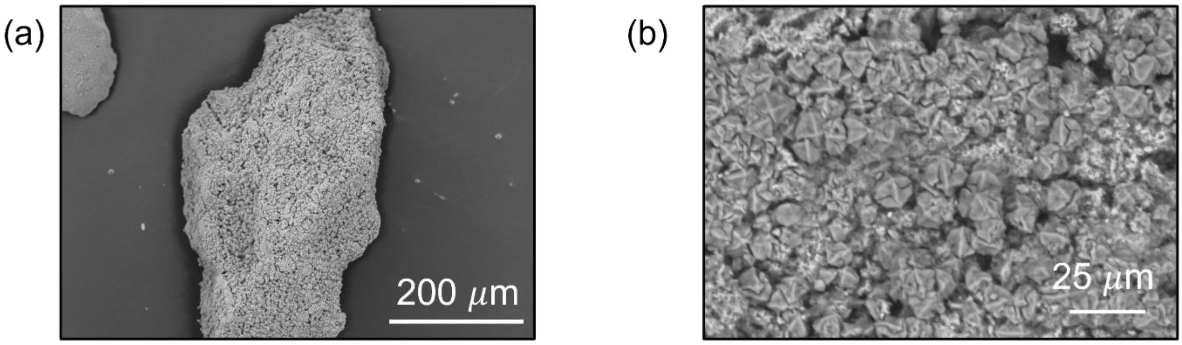

Figure 4.20. SEM images (15 keV) of a CG10 granule (42:37 HEU:GIS ratio).

A cross-sectional image obtained from tomography measurements of a CG10 granule is presented in Figure 4.21, in addition to diffraction data collected from two diffraction beam trajectories, ‘b’ and ‘c’.

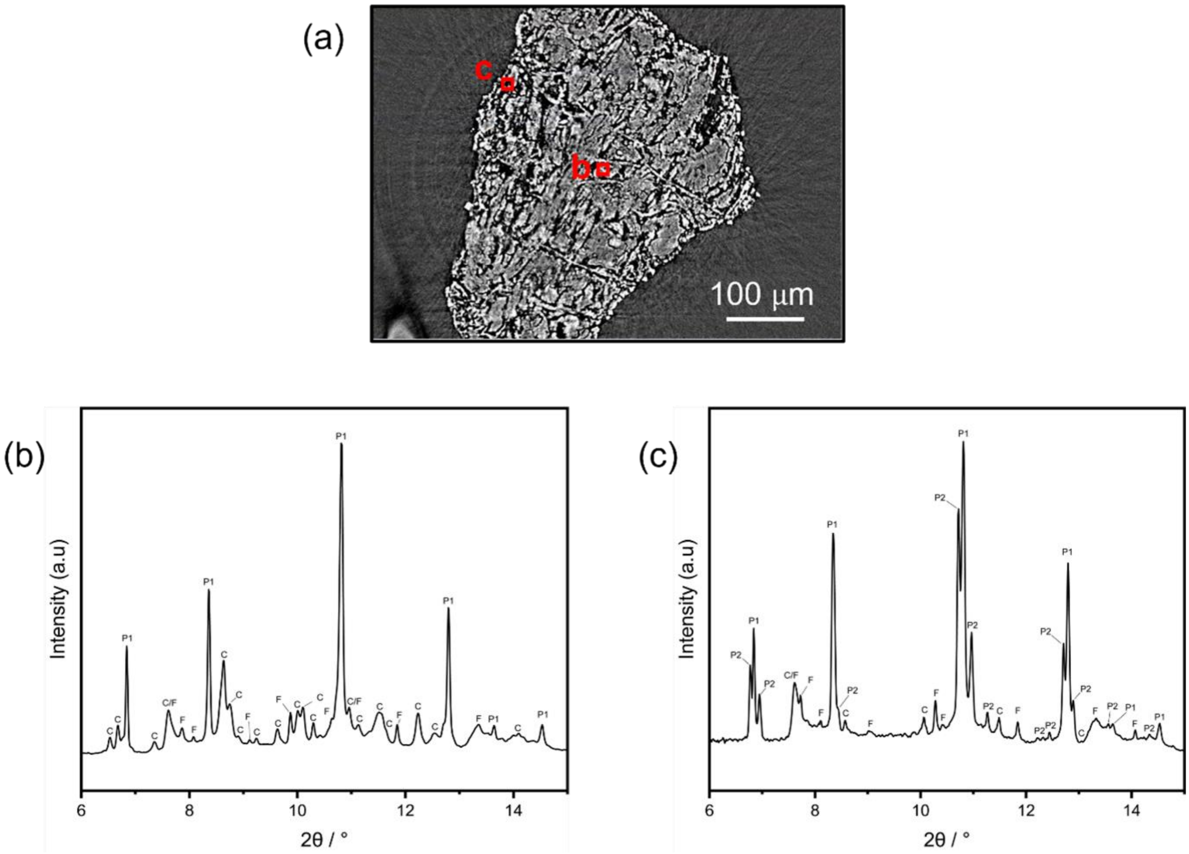

Figure 4.21. Tomography cross-section of a CG10 granule with annotated diffraction beam trajectories, (b) local PXRD pattern obtained from beam trajectory ‘b’. Clinoptilolite (C), Na-P1 (P1) and feldspar (F) reflections are labelled. (c) local PXRD pattern obtained from beam trajectory ‘c’. Clinoptilolite (C), Na-P1 (P1), Na-P2 (P2) and feldspar (F) reflections are labelled.

The tomography cross-section, Figure 4.21a, clearly displays the presence of a lighter contrast phase, both on the exterior of the granule and as ‘veins’ throughout the interior of the granule. Domains of material comparable to that seen in the parent are also present in multiple distinct regions within the granule, surrounded by the lighter contrast ‘veins’ and darker ‘void’ regions, which could indicate an increased internal porosity. Data collected from diffraction beam trajectory ‘b’ (Figure 4.21b), which passes through the centre of the granule, shows the presence of both clinoptilolite and zeolite P, with smaller quantities of feldspar; this is consistent with powder diffraction data (4.2.6). Diffraction data obtained from a beam trajectory through the edge of the granule, diffraction beam trajectory ‘c’ (Figure 4.21c), suggests that zeolite P is the most abundant phase within these lighter contract regions, such as at the surface. Also, smaller quantities of clinoptilolite and feldspar remain, consistent with laboratory diffraction data (4.2.2). Interestingly, significant quantities of Na-P1 and Na-P2 are observed at the edge of the granule, whereas only reflections attributed to Na-P1 are observed from the 'central' trajectory; this suggests that Na-P2 is not homogeneously distributed throughout the newly crystalised material and instead nucleates locally.

4.2.7.3 SEM, XCT and Local Diffraction Studies of CG12

CG12 was formed in a 0.50M NaOH solution and has estimated phase ratios of 18:59 clinoptilolite to zeolite P. SEM images of a CG12 granule are presented in Figure 4.22. Analogous to CG10, the surface of the granule appears to be populated with star-shaped moieties, which appear to have an approximate diameter of 10 μm. Despite being similar in size to those observed on the surface of CG10, there appears to be significantly more on the surface, to such an extent that the parent's surface is barely visible.

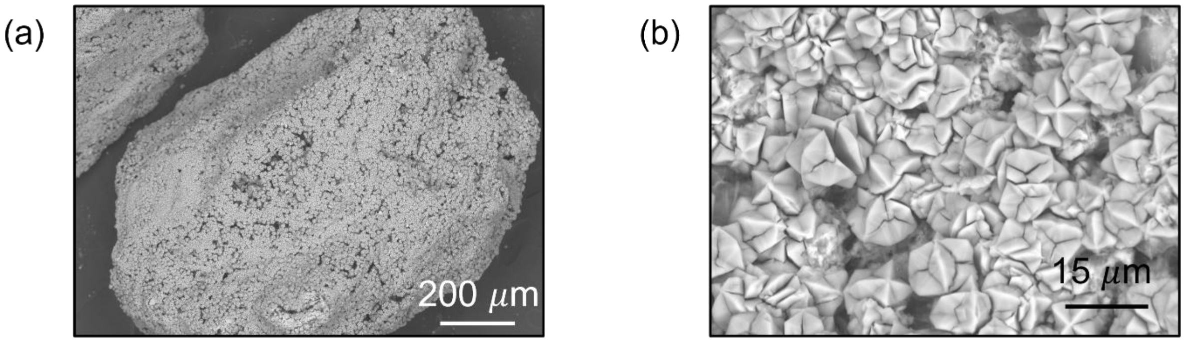

Figure 4.22. SEM images (15 keV) of a CG12 granule (18:59 HEU:GIS ratio).

A cross-sectional tomogram of a CG12 granule is presented in Figure 4.23, in addition to diffraction data collected from two diffraction beam trajectories, 'd' and 'e'.

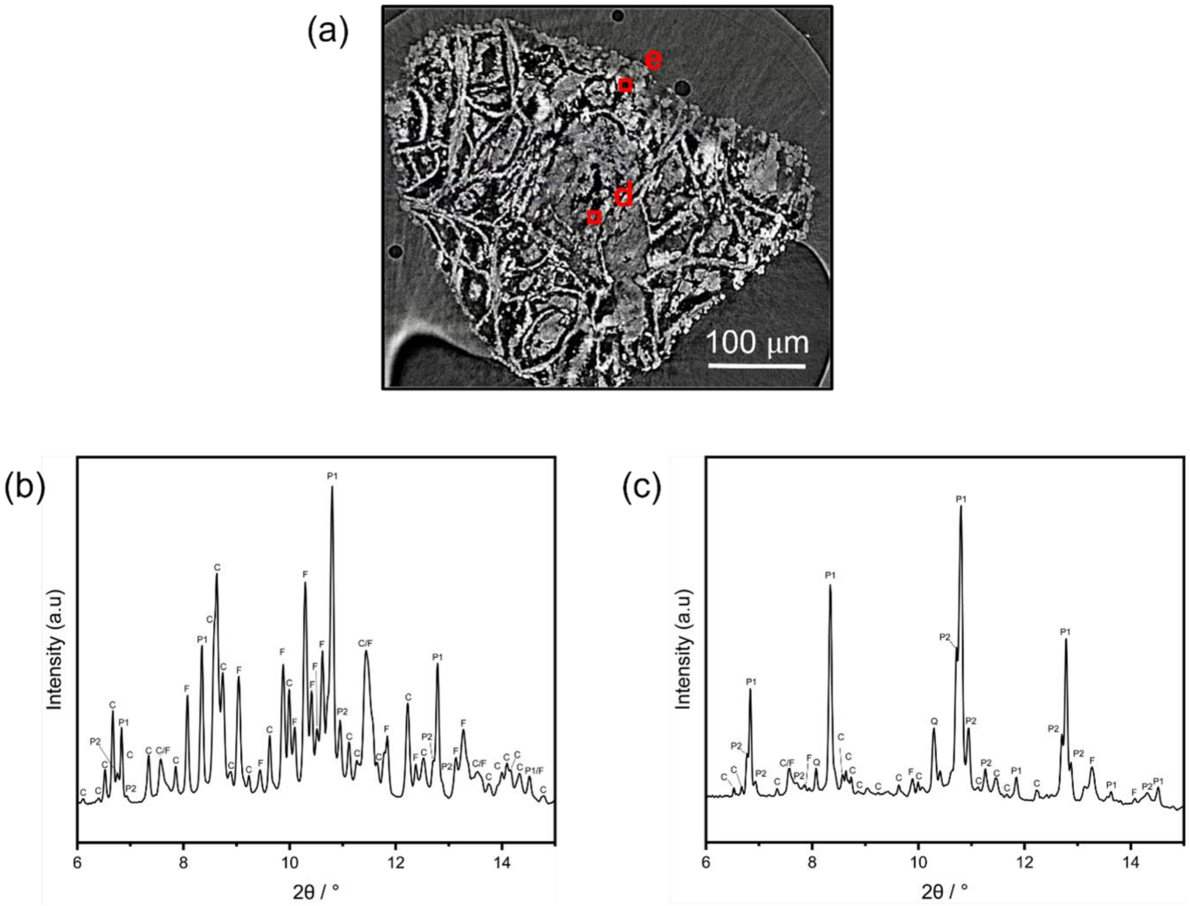

Figure 4.23. Tomography cross-section of a CG12 granule with annotated diffraction beam trajectories, (b) local PXRD pattern obtained from beam trajectory ‘d’. Clinoptilolite (C), Na-P1 (P1) and feldspar (F) reflections are labelled. (c) local PXRD pattern obtained from beam trajectory ‘e’. Clinoptilolite (C), Na-P1 (P1), Na-P2 (P2), feldspar (F) and quartz (Q) reflections are labelled.

In the tomogram (Figure 4.23a), a network of internal, lighter contrast ‘veins’ is visible, surrounded by both ‘void’ regions and domains which resemble the parent clinoptilolite. This could indicate increased internal porosity. In comparison to CG10, the lighter contrast network is more extensive and ‘void’ regions are typically larger. This is in agreement with the diffraction data, which suggests CG12 is significantly more transformed (4.2.6). It should be stated, however, that caution must be taken to avoid over-interpretation of data obtained from single granules of a given material, as it is unclear how representative this is of the bulk.

Data collected from diffraction beam trajectory ‘d’ (4.23b), which passes through the centre of the granule, shows the presence of both clinoptilolite and zeolite P in significant quantities. The clinoptilolite reflections are considerably more intense (in comparison to the peaks attributed to zeolite P) than in the laboratory diffraction pattern from the bulk sample. This suggests either this granule is not representative of the bulk or the diffraction beam just happened to pass through more clinoptilolite material by chance. Diffraction data obtained from a beam trajectory through the edge of the granule, diffraction beam trajectory 'e' (Figure 4.23c), re-affirms that zeolite P is the most abundant phase at the surface. Reflections attributed to Na-P1 and Na-P2 are observed in both diffraction beam trajectories.

4.2.7.4 Summary and Proposed Mechanism

Considering the SEM, XCT and local diffraction data examined in this chapter, a macroscale mechanism of transformation can be proposed. Firstly, the parent clinoptilolite is dissolved *via* hydrolysis in the highly alkaline media. Unlike the mordenite transformation discussed in Chapter 3 (3.2.8.3), dissolution rates appear to be inconsistent across the surface of the granule, with the solution 'tunnelling' into the structure. Once the supersaturation threshold is reached, crystallisation of zeolite P commences, both on the surface and in the internal tunnels. This results in both a zeolite P outer shell and a network of internal zeolite P 'veins'. This process can then continue to higher levels of conversion. A schematic of this process is depicted in Figure 4.24.

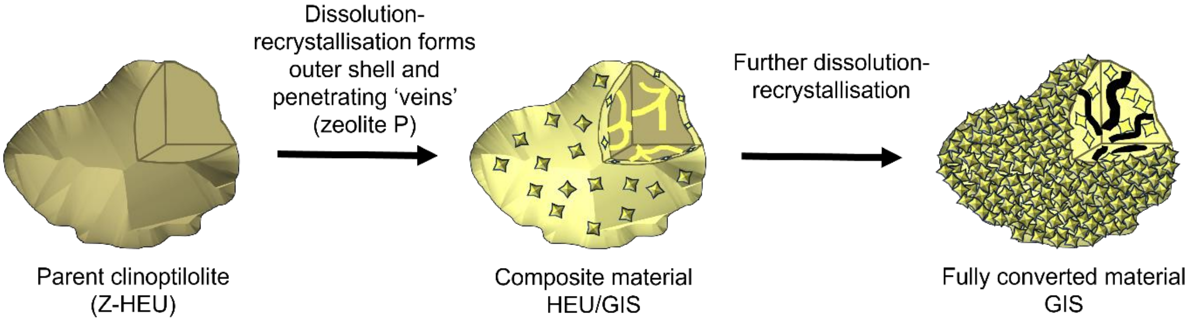

Figure 4.24. Proposed macroscale-mechanism of interzeolite transformation of natural clinoptilolite (Z-HEU).

4.2.8 Rapid Ion Exchange (RIX) Experiments

Previous ion-exchange experiments in this chapter (4.2.3, 4.2.4 and 4.2.5) have been useful in scoping the materials and providing valuable insight into the fundamental properties, such as the capacity for caesium and strontium. However, the experimental conditions are not representative of industry. Firstly, caesium and strontium concentrations are orders of magnitude higher than typical industrial feeds (typical SIXEP feeds contain approximately 17 ppb Cs-137 and 0.5 ppb Sr-90)[70]. Secondly, industrial materials are typically deployed as granular material in dynamic, flow systems; previous work in this chapter has been conducted on powdered materials in batch systems.

Full column studies[70] best replicate the plant conditions and therefore provide excellent insight into a material's potential performance on plant. However, these trials take several months to perform and produce significant quantities of active waste, meaning they are very expensive, whilst simultaneously occupying a meaningful quantity of limited active laboratory capacity. The Rapid Ion Exchange (RIX) methodology (2.2.2.1), recently developed by Sellafield Ltd and National Nuclear Laboratory (NNL), facilitates rapid analysis in a dynamic flow system, with significantly less waste. In RIX experiments, an active simulant liquor is recirculated though a small bed (0.1 g) of ion-exchange material, with the liquor activity monitored as a function of volume (though column).

Preliminary RIX experiments were conducted on the parent clinoptilolite, Z-HEU, in addition to composite materials CG8 and CG10, which contain 58:17 and 42:37 HEU:GIS ratios by weight, respectively. Uptake curves of both Cs-137 and Sr-90 are displayed in Figure 4.25. For comparison, data obtained from Mud Hills clinoptilolite (3.2.10), the material currently used at SIXEP, is also presented. Two-parameter exponential decay functions are also fitted to the datasets (exponential parameters and fitting data are available in Appendix A.14).

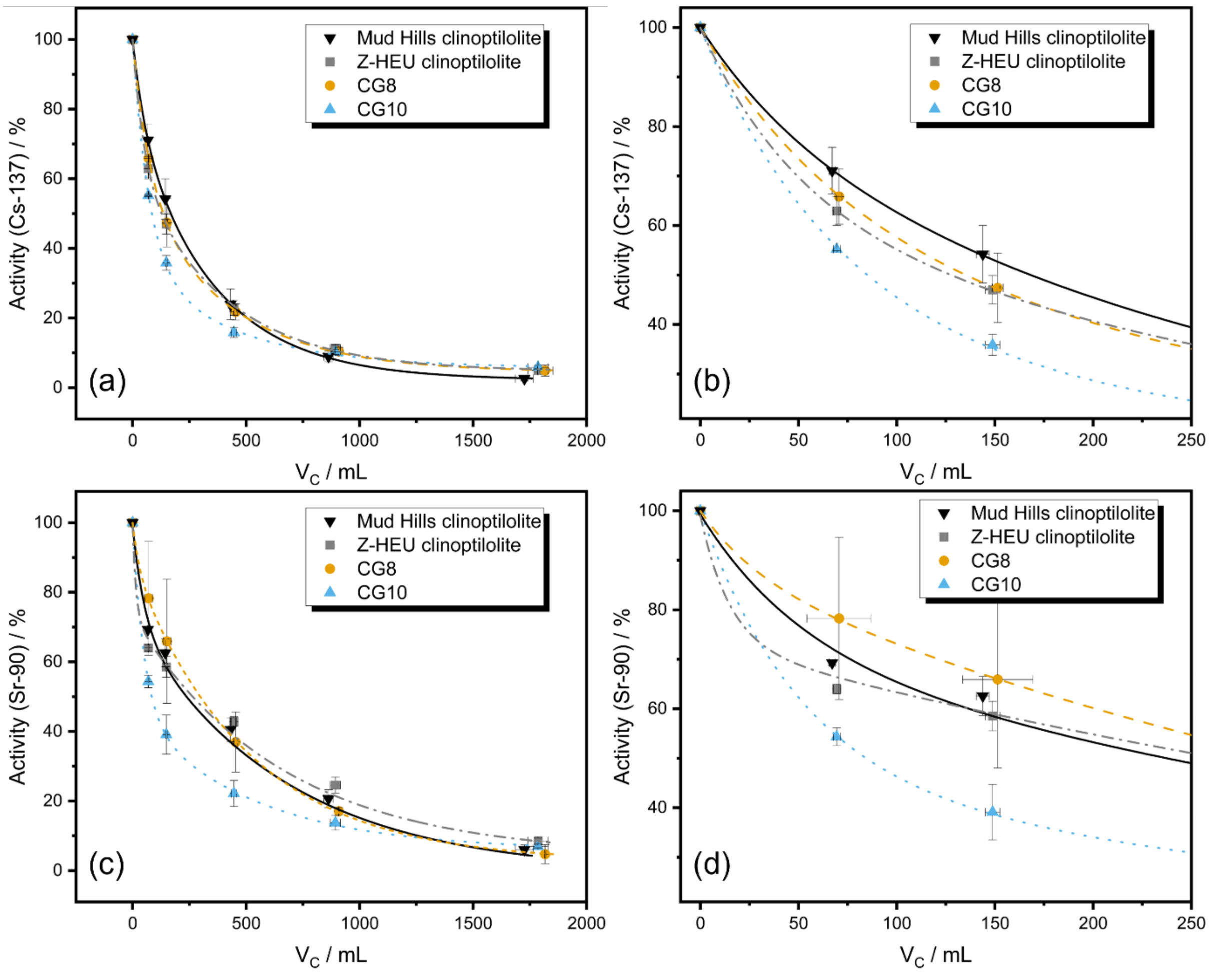

Figure 4.25. RIX uptake data for Mud Hills clinoptilolite, parent clinoptilolite (Z-HEU, Na washed), CG8 and CG10. (a) Cs-137 activity throughout duration of experiment. (b) Cs-137 activity during initial stages of experiment (first 250 mL). (c) Sr-90 activity throughout duration of experiment. (d) Sr-90 activity during initial stages of experiment (first 250 mL).

The fit of two-parameter exponential decay functions to the caesium-137 uptake data are generally excellent ($R^2 > 0.98$, A.14). Fits to strontium-90 uptake data are also good for Mud Hills clinoptilolite, Z-HEU and CG10 ($R^2 > 0.98$, A.14). The fit is poorer to the data from CG8 ($R^2 = 0.92$), due to the significant variance observed in the replicates.

In these experiments, the lower the activity at a given volume, V_C, the more radionuclides the ion-exchange material has adsorbed. Therefore, steeper curves reaching lower activities faster are desirable. To quantify this, the probability of adsorption at a given throughput volume, α, can be mathematically determined using Equation 2.21. For further information regarding this equation, including its derivation, please refer to Section 2.2.2.1. A summary of adsorption probabilities for all materials at V_C = 50, 300 and 1500 mL is provided in Table 4.8.

Table 4.8. Adsorption probability (α_v) of Cs-137 and Sr-90 by Mud Hills clinoptilolite, parent clinoptilolite (Z-HEU, Na washed), CG8 and CG10 after 50, 300 and 1500 mL of solution pass through in RIX experiments.

	Cs-137			**Sr-90**		
Material	α_{50}	α_{300}	α_{1500}	α_{50}	α_{300}	α_{1500}
Mud Hills clinoptilolite	0.53	0.36	0.23	0.53	0.26	0.18
Z-HEU clinoptilolite	0.72	0.38	0.19	0.74	0.25	0.15
CG8 (58:17 HEU: GIS ratio)	0.62	0.39	0.19	0.39	0.23	0.18
CG10 (42:37 HEU:GIS ratio)	0.88	0.51	0.18	0.95	0.42	0.17

The parent clinoptilolite material, Z-HEU, displayed faster initial uptake of Cs-137 than Mud Hills clinoptilolite (Figure 4.25b). This is evidenced with an α_{50} value of 0.72, compared to 0.53 for Mud Hills clinoptilolite. After approximately 500 mL throughput, Mud Hills clinoptilolite has removed more activity from solution, potentially indicating a more permeable internal structure. Interestingly, the removal of Cs-137 by CG8 was slightly poorer than the parent Z-HEU, particularly during the early stages of exchange, as evidenced by an α_{50} value of 0.62, compared to 0.72 for Z-HEU. The more transformed composite material, CG10, exhibited much faster Cs-137 uptake than the parent material. This is reflected in higher α_{50} and α_{300} values (0.88 and 0.51 vs 0.72 and 0.38 for CG10 and Z-HEU, respectively). This increased rate of uptake is unlikely to originate from enhanced ionic diffusion in the nascent zeolite P, given that the GIS framework contains relatively narrow 8- and 4-MR units. Alternatively, this could reflect an enhanced diffusion through the bulk structure thanks to desilication and the presence of a more porous composite[193]. Further, an increase in surface area is also likely as a result of the zeolite P moieties on the surface of the granules (4.2.7).

In the early stages of the experiment, Z-HEU exhibited faster uptake of Sr-90 than Mud Hills clinoptilolite (Figure 4.25d). The is reflected by a probability of adsorption after 50 mL of 0.74, in comparison to 0.53 for Mud Hills clinoptilolite. However, after approximately 150 mL of throughput, more strontium is removed by Mud Hills clinoptilolite compared to the parent Z-HEU (α_{300} and α_{1500} values of 0.26 vs 0.25 and 0.18 vs 0.15, respectively), resulting in a lower reservoir activity at the end of the experiment. This is consistent with the superiority of Mud Hills clinoptilolite, which was selected due to its proficiency in adsorbing strontium[70]. Unfortunately, the replicates for the strontium uptake of CG8 are inconsistent, making it difficult to draw conclusions, although the data obtained does not suggest any meaningful improvement in performance. On the other hand, CG10, the 42:37 HEU:GIS composite, showed a drastic increase in the rate of strontium uptake, when compared to both its parent material, Z-HEU, and Mud Hills clinoptilolite, particularly in the initial and middle portions of the experiment. This is reflected in higher α_{50} and α_{300} values (0.95 vs 0.74 and 0.53 and 0.42 vs 0.25 and 0.26 for CG10 vs Z-HEU and Mud Hills clinoptilolite, respectively). This is likely to originate from both the enhanced strontium capacity, revealed through adsorption isotherms (4.2.4), and the increased surface area and porosity, as observed in SEM (4.2.7) and XCT images (4.2.7). This facilitates easier access of ions to surface sorption sites, which is more likely to be significant for the larger hydrated strontium ion when compared to caesium.

In equivalent experiments outlined in Chapter 3, more transformed mordenite-zeolite P composites were shown to be more proficient in both caesium and strontium exchange. In these experiments, the slightly transformed clinoptilolite-zeolite P composite, CG8, displayed slower uptake than the parent clinoptilolite. It is possible that this indicates a disparity in performance between desilicated mordenites and clinoptilolite parents. Further trials would be required to confirm this.

Overall, these RIX results suggest CG10, which was formed in a 0.40M NaOH solution with an approximate 42:37 HEU:GIS ratio, is an excellent ion-exchange material for the removal of caesium and strontium in these conditions. A significant improvement in the rate of uptake of both radionuclides was observed in comparison to the parent clinoptilolite, Z-HEU, and industry used Mud Hills clinoptilolite.

4.3 Conclusion

Natural zeolites are ideal candidates for industrial ion-exchange materials as they are incredibly affordable and are readily available in granular, deployment-ready morphologies. However, due to the limited number of framework topologies abundant enough to be widely utilised, there is an overreliance on particular natural sources, with restricted routes to tailor functionality. In Chapter 3, the ion-exchange properties of a natural mordenite (MOR) were enhanced through means of a partial interzeolite transformation to zeolite P, outlining a simple methodology to diversify natural zeolite sources. Work in this chapter explored the applicability of this method to the most abundant natural zeolite: clinoptilolite, of which three natural analogues were investigated.

The use of sodium hydroxide concentrations < 0.5 M were effective at reducing the rate of parent clinoptilolite dissolution, thus allowing the straightforward formation of clinoptilolite:zeolite P composite materials. In comparison to Chapter 3, less caustic solutions facilitated full transformation to zeolite P, potentially indicating that the clinoptilolite structure is less resistant to hydrolysis in comparison to mordenite, an observation consistent with literature[213]. This accelerates the rate-determining dissolution stage of the transformation, resulting in more complete transformations from equal molarity solutions. As observed with a natural mordenite (3.2.2.1), a high degree of control over the ratios of phases is demonstrated. Given the contrasting ion-exchange properties of clinoptilolite and zeolite P, this provides a possible route to tune a material to a given waste stream. In batch scoping experiments (4.2.3), a small increase in the strontium uptake was observed as composites contained more zeolite P. The increase was less than that observed the mordenite systems, potentially indicating these treatments may not be as effective on clinoptilolites, due to their innate proficiency in adsorbing strontium. As observed in Chapter 3, composites with large quantities of zeolite P exhibited poor caesium uptake in the presence of excess potassium (4.2.3).

Adsorption isotherms were utilised to determine how caesium and strontium capacity varied in both partially and fully converted materials (4.2.4). Caesium capacity increased by 52 % upon 57 %

conversion, with complete transformation increasing caesium capacity by 64 %. The change in strontium capacity was far more significant; increases of 190 and 380 % were observed from partial and full transformations, respectively. Additionally, kinetic studies (4.2.5.2) suggest strontium equilibrium is attained in significantly shorter timeframes for both partially and fully converted materials, in comparison to the parent clinoptilolite, Z-HEU. Therefore, the materials generated in this chapter possess a higher capacity for strontium and reach equilibrium faster than the parent clinoptilolite. This translates to significantly more adsorption events in a given timeframe, which would lead to more effective removal when deployed in a column system. Furthermore, increases in caesium capacity and rate were also observed (4.2.4.1, 4.2.5.1) in partially and fully converted materials when compared to the parent clinoptilolite.

As achieved in Chapter 3, granular composite zeolites were developed using an identical methodology to powdered composites, with similar levels of control over the ratios of phases (4.2.6). A combination of SEM, XCT and local, image-guided micro-diffraction experiments showed composite materials to possess a shell comprised of polycrystalline zeolite P moieties, in addition to 'veins' of zeolite P. This suggests dissolution does not occur evenly around the surface of the granule and is instead preferred at certain sites on the surface. It is unclear whether the origin of this is geological or related to the composition of the material. Overall, however, the dissolution-recrystallisation mechanism discussed in Chapter 3 persists, although the targeted dissolution produces a core-shell composite with a network of zeolite P 'veins'. RIX experiments show that a composite with a clinoptilolite: zeolite P ratio of 42:37 outperform both the parent clinoptilolite, Z-HEU and Mud Hills clinoptilolite in flow experiments with industrially relevant simulant liquor.

Overall, results discussed in this chapter confirm clinoptilolites as materials capable of enhancement by partial interzeolite transformation to zeolite P. This provides a route of property diversification which could prove useful in decontamination of nuclear wastewaters, in addition to other applications, such as water purification, multi-gas adsorption[207, 208], multi-molecular separation[209] and multi-process catalysts[210]. As clinoptilolites are so abundant[56, 57], a plethora of ion-exchange materials can be generated from a wealth of existing natural sources. A summary of key findings from this chapter are displayed in Table 4.9.

Table 4.9. Summary of key findings from this chapter.

Section	Key findings
Generation of powder composites (4.2.2)	▪ A lower (< 0.50 M) NaOH concentration facilitates composite formation. ▪ Concurrent clinoptilolite desilication is observed during transformation. ▪ Ratios of phases can readily be controlled though manipulation of NaOH concentration. ▪ Observations were consistent across three parent clinoptilolites.
Batch ion-exchange scoping (4.2.3)	▪ Ratio of zeolitic phases has some effect on the uptake of caesium and strontium. ▪ Improvements in strontium uptake were more drastic in parent clinoptilolites that exhibited lower strontium uptake levels.
Equilibrium adsorption studies (4.2.4)	▪ Small increase in caesium capacity upon transformation. ▪ Drastic increase in strontium capacity upon transformation.
Kinetic studies (4.2.5)	▪ Strontium equilibrium reached much faster upon transformation.

	▪ Caesium equilibrium reached slightly faster upon transformation.
Formation of granular composites (4.2.6)	▪ Granular analogues can be formed with control over ratios of both zeolite phases.
SEM, XCT and local diffraction studies (4.2.7)	▪ Granular composite materials possess a zeolite P shell, with additional zeolite P veins penetrating the structure. Domains of intact clinoptilolite remain in the core.
Rapid Ion Exchange experiments (4.2.8)	▪ Composite material with 42:37 clinoptilolite: zeolite P phase ratio is superior to both Mud Hills clinoptilolite and parent clinoptilolite for sequestration of caesium/strontium solutions.

CHAPTER 5: INVESTIGATING THE PECULIARITY OF MUD HILLS CLINOPTILOLITE

5.1 Introduction

Clinoptilolites are the most geologically abundant zeolite worldwide, found on every continent[57]. Due to their low cost and versatile sorption properties, clinoptilolites are utilised across a wide range of applications (for more information on such applications and structure please refer to section 1.2). However, one drawback of using natural materials is that there can be significant geological variation. For example, the purity, crystallinity, and elemental composition can vary significantly between samples, even when sourced from identical sites[70, 196]. This adds complication in characterising the material and can result in stark variations in performance. A striking example of this is Mud Hills clinoptilolite, which exhibits a superior ability to abate strontium from nuclear effluent, in comparison to other clinoptilolites[211]. This has led to its deployment at the SIXEP plant, Sellafield, where it remediates 100's m^3 of contaminated effluent per day (1.1.3)[20, 70]. Whilst this superior ability to sorb strontium has been of great benefit to the nuclear industry, its origins are unknown. To add further complications, material used in SIXEP was extracted across approximately 4 square kilometres of a region where significant geological variations, such as identity and concentration of impurities, are observed[70, 196]. Nonetheless, an explanation for this superiority would be greatly beneficial to the nuclear industry, assisting in streamlining the sourcing of future ion-exchange materials which are a necessity to meet future decommissioning requirements, as the current stock of Mud Hills is forecast to deplete in the mid 2030's.

Possible rationale for the superiority of Mud Hills clinoptilolite, in comparison to other clinoptilolites, includes: a higher zeolitic content, less strongly bound counter ions, a more favourable aluminium distribution, or macroscopic structural properties, such as enhanced macroporosity. In this chapter, the properties of three lower performing clinoptilolites, in addition to the variety sourced from Mud

Hills, are examined to investigate these rationale. Crystallinity and impurities are assessed through analysis of PXRD data; XRF and SEM-EDS are employed for elemental analysis. Both ^{29}Si and ^{27}Al NMR reveal element-specific chemical environments and XPDF studies provide local structural information. Further, cation capacities for both caesium and strontium are determined through adsorption isotherms and the rate of uptake assessed through kinetic isotherms. Lastly, some peculiar hydrothermal transformation behaviour that has been observed as part of the wider scope of this project is explored. This chapter will assess the properties of the four clinoptilolites in attempt to suggest rationales for the superior performance of Mud Hills clinoptilolite.

5.2 Results and Discussion

5.2.1 PXRD Analysis

The four clinoptilolites of interest are all naturally sourced so may be comprised of multiple crystalline, and indeed amorphous, phases. Such phase variety is dependent on local geological conditions. To understand any disparities in performance it is crucial to have knowledge of such phases as they can impose their own effects, for example in ion-exchange applications. Expectedly, the most abundant phase observed in all four materials was clinoptilolite, which made up between 67 and 72 Wt. % of the samples. A diverse range of impurity phases, and differing crystallinities, were also determined. A breakdown of all four materials is hereby discussed in turn.

5.2.1.1 MH-HEU

The PXRD pattern of MH-HEU and subsequent Rietveld fit are presented in Figure 5.1. The fit to the data is satisfactory, although limitations in diffraction data quality, combined with the presence of amorphous content and likely presence of unidentified trace impurities means a significantly high coefficient of determination (wR = 8.48 %) is obtained. Reflections attributed to clinoptilolite (67 %), mordenite (10 %) and quartz (4 %) were observed in the diffraction data of Mud Hills clinoptilolite, in addition to the added standard, corundum (Figure 5.1). An amorphous content of 19 % was also determined though quantitative analysis of the corundum reflection intensities. These values are summarised in Table 5.2. Significantly less clinoptilolite is observed compared to that reported by Dyer[70] (95 %) and Palmer[219] (100%), even when the lack of crystallinity determinations are considered. Regrettably, there is no published diffraction data available for comparison. However, the variation is consistent with the geological survey by Sheppard[196], although this work reported clinoptilolite concentrations between 0 and 100% within the Mud Hills' locality. Furthermore, the considerable variations in performance of SIXEP clinoptilolite obtained from various boreholes supports the premise of significant variation between local samples[70]. No chemical analysis of these samples was undertaken and the disparities were attributed to change in framework Si/Al ratios, which were not evaluated[70].

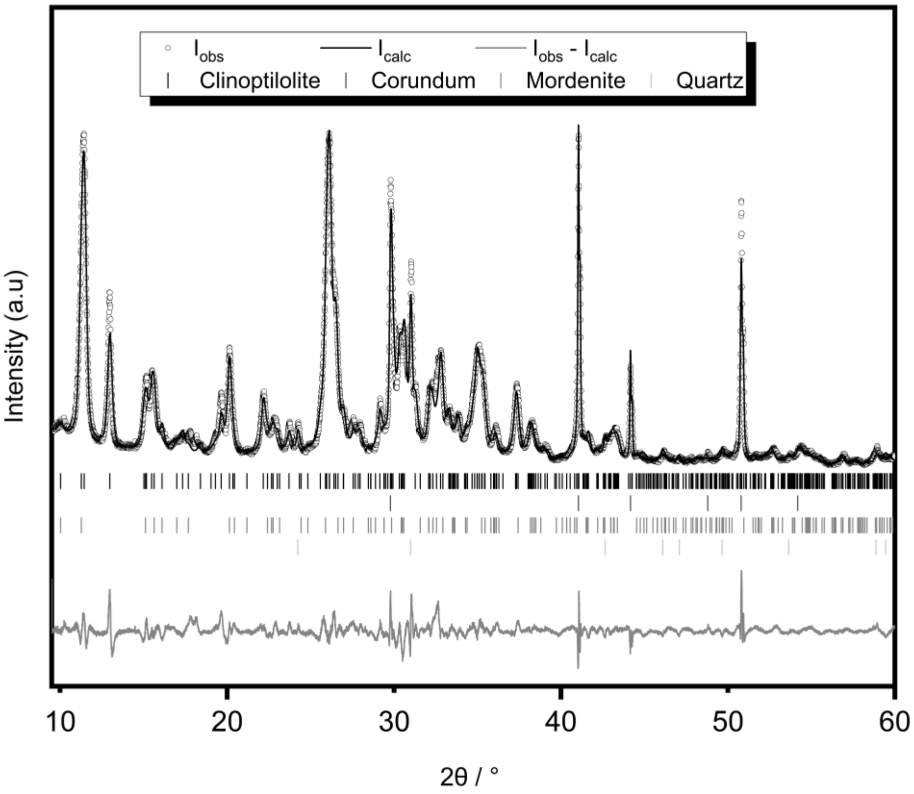

Figure 5.1. Rietveld refinement of the clinoptilolite structure against PXRD data for MH-HEU with added corundum standard (λ = 1.7926 Å).

Table 5.1. Estimated weight fractions of detected phases in MH-HEU (including added corundum standard). Adjusted weight fractions derived from the calculated corundum weight fraction are also reported. Reported uncertainties from GSAS-ii are consistently <1%.

Phase	Weight % (refinement)	Weight % (adjusted)
Clinoptilolite	66	67
Corundum	20	-
Mordenite	10	10
Quartz	4	4
Volcanic glass	-	19

After clinoptilolite, mordenite is the second most abundant natural zeolite. The two are commonly found together in nature[76, 80, 149, 152, 196, 220], including in the Barstow formation where Mud Hills clinoptilolite is mined[196]. In this analysis, the material was comprised of 10 wt. % mordenite, which is higher than average for the Barstow formation[196]. However, up to 20 wt. % has been reported locally[196]. As previously discussed in section 1.2.4, the zeolitic structure of mordenite renders it an excellent ion-exchange material for adsorption of radionuclides: work in section 3.2.4 found capacities of 164 and 54 mg g^{-1} for caesium and strontium, respectively, for an impure natural mordenite. A widely accepted rational for this performance is the large, 12-ring channels which facilitate rapid internal diffusion of cations[34]. Considering this information, the potential presence of mordenite could be a significant contributing factor to the unexpectedly superior performance of Mud Hills clinoptilolite when utilised for remediation of aqueous nuclear decommissioning waste. Another impurity phase detected was quartz (SiO_2), the densest form of silica routinely observed in tuffs. Significant quantities of quartz have been reported at the Mud Hills site, varying between 0 and 80 %[196]. The dense structure has no open internal space, so no ion-exchange is possible, although surface adsorption can still occur[189, 190]. Quantitative analysis of the added corundum reflections divulges an approximate 19 Wt. % amorphous content within the material. This is consistent with geological data of the region, where up to 90 Wt. % amorphous content is observed locally[196]. As conventional diffraction studies are ineffective at studying disordered solids, characterisation is difficult. However, amorphous material can be effective in ion-exchange applications[221-223], so its presence in Mud Hills clinoptilolite could be impactful.

This analysis somewhat reflects the problems in the characterisation of natural minerals: each sample has the potential to contain a multitude of difference crystalline and non-crystalline phases, which themselves can possess more subtle changes (e.g., elemental composition). Mica, gympsum, dolomite, feldspars, barite, magnetite, montmillerite and illite are all reported to be present in SIXEP clinoptilolite[70], but none are detected here. Another study only observed reflections attributed to clinoptilolite[219]; regrettably, no diffraction data has been reported for comparison.

5.2.1.2 Z-HEU

The PXRD pattern of Z-HEU and subsequent Rietveld fit are presented in Figure 5.2. The Rietveld fit to the data is satisfactory, although limitations in diffraction data quality, combined with amorphous content and likely presence of trace or hidden impurities, means a high weighted R-factor (*wR* = 9.56 %) is obtained. Reflections attributed to clinoptilolite (67 %), feldspar (13 %) and cristobalite (12%) were observed in the diffraction data of Z-HEU, in addition to the added standard corundum (Table 5.2). An amorphous content of 8 Wt. % was also calculated. Supplier documentation suggests a purity of 80 - 85 % clinoptilolite with smaller quantities of opaline, cristobalite and feldspar also observed[178]. Whilst the identified phases in this work are consistent with the supplier information, the relative quantity of clinoptilolite is significantly lower. As weight fractions of the impurities are not included, it cannot be commented on what secondary phases this work has observed in greater abundances; regrettably, no diffraction data was provided by the supplier for comparison.

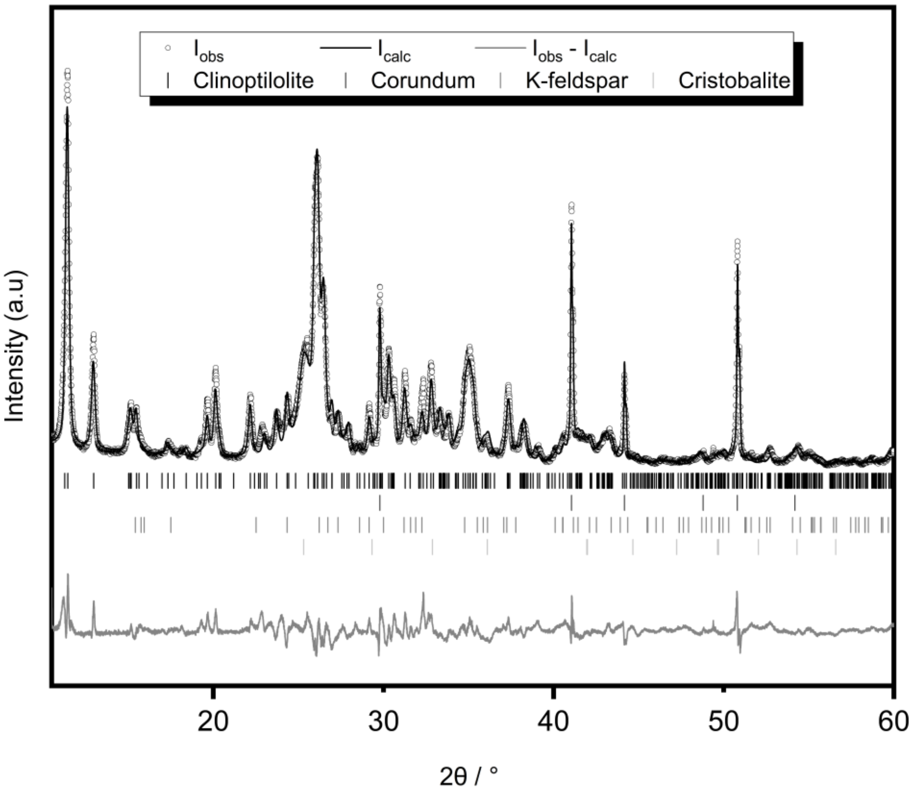

Figure 5.2. PXRD data and subsequent Rietveld refinement of Z-HEU with corundum standard (λ = 1.7926 Å).

Table 5.2. Estimated weight fractions of detected phases in Z-HEU (including added corundum standard). Adjusted weight fractions derived from the calculated corundum weight fraction are also reported. Reported uncertainties from GSAS-ii are consistently > 1%.

Phase	Weight % (refinement)	Weight % (adjusted)
Clinoptilolite	60	67
Corundum	18	-
Feldspar	12	13
Cristobalite	11	12
Volcanic glass	-	8

The presence of feldspars in any natural zeolitic material is unsurprising as they comprise over 50% of Earth's crust and can found across igneous, metamorphic and sedimentary rocks[224]. They possess a general formula $X(Al,Si)_4O_8$, where X is typically Na, K or Ca. An assortment of feldspar minerals are widespread with different cationic ratios giving various crystal structures, which are generally distinguishable though conventional diffraction experiments[224]. As cations reside in a fixed, closed system, felspars are not well suited to ion-exchange. However, surface adsorption processes are likely to still occur[225]. Another impurity detected in Z-HEU is cristobalite, a tetragonal polymorph of silica, SiO_2. The lack of structural cations to participate in ion-exchange processes limit adsorption to the surface, where the material adsorbs even less than quartz[190]. An amorphous content of 8% was determined through analysis of the added corundum peak intensities. As with Mud Hills clinoptilolite, the local structure of the amorphous content is difficult to determine; as such its usefulness as an ion-exchange material could vary significantly. One possible identification is opal, a hydrated amorphous form of silica, as suggested by the supplier[178]. If true, this would limit any adsorption potential to the surface[226, 227].

5.2.1.3 N-HEU

Reflections attributed to clinoptilolite (72 %), feldspar (25 %), quartz (2 %) and mica (<1 %), in addition to the added corundum, are observed in the diffraction data of N-HEU (Figure 5.3). The Rietveld fit to the data is satisfactory (wR = 9.61 %), despite the presence of an unidentified peak at ~32° 2θ and limited quality of the diffraction data. The weight % of corundum determined from the refinement was equal to the calculated value, suggesting that negligible quantities of amorphous content are present in N-HEU. As previously discussed (5.2.1.1, 5.2.1.2), the presence of feldspar and quartz are unlikely to have any significant effect on the ion-exchange characteristics of the material. Mica's consist of aluminosilicate layers with interstitial, exchangeable cations[228, 229]; while this could impact the ion-exchange properties of the material, the low quantity (<1 %) likely renders its presence insignificant. Unfortunately, a material data sheet could not be sourced for comparison.

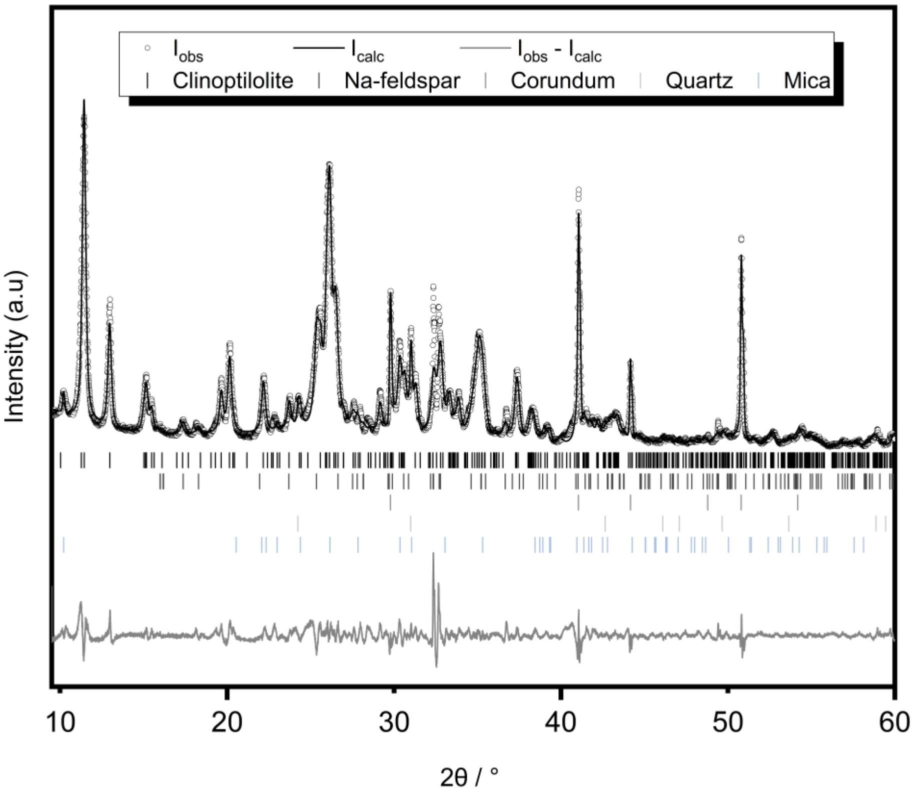

Figure 5.3. PXRD data and subsequent Rietveld refinement of N-HEU with corundum standard (λ = 1.7926 Å).

Table 5.3. Estimated weight fractions of detected phases in N-HEU (including added corundum standard). Adjusted weight fractions derived from the calculated corundum weight fraction are also reported. Reported uncertainties from GSAS-ii are consistently > 1%.

Phase	Weight % (refinement)	Weight % (adjusted)
Clinoptilolite	60	72
Feldspar	21	25
Corundum	17	-
Quartz	2	2
Mica	<1	<1
Volcanic glass	-	0

5.2.1.4 S-HEU

Slovakian sourced S-HEU produces a very comparable diffraction pattern to N-HEU: reflections attributed to clinoptilolite (67 %), feldspar (29 %), quartz (4 %) and mica (<1 %) are again observed, in addition to reflections from the added corundum (Figure 5.4). The Rietveld fit to the diffraction data is satisfactory (*wR* = 8.91 %), although, similarly to N-HEU, an unidentified peak at ~32° 2θ is present. Matching phases are reported in the material data sheet, although the supplier suggests a higher clinoptilolite content (~90 %) and less feldspar (<10 %)[179]. Akin to N-HEU, no evidence for amorphous content was observed.

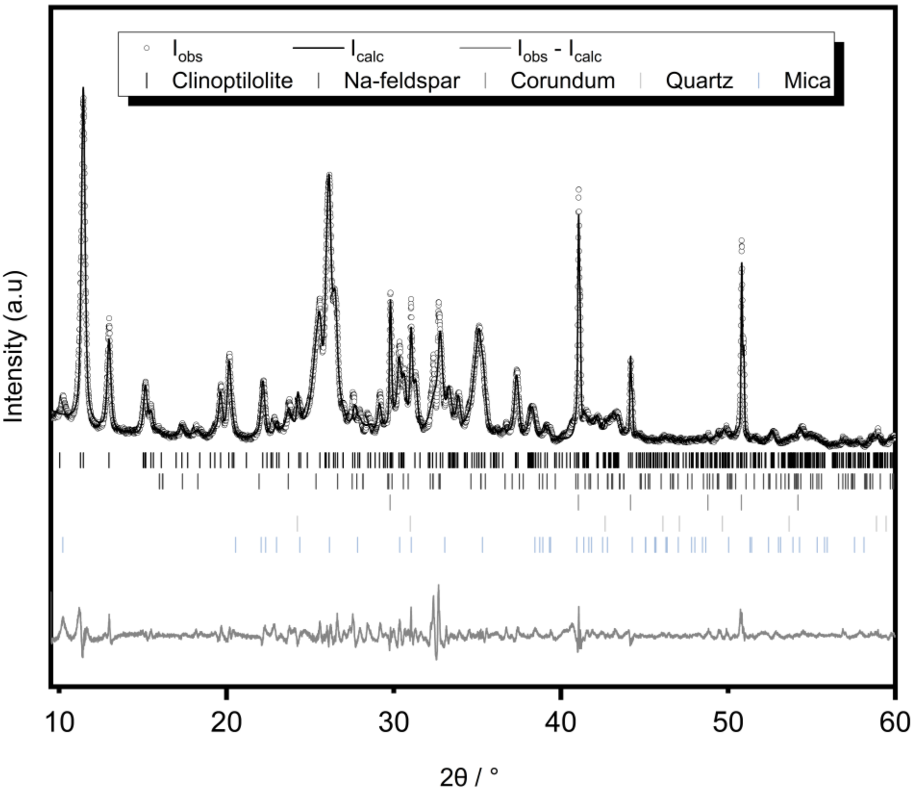

Figure 5.4. PXRD data and subsequent Rietveld refinement of S-HEU with corundum standard (λ = 1.7926 Å).

Table 5.4. Estimated weight fractions of detected phases in S-HEU (including added corundum standard). Adjusted weight fractions derived from the calculated corundum weight fraction are also reported. Reported uncertainties from GSAS-ii are consistently > 1%.

Phase	Weight % (refinement)	Weight % (adjusted)
Clinoptilolite	55	67
Feldspar	24	29
Corundum	18	-
Quartz	3	4
Mica	<1	<1
Volcanic glass	-	0

5.2.1.5 PXRD Summary

Despite the complex composition and natural variation exhibited, impurity phases and glass content have been identified for all four clinoptilolites. Compositions were generally qualitatively consistent to reported values: identical impurities were observed Z-HEU and S-HEU, although quantities varied. Available literature which contains analysis of Mud Hills clinoptilolite, however, is inconsistent and shows little concordance to this work[70, 196, 219]; it is unclear whether these disparities are a product of varied analysis techniques or geological sample variation. An outline of the phases comprising the four clinoptilolites is presented in Table 5.5. The adsorption capabilities of quartz, feldspar and cristobalite are limited to the surface and are therefore unlikely to have a significant impact on the overall ion-exchange properties[189, 190, 225].

Furthermore, the ~10 Wt. % mordenite content in Mud Hills clinoptilolite could be significant; mordenite is an excellent ion-exchange material and the presence of two, potentially complementary zeolites could be beneficial (as demonstrated in Chapters 3 and 4). It has been suggested that the large, 12-ring mordenite channels can facilitate rapid exchange by functioning as a 'molecular motorway' and accelerating internal cation diffusion[34]. This could be especially significant when deployed in fixed-bed columns, where the kinetics of exchange are critical. The absence of long-range order renders amorphous content difficult to study by means of conventional diffraction experiments, even when isolated. It is therefore impossible to comment on the potential functionality of any amorphous content from this data, although local environments can possess useful ion-exchange characteristics[221-223].

Table 5.5. Summary of clinoptilolite compositions, as determined though Rietveld refinement.

	Weight fraction / %						
Material	**Clinoptilolite**	**Mordenite**	**Quartz**	**Feldspar**	**Cristobalite**	**Mica**	**Glass**
MH-HEU	67	10	4	-	-	-	18
Z-HEU	67	-	-	13	12	-	8
N-HEU	72	-	2	25	-	<1	-
S-HEU	67	-	4	29	-	<1	-

Overall, these results indicate that Mud Hills clinoptilolite is comprised of a greater proportion of beneficial materials: 77 – 95 %, dependent on the local environments in the amorphous content, in comparison to 67 - 75, 73 and 68 % for Z-, N- and S-HEU, respectively. This is likely to be a contributing factor in the improved ion-exchange properties of Mud Hills clinoptilolite and will be considered when discussing other, complementary techniques in future sections of this chapter.

5.2.2 Hydrothermal Breakdown of Clinoptilolites in Acidic Media

Clinoptilolite and mordenite produce complex diffraction patterns with many overlapping peaks. It can therefore be difficult to confirm the presence of small quantities of mordenite in clinoptilolite tuffs, particularly in the presence of other impurities and amorphous material. Hydrothermal acidic treatment (6M HCl) helps in discriminating between these phases; the clinoptilolite structure is mostly decomposed whereas mordenite reflections persist[213]. The resultant diffraction pattern of treated Mud Hills clinoptilolite is displayed in Figure 5.5.

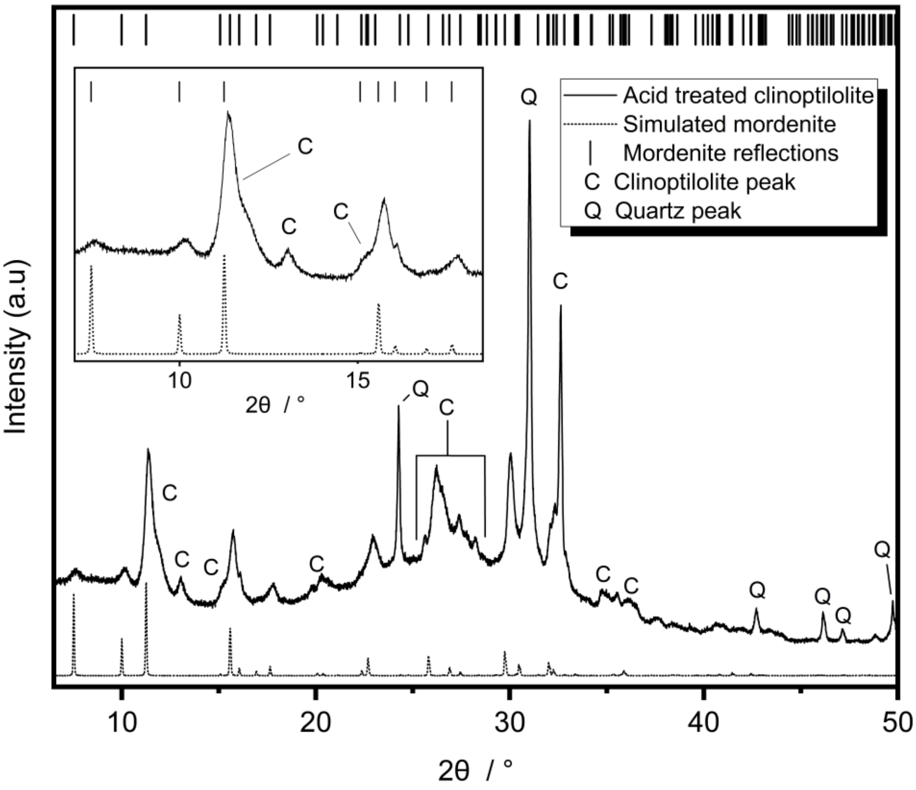

Figure 5.5. PXRD pattern of acid-treated MH-HEU (λ = 1.7926 Å).

As reported by Sudo[213], the intensity of clinoptilolite reflections diminished due to breakdown of the zeolitic framework in acidic media. Reflections attributed to mordenite framework are more clearly observed, particularly at low angle (see Figure 5.5 inset); this reaffirms the suspected presence of mordenite from section 5.2.1. Expectantly, the quartz impurity showed excellent resistance to the acidic treatment. After equivalent hydrothermal treatments, Z-, N- and S-HEU produced diffraction patterns which did not contain mordenite reflections, indicating that that mordenite impurity is specific to Mud Hills clinoptilolite (A.15).

5.2.3 Elemental Analysis

The elemental composition of zeolitic structures plays a crucial role in steering their functionality. Namely, the framework aluminium content, typically reported as a Si/Al ratio, and cation content are important characteristics, which could aid in explaining Mud Hills clinoptilolite’s enhanced affinity for strontium.

5.2.3.1 Si/Al Ratio

The most significant elemental factor is the framework Si/Al ratio, which determines the cationic content of the zeolite framework. When considering ion-exchange materials, the fine tuning of the Si/Al ratio can also dictate affinity towards a particular species, as more aluminous, charge dense frameworks will exert a greater electrostatic attraction to cations with higher charge densities[34]. In the context of clinoptilolites for the sorption of caesium and strontium, a lower Si/Al would be expected to display a greater affinity for divalent strontium cations, as the more aluminous framework would exhibit a greater electrostatic attraction on the charge-dense divalent strontium species, in addition to possessing a greater density of aluminium pairs[34]. Therefore, a more aluminous framework for Mud Hills clinoptilolite would provide excellent rationale for its enhanced ability to adsorb strontium. Si/Al ratios for the studied clinoptilolites, determined through two experimental methods, are displayed in Table 5.6.

Table 5.6. Si/Al ratio of studied clinoptilolites as determined through XRF and SEM-EDS.

Material	XRF	EDS
MH-HEU	4.9(1)	4.85(4)
Z-HEU	4.7(1)	4.72(8)
N-HEU	5.0(1)	5.01(9)
S-HEU	5.0(1)	4.95(5)

The data suggests that MH-HEU has an overall Si/Al ratio of approximately 4.9; this is concordant with literature, where a value of 5.0 is proposed[70]. Values of 4.7, 5.0 and 5.0 are observed for Z-, N- and S-HEU, respectively. This suggests that Mud Hills clinoptilolite is no more aluminous than the other materials and, in fact, Z-HEU actually possesses the greatest aluminium content (although this observation is inconsistent with the material data sheet, which suggests a Si/Al ratio of approximately 5.2)[178].

However, the values reported are representative of the bulk sample, as opposed to the clinoptilolite framework itself. Silica-based impurities (quartz, cristobalite) will artificially inflate the Si/Al ratio, whereas aluminous moieties, such as feldspars, will decrease the Si/Al ratio. Consequently, the actual framework Si/Al ratios of N- and S-HEU will be higher than reported due to large quantities of feldspars. Due to the unknown composition of the amorphous content in MH-HEU and Z-HEU, it is difficult to draw conclusions on the framework Si/Al ratios in these materials.

5.2.3.2 Cation Content and Exchangeable Species

Further factors which influence functionality are the cation content and to what extent these are mobile. Elementally, zeolite frameworks are comprised of silicon, oxygen and aluminium. Other elements present include cationic species, which fill pores inside the anionic framework, and extra-framework species, such as iron. Different pore cations are displaced by incoming species with varied favourabilities dependent on cationic geometry and charge distribution (of both species), in addition to the zeolite site accessibility and local environment[219]. These factors determine the selectivity series for a given material, which are experimentally derived. A clinoptilolite selectivity series is reported as follows: Cs > K > Sr > Ca > Mg > Na, where caesium is the most preferred species to sorb and sodium the most readily expelled[211].

Additionally, divalent species require two aluminium sites within locality, otherwise referred to as an aluminium pair, to adhere. The presence of divalent species within the zeolite could indicate an aluminium distribution with increased pairing, which could lead to strontium-favouring systems. Alternatively, it could merely be a result of available cations in the given geological synthesis conditions or even due to post-synthetic geological ion-exchange. The elemental composition of the four clinoptilolites, excluding silicon, aluminium, and oxygen, is presented in Table 5.7.

Table 5.7. Cationic content of the four clinoptilolites as obtained from EDS measurements (reported as a proportion of aluminium concentration).

Cation (X)	X/Al			
	MH-HEU	**Z-HEU**	**N-HEU**	**S-HEU**
Sodium	0.37(2)	0.22(2)	0.06(4)	0.03(1)
Potassium	0.15(1)	0.29(2)	0.29(2)	0.30(2)
Magnesium	0.07(1)	0.08(2)	0.07(1)	0.07(2)
Calcium	0.15(2)	0.09(1)	0.20(2)	0.20(2)
Iron	0.07(2)	0.07(1)	0.10(1)	0.10(2)

Identical species are observed across the materials: sodium, potassium, calcium, magnesium and iron, which is generally located either in the framework (Fe^{3+}) or in extraframework octahedral sites as $[Fe(H_2O)_6]^{3+}$ or Fe^{2+} [194]. Interestingly, MH-HEU and Z-HEU contained similar quantities of divalent species (20 – 30 %), but significantly less than N-HEU and S-HEU (35 - 40 %), contradicting a hypothesis that the origin of the excellent Sr uptake in Mud Hills clinoptilolite is because this material contains more divalent species due to the inclusion of more aluminium pairs.

Considering monovalent species, Mud Hills clinoptilolite possesses the significantly highest sodium content (46 %), followed by Z-HEU (29 %), with N-HEU and S-HEU having a comparatively low sodium content (5 – 10 %). Sodium is the most thermodynamically and kinetically exchangeable species observed and therefore could enhance the exchange performance of Mud Hills clinoptilolite. In industrial systems, sodium is routinely exchanged into the material for this reason[70, 230].

Compared to the other clinoptilolites, MH-HEU also contains approximately half the potassium, which, after caesium, is the most strongly bound species to clinoptilolite and can impede ion-exchange[230]. To investigate, sodium-washing (1M NaCl, 24h) and subsequent elemental analysis was conducted. The cation concentrations before and after exchange with sodium are presented in Figure 5.6.

In these experiments, the percentage of a particular species exchanged for sodium (M_{ex}) can be determined. These data highlight the ease to which a given cation is released from the framework, which could provide rationale for Mud Hills' superiority. The proportion of potassium, magnesium and calcium released from the framework for each clinoptilolite is presented in Table 5.8. Additionally, the Na/ Al ratio of the material after sodium washing is displayed.

(a) MH-HEU

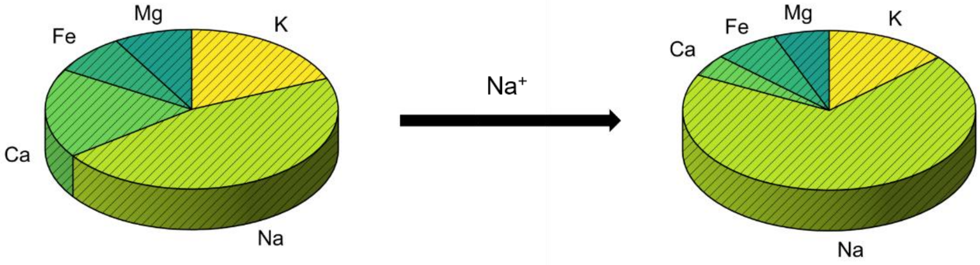

(b) Z-HEU

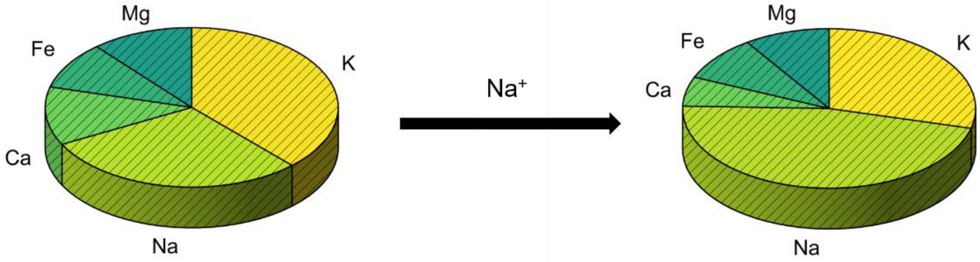

(c) N-HEU

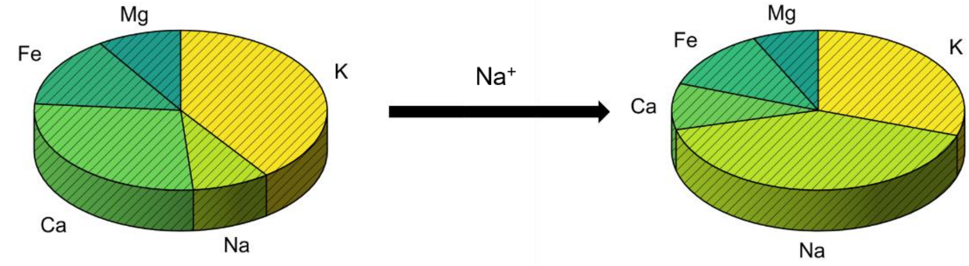

(d) S-HEU

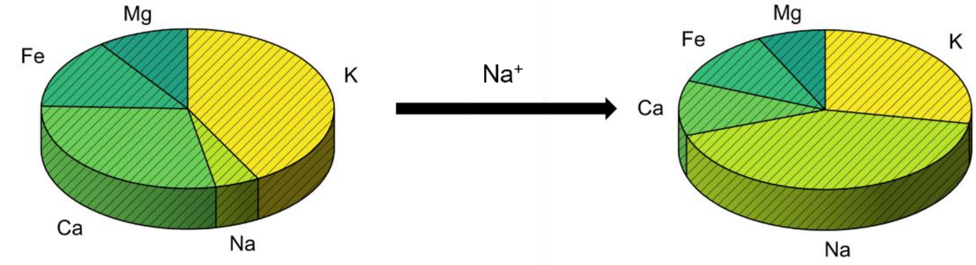

Figure 5.6. Cation compositions of the raw clinoptilolites both before and after treatment with sodium (1M NaOH, 24h).

Table 5.8. Percentage of each cationic species expelled by sodium *via* a 1M NaCl washing for each clinoptilolite.

Material	K_{ex} / %	Mg_{ex} / %	Ca_{ex} / %	Resultant Na/ Al
MH-HEU	15	16	71	0.67
Z-HEU	16	8	45	0.38
N-HEU	10	7	60	0.37
S-HEU	20	9	52	0.38

Mud Hills clinoptilolite expels comparable quantities of potassium to Z-HEU and is intermediate in the disparity between N- and S-HEU. Conversely, the material exhibited significantly higher levels of both magnesium and calcium expulsion; these enhanced removal rates of divalent species, combined with the greatest sodium content in the raw form result in a Na/Al ratio of 0.67 in the washed sample, markedly higher than Z-, N- and S-HEU which only reached Na/Al ratios of 0.38, 0.37 and 0.38, respectively. Therefore, the 'availability' of the cations present within the zeolitic framework of Mud Hills clinoptilolite could be responsible for the improved ion-exchange performance. The exchange of divalent species is slow due to the requirement to shed/gain a large hydration shell; the improved expulsion of calcium and magnesium in these treatments could be a result of increased kinetics, as opposed to cation selectivity. The quantity of iron in the materials remained constant during the sodium washing; this is consistent with the assumption that iron is present as either in the framework or in octahedral sites, as opposed to an exchangeable cation[194]. The calculated quantities of this framework iron for each clinoptilolite are presented in Table 5.8 - MH-HEU contains the least iron (0.9%) followed by Z-HEU (1.0 %). N- and S-HEU are found to contain greater quantities of iron (~1.4 %). In all cases these quantities are small.

Table 5.8. Calculated iron contents from SEM-EDS measurements.

Material	Iron content / Wt. %
MH-HEU	0.90(6)
Z-HEU	0.98(7)
N-HEU	1.43(5)
S-HEU	1.43(8)

5.2.4 Imaging

5.2.4.1 Scanning Electron Microscopy

Scanning electron microscopy (SEM) images of the four clinoptilolites are displayed in Figure 5.7. MH-HEU and Z-HEU are imaged as granules, whereas N- and S-HEU are imaged as the fine powders they were received as.

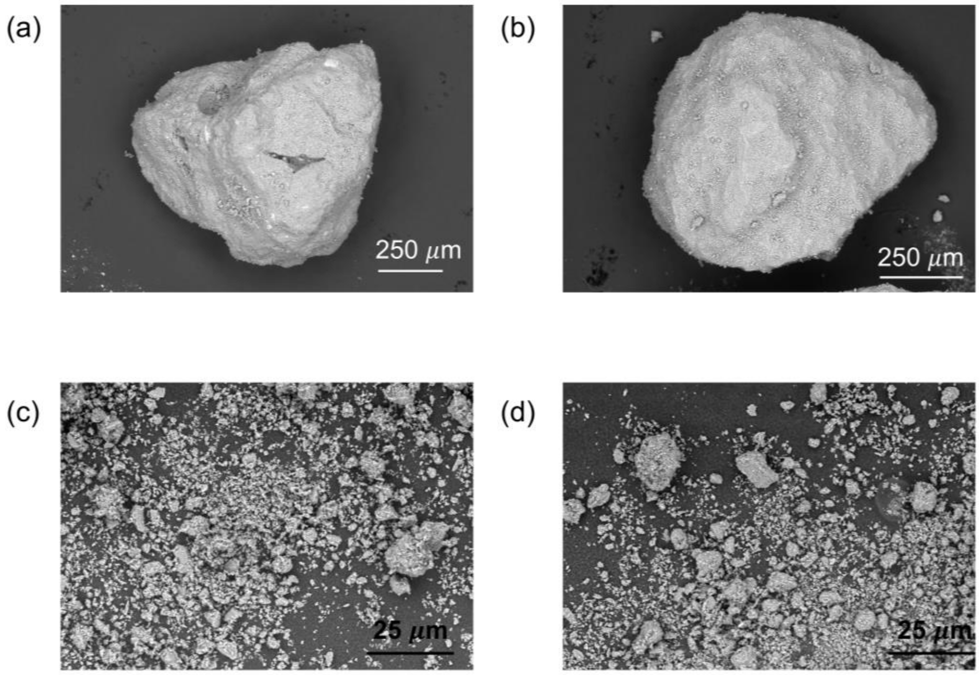

Figure 5.7. SEM images of the studied clinoptilolites: (a) MH-HEU, (b) Z-HEU, (c) N-HEU and (d) S-HEU. MH- and Z-HEU are 400 – 600 μm granules whereas N- and S-HEU are fine powders.

The exterior of the granular materials, MH-HEU and Z-HEU, are very similar and somewhat featureless; there is no obvious increase in surface area or mesoporosity between the materials, which could rationalise the ion-exchange properties of Mud Hills clinoptilolite. Images of N- and S-HEU are also similar, with a wide variety of particle sizes observed and many small (<5 μm) granules. This is typical of a fine powder of a natural zeolite.

5.2.4.2 X-ray Computed Tomography

X-ray computed tomography (XCT) imaging allows for the internal morphology of granular materials to be assessed. As N- and S-HEU are in powder form, they are excluded from this analysis. Two reconstructed cross-sectional images obtained from a granule of MH-HEU are presented in Figure 5.8. A clear lack of homogeneity is present within MH-HEU, with clusters possessing lighter and darker contrast distributed throughout. As image contrast is proportional to electron density, it can be assumed that these domains represent non-clinoptilolite phases such as quartz or amorphous material not observed though conventional diffraction experiments. It is unclear whether mordenite would appear visibly different to clinoptilolite, as they have somewhat comparable framework densities (17.5 (HEU) and 17.0 (MOR) T / 1000 Å^3).

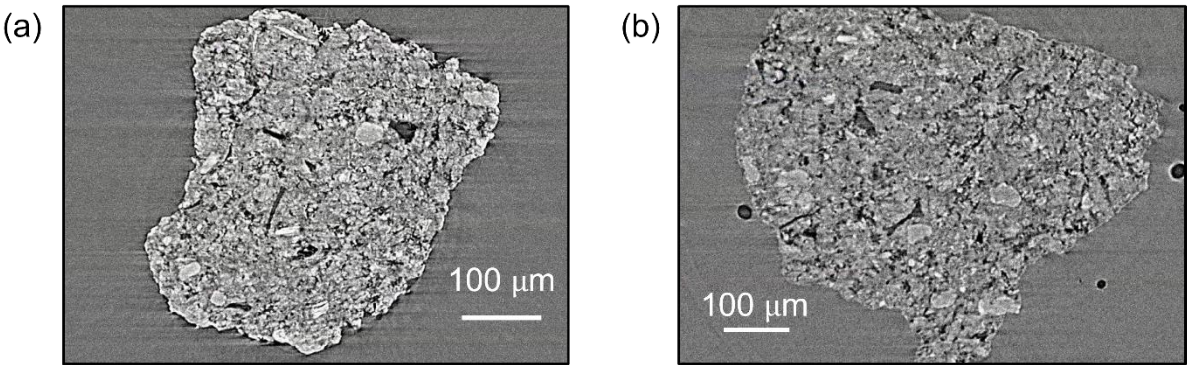

Figure 5.8. XCT cross-sectional images of a MH-HEU granule.

Equivalent images of Z-HEU granules are displayed in Figure 5.9. The interior is comparatively featureless, with no large regions with contrast different to the bulk - this suggests a more homogeneous interior morphology, where impurity phases are either so well distributed within the bulk or merely not present in the imaging presented. Overall, the significant differences in the internal macrostructure observed could be significant in rationalising Mud Hills clinoptilolites unusual proficiency in the remediation of aqueous nuclear decommissioning waste. MH-HEU qualitatively seems to possess a greater ‘internal surface area’, which could result faster internal macro-diffusion of aqueous solutions and enhanced uptake. The imaging of further clinoptilolite granules from other sources is required to further investigate this.

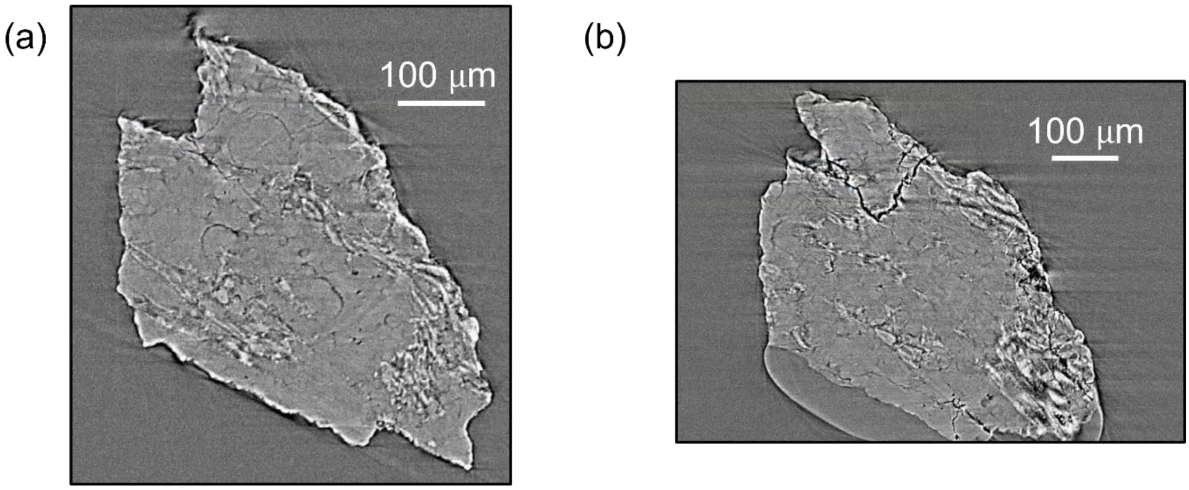

Figure 5.9. XCT cross-sectional images of a Z-HEU granule.

5.2.4.3 Crystallographic Homogeneity

MH-HEU appears to have a less homogeneous internal morphology in comparison to Z-HEU, according to previously discussed XCT cross-sectional images (Figures 5.8 and 5.9). To probe this from a crystallographic viewpoint, local diffraction experiments were performed at K11 DIAD, Diamond Light Source, UK, using a monochromatic X-ray beam (25 μm × 25 μm). Normalised PXRD patterns produced from five diffraction beam trajectories are presented in Figure 5.10, in addition to the beam trajectories themselves. There are no observable differences in the patterns, suggesting distinct crystallographic regions may be insufficient in size for meaningful differences in diffraction data to be observed.

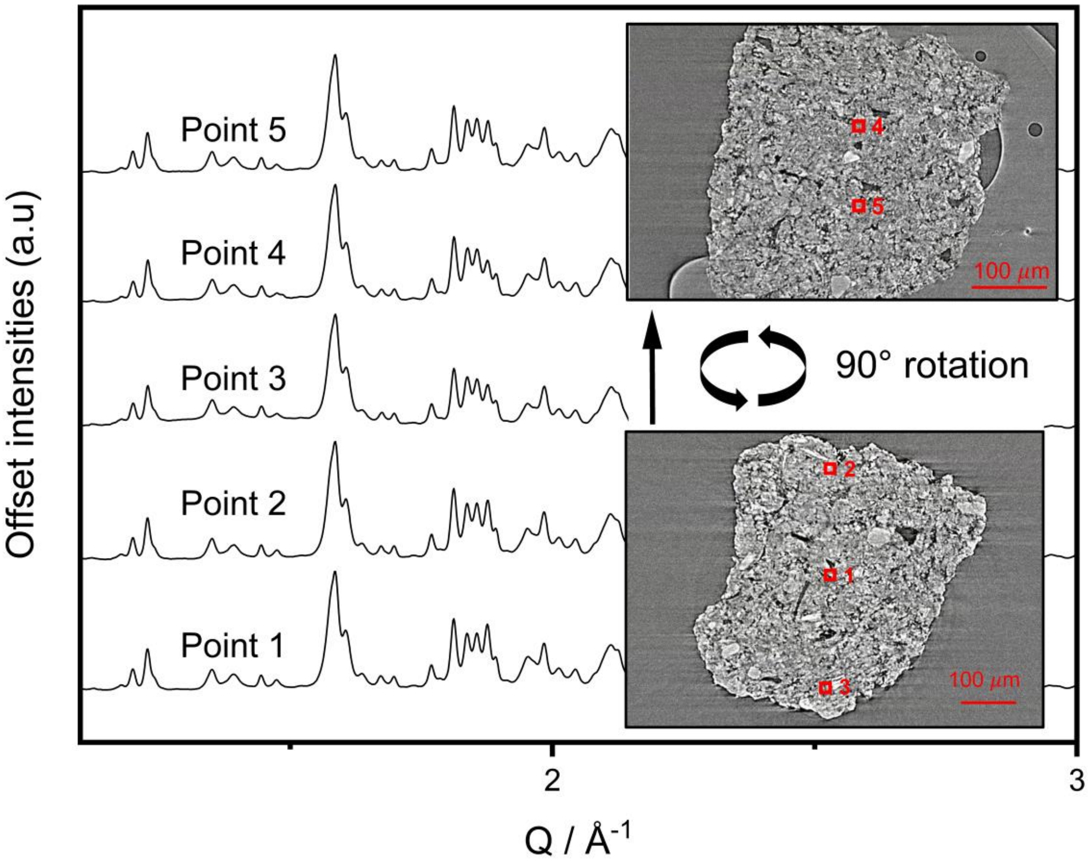

Figure 5.10. Local diffraction data of a MH-HEU granule obtained from five X-ray beam trajectories (λ = 0.5965 Å).

Cross-sectional tomography imaging of Z-HEU suggests a more homogenous distribution of phases (Figure 5.9). Normalised local diffraction data using five X-ray beam trajectories is presented in Figure 5.11; surprisingly, the data suggests a somewhat heterogeneous distribution of phases, with peak intensities varying significantly. A prominent example of this is the broad peak at 1.6 Q ($Å^{-1}$), although plenty of discernible differences are visible across the patterns. The local diffraction data from these datasets highlights the significance of not relying solely on imaging techniques when assessing the phase distribution of natural materials.

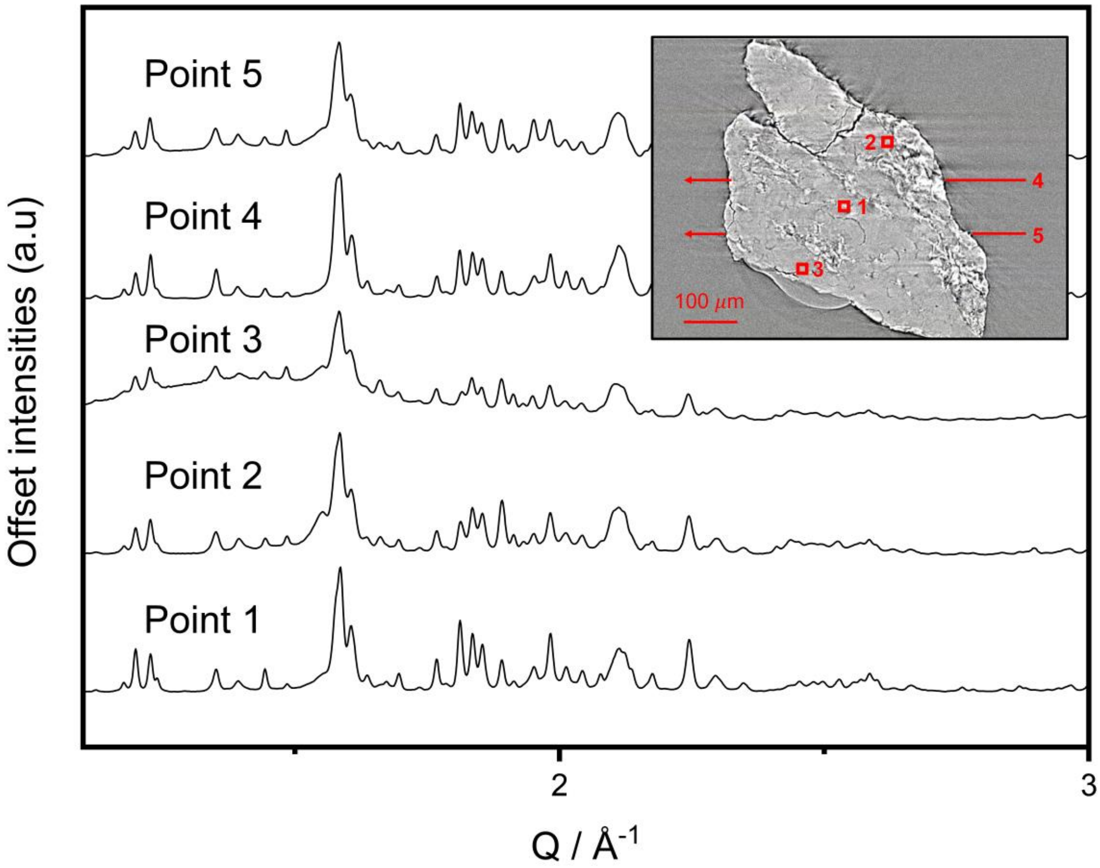

Figure 5.11. Local diffraction data of a Z-HEU granule obtained from five X-ray beam trajectories (λ = 0.5965 Å).

5.2.5 NMR

5.2.5.1 ^{29}Si

^{29}Si NMR spectra of clinoptilolites typically resemble a broad hump between -90 and -120 ppm; this is consistent with the silicon environments Si(0Al), Si(1Al) and Si(2Al), from which the structure is predominantly assembled[231-233]. Silicon tetrahedra co-ordinated to four other silicon tetrahedra, termed Si(0Al), produce a peak at ~113 ppm. Two discernible peaks, positioned at ~107 and ~102 ppm, are observed for silicon tetrahedra coordinated to three silicon and one aluminium tetrahedra (Si(1Al)), with the peak at ~107 ppm exhibiting the greatest intensity. Finally, a peak corresponding to silicon tetrahedra coordinated to two silicon and two aluminium tetrahedra is located at ~95 ppm. Other, smaller peaks are also often observed. These can be attributed to impurities, coordination to Fe^{2+} and presence of silanol moieties – all of which arise from the geological and chemical variation associated with naturally sourced materials[232, 233]. The presence of these 'extra' peaks, coupled with the significant overlap of the larger peaks, makes fitting the spectra challenging; as such, any quantitative information derived from such fitting should be interpreted carefully.

In this work, ^{29}Si NMR spectra were collected and interpreted in attempt to discern any structural disparities between the clinoptilolites that could rationalise Mud Hills' superior performance as an ion-exchange material, in particular its ability to sorb strontium.

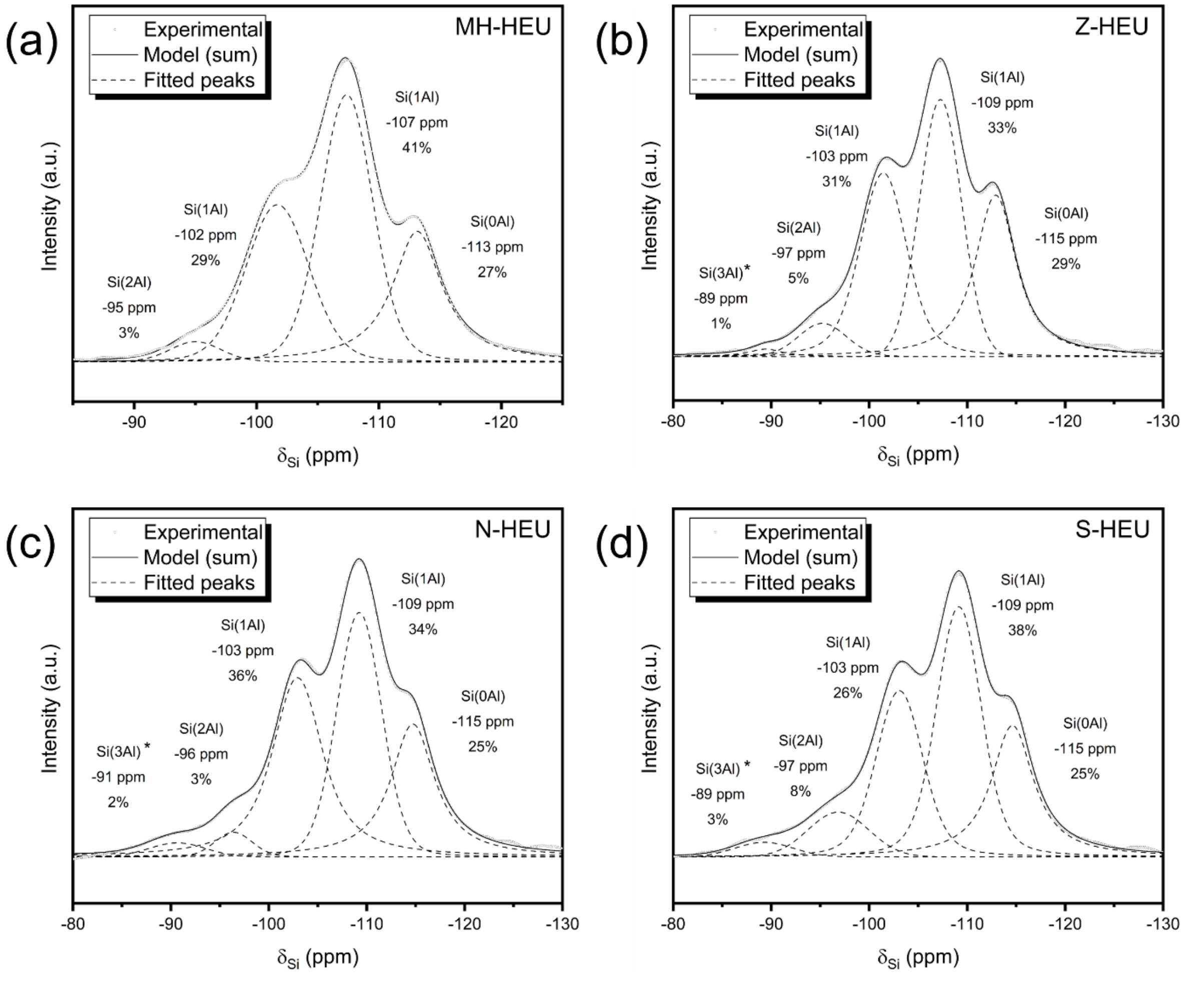

Figure 5.12. ^{29}Si NMR spectra of clinoptilolites, with fitted peaks corresponding to various silicon environments. * Indicates tentative assignment.

All four clinoptilolites produced spectra consisting of broad, overlapping peaks between ~ -90 and -120 ppm (Figure 5.12). Reportedly, the main resonances observed from natural clinoptilolites are positioned at approximately -113, -107 and -102 ppm[232]; this is consistent with the measured spectra of all four samples (Figure 5.12), as clinoptilolite was shown to be the significantly most abundant phase within these materials (5.2.1). It is important to note that resonances attributed to SiO_2 (quartz/cristobalite) are likely present between -107 and -110 ppm, although they are not discernible in these spectra. A smaller peak between -95 and -97 ppm was also observed for all four clinoptilolites; this has been assigned to the Si(2Al) framework environments. However, in the case of Z-, N- and S-HEU, the assignment is tentative due to the significant quantity of feldspars within the materials, which also produce resonances in this region[202]. Furthermore, elemental analysis and sodium-washing experiments (5.2.3) revealed a significant quantity of framework iron within the four clinoptilolites (0.06 – 0.11 Fe/Al ratio). The presence of iron within the secondary coordination sphere of silicon would also produce resonances at approximately -97 ppm, adding further ambiguity to this portion of the spectra. Peaks at ~ -90 ppm were observed in spectra produced by Z-, N- and S-HEU. These have been tentatively assigned to Si(3) environments, which are observed at this chemical shift in other zeolitic systems[231] but are, however, statistically unlikely to be present in detectable concentrations. MH-HEU contains the least iron and, according to diffraction data, no feldspathic phases; assignment in the ~ -96 ppm region is more reliable. There is, however, a significant quantity of mordenite present in MH-HEU (5.2.1), which would produce resonances at -100, -106 and -113 ppm from its Si(2), Si(1) and Si(0) environments, respectively[198]. These peaks are likely lost under the clinoptilolite peaks of far greater intensity. Qualitative inspection of the spectra suggests that the Si(1) peak widths of MH-HEU are greater than the other three clinoptilolites, indicating a greater variation of chemical environments. This is consistent with previous observations (5.2.1) suggesting a greater glass content in MH-HEU. However, it is difficult to comment on the minor differences observed in the spectra and whether these provide rationale for the superiority of Mud Hills clinoptilolite (due to the similarity and complexity of the four spectra).

5.2.5.2 ^{27}Al

As stated by Loewenstein in 1954[37], the unfavorability of Al-O-Al linkages mean they generally do not exist in zeolite frameworks. Therefore, there is only a single resolvable aluminium environment in zeolites: framework aluminium, or aluminium tetrahedrally coordinated to four oxygen atoms, termed Al_{IV}. In natural clinoptilolites this environment produces a peak at a chemical shift of approximately 55 ppm[204]. Aluminium with octahedral coordination geometry, termed extra-framework aluminium, Al_{VI} is also observed in zeolites and produces a peak at a ~0 ppm chemical shift[204]. A significant quantity of extra-framework aluminium would produce lower Si/Al ratio than observed in the framework.

^{27}Al NMR spectra of the four clinoptilolites are presented in Figure 5.13. The tetrahedral environment at ~55 ppm is only significant peak in the spectra for all four materials. Downfield 'shoulder' peaks are visible in all four spectra; these can largely be attributed to the presence of feldspars within the natural samples[234, 235], although contributions from glass are possible in MH-HEU and Z-HEU. The absence of a peak at 0 ppm suggests that negligible quantities of octahedrally coordinated aluminium are present in all four materials. A lower quantity of octahedral aluminium in comparison with other natural clinoptilolites is not responsible for Mud Hills clinoptilolite's abnormal affinity for strontium.

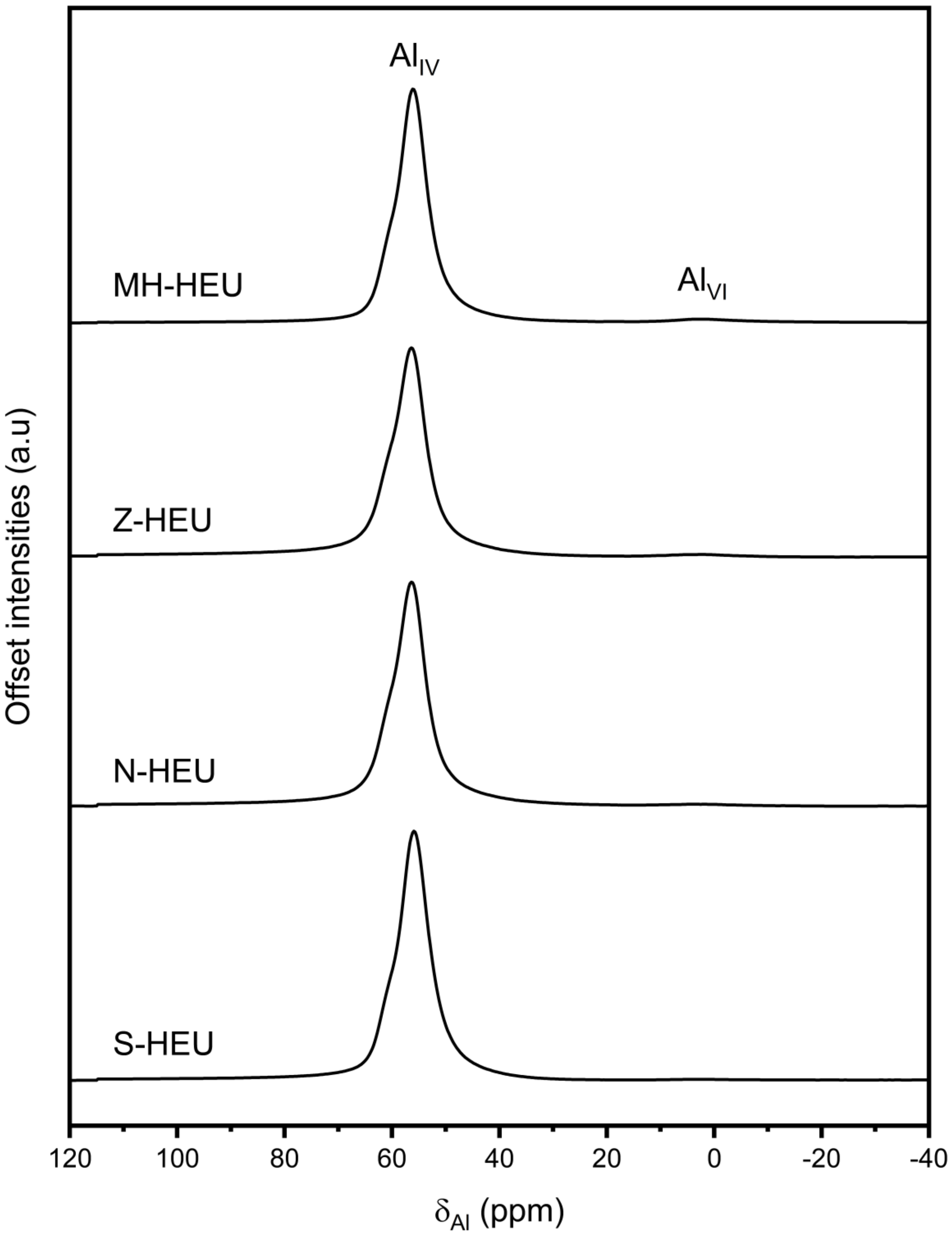

Figure 5.13. ^{27}Al NMR spectra of all four studied clinoptilolites. Tetrahedral (Al$_{IV}$) and octahedral (Al$_{VI}$) environments are labelled.

5.2.6 XPDF

The pair distribution function of the four clinoptilolites is displayed in Figure 5.14 (< 5.6 Å). Typical peaks corresponding to T-O, O-O and T-T atom-atom distances are expectantly observed for all four materials at approximately 1.6, 2.6 and 3.1 Å, respectively. However, the T-O and O-O peaks appear significantly sharper in MH-HEU compared to the other materials, indicating more well-defined tetrahedra and local distribution of tetrahedra. Further analysis into the origins of these discrepancies fall without the remit of this work.

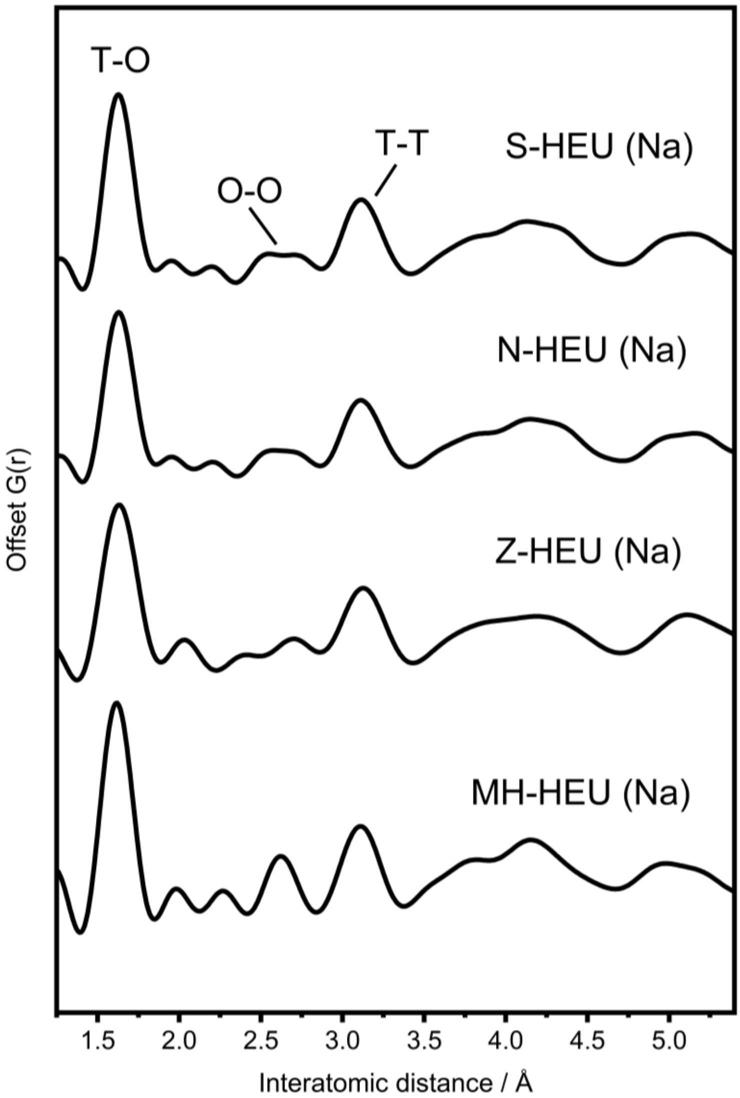

Figure 5.14. Pair distribution function (PDF) of the four natural clinoptilolites.

5.2.7 Equilibrium Ion-Exchange

One of the most important properties of an ion-exchange material is its capacity, which is defined as the maximum quantity of adsorbate per mass of material. Typically, a higher capacity is desirable for ion-exchange materials as more contaminant can be sequestered with a given mass of ion-exchanger. In fixed bed columns this means more effluent can be treated per bed prior to breakthrough, and therefore beds require substitution less frequently. In nuclear applications, acceptable breakthrough levels are exceptionally low, meaning materials are only at <1% capacity when they need to be substituted; the main priority is efficient sorption at low uptake levels. In the context of this chapter, nonetheless, capacity is assessed in attempt to probe which properties of Mud Hills clinoptilolite render it a superior dual ion-exchange material for caesium and strontium in comparison to other clinoptilolites.

5.2.7.1 Caesium Equilibrium Ion-Exchange

Adsorption isotherms have been applied to the caesium uptake of all four clinoptilolites; fits to the Freundlich, Temkin and Langmuir-Freundlich isotherms are displayed in Figure 5.15 (50 -1000 ppm Cs solutions). Coefficients of determination for each fit are presented in Table 5.9. Parameters for all fits are available in Appendix A.16. Both these values and qualitative inspection suggest that the data is best modelled by the Langmuir-Freundlich adsorption isotherm; an estimated value for capacity for all four materials determined from this fit is provided in Table 5.9. MH-HEU exhibits the greatest caesium capacity (203 mg g^{-1}), significantly higher than the other clinoptilolites (140, 134 and 157 mg g^{-1} for Z-, N- and S-HEU, respectively). These values are well below the theoretical clinoptilolite caesium capacity of 292 mg g^{-1} suggesting a significant proportion of resident cations cannot be exchanged with caesium, even when the clinoptilolite weight fractions are taken into account. These observations are consistent with those in section 5.2.3.2, where significantly more cations were exchanged for sodium in MH-HEU than for the other clinoptilolites.

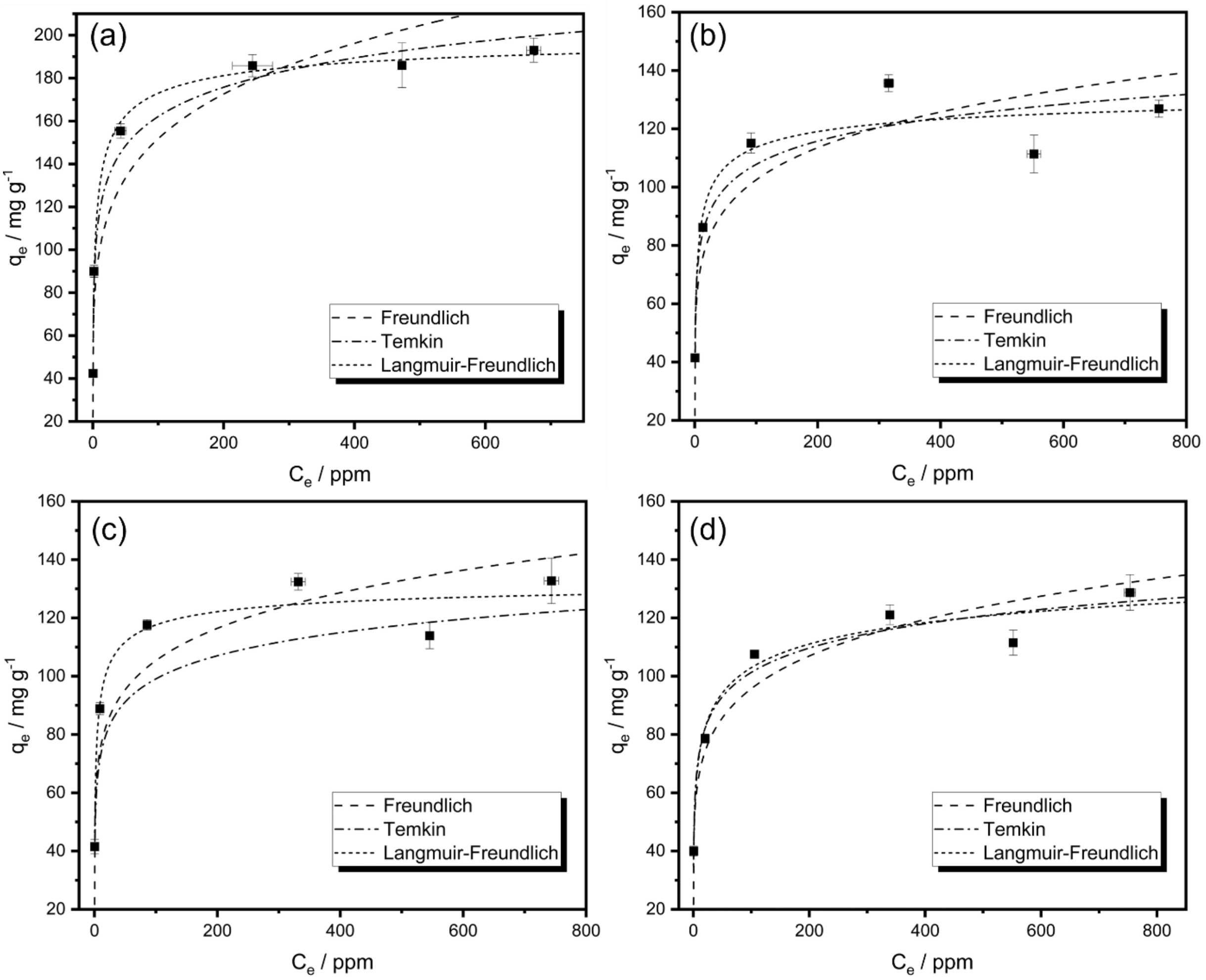

Figure 5.15. Caesium adsorption isotherms obtained through batch ion-exchange experiments. Freundlich, Temkin and Langmuir-Freundlich isotherm models have been applied to each dataset. (a) MH-HEU, (b) Z-HEU, (c) N-HEU and (d) S-HEU.

Table 5.9. Coefficients of determination for Freundlich, Temkin and Langmuir-Freundlich isotherm models applied to the equilibrium caesium uptake of the studied clinoptilolites. Caesium capacities (q_{max}) determined using the Langmuir-Freundlich isotherm are also presented.

Material	**Freundlich**	**Temkin**	**Langmuir-Freundlich**	**q_{max} / mg g^{-1}**
MH-HEU	0.917	0.982	0.996	203(8)
Z-HEU	0.904	0.902	0.933	140(20)
N-HEU	0.894	0.920	0.958	134(12)
S-HEU	0.964	0.966	0.969	157(38)

5.2.7.2 Strontium Equilibrium Ion-Exchange

Adsorption isotherms have been applied to the strontium uptake of all four clinoptilolites in 50 – 500 ppm solutions; fits to the Freundlich, Temkin and Langmuir-Freundlich isotherms are displayed in Figure 5.16. Fit qualities for each of the models and calculated equilibrium capacities are presented in Table 5.10, with details of fitting parameters displayed in Appendix A.16. For every material, the Langmuir-Freundlich model best fits the experimental data. Fits are best to MH-HEU and N-HEU datasets as the data best resembles the characteristic isotherm shape. Both Z-HEU and S-HEU contain somewhat unexpected uptake values at particular concentrations, resulting in a worse fit – although the produced capacities are reasonable from the data obtained, when the derived uncertainty is considered. It is possible that these spurious data points are somewhat a product of temperature variations within the laboratory. Mud Hills clinoptilolite, MH-HEU, displays the highest strontium capacity at 56 mg g^{-1} with N-HEU, S-HEU and Z-HEU showing respective capacities of 44, 33 and 30 mg g^{-1}. These values are significantly lower than the theoretical clinoptilolite strontium capacity of 96 mg g^{-1}; this is due to a combination of inaccessible cations, shortage of suitable strontium binding sites and the reduced zeolitic content (5.2.1).

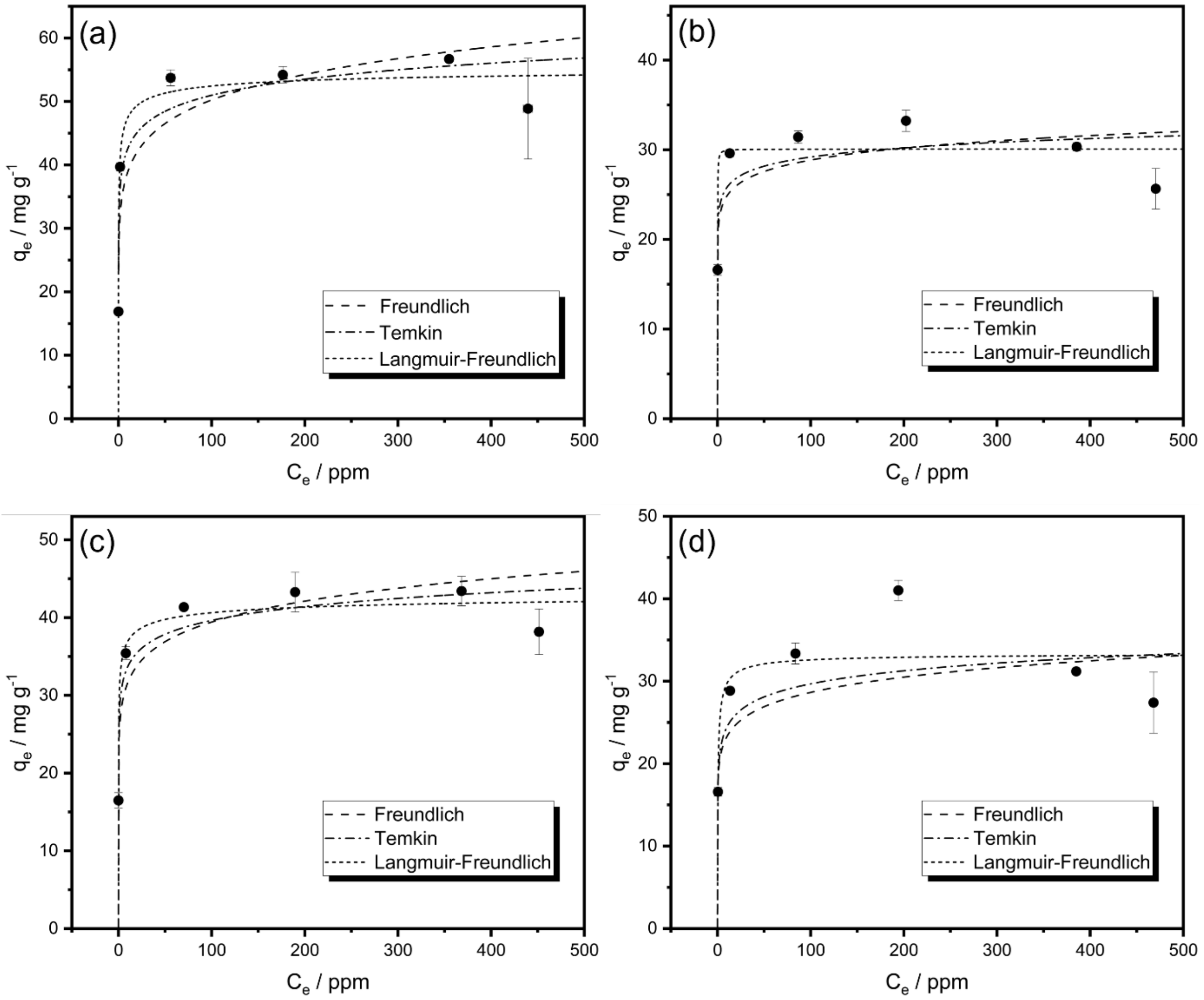

Figure 5.16. Strontium adsorption isotherms obtained through batch ion-exchange experiments. Freundlich, Temkin and Langmuir-Freundlich isotherm models have been applied to each dataset. (a) MH-HEU, (b) Z-HEU, (c) N-HEU and (d) S-HEU.

Table 5.10. Coefficients of determination for Freundlich, Temkin and Langmuir-Freundlich isotherm models applied to the equilibrium strontium uptake of the studied clinoptilolites. Strontium capacities (q_{max}) determined using the Langmuir-Freundlich isotherm are also presented.

Material	Freundlich	Temkin	Langmuir-Freundlich	Capacity$_{LF}$ / mg g^{-1}
MH-HEU	0.887	0.909	0.963	56(5)
Z-HEU	0.692	0.638	0.827	30(2)
N-HEU	0.901	0.897	0.955	44(5)
S-HEU	0.181	0.166	0.672	33(5)

Previous work by Palmer found MH-HEU capable of 98 % exchange of strontium for calcium, but only 75, 56 and 37 % of sodium, magnesium and potassium are displaced, respectively[219]. When cationic compositions (Section 5.2.3.2) are considered, this equates to an approximate 65 % release of framework cations for strontium and a strontium capacity of ~60 mg g^{-1}, within error of the capacity derived from the Langmuir-Freundlich model.

5.2.7.3 Caesium and Strontium Capacity Comparison

Caesium and strontium capacities calculated from the adsorption isotherms, Cs q_{max} and Sr q_{max}, are plotted against each other in Figure 5.17. Additionally, the straight line $y = 0.33x$ is also plotted; this represents the 'perfect' balance of cation sorption, whereby equal amounts of caesium and strontium charge can be accommodated within the framework.

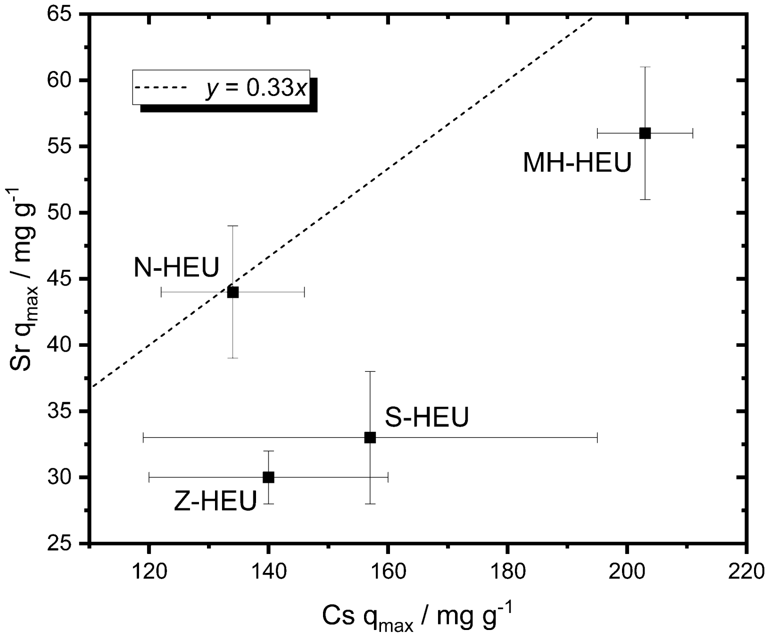

Figure 5.17. Caesium and strontium capacities (q_{max}) of the four clinoptilolites as determined from equilibrium adsorption isotherms. The straight line $y = 0.33x$ is plotted to depict region where equal quantities of charge from both caesium and strontium can be accommodated.

It is apparent that MH-HEU has the highest capacity for both target species; this is considered abnormal in comparison to the other clinoptilolites. In line with expectations of moderately siliceous frameworks, MH-, Z- and S-HEU are capable of less strontium sorption than their caesium capacity suggests, likely due to limited availability of cation pairs within the material for strontium to adhere.

N-HEU is capable is accommodating relatively equal amounts of charge from both caesium and strontium. This could be a result of an alumina distribution with more available aluminium pairs.

The observation of an enhanced capacity for MH-HEU in comparison to its other clinoptilolites provides a rationale to why it 'overperforms'. As previously discussed, framework charge is not responsible for the observed capacity increase, as Mud Hills clinoptilolite contains similar alumina quantities to the other clinoptilolites. The origin inherently arises from the increased zeolitic content (5.2.1) and the ease of which resident framework species are released (5.2.3.2).

5.2.8 Rate Experiments

In industry, the separation of radionuclides from nuclear wastewater is typically achieved though deployment of fixed bed columns; effluent is pumped though a bed of ion-exchange material which selectively adsorbs radionuclides. Residence times within these columns can be as short as a few minutes[70]; it is therefore imperative that the kinetics of exchange are suitably fast to ensure adequate remediation. Here, the rate of adsorption for caesium and strontium is assessed for all four clinoptilolites using kinetic isotherms. Any observed improvements in the rate of exchange of MH-HEU, in comparison to the other clinoptilolites, would rationalise the improved performance in fixed-bed columns.

5.2.8.1 Rate of Caesium Exchange

Kinetic isotherms depicting the adsorption of caesium for MH-HEU, Z-HEU, N-HEU and S-HEU are presented in Figure 5.18; the 2nd order kinetic model has been fitted to the datasets, with excellent accordance shown ($R^2 > 0.99$). Qualitatively, equilibrium was comfortably reached within the three-hour experiment. Derived isotherm parameters, in addition to the time required to reach 95% of the equilibrium uptake for all four materials is reported in Table 5.11.

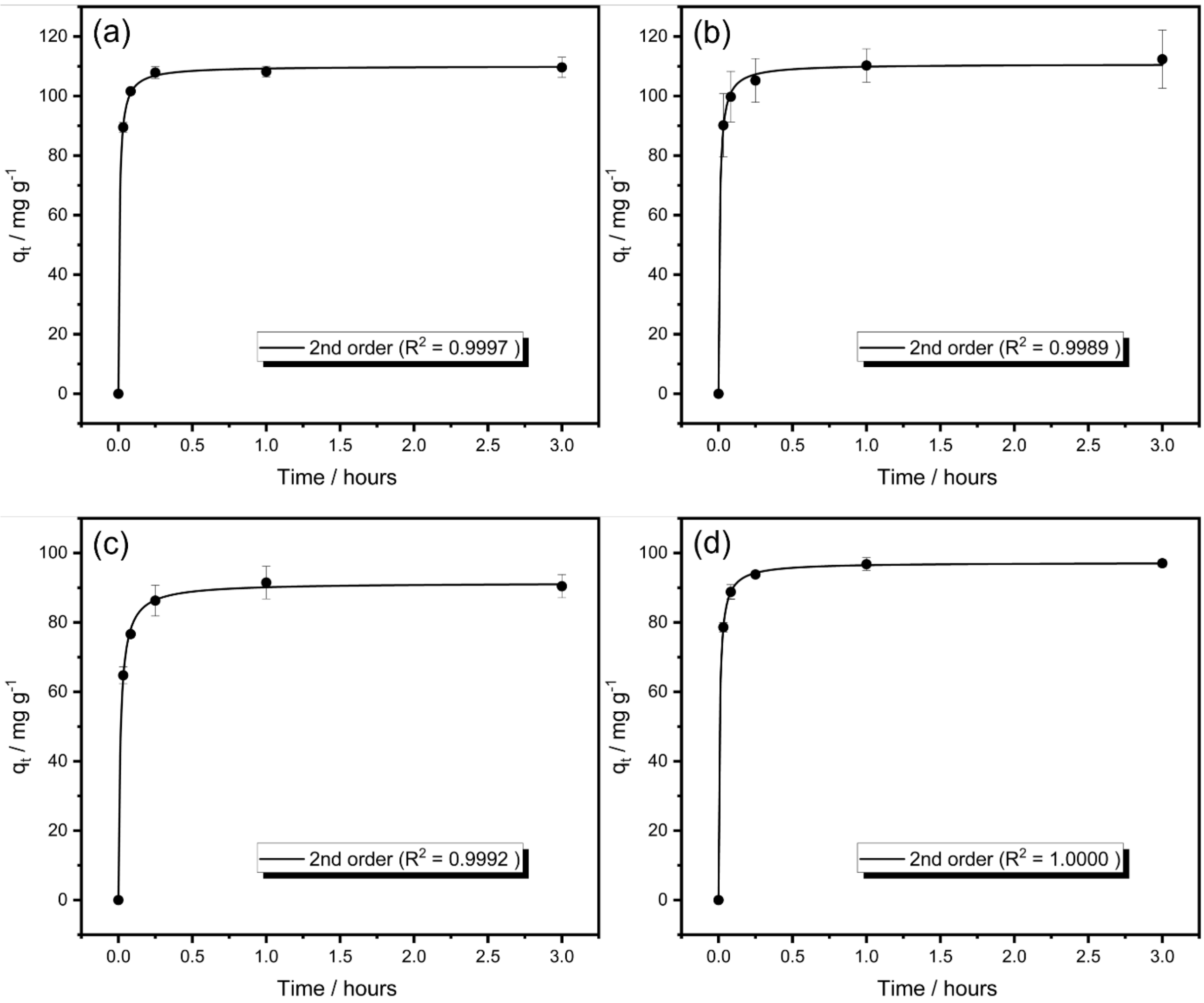

Figure 5.18 Kinetic isotherms of caesium adsorption for (a) MH-HEU, (b) Z-HEU, (c) N-HEU and (d) S-HEU. Fits to the 2nd order kinetic model are displayed.

Table 5.11. Second order kinetic model parameters of isotherms applied to the adsorption of caesium on the studied clinoptilolites. Estimated timeframes required to reach 95 % of equilibrium are also presented for each material.

Material	**q_e / mg g^{-1}**	**k / g mg^{-1} h^{-1}**	**R^2**	**$t_{(95\%)}$ / minutes**
MH-HEU	110(1)	1.22(8)	0.9997	8(3)
Z-HEU	111(1)	1.12(13)	0.9989	9(4)
N-HEU	91(1)	0.76(6)	0.9992	16(5)
S-HEU	97(1)	1.29(3)	1.0000	9(2)

Isotherms corresponding to MH-HEU, Z-HEU and S-HEU have similar rate constants: 1.22, 1.12 and 1.29 g mg^{-1} h^{-1}, respectively, and almost within error of each other. This corresponds to the system only taking 8-9 minutes to reach 95% of equilibrium. N-HEU displayed slightly slower kinetics of exchange and produced a 2nd order rate constant of 0.76, resulting in the system taking 16 minutes to reach $t_{95\%}$.

It is important to note that these values are still considerably close and there almost overlap when errors are considered; it is therefore difficult to draw any conclusions from the data.

5.2.8.2 Rate of Strontium Exchange

Kinetic isotherms depicting the adsorption of strontium for MH-HEU, Z-HEU, N-HEU and S-HEU are displayed in Figure 5.19. Fits to the Elovich kinetic model are also shown with good accordance to the datasets ($R^2 > 0.96$). The rate of strontium uptake is markedly slower than equivalent caesium experiments in section 5.2.8.1, with equilibrium not being reached after 24 hours. This can be attributed to the larger hydration sphere associated with the more charge-dense cation. Derived isotherm parameters, in addition to the time required to reach 95% of the equilibrium uptake for all four materials is reported in Table 5.12. As estimated equilibrium values have to be estimated from the Elovich fitting as equilibrium was not reached, there is a significant error associated with these values.

The data suggests that there is little variation in the kinetics of strontium exchange between the four clinoptilolites; all four reach 95 % of the equilibrium loading in approximately 60 hours and all well within the determined associated errors of each other. However, it is evident that Mud Hills clinoptilolite has a much higher equilibrium loading for strontium – this is consistent with the increased capacity observed (5.2.7). Therefore, despite the fact that equilibrium is reached in a similar timeframe, Mud Hills clinoptilolite is actually adsorbing at a faster rate due to the increased quantity of adsorption sites.

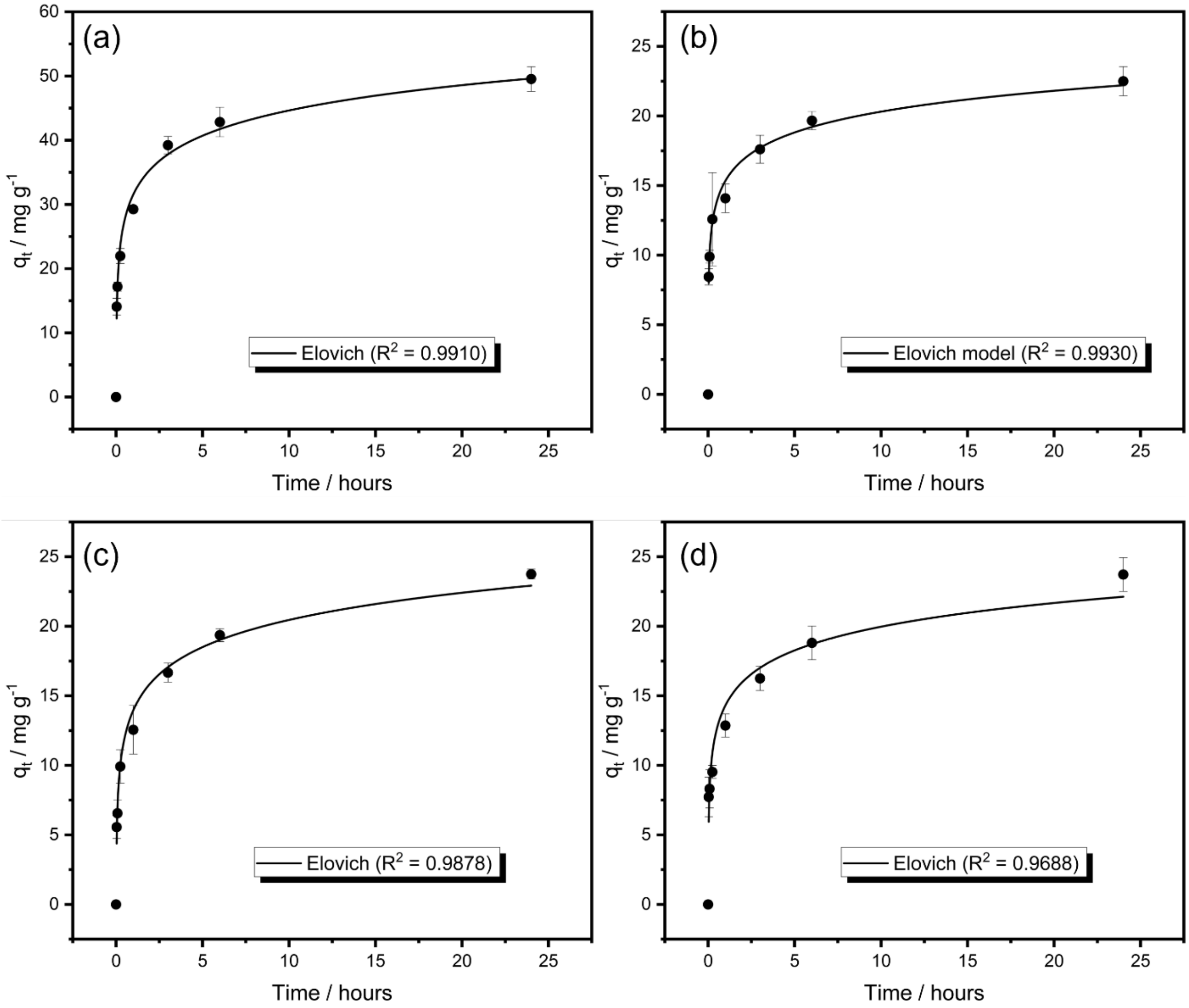

Figure 5.19. Kinetic isotherms of strontium adsorption for (a) MH-HEU, (b) Z-HEU, (c) N-HEU and (d) S-HEU. Fits to the Elovich kinetic model are displayed.

Table 5.12. Second order kinetic model parameters of isotherms applied to the adsorption of strontium on the studied clinoptilolites. Estimated timeframes required to reach 95 % of equilibrium are also presented for each material.

Material	α	β	**R^2**	**$t_{(95\%)}$ / hours**
MH-HEU	1471(345)	0.18(1)	0.9910	60(15)
Z-HEU	2625(792)	0.46(3)	0.9930	56(17)
N-HEU	400(93)	0.35(2)	0.9878	62(15)
S-HEU	827(390)	0.41(4)	0.9688	59(29)

5.2.9 Hydrothermal Transformation Products

In Chapters 3 and 4, natural clinoptilolites and mordenite were converted to zeolite P by means of a caustic hydrothermal transformation. This dissolution-recrystallisation reaction is widely observed in literature, with Na-P being the phase produced[76-80, 147-149]. The subsequent section summarises some peculiar, unreported transformation behaviours of Mud Hills clinoptilolite. While this is not necessarily linked to what makes Mud Hills a superior ion-exchange material, it certainly adds to Mud Hills' peculiarity and could be a significant observation.

5.2.9.1 Basic Transformation of Mud Hills Clinoptilolite

In contrast to other both a mordenite and clinoptilolites studied in this work, Mud Hills clinoptilolite undergoes interzeolite transformation into two zeolite products upon hydrothermal treatment in sodium hydroxide solutions: zeolite P (GIS) and chabazite (CHA). Diffraction data from a material produced from a 1M NaOH solution, and subsequent Rietveld analysis, is presented in Figure 5.20.

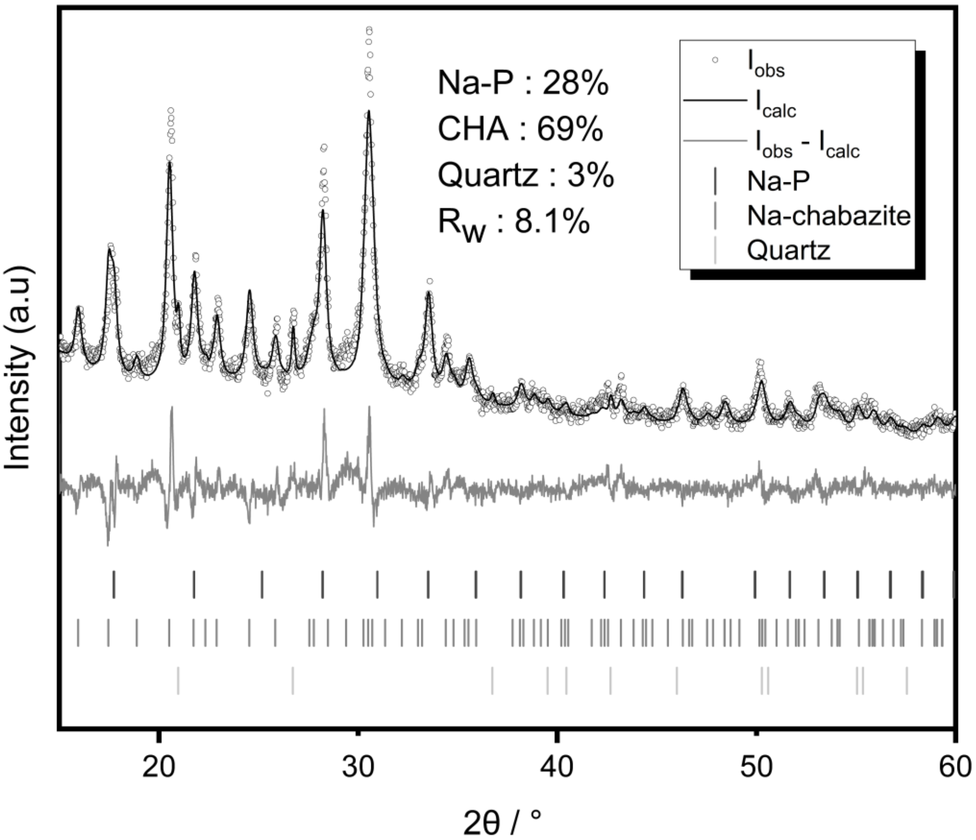

Figure 5.20 PXRD data and subsequent Rietveld analysis of fully transformed Mud Hills clinoptilolite, with calculate weight fractions displayed (λ = 1.5406 Å).

Crude Rietveld analysis suggests chabazite is the most abundant phase (69 %), although significant quantities of zeolite P are also present (28 %). XRF data suggests the converted material has a Si/Al ratio of 2.3; this is somewhat lower than the value of 2.5 obtained for the other fully converted clinoptilolites covered in Chapter 4 – implying either the nascent chabazite framework is more aluminous or contrasting zeolite P compositions are being generated. Assuming the Na-P formed in this process has a Si/Al of 2.5, an estimated Si/Al ratio of the chabazite of 2.1 is calculated. This is identical to the reported material produced by the IZA verified synthesis route[236]. Coincidentally, this synthesis procedure is also an interzeolite transformation, albeit from a zeolite Y precursor at 97 °C.

The co-crystallisation of the chabazite framework from hydrothermally treated natural zeolites is not reported in the literature, although faujasite type zeolites (FAU), which readily convert to chabazite[236], have been reported as intermediates in transformations to zeolite P[78]. Chabazite crystallisation times are also routinely on the order of many days[236, 237], although the presence of various cationic species can accelerate the process[237]. Based on the fundamental concepts of zeolite crystallisation, several hypotheses can be postulated to rationalise this behaviour. Namely, the chemistry of the mother liquor could be significant, for example if there are different ratios of silica and alumina. This is unlikely as the Si/Al ratio of the starting material lies between the other clinoptilolites, although experimental evidence (e.g., elemental analysis of the mother liquor) has not been obtained to confirm this. Alternatively, previously intrapore cations could be acting as an SDA following framework dissolution. However, chabazite is typically synthesised using potassium as an SDA[236] and elemental analysis (Section 5.2.3) implies that MH-HEU had the lowest potassium content of the four clinoptilolites. Further, the low abundance of newly released framework cations in the mother liquor, in comparison to the ubiquitous sodium cations provided by sodium hydroxide, weakens this hypothesis. As Mud Hills clinoptilolite is a naturally sourced material there are potentially many more trace impurities not observed in section 5.2.1. It is possible that one of these is a chabazite seed; this would decrease the kinetic barrier for crystallisation and possibly induce the co-crystallisation of chabazite. Alternatively, opposed to co-crystallisation, chabazite could materialise from metastable zeolite P as the more thermodynamically favoured product, as per Ostwald's rule of stages, which states that the first phase is the least thermodynamically stable and is formed on kinetic grounds[134].

5.2.9.2 Granular Mud Hills Transformations

Equivalent transformations were also attempted on granular Mud Hills clinoptilolite to allow structural and mechanistic comparisons to the systems studied in Chapters 3 and 4. 'Full' conversion to chabazite was achieved in 0.80 M NaOH solution; a composite material with significant quantities of clinoptilolite and chabazite were attained using a 0.50 M solution. No reflections attributed to zeolite P are observed in the diffraction data. This could be a result of the lower basicity used in these transformations, or a product of the reduced dissolution kinetics associated with granular transformations.

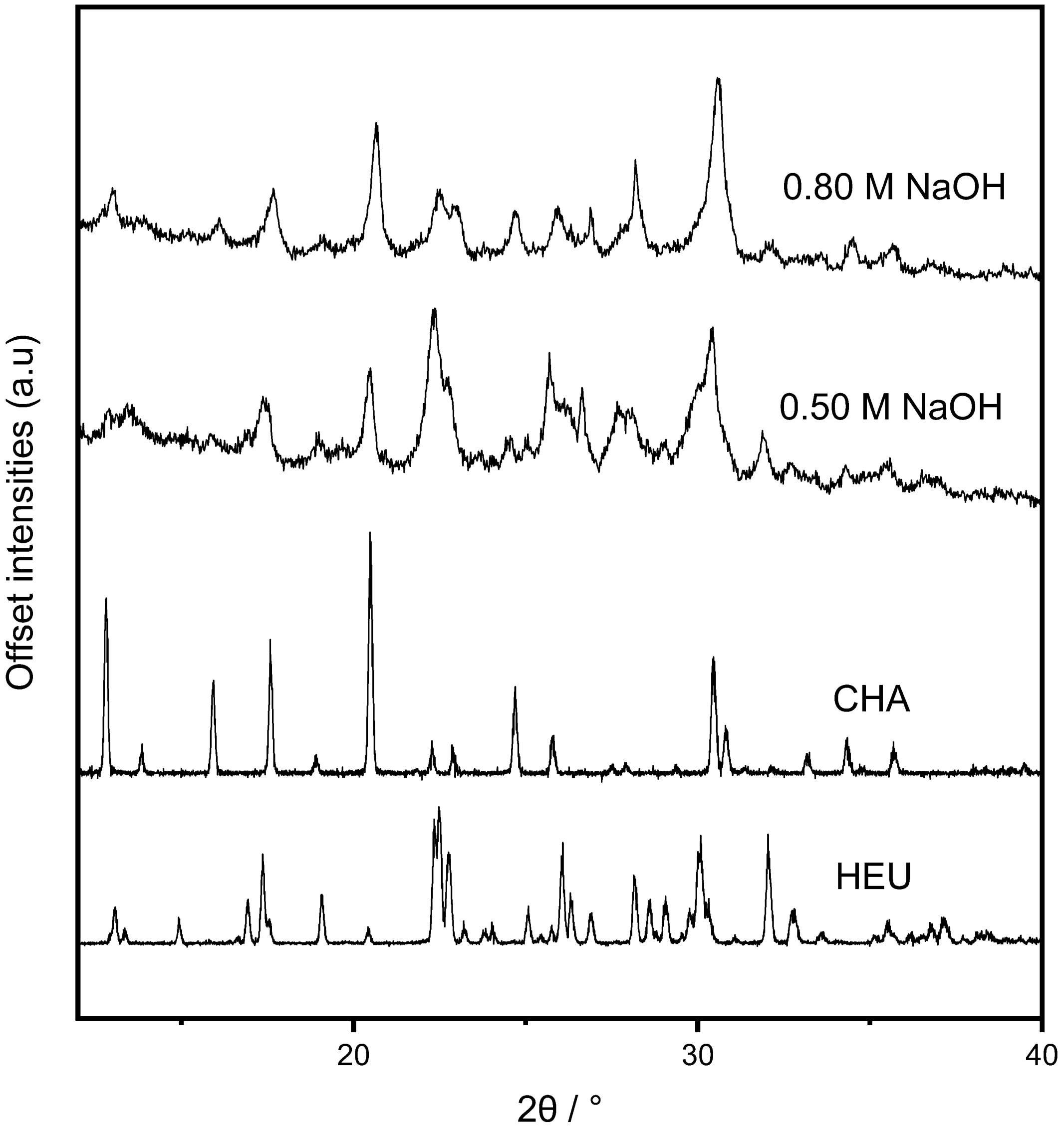

Figure 5.21. PXRD patterns of granular MH-HEU after hydrothermal treatment in 0.50 and 0.80 M NaOH solutions. Simulated clinoptilolite and chabazite patterns are also presented (λ = 1.5406 Å).

SEM imaging of the composite material, generated in 0.5 M NaOH, shows granularity is maintained (Figure 5.22). Closer inspection reveals the presence of plate-like polycrystalline moieties on the surface of the granules. In some regions, plates have assembled into larger structures with flower-like and spherical appearances. XCT and local diffraction measurements are presented in Figure 5.23. The inset cross-sectional tomography slice suggests a 'core-shell' composite is formed, similarly to the mordenite-zeolite P composites discussed in Chapter 3 (3.2.8.1). A diffraction beam trajectory through the centre of the granule yielded a diffraction pattern where reflections attributed to both clinoptilolite and chabazite were observed, although clinoptilolite was qualitatively the most abundant phase

(Figure 5.23, Point 1). Image-guided diffraction beam trajectories targeted towards the edge of the granule (Figure 5.23, Points 3 and 4) saw a significant increase in the chabazite reflection intensities, whereas clinoptilolite reflections decreased in intensity. Combined with the XCT imaging, this data confirms the ‘core-shell’ nature of the material. Interestingly, reflections from quartz were only observed in diffraction data from Points 1 and 3, thus providing strong evidence for a heterogeneous distribution of quartz in Mud Hills clinoptilolite.

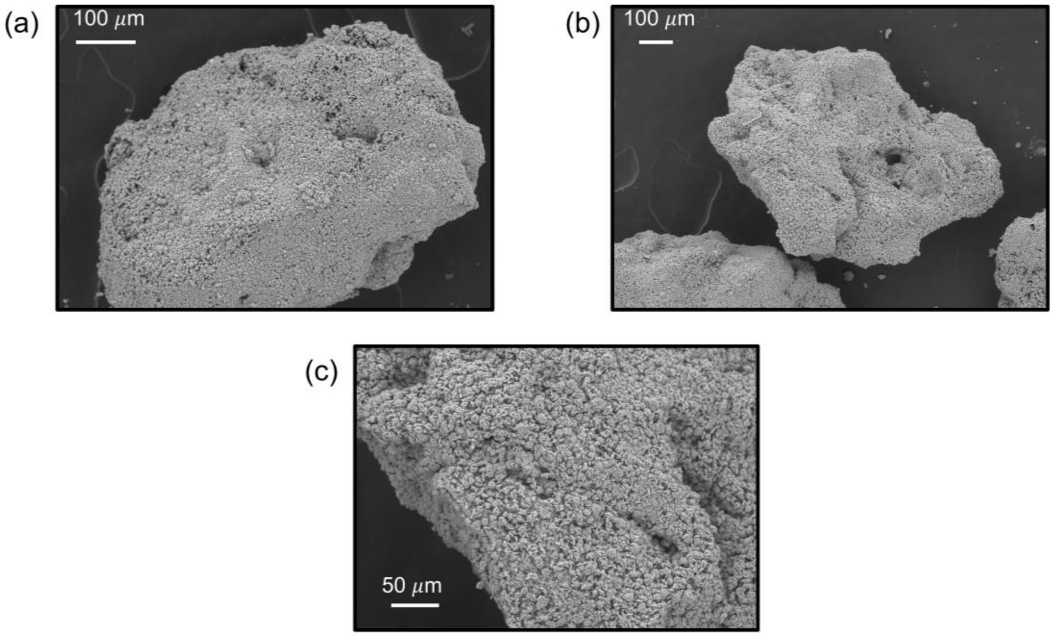

Figure 5.22. SEM images of clinoptilolite-chabazite composite granules generated from 0.50 M NaOH hydrothermal treatment (15 keV).

SEM imaging of a ‘fully converted’ granule (0.80 M NaOH treatment conditions) is provided in Figure 5.24. Like with the composite material, plate-like crystallites are observed on the surface; these can be assumed to be chabazite based of the local diffraction experiments of the composite (Figure 5.23).

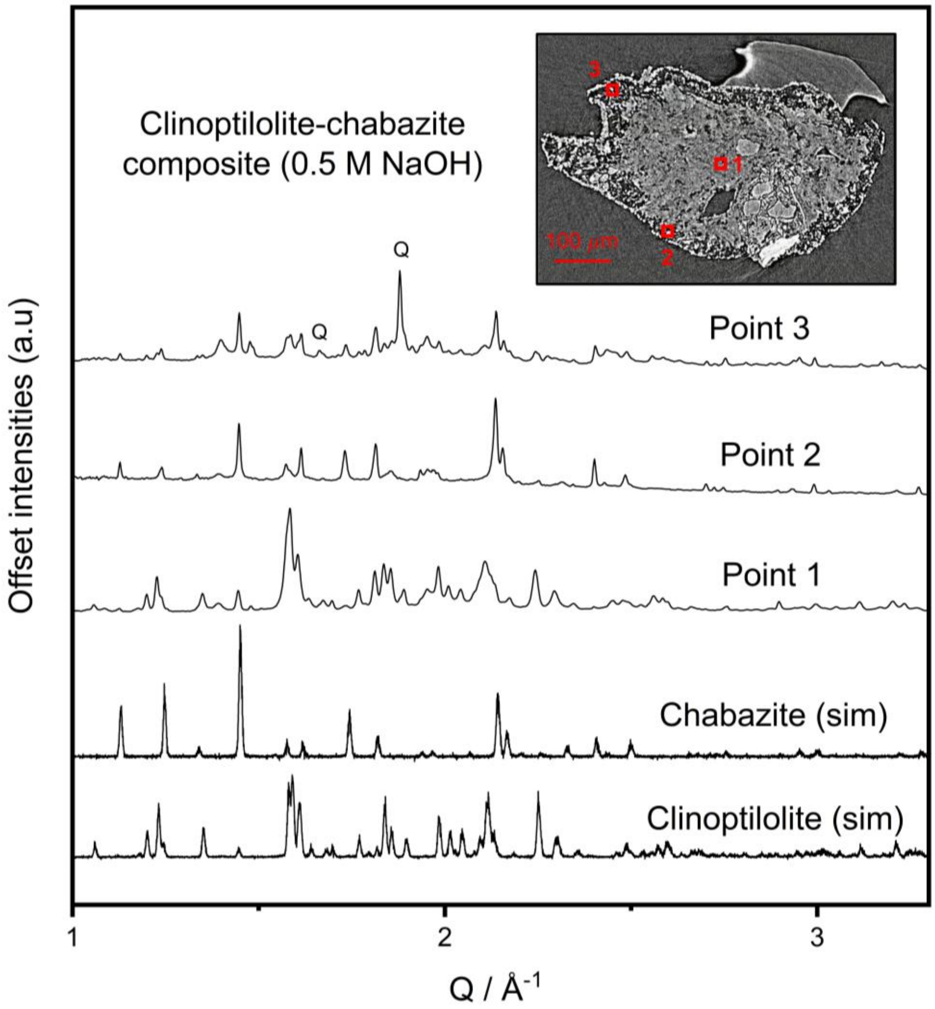

Figure 5.23. Local diffraction data obtained from three diffraction beam trajectories on a clinoptilolite-chabazite composite granule (0.50 M NaOH hydrothermal treatment, λ = 0.5965 Å). Simulated clinoptilolite and chabazite patterns are also presented. X-ray trajectories are displayed on a cross-sectional image obtained from XCT data.

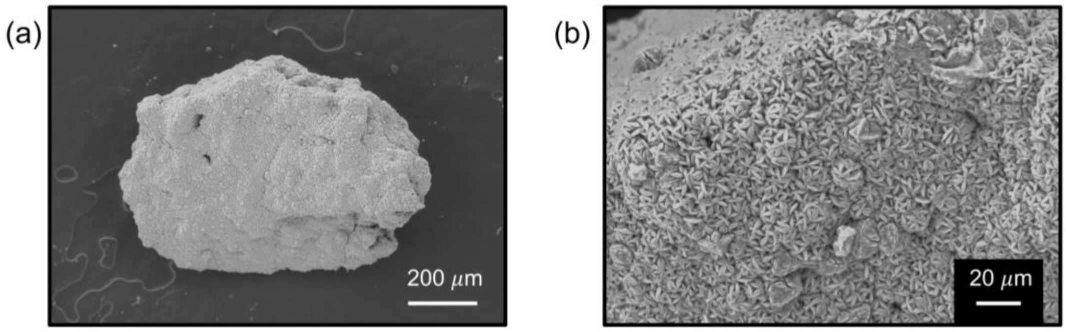

Figure 5.24. SEM images of 'fully converted' MH-HEU granule produced *via* hydrothermal transformation in 0.80 M NaOH.

5.2.9.3 Pre-Treated Mud Hills Transformations

In attempt to gain insight into Mud Hills clinoptilolite's transformation behaviours, conversions were performed after several pre-treatments: a sodium chloride wash, which exchanges Na for other cations without transforming the material, a nitric acid wash, and a nitric acid followed by sodium chloride wash. After all the treatments the clinoptilolite framework remained intact: only minor differences in reflection intensities were observed (A.17). PXRD patterns of the materials after transformation are displayed in Figure 5.25.

As observed in section 5.2.3.2, pre-treatment with sodium chloride replaces some of the incumbent cations with sodium, resulting in an Na/Al ratio of approximately 0.67. Subsequent transformation affords a mixture of zeolite P and chabazite, analogous to the untreated material. Interestingly, MH-HEU treated in 1M HNO_3 produced zeolite P as the main phase. The effect of the acid-wash facilitating this is two-fold: some phases may solubilise in the acidic media and protons will exchange with pore cations to form the protonated zeolite. Hydrothermal transformation conditions were also applied on some Mud Hills clinoptilolite that had been first acid-treated, then NaCl-treated; this was in attempt to discriminate why the lone acidic treatment resulted in transformation to zeolite P. The sequential treatments produced a zeolite P-chabazite mixture upon exposure to hydrothermal conditions, thus implying that the protons in the framework are responsible for the change in transformation selectivity to zeolite P, opposed to the dissolution of a species which may favour crystallisation of zeolite P. This could be due to a subtle change in mother liquor pH or altered dissolution kinetics. Further evidence supporting this hypothesis is the result of seeding studies, whereby small quantities of chabazite seeds were added to the acid-treated Mud Hills clinoptilolite prior to transformation. Zeolite P crystallised as the major product despite the inclusion of chabazite seeds (A.18). SEM images of granular MH-HEU converted after pre-treatment with NaCl, HNO_3 and NaCl then HNO_3 are shown in Figures 5.26, 5.27 and 5.28, respectively. There are no obvious differences in the crystallite morphologies in each of the transformed materials, despite the acid-washed material containing predominantly zeolite P. A combination of prism- and plate-like and crystallites are observed on the exterior of all three granules.

In the case of the acid-washed, transformed material (Figure 5.27), the different crystallite morphologies could be due to the two synthesised polymorphs of zeolite P (P1 and P2).

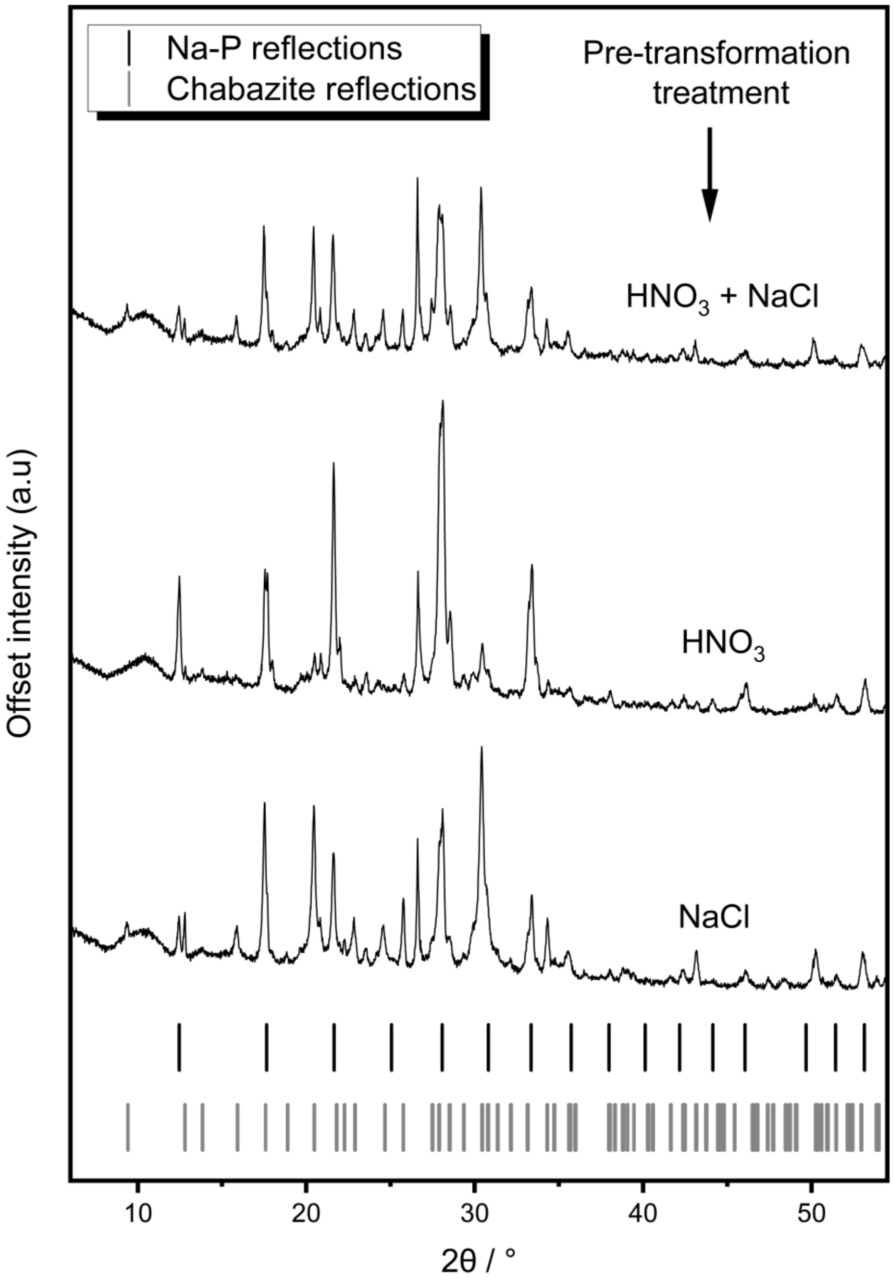

Figure 5.25. PXRD patterns of hydrothermally transformed, pre-treated MH-HEU (λ = 1.5406 Å).

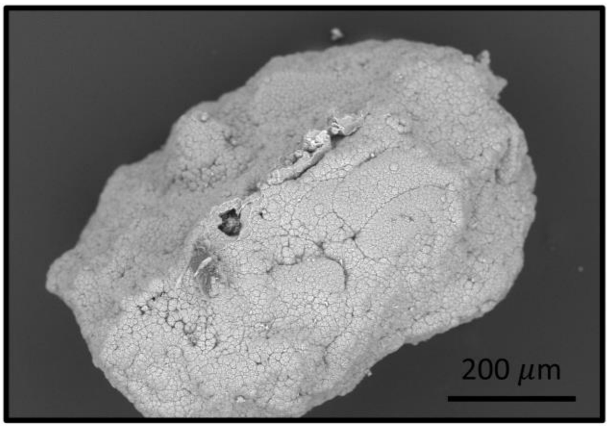

Figure 5.26. SEM image of transformed, NaCl treated MH-HEU (15 keV).

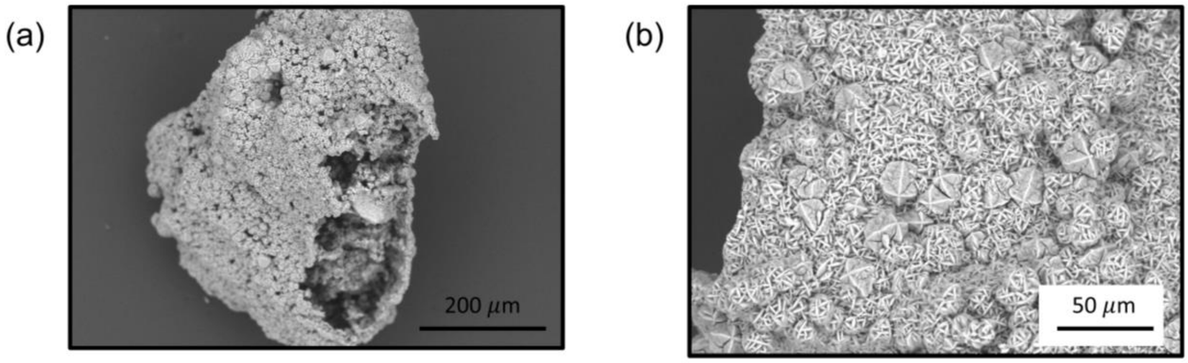

Figure 5.27. SEM images of transformed, acid-treated MH-HEU (15 keV).

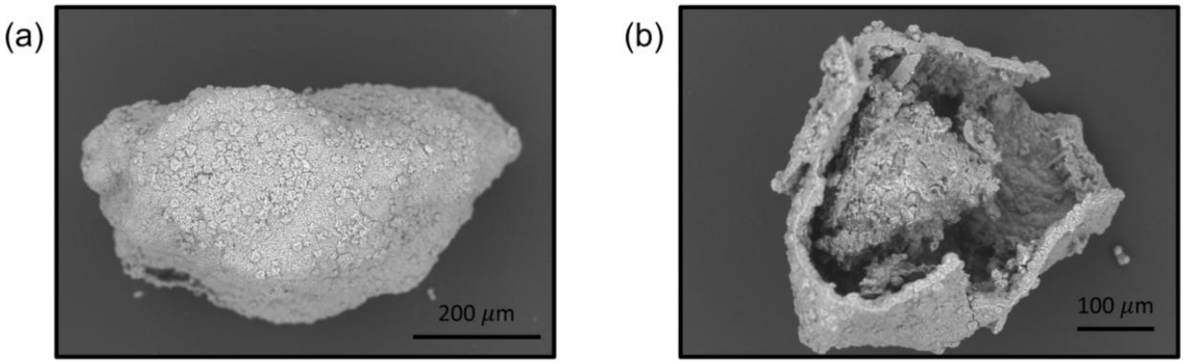

Figure 5.28. SEM images of transformed, acid- and NaCl-treated MH-HEU.

5.2.9.4 Pre-treated Z-, N- and S-HEU Transformations

In Chapter 4, the transformation of Z-, N- and S-HEU into zeolite P was exploited to enhance the ability to sorb strontium from nuclear waste streams. Hydrothermal treatment of these three clinoptilolites, pre-treated with NaCl, HNO_3, and NaCl + HNO_3, afforded zeolite P as the main product, (A.19). Analogous to the transformation of untreated material, both Na-P1 and Na-P2 polymorphs were detected.

5.2.9.5 Transformation Products Summary

The transformation products of powdered materials, from both this section and previous chapters, are summarised in Table 5.13. The observed conversion from Mud Hills clinoptilolite (MH-HEU) to chabazite is unusual - all other natural materials in this work, in addition to numerous literature examples, convert to zeolite P. The only pre-treatment of MH-HEU that prevented the crystallisation of chabazite was a sole acid wash; even the acid-washed then sodium-washed material produced both chabazite and zeolite P. When this is considered alongside the seeded, acid-treated material transformation (which produced zeolite P), it can be assumed that the elevated concentration of protons within the zeolite framework is responsible for the production of zeolite P, in this case. Possible explanations for this phenomenon include: altered kinetics of dissolution, subtle differences in the pH of the mother liquor, or selective framework breakdown. Further work is required to draw any further conclusions.

Table 5.13. Summary of the transformation products at 100°C of the natural zeolites studied in this work. *Data presented in Chapter 4. ‡Data presented in Chapter 3.

Staring material	Pre-treatment	Transformation framework topologies
MH-HEU	-	Chabazite (CHA) and zeolite P (GIS)
MH-HEU	NaCl	Chabazite (CHA) and zeolite P (GIS)
MH-HEU	HNO_3	Zeolite P (GIS)
MH-HEU	HNO_3 then NaCl	Chabazite (CHA) and zeolite P (GIS)
MH-HEU	HNO_3 (5 % CHA seeded)	Zeolite P (GIS)
Z-, N- and S-HEU*	-	Zeolite P (GIS)
Z-, N- and S-HEU	NaCl, HNO_3 or NaCl then HNO_3	Zeolite P (GIS)
I-MOR‡	-	Zeolite P (GIS)

5.3 Conclusion

Over the course of this chapter, a significant amount of information about the four clinoptilolites has been attained and discussed. The remainder of this section will focus on drawing the significant observations together in attempt to summarise possible rationale explaining the superiority of Mud Hills clinoptilolite for the remediation of aqueous nuclear decommissioning waste. Key properties of the four clinoptilolite materials studied in this work are summarised in Table 5.14. Compositionally, PXRD data (5.2.1) suggests MH-HEU contains the most zeolitic material (77 %) of the four studied materials (1.1 - 1.4 × more than the other clinoptilolites). This inherently increases the cation exchange capacity, which is observed in the experimentally determined capacity values (q_{max}) of caesium and strontium. However, the higher capacities of MH-HEU for both caesium and strontium cannot be fully rationalised by the greater zeolitic content in most cases – meaning there is likely some 'extra' capacity for these species.

Table 5.14. Summary of properties of the studied clinoptilolites in this chapter. HEU Wt. % and impurities determined though PXRD and subsequent Rietveld refinement, parentheses indicate the approximate Wt. % of the given impurity. Si/Al ratios obtained though XRF and SEM-EDS analysis (5.2.3.1). Cationic species are listed in order of abundance, determined by SEM-EDS measurements (5.2.3.2). Caesium and strontium capacities (q_{max}) determined though adsorption equilibrium isotherms (5.2.7). Times required to reach 95% of equilibrium calculated from kinetic adsorption isotherms (5.2.8). Transformation products were observed in various earlier sections of this work.

Material	**HEU Wt. %**	**Impurities**	**Si/Al**	**Cationic species**	**q_{max} (Cs) / mg g^{-1}**	**q_{max} (Sr) / mg g^{-1}**	**$T_{95\%}$ (Cs) / mins**	**$T_{95\%}$ (Sr) / hours**	**Trans. Product**
MH-HEU	67	mordenite (10), quartz (4)	4.7	Na, Ca, K, Mg	203 (8)	56(5)	8(3)	60(15)	CHA/GIS
Z-HEU	67	feldspar (13), cristabolite (12)	4.6	K, Na, Mg, Ca	140 (20)	30(2)	9(4)	56(17)	GIS
N-HEU	72	feldspar (25), quartz (2)	5.0	K, Ca, Mg, Na	134 (12)	44(5)	16(5)	62(15)	GIS

S-HEU	67	feldspar (29), quartz (4)	5.0	K, Ca, Mg, Na	157 (38)	33(5)	9(2)	59(29)	GIS

The framework Si/Al ratio of a zeolite is a key trait in determining its ability to adsorb cationic species, from both a capacity and a selectivity perspective. A more aluminous framework in Mud Hills clinoptilolite could rationalise the enhanced exchange performance, particularly its ability to adsorb strontium effectively. However, bulk elemental analysis suggests that MH-HEU has a Si/Al ratio comparable to the other species (5.2.3). Further analysis estimating the clinoptilolite framework Si/Al ratio is not viable due to the presence of elementally variable constituents such as mordenite and glass (however, the Si/Al ratio of clinoptilolite in N- and S-HEU is likely greater than the bulk values, due to the significant feldspar content). Further, ^{27}Al NMR data suggests insignificant quantities of extra-framework aluminium, which could artificially decrease framework Si/Al ratios, for all four materials (5.2.5.2). No credible evidence has been found to suggest that MH-HEU possesses a more aluminous framework than the other clinoptilolites in studied in this work.

The species of incumbent cations are also critical when considering the properties of ion-exchange materials. The cation's fundamental properties (diameter, charge density) dictate the strength of the adhesion and hence how likely ion-exchange is to occur. According to XRF and SEM-EDS analysis (5.2.3.2), MH-HEU has been shown to contain approximately half the quantity of potassium, a notorious strong-binding cation to clinoptilolite, compared to the other materials (5.2.3.2). This is likely to have a positive effect on the ion-exchange performance. Furthermore, all four clinoptilolites contain significant quantities of divalent species, namely calcium and magnesium (5.2.3.2). In sodium washing experiments (5.2.3.2), MH-HEU expels approximately twice the quantity of these species in comparison to the other clinoptilolites. From the current data, it is impossible to discern whether magnesium and calcium are thermodynamically or kinetically less favoured inside Mud Hills clinoptilolite's framework. However, the fact they appear to be more readily expelled could be a key factor in explaining the improved performance of Mud Hills clinoptilolite, especially as strontium cations are likely to reside in similar sites due to chemical similarity. When combined, the low potassium content and readily expelled divalent species also result in a much greater sodium content being attained after sodium-wash.

Rate studies (5.2.8) suggest all four clinoptilolites studied in this work reached equilibrium in similar timeframes, for both caesium and strontium sorption. However, MH-HEU does adsorb at a faster rate because of its increased capacity (there are a greater number of available binding sites). Another factor that could render Mud Hills more effective than its isostructural counterparts is its amorphous content, which makes up $\sim$14 % of its total composition. This hypothesis would be difficult to probe as characterisation of amorphous materials is notoriously difficult, even when in isolation. Another complex possibility is that MH-HEU has an inherently superior framework aluminium distribution for the sorption of strontium – likely in the form of more aluminium pairs in proximity of the strontium binding sites. Experimentally determining this would likely require a multitude of solid-state NMR experiments and modelling support, so is outside the scope of this project. However, inspection of the caesium and strontium capacity plot (Figure 5.17) does not support this theory, with MH-HEU falling significantly below the $y = 0.33x$ reference line (similarly to Z- and S-HEU), which depicts a 'perfect' balance between caesium and strontium adsorption capacity. A summary of the hypotheses discussed is presented in Table 5.15.

Table 5.15. Summary of hypotheses for Mud Hills clinoptilolite's superiority discussed in this chapter.

Hypothesis	**Comments**
More aluminous framework	Not likely to be a factor. Elemental analysis (XRF, SEM-EDS) and ^{29}Si NMR suggest comparable bulk aluminium content. ^{27}Al NMR also suggests negligible extra-framework aluminium for all four materials. However, Si/Al estimates for the frameworks in isolation are unobtainable.
Favourable resident cationic species	Likely to be a factor. Fewest incumbent potassium cations of all the clinoptilolites. Also possesses the greatest sodium content.

Higher zeolitic content	Likely to be a factor. PXRD and Rietveld analysis suggest greater zeolitic content. MH-HEU also has a greater caesium and strontium capacity in comparison to other clinoptilolites (although this is not fully accounted for when considering the zeolitic contents).
Favourable framework aluminium distribution (more Al pairs)	Unlikely to be a factor; MH-HEU resides similarly below $y = 0.33x$ line in capacity comparison graph.
Higher proportion of 'mobile' cations	Likely to be a factor. Approximately 50 % more expulsion of divalent species observed in sodium-washing experiments.
Beneficial amorphous content	Insufficient evidence to make a judgment, although MH-HEU has more amorphous content than the other clinoptilolites.
Faster rate of exchange	Possibly a factor. The time required to reach equilibrium is comparable with other clinoptilolites; however, the greater capacity of MH-HEU essentially means it can adsorb at a faster rate.
Faster internal macroscopic diffusion	Possibly a factor. XCT imaging suggests larger crystallite domains, which could accelerate solution diffusion.

In conclusion, this work has identified several potential factors which could rationalise the enhanced ion-exchange performance of Mud Hills clinoptilolite. The most significant of these being: more zeolitic material, fewer incumbent potassium cations and more mobile divalent species. Overall, it is probably a combination of these factors (among others) contributing to the improved performance, as opposed to a single factor. Whilst this work is certainly not exhaustive, it has highlighted some base-level findings which could aid in the streamlining of future industrial ion-exchange material sourcing, in addition to providing solid foundations for further work.

CHAPTER 6: CONCLUSIONS

6.1 The Development of Composite Zeolite Materials for Caesium and Strontium Abatement

Currently, ion-exchange materials play a key role in the remediation of nuclear effluent, notably for the sequestration of caesium-137 and strontium-90. A variety of both synthetic and natural materials, including zeolites, crystalline silicotitanates and hexacyanoferrates, have been successfully deployed to selectively remove either (or both) of the radionuclides from a variety of aqueous waste streams[21, 70]. However, the decommissioning of nuclear sites worldwide is expected to produce contaminated effluent with previously unseen compositions, where established materials may prove unsuitable. It is therefore paramount that research is undertaken to develop new ion-exchange materials, facilitating efficient processing of future waste.

This work investigated the production of composite zeolite materials from existing natural zeolite sources, by means of a partial interzeolite transformation. In Chapter 3, the partial transformation from a natural mordenite to zeolite P was explored, whereas Chapter 4 investigated the partial transformation of four natural clinoptilolites into zeolite P. From both parent material framework types, a high level of control of the respective phase ratios was exhibited through manipulation of the solution basicity: a composite with a desired blend of phases was readily produced from all precursors. Partial transformation enhanced the strontium uptake in excess calcium, whereas caesium uptake was poor in fully-transformed materials in the presence of potassium.

Caesium and strontium capacities of the parent materials and selected partially/fully converted analogues, were determined through equilibrium adsorption isotherms. The determined capacities of all materials tested is displayed in Figure 6.1. Transformation induced a significant increase in both caesium and strontium capacity (although overall a greater increase was observed in the case of strontium). Batch experimental trials also showed a remarkable increase in the rate of strontium uptake by both partially and fully transformed materials, in comparison to their parent materials.

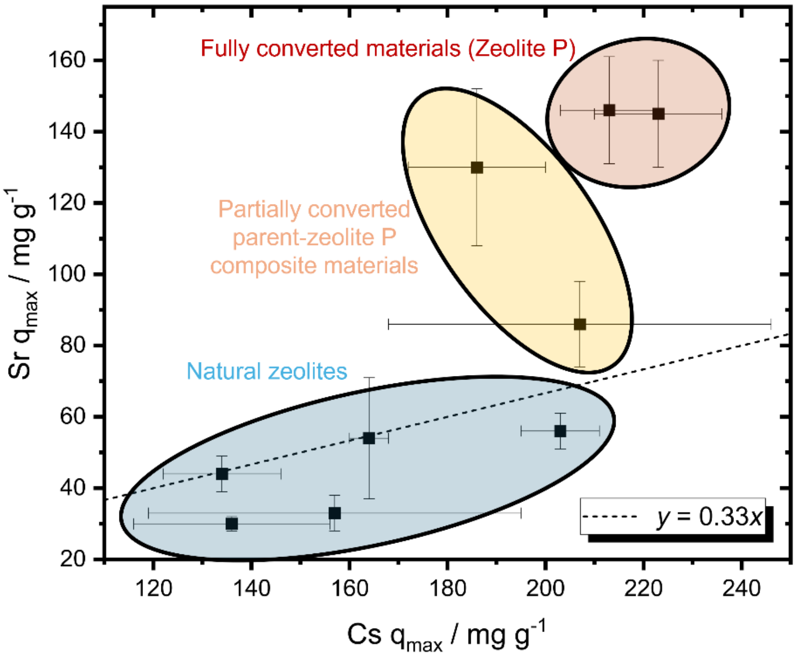

Figure 6.1. Caesium and strontium capacities of all materials tested in this work, as determined through adsorption isotherms.

Further, a methodology to develop granular composite zeolites from mordenite and clinoptilolite precursors has been established. These materials have been extensively imaged using a combination of SEM and XCT, which, when combined with image-guided, local diffraction patterns, has enabled macroscale mechanisms of transformation to be postulated. Additionally, *in-situ* local diffraction experiments demonstrated the parent framework remains functional after partial transformation, even when it appears enclosed by nascent zeolite P. Due to the large (400-600 μm) diameter, these granules are also capable of deployment in flow systems, a desirable trait from an industrial perspective. This has been demonstrated in a series of column-based RIX experiments, where a significant improvement in radionuclide abatement was demonstrated in composite zeolites compared to natural precursors and Mud Hills clinoptilolite.

Previous studies investigating the hydrothermal interzeolite transformations of natural zeolites have generally worked with powdered material and targeted full conversion[76-80]. This work has pioneered the utilisation of partial transformation to enhance performance. There are several possible benefits to this approach, including retention of parent selectivity, the development of mesoporosity and the ability to form column-ready granular analogues. Furthermore, materials developed *via* this route are inherently cheap to produce and essentially infinite in supply, given the immense abundance of natural zeolites. At time of writing, in-depth analysis of granules produced though hydrothermal transformation of natural zeolite analogues has not been reported. This work details the macrostructure of both partially- and fully-converted granules using a combination of XCT and image-guided local diffraction measurements. Furthermore, a methodology for tracking the caesium exchange into a single bi-phasic granule has been established, highlighting the power and versatility of K11 DIAD.

Results presented in this work indicate that these composite materials are proficient alternatives to Mud Hills clinoptilolite and have serious potential in the field of nuclear decommissioning. This was further confirmed in recent studies conducted by NNL, where composite zeolite materials presented in this work outperformed Mud Hills clinoptilolite in Harwell simulant: a simulant liquor containing a matrix of competitive cations. RIX uptake curves from these experiments are presented in Figure 6.2.

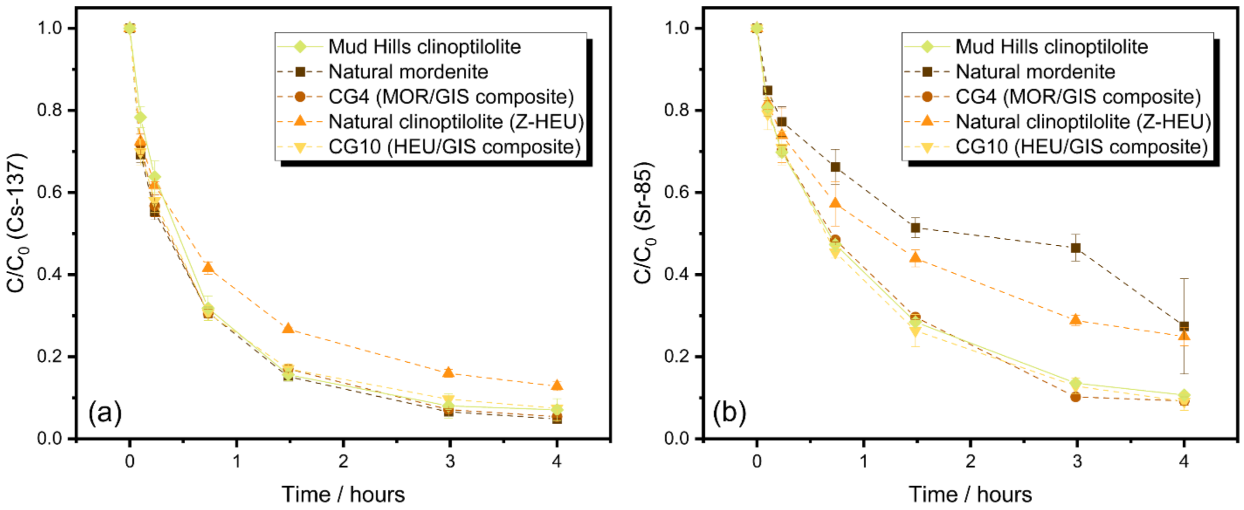

Figure 6.2. Reservoir activities from RIX trials using Harwell simulant (conducted by NNL). (a) Cs-137 activity throughout duration of experiment. (b) Sr-85 activity throughout duration of experiment.

6.2. The Peculiarity of Mud Hills Clinoptilolite

Mud Hills clinoptilolite was initially selected as the ion-exchange material for SIXEP, Sellafield, due to its ability to remove caesium and strontium from nuclear wastewaters[70]. During the selection process, it interestingly outperformed other clinoptilolites, particularly in its ability to take up strontium[70]. To date, a rationale for these enhanced adsorption properties has not been presented. Furthermore, at the current rate of usage, material stockpiles will deplete in the mid 2030's, meaning it is important alternatives are explored[70]. Both natural zeolites and materials produced by other means (such as the composites from this work) are potential possible solutions. To streamline the selection process, understanding of the origins behind the adsorption behaviours of Mud Hills clinoptilolite would be beneficial, especially if the natural zeolite route is eventually preferred. In this work, factors including the resident cationic species, zeolitic content, cationic exchange capacity, increased mobility of cations (particularly divalent species) and a more porous internal morphology are all presented as possible explanations for the materials' inherent superiority. Overall, it is likely that a combination of these factors are responsible. Despite additional experiments being required to draw definitive conclusions, this work provides an excellent foundation to build from and could aid in streamlining the selection process of future ion-exchange materials for the nuclear industry.

CHAPTER 7: FURTHER WORK

One of the key aims of this research was to develop a process that produced viable ion-exchange materials for the nuclear industry. While the caesium and strontium uptake data are promising, no quantitative measurements have been conducted regarding the structural integrity of the granular materials produced (friable materials are undesirable in flow systems). Further, despite the focus of this work being how the solution basicity influences the transformation, changing other parameters, such as temperature or time, can also produce a series of composites from the studied parent zeolites. A complete set of structural integrity data for a vast library of composites produced through a suite of parameters would allow for the most suitable materials, where ion-exchange performance is not compromised for mechanical strength, to be carried forward. Another key area of future work is investigating the applicability of this method to other materials, such as other mordenites and clinoptilolites, in addition to other natural zeolites. It would be particularly interesting to see the effect of more siliceous/aluminous parent zeolites.

To further understand the origins of the enhanced ion-exchange properties, further characterisation on the composites is necessary. Notably, porosimetry measurements would enable surface areas and pore distributions to be determined, which would reveal the development of any mesopores. Additionally, more work investigating the individual ion-exchange performance of both the parent phase and nascent zeolite P within the composite materials would streamline the development future composites formed *via* this route. Initially, this could be achieved through a combination of ion-exchange experiments and cross-sectional elemental mapping, which could be achieved *via* granule dissection and subsequent SEM-EDS measurements. Furthermore, the *in-situ* elemental tracking methodology could be expanded to include strontium and quantified. This would enable the real-time, space-resolved tracking of both caesium and strontium within a single composite granule.

Work following on from research presented in Chapter 5 could consolidate rationale explaining the enhanced ion-exchange properties of Mud Hills clinoptilolite, in comparison to other natural clinoptilolites. Firstly, similar analysis of more clinoptilolites could be performed; this would build up a database of material properties from which any disparities of Mud Hills clinoptilolite could readily be identified. XCT measurements should be a priority given the vast differences observed between Mud Hills clinoptilolite and the other natural zeolites assessed in this work. If Mud Hills clinoptilolite does have a seemingly more porous internal morphology, then the rate of exchange at different depths within a granule should be probed using methods akin to those described in Chapter 3 (3.2.9). Other avenues for exploration include investigating the rate of expulsion of the resident divalent species, high resolution diffraction studies to determine the cationic positions in different clinoptilolites and XPDF analysis for enhanced characterisation of amorphous content.

LIST OF REFERENCES

1. IAEA, *Climate Change and Nuclear Power 2020*, IAEA, 2020.
2. NEI, Nuclear Fuel, https://www.nei.org/fundamentals/nuclear-fuel, (accessed 8/03/2024).
3. WNA, How is uranium made into nuclear fuel?, https://world-nuclear.org/nuclear-essentials/how-is-uranium-made-into-nuclear-fuel.aspx, (accessed 08/03/2023).
4. WNA, Physics of Uranium and Nuclear Energy, https://world-nuclear.org/information-library/nuclear-fuel-cycle/introduction/physics-of-nuclear-energy.aspx, (accessed 31/1/2024).
5. APS, December 1938: Discovery of Nuclear Fission, https://www.aps.org/publications/apsnews/200712/physicshistory.cfm, (accessed 8/03/2024).
6. WNA, Outline History of Nuclear Energy, https://www.world-nuclear.org/information-library/current-and-future-generation/outline-history-of-nuclear-energy.aspx, (accessed 21/1/2020, 2020).
7. UK_Health_Security_Agency, Basic concepts of radiation, https://www.gov.uk/government/publications/nuclear-emergencies-information-for-the-public/basic-concepts-of-radiation).
8. Live Chart of Nuclides, https://www-nds.iaea.org/relnsd/vcharthtml/VChartHTML.html, (accessed 18/12/19).
9. W. E. Grummitt and G. Wilkinson, *Nature*, 1946, **158**, 163-163.
10. NDA, UK Radioactive Waste Inventory 2022, https://www.gov.uk/government/publications/uk-radioactive-waste-and-material-inventory-2022/uk-radioactive-waste-inventory-2022).
11. ONR, Low Level Waste Repository, https://www.onr.org.uk/sites/low-level-waste-repository.htm, (accessed 31/1/2024).
12. M. C. G. C. Partnership, Finland first country to start disposal of spent fuel, https://midcopeland.workinginpartnership.org.uk/finland-first-country-to-start-final-disposal-of-spent-fuel, 2023).
13. R. O. A. Rahman, H. A. Ibrahium and Y. T. Hung, *Water*, 2011, **3**, 551-565.
14. J. C. Fanning, *Coordination Chemistry Reviews*, 1995, **140**, 27-36.
15. A. Burger and I. Lichtscheidl, *Science of the Total Environment*, 2018, **618**, 1459-1485.
16. K. C. Stamoulis, P. A. Assimakopoulos, K. G. Ioannides, E. Johnson and P. N. Soucacos, *Science of the Total Environment*, 1999, **229**, 165-182.
17. F. E. Butler, *Nature*, 1961, **189**, 848-849.
18. M. T. Harrison, presented in part at the 2nd International Summer School on Nuclear Glass Wasteform - Structure, Properties and Long-Term Behavior (SumGLASS), France, Sep 23-27, 2013.
19. J. Weatherill, PhD, University of Manchester 2018.
20. M. Howden, *Proceedings of the Institution of Mechanical Engineers Part a-Journal of Power and Energy*, 1987, **201**, 1-15.
21. J. Lehto, R. Koivula, H. Leinonen, E. Tusa and R. Harjula, *Separation and Purification Reviews*, 2019, **48**, 122-142.
22. BBC, Fukushima disaster: What happened at the nuclear plant?, https://www.bbc.co.uk/news/world-asia-56252695, (accessed 3/2/2024).
23. BBC, The science behind the Fukushima waste water release, https://www.bbc.co.uk/news/world-asia-66610977, (accessed 03/02/2024).
24. B. Nogrady, *Nature*, 2023, **618**, 894-895.

25. M. Moshoeshoe, M. Nadiye-Tabbiruka and V. Obuseng, *Am. J. Mater. Sci*, 2017, **7**, 196-221.
26. IZA, Zeolite Framework Types, https://europe.iza-structure.org/IZA-SC/ftc_table.php, (accessed 4/5/2022).
27. L. Tosheva, K. Garbev, G. J. Miller and B. Mihailova, *Crystal Growth & Design*, 2023, **23**, 3834-3844.
28. IZA, Framework Type GIS, https://europe.iza-structure.org/IZA-SC/material_tm.php?STC=GIS, (accessed 31/1/2024).
29. IZA, Mordenite, http://www.iza-online.org/natural/Datasheets/Mordenite/mordenite.htm, (accessed 19/1/2024).
30. IZA, Framework Type LTA, https://europe.iza-structure.org/IZA-SC/material_tm.php?STC=LTA, (accessed 31/1/2024).
31. M. Stöcker, *Microporous and Mesoporous Materials*, 2005, **82**, 257-292.
32. J. Dedecek, D. Kaucky, B. Wichterlová and O. Gonsiorová, *Physical Chemistry Chemical Physics*, 2002, **4**, 5406-5413.
33. B. C. Knott, C. T. Nimlos, D. J. Robichaud, M. R. Nimlos, S. Kim and R. Gounder, *Acs Catalysis*, 2018, **8**, 770-784.
34. S. Kwon, C. Kim, E. Han, H. Lee, H. S. Cho and M. Choi, *J. Hazard. Mater.*, 2021, **408**, 124419.
35. Z. R. Mi, T. T. Lu, J. N. Zhang, R. R. Xu and W. F. Yan, *Chemical Research in Chinese Universities*, 2022, **38**, 9-17.
36. C. J. Adams, A. Araya, S. W. Carr, A. P. Chapple, K. R. Franklin, P. Graham, A. R. Minihan, T. J. Osinga and J. A. Stuart, in *Progress in Zeolite and Microporous Materials, Pts a-C*, eds. H. Chon, S. K. Ihm and Y. S. Uh, 1997, vol. 105, pp. 1667-1674.
37. W. Loewenstein, *American Mineralogist*, 1954, **39**, 92-96.
38. W. Depmeier, *Physics and Chemistry of Minerals*, 1988, **15**, 419-426.
39. R. Thompson, Nucleation, growth and seeding in zeolite synthesis, http://www.iza-online.org/synthesis/VS_2ndEd/Nucleation.htm, (accessed 31/1/2024).
40. J. Grand, H. Awala and S. Mintova, *Crystengcomm*, 2016, **18**, 650-664.
41. S. Mintova, *Verified Sytheses of Zeolitic Materials* Sythesis Commission of the International Zeolite Association 2016.
42. R. L. Hay, *Pure and Applied Chemistry*, 1986, **58**, 1339-1342.
43. New_World_Encyclopedia, Zeolite, https://www.newworldencyclopedia.org/entry/Zeolite, (accessed 1/2/2024).
44. J. Williams, *Zeolites (Natural)*, U.S. Geological Survey, 2023.
45. J. Robert D. Crangle, *Zeolites*, USGS, 2018.
46. C. Baerlocher, *Atlas of Zeolite Framework Types* Elsevier, 2001.
47. J. v. B. Cejka, H. Corma, A. Schueth, F, *Introduction to Zeolite Molecular Sieves*, Elsevier, 2007.
48. S. Narayanan, P. Tamizhdurai, V. L. Mangesh, C. Ragupathi, P. S. Krishnan and A. Ramesh, *Rsc Advances*, 2021, **11**, 250-267.
49. R. Bingre, B. Louis and P. Nguyen, *Catalysts*, 2018, **8**, 163.
50. C. P. Huang and O. J. Hao, *Environmental Technology Letters*, 1989, **10**, 863-874.
51. X. S. Wang, H. Q. Hu and C. Sun, *Separation Science and Technology*, 2007, **42**, 1215-1230.
52. S. B. Wang and Y. L. Peng, *Chemical Engineering Journal*, 2010, **156**, 11-24.
53. M. Jimenez-Reyes, P. T. Almazan-Sanchez and M. Solache-Rios, *Journal of Environmental Radioactivity*, 2021, **233**, 106610.
54. E. Johan, T. Yamada, M. W. Munthali, P. Kabwadza-Corner, H. Aono and N. Matsue, in *5th Sustainable Future for Human Security*, eds. A. Trihartono and B. McLellan, 2015, vol. 28, pp. 52-56.

55. M. W. Munthali, E. Johan, H. Aono and N. Matsue, *Journal of Asian Ceramic Societies*, 2015, **3**, 245-250.
56. IZA, Clinoptilolite, http://www.iza-online.org/natural/Datasheets/Clinoptilolite/clinoptilolite.htm, (accessed 19/1/2024, 2024).
57. Mindat, Clinoptilolite Subgroup, https://www.mindat.org/min-1082.html, (accessed 24/11/2023).
58. D. L. Bish and J. M. Boak, *Natural Zeolites: Occurrence, Properties, Applications*, 2001, **45**, 207-216.
59. P. Ambrozova, J. Kynicky, T. Urubek and V. D. Nguyen, *Molecules*, 2017, **22**, 1107.
60. H. Oguz and V. Kurtoglu, *British Poultry Science*, 2000, **41**, 512-517.
61. A. Liebscher, *Bodenkultur*, 1991, **42**, 367-376.
62. A. Acosta, E. Lon-Wo and O. Dieppa, *Cuban Journal of Agricultural Science*, 2005, **39**, 311-316.
63. I. Nikolakakis, V. Dotas, A. Kargopoulos, L. Hatzizisis, D. Dotas and Z. Ampas, *Turkish Journal of Veterinary & Animal Sciences*, 2013, **37**, 682-686.
64. S. Leung, S. Barrington, Y. Wan, X. Zhao and B. El-Husseini, *Bioresource Technology*, 2007, **98**, 3309-3316.
65. P. J. Leggo, B. Ledesert and G. Christie, *Science of the Total Environment*, 2006, **363**, 1-10.
66. H. N. Aainaa, O. H. Ahmed and N. M. Ab Majid, *Plos One*, 2018, **13**, 1-19.
67. S. K. Pavelic, J. S. Medica, D. Gumbarevic, A. Filosevic, N. Przulj and K. Pavelic, *Frontiers in Pharmacology*, 2018, **9**, 1350.
68. S. Wasielewski, E. Rott, R. Minke and H. Steinmetz, *Molecules*, 2021, **26**, 114.
69. M. Vocciante, A. D. D'Auris, A. Finocchi, M. Tagliabue, M. Bellettato, A. Ferrucci, A. P. Reverberi and S. Ferro, *Journal of Cleaner Production*, 2018, **198**, 480-487.
70. A. Dyer, J. Hriljac, N. Evans, I. Stokes, P. Rand, S. Kellet, R. Harjula, T. Moller, Z. Maher, R. Heatlie-Branson, J. Austin, S. Williamson-Owens, M. Higgins-Bos, K. Smith, L. O'Brien, N. Smith and N. Bryan, *Journal of Radioanalytical and Nuclear Chemistry*, 2018, **318**, 2473-2491.
71. A. Abusafa and H. Yucel, *Separation and Purification Technology*, 2002, **28**, 103-116.
72. C. Baerlocher and W. M. Meier, *Zeitschrift Fur Kristallographie Kristallgeometrie Kristallphysik Kristallchemie*, 1972, **135**, 339-346.
73. X. Querol, N. Moreno, J. C. Umana, A. Alastuey, E. Hernandez, A. Lopez-Soler and F. Plana, *International Journal of Coal Geology*, 2002, **50**, 413-423.
74. C. C. Chen, N. Zhang, Y. C. Liu, Y. J. Wang and J. Chen, *Acta Physico-Chimica Sinica*, 2016, **32**, 349-355.
75. D. Novembre, D. Gimeno and A. Del Vecchio, *Scientific Reports*, 2021, **11**, 4872.
76. H. Mimura and K. Akiba, *Journal of Nuclear Science and Technology*, 1993, **30**, 436-443.
77. S. J. Kang, K. Egashira and A. Yoshida, *Applied Clay Science*, 1998, **13**, 117-135.
78. C. Delaspozas, D. D. Quintanilla, J. Perezpariente, R. Roquemalherbe and M. Magi, *Zeolites*, 1989, **9**, 33-39.
79. Y. F. Wang and F. Lin, *J. Hazard. Mater.*, 2009, **166**, 1014-1019.
80. J. Minato, Y. J. Kim, H. Yamada, Y. Watanabe, K. Tamura, S. Yokoyama, S. B. Cho, Y. Komatsu and G. W. Stevens, *Separation Science and Technology*, 2004, **39**, 3739-3751.
81. M. D. Oleksiak, A. Ghorbanpour, M. T. Conato, B. P. McGrail, L. C. Grabow, R. K. Motkuri and J. D. Rimer, *Chemistry-a European Journal*, 2016, **22**, 16078-16088.
82. S. Hansen, U. Hakansson and L. Falth, *Acta Crystallographica Section C-Crystal Structure Communications*, 1990, **46**, 1361-1362.
83. J. G. Nery, Y. P. Mascarenhas and A. K. Cheetham, *Microporous and Mesoporous Materials*, 2003, **57**, 229-248.

84. M. Atkins, F. P. Glasser and J. J. Jack, *Waste Management*, 1995, **15**, 127-135.
85. IZA, Chabazite Series, http://www.iza-online.org/natural/Datasheets/Chabazite/chabazite.htm, (accessed 19/1/2024).
86. A. F. Gualtieri and E. Passaglia, *European Journal of Mineralogy*, 2006, **18**, 351-359.
87. St._Cloud_Mining, Bowie, https://www.stcloudmining.com/operations-products/bowie-chabazite/, (accessed 02/02/2024).
88. A. Saini and T. Koyama, *Mrs Bulletin*, 2016, **41**, 952-953.
89. T. Tsukada, K. Uozumi, T. Hijikata, T. Koyama, K. Ishikawa, S. Ono, S. Suzuki, M. S. Denton, R. Keenan and G. Bonhomme, *Journal of Nuclear Science and Technology*, 2014, **51**, 886-893.
90. W. Baek, S. Ha, S. Hong, S. Kim and Y. Kim, *Microporous and Mesoporous Materials*, 2018, **264**, 159-166.
91. J. H. Wang, H. W. Zhao, G. Haller and Y. D. Li, *Applied Catalysis B-Environmental*, 2017, **202**, 346-354.
92. J. Pan, S. Shi, Y. Yuan and R. F. Lobo, *Chemcatchem*, 2022, **14**, 1867.
93. I. M. Dahl, H. Mostad, D. Akporiaye and R. Wendelbo, *Microporous and Mesoporous Materials*, 1999, **29**, 185-190.
94. Q. J. Zhu, M. Hinode, T. Yokoi, J. N. Kondo, Y. Kubota and T. Tatsumi, *Microporous and Mesoporous Materials*, 2008, **116**, 253-257.
95. J. E. Miller, N. E. Brown, J. L. Krumhansl, D. E. Trudell, R. G. Anthony and C. V. Philip, presented in part at the American-Chemical-Society Symposium on Science Technology for Disposal of Radioactive Tank Wastes, Las Vegas, Nv, Sep 07-11, 1997.
96. E. L. Campbell, A. M. Westesen, S. K. Fiskum, G. J. Lumetta and R. A. Peterson, *Separation Science and Technology*, 2022, **57**, 1714-1723.
97. A. Nearchou, T. Y. Chen, D. S. Parsons, L. O'Brien, N. A. Hodge, L. Abrahamsen-Mills, P. K. Allan and J. A. Hriljac, *Apl Materials*, 2023, **11**, 011105.
98. R. George and J. A. Hriljac, *Mrs Advances*, 2017, **2**, 729-734.
99. R. Pophale, P. A. Cheeseman and M. W. Deem, *Physical Chemistry Chemical Physics*, 2011, **13**, 12407-12412.
100. J. L. Li, M. K. Gao, W. F. Yan and J. H. Yu, *Chemical Science*, 2023, **14**, 1935-1959.
101. V. Valtchev, G. Majano, S. Mintova and J. Pérez-Ramírez, *Chemical Society Reviews*, 2013, **42**, 263-290.
102. A. Ates and C. Hardacre, *Journal of Colloid and Interface Science*, 2012, **372**, 130-140.
103. M. Y. Prajitno, D. Harbottle, N. Hondow, H. G. Zhang and T. N. Hunter, *Journal of Environmental Chemical Engineering*, 2020, **8**, 102991.
104. B. K. Singh, Y. Kim, S. Kwon and K. Na, *Catalysts*, 2021, **11**, 1541.
105. R. L. Hartman and H. S. Fogler, *Langmuir*, 2007, **23**, 5477-5484.
106. K. Valdivies-Cruz, A. Lam and C. M. Zicovich-Wilson, *Journal of Physical Chemistry C*, 2017, **121**, 2652-2660.
107. G. T. Kerr, *Journal of Physical Chemistry*, 1967, **71**, 4155-4167.
108. D. L. Gallup, *Geothermics*, 1998, **27**, 485-501.
109. J. C. Groen, J. A. Moulijn and J. Perez-Ramirez, *Journal of Materials Chemistry*, 2006, **16**, 2121-2131.
110. A. Ates and G. Akgul, *Powder Technology*, 2016, **287**, 285-291.
111. D. Verboekend, G. Vilé and J. Pérez-Ramírez, *Crystal Growth & Design*, 2012, **12**, 3123-3132.
112. D. Verboekend and J. Perez-Ramirez, *Catalysis Science & Technology*, 2011, **1**, 879-890.
113. Z. Hasan, J. W. Jun, C. U. Kim, K. E. Jeong, S. Y. Jeong and S. H. Jhung, *Materials Research Bulletin*, 2015, **61**, 469-474.
114. J. C. Groen, J. C. Jansen, J. A. Moulijn and J. Perez-Ramirez, *Journal of Physical Chemistry B*, 2004, **108**, 13062-13065.

115. J. Devos, M. A. Shah and M. Dusselier, *Rsc Advances*, 2021, **11**, 26188-26210.
116. R. M. Barrer, *Journal of the Chemical Society*, 1948, 127-132.
117. M. Dusselier and M. E. Davis, *Chemical Reviews*, 2018, **118**, 5265-5329.
118. C. G. Li, M. Moliner and A. Corma, *Angewandte Chemie-International Edition*, 2018, **57**, 15330-15353.
119. D. Suhendar, Buchari, R. R. Mukti, Ismunandar and Iop, Semarang, INDONESIA, 2017.
120. T. Sano, M. Itakura and M. Sadakane, *Journal of the Japan Petroleum Institute*, 2013, **56**, 183-197.
121. S. Goel, S. I. Zones and E. Iglesia, *Chemistry of Materials*, 2015, **27**, 2056-2066.
122. S. I. Zones, *Journal of the Chemical Society-Faraday Transactions*, 1991, **87**, 3709-3716.
123. S. Abelló, A. Bonilla and J. Pérez-Ramírez, *Applied Catalysis a-General*, 2009, **364**, 191-198.
124. J. Devos, M. L. Bols, D. Plessers, C. Van Goethem, J. W. Seo, S. J. Hwang, B. F. Sels and M. Dusselier, *Chemistry of Materials*, 2020, **32**, 273-285.
125. H. Jon, K. Nakahata, B. W. Lu, Y. Oumi and T. Sano, *Microporous and Mesoporous Materials*, 2006, **96**, 72-78.
126. P. Wagner, Y. Nakagawa, G. S. Lee, M. E. Davis, S. Elomari, R. C. Medrud and S. I. Zones, *Journal of the American Chemical Society*, 2000, **122**, 263-273.
127. K. Honda, M. Itakura, Y. Matsuura, A. Onda, Y. Ide, M. Sadakane and T. Sano, *Journal of Nanoscience and Nanotechnology*, 2013, **13**, 3020-3026.
128. W. Qin, R. Jain, F. C. R. Hernandez and J. D. Rimer, *Chemistry-a European Journal*, 2019, **25**, 5893-5898.
129. D. Schwalbe-Koda, Z. Jensen, E. Olivetti and R. Gómez-Bombarelli, *Nature Materials*, 2019, **18**, 1177-1181.
130. M. B. dos Santos, K. C. Vianna, H. O. Pastore, H. M. G. Andrade and A. J. S. Mascarenhas, *Microporous and Mesoporous Materials*, 2020, **306**, 110413.
131. J. Devos, S. Robijns, C. Van Goethem, I. Khalil and M. Dusselier, *Chemistry of Materials*, 2021, **33**, 2516-2531.
132. H. Fichtnerschmittler, U. Lohse, G. Engelhardt and V. Patzelova, *Crystal Research and Technology*, 1984, **19**, 1-3.
133. T. W. Swaddle, *Coordination Chemistry Reviews*, 2001, **219**, 665-686.
134. C. S. Cundy and P. A. Cox, *Microporous and Mesoporous Materials*, 2005, **82**, 1-78.
135. M. D. Oleksiak, J. A. Soltis, M. T. Conato, R. L. Penn and J. D. Rimer, *Chemistry of Materials*, 2016, **28**, 4906-4916.
136. T. Nishitoba, T. Nozaki, S. Park, Y. Wang, J. N. Kondo, H. Gies and T. Yokoi, *Catalysts*, 2020, **10**, 1204.
137. D. V. Bruter, V. S. Pavlov and Ivanova, II, *Petroleum Chemistry*, 2021, **61**, 251-275.
138. L. X. Tang, K. G. Haw, Y. Y. Zhang, Q. R. Fang, S. L. Qiu and V. Valtchev, *Microporous and Mesoporous Materials*, 2019, **280**, 306-314.
139. O. E. Kartal and I. Onal, *Chemical Engineering Communications*, 2008, **195**, 1043-1057.
140. W. W. Lestari, D. N. Hasanah, R. Putra, R. R. Mukti, K. D. Nugrahaningtyas and Iop, Semarang, INDONESIA, 2017.
141. G. A. Mamedova, *Moscow University Chemistry Bulletin*, 2019, **74**, 46-53.
142. I. Goto, M. Itakura, S. Shibata, K. Honda, Y. Ide, M. Sadakane and T. Sano, *Microporous and Mesoporous Materials*, 2012, **158**, 117-122.
143. Z. F. Shi, Y. Wang, C. G. Meng and X. Y. Liu, *Microporous and Mesoporous Materials*, 2013, **176**, 155-161.
144. L. Van Tendeloo, E. Gobechiya, E. Breynaert, J. A. Martens and C. E. A. Kirschhock, *Chemical Communications*, 2013, **49**, 11737-11739.
145. S. Khodabandeh and M. E. Davis, *Chemical Communications*, 1996, DOI: 10.1039/cc9960001205, 1205-1206.

146. S. Khodabandeh and M. E. Davis, *Microporous Materials*, 1997, **12**, 347-359.
147. H. Kazemian, H. Modarres and H. G. Mobtaker, *Journal of Radioanalytical and Nuclear Chemistry*, 2003, **258**, 551-556.
148. A. De Fazio, P. Brotzu, M. R. Ghiara, M. L. Fercia, R. Lonis and A. Sau, *Periodico Di Mineralogia*, 2008, **77**, 79-91.
149. S. Hong and W. Um, *Minerals*, 2021, **11**, 252.
150. H. Kazemian, H. Modarress, M. Kazemi and F. Farhadi, *Powder Technology*, 2009, **196**, 22-25.
151. M. Kamali, S. Vaezifar, H. Kolahduzan, A. Malekpour and M. R. Abdi, *Powder Technology*, 2009, **189**, 52-56.
152. Mindat, Mordenite, https://www.mindat.org/min-2779.html, (accessed 14.9.2023, 2023).
153. E. T. C. Vogt and B. M. Weckhuysen, *Chemical Society Reviews*, 2015, **44**, 7342-7370.
154. C. Duan, X. Zhang, R. Zhou, Y. Hua, J. Chen and L. Zhang, *Catalysis Letters*, 2011, **141**, 1821-1827.
155. J. J. Zheng, J. H. Ma, Y. Wang, Y. D. Bai, X. W. Zhang and R. F. Li, *Catalysis Letters*, 2009, **130**, 672-678.
156. M. J. Mendoza-Castro, Z. P. Qie, X. L. Fan, N. Linares and J. Garcia-Martinez, *Nature Communications*, 2023, **14**, 1256.
157. M. J. Mendoza-Castro, E. De Oliveira-Jardim, N. T. Ramirez-Marquez, C. A. Trujillo, N. Linares and J. Garcia-Martinez, *Journal of the American Chemical Society*, 2022, **144**, 5163-5171.
158. P. Atkins, *Physical Chemistry*, Oxford University Press, 2014.
159. A. R. West, *Basic Solid State Chemistry*, Wiley, 1993.
160. A. M. Glazer, *Crystallography - A Very Short Introduction*, Oxford University Press, 2016.
161. S. V. Borisov and N. V. Podberezskaya, *Journal of Structural Chemistry*, 2012, **53**, 1-3.
162. H. M. Rietveld, *Acta Crystallographica*, 1967, **22**, 151-152.
163. H. M. Rietveld, *Journal of Applied Crystallography*, 1969, **2**, 65-71.
164. T. Egami and S. J. L. Billinge, *Underneath the Bragg peaks: structural analysis of complaex materials* Pergamon, 2003.
165. V. Petkov, S. J. L. Billinge, P. Larson, S. D. Mahanti, T. Vogt, K. K. Rangan and M. G. Kanatzidis, *Physical Review B*, 2002, **65**, 092105.
166. E. Margui and R. van Grieken, *X-ray fluorescence spectrometry and related techniques: an introduction*, Momentum Press, New York, 2013.
167. J. Nolte, *ICP Emission Spectrometry: A Practicle Guide* Wiley, 2021.
168. R. Thomas, *Practical Guide to ICP-MS*, Taylor and Francis Group, 2013.
169. L. Reimer, *Scanning Electron Microscopy - Physics of Image Formation and Microanalysis* Springer, 1998.
170. NHS, CT scan, https://www.nhs.uk/conditions/ct-scan/, (accessed 21/3/2014).
171. E. Samei and P. Norbert, *Computed Tomography: Approaches, Applications, and Operations*, Springer, 2020.
172. C. Reinhard, M. Drakopoulos, S. I. Ahmed, H. Deyhle, A. James, C. M. Charlesworth, M. Burt, J. Sutter, S. Alexander, P. Garland, T. Yates, R. Marshall, B. Kemp, E. Warrick, A. Pueyos, B. Bradnick, M. Nagni, A. D. Winter, J. Filik, M. Basham, N. Wadeson, O. N. F. King, N. Aslani and A. J. Dent, *Journal of Synchrotron Radiation*, 2021, **28**, 1985-1995.
173. R. J. Abraham, *Introduction to NMR Spectroscopy*, Wiley, 1988.
174. S. E. Ashbrook and D. M. Dawson, *Nuclear Magnetic Resonance, Vol 45*, 2016, **45**, 1-52.
175. IAEA, Live Chart of Nuclides, https://www-nds.iaea.org/relnsd/vcharthtml/VChartHTML.html, (accessed 21/3/2024).
176. W. Ehmann and D. Vance, *Radiochemistry and Nuclear methods of Analysis*, Wiley-Blackwell, 1993.

177. M. Musah, Y. Azeh, J. Matthew, M. Umar, Z. Abdulhamid and A. Muhammad, *Caliphate Journal of Science and Technology.*, 2022, **1**, 20-26.
178. MSI - Zeoclere 30 Material Specification Data Sheet, https://www.pool-chem.co.uk/prodpdf/Zeoclere%2030%20Specification.pdf, (accessed 24/8/2023).
179. Heiltropfen, *Zeolite - general info*, 2023.
180. B. H. Toby and R. B. Von Dreele, *Journal of Applied Crystallography*, 2013, **46**, 544-549.
181. D. R. Black, D. Windover, A. Henins, J. Filliben and J. P. Cline, *Powder Diffraction*, 2011, **26**, 155-158.
182. J. Filik, A. W. Ashton, P. C. Y. Chang, P. A. Chater, S. J. Day, M. Drakopoulos, M. W. Gerring, M. L. Hart, O. V. Magdysyuk, S. Michalik, A. Smith, C. C. Tang, N. J. Terrill, M. T. Wharmby and H. Wilhelm, *Journal of Applied Crystallography*, 2017, **50**, 959-966.
183. R. Harjula, J. Lehto, E. H. Tusa and A. Paavola, *Nuclear Technology*, 1994, **107**, 272-278.
184. R. Harjula, J. Lehto, A. Paajanen, L. Brodkin and E. Tusa, *Nuclear Science and Engineering*, 2001, **137**, 206-214.
185. P. Yarnell, presented in part at the Waste Manegment 2007, Tucson, AZ, 2007.
186. J. D. Sherman, *Proceedings of the National Academy of Sciences of the United States of America*, 1999, **96**, 3471-3478.
187. G. S. Lisichenko, M; Chumak, D; Prokip, A; Shutyak, S; Maskalevich, I and Vasilkivskiy, B., *The Ukrainian Nuclear Industry: Expert review*, Bellona, 2017.
188. P. Misaelides, *Microporous and Mesoporous Materials*, 2011, **144**, 15-18.
189. S. Antkiw, *Surface Adsorptionof Cs-137 Ions on Quartz Crystals* 1954.
190. C. H. Tang, J. X. Zhu, Z. H. Li, R. L. Zhu, Q. Zhou, J. M. Wei, H. P. He and Q. Tao, *Applied Surface Science*, 2015, **355**, 1161-1167.
191. R. M. Barrer and J. Klinowski, *Journal of the Chemical Society-Faraday Transactions I*, 1974, **70**, 2362-2367.
192. L. L. Ames, *American Mineralogist*, 1961, **46**, 1120-1131.
193. J. P. Soetardji, J. C. Claudia, Y. H. Ju, J. A. Hriljac, T. Y. Chen, F. E. Soetaredjo, S. P. Santoso, A. Kurniawan and S. Ismadji, *Rsc Advances*, 2015, **5**, 83689-83699.
194. R. Roquemalherbe, C. Diazaguila, E. Regueraruiz, J. Fundoralliteras, L. Lopezcolado and M. Hernandezvelez, *Zeolites*, 1990, **10**, 685-689.
195. IZA, Analcime, http://www.iza-online.org/natural/Datasheets/Analcime/analcime, (accessed 25/11/2023, 2023).
196. R. A. Sheppard, *Diagenesis of Tuffs in the Barstow Formation, Mud Hills, San Bernardino County, California*, United States Printing Office Geological Survey, 1969.
197. G. Maurin, P. Senet, S. Devautour, P. Gaveau, F. Henn, V. E. Van Doren and J. C. Giuntini, *Journal of Physical Chemistry B*, 2001, **105**, 9157-9161.
198. G. R. Hays, W. A. Vanerp, N. C. M. Alma, P. A. Couperus, R. Huis and A. E. Wilson, *Zeolites*, 1984, **4**, 377-383.
199. J. Xu, *Solid-State NMR in Zeolite Catalysis*, Springer, 2019.
200. Y. G. Chen, T. T. Xu, C. H. Xie, H. J. Han, F. J. Zhao, J. Zhang, H. Song and B. H. Wang, *Journal of Chemical Technology and Biotechnology*, 2016, **91**, 2018-2025.
201. S. E. Ashbrook and P. Hodgkinson, *Journal of Chemical Physics*, 2018, **149**.
202. E. Lippmaa, M. Magi, A. Samoson, G. Engelhardt and A. R. Grimmer, *Journal of the American Chemical Society*, 1980, **102**, 4889-4893.
203. R. Oestrike, W. H. Yang, R. J. Kirkpatrick, R. L. Hervig, A. Navrotsky and B. Montez, *Geochimica Et Cosmochimica Acta*, 1987, **51**, 2199-2209.
204. J. B. Nagy, Z. Gabelica, G. Debras, E. G. Derouane, J. P. Gilson and P. A. Jacobs, *Zeolites*, 1984, **4**, 133-139.
205. J. Lehto, L. Brodkin, R. Harjula and E. Tusa, *Nuclear Technology*, 1999, **127**, 81-87.
206. P. Yang and T. Armbruster, *Journal of Solid State Chemistry*, 1996, **123**, 140-149.

207. V. P. Mulgundmath, F. H. Tezel, T. Saatcioglu and T. C. Golden, *Canadian Journal of Chemical Engineering*, 2012, **90**, 730-738.
208. S. P. Lee, N. Mellon, A. M. Shariff and J. M. Leveque, Univ Gadjah Mada, Dept Nucl Engn & Engn Phys, Yogyakarta, INDONESIA, 2017.
209. Q. J. Wang, J. B. Hu, L. F. Yang, Z. Q. Zhang, T. Ke, X. L. Cui and H. B. Xing, *Nature Communications*, 2022, **13**, 2955.
210. N. Li, B. Huang, X. Dong, J. S. Luo, Y. Wang, H. Wang, D. Y. Miao, Y. Pan, F. Jiao, J. P. Xiao and Z. P. Qu, *Nature Communications*, 2022, **13**, 2209.
211. L. L. Ames, *American Mineralogist*, 1960, **45**, 689-700.
212. M. Fertani-Gmati, K. Brahim, I. Khattech and M. Jemal, *Thermochimica Acta*, 2014, **594**, 58-67.
213. T. Sudo, Nisiyama, Tsutomu, Chin, Keshin and Hayashi *Geological Society of Japan* 1963, **69**, 1-14.
214. Y. Watanabe, H. Yamada, J. Tanaka and Y. Moriyoshi, *Journal of Chemical Technology and Biotechnology*, 2005, **80**, 376-380.
215. C. J. Liu, H. W. Ma and Y. Gao, *Asia-Pacific Journal of Chemical Engineering*, 2019, **14**, 2280.
216. C. J. Liu and H. W. Ma, *Asia-Pacific Journal of Chemical Engineering*, 2021, **16**, 2578.
217. J. Schwartzentruber, W. Furst and H. Renon, *Geochimica Et Cosmochimica Acta*, 1987, **51**, 1867-1874.
218. Z. P. Huo, X. Y. Xu, Z. Lü, J. Q. Song, M. Y. He, Z. F. Li, Q. Wang and L. J. Yan, *Microporous and Mesoporous Materials*, 2012, **158**, 137-140.
219. J. L. Palmer and M. E. Gunter, *American Mineralogist*, 2001, **86**, 431-437.
220. J. L. Costafreda and D. A. Martin, *Molecules*, 2021, **26**, 4676.
221. M. Abe, M. Tsuji, S. P. Qureshi and H. Uchikoshi, *Chromatographia*, 1980, **13**, 626-632.
222. N. Hikichi, K. Iyoki, Y. Yanaba, K. Ohara, T. Okubo and T. Wakihara, *Chemistry-an Asian Journal*, 2020, **15**, 2029-2034.
223. R. Simancas, M. Takemura, C. T. Chen, K. Iyoki, T. Okubo and T. Wakihara, *Journal of Non-Crystalline Solids*, 2023, **605**.
224. H. King, Feldspar, https://geology.com/minerals/feldspar.shtml#google_vignette, (accessed 10/1/2023).
225. C. M. V Nash, *The Surface Reactions of Silicate Minerals* University of Missouri, 1956.
226. M. A. Al-Ghouti, M. A. M. Khraisheh, S. J. Allen and M. N. Ahmad, *Journal of Environmental Management*, 2003, **69**, 229-238.
227. W. Ma, X. Y. Song, Y. Q. Pan, Z. H. Cheng, G. Xin, B. D. Wang and X. G. Wang, *Chemical Engineering Journal*, 2012, **193**, 381-390.
228. R. A. Shelden, W. R. Caseri and U. W. Suter, *Journal of Colloid and Interface Science*, 1993, **157**, 318-327.
229. Y. C. Zou, L. Mogg, N. Clark, C. Bacaksiz, S. Milanovic, V. Sreepal, G. P. Hao, Y. C. Wang, D. G. Hopkinson, R. Gorbachev, S. Shaw, K. S. Novoselov, R. Raveendran-Nair, F. M. Peeters, M. Lozada-Hidalgo and S. J. Haigh, *Nature Materials*, 2021, **20**, 1677-1682.
230. M. J. Semmens and W. P. Martin, *Water Research*, 1988, **22**, 537-542.
231. E. Lippmaa, M. Magi, A. Samoson, M. Tarmak and G. Engelhardt, *Journal of the American Chemical Society*, 1981, **103**, 4992-4996.
232. Y. Garcia-Basabe, I. Rodriguez-Iznaga, L. C. de Menorval, P. Llewellyn, G. Maurin, D. W. Lewis, R. Binions, M. Autie and A. R. Ruiz-Salvador, *Microporous and Mesoporous Materials*, 2010, **135**, 187-196.
233. G. M. Huntley, R. L. Luck, M. E. Mullins and N. K. Newberry, *Processes*, 2021, **9**.
234. L. D. Zhou, J. G. Guo, N. H. Yang and L. Y. Li, *Science in China Series D-Earth Sciences*, 1997, **40**, 159-165.

235. R. J. Kirkpatrick, R. A. Kinsey, K. A. Smith, D. M. Henderson and E. Oldfield, *American Mineralogist*, 1985, **70**, 106-123.
236. *US Pat.,* US4503024A, 1985.
237. Y. Liang, A. J. Jacobson and J. D. Rimer, *Acs Materials Letters*, 2021, **3**, 187-192.
238. W. van Aarle, W. J. Palenstijn, J. Cant, E. Janssens, F. Bleichrodt, A. Dabravolski, J. De Beenhouwer, K. J. Batenburg and J. Sijbers, *Optics Express*, 2016, **24**, 25129-25147.
239. N. T. Vo, M. Drakopoulos, R. C. Atwood and C. Reinhard, *Optics Express*, 2014, **22**, 19078-19086.

APPENDICES

A.1 Supplementary Information Regarding DIAD Data Acquisition

Specimen mounting, positioning, and alignment

Specimens were mounted on the top of a short length of 0.5 mm diameter polyamide tubing using Araldite two-part setting resin. The tubing was then attached to a 3 mm Huber goniometer mounting pin and placed on a Huber 1005 manual goniometer stage. This stage was then placed onto the General Tomography Stage (GTS) on the instrument. The GTS stage facilitated specimen alignment to the rotation axis (using translational stages) and provided rotation during the tomographic measurements.

Data Analysis (automated and manual)

Automatic tomographic reconstruction for the imaging data was provided through a configured SAVU plugin chain consisting of the steps outlined in Table A.1. Automated reduction of 2D diffraction data to 1-dimension (I vs. Q) plots was configured through DAWN.

Manual tomographic reconstruction of the diffraction data proceeded after integration of the diffracted intensity between the following q-ranges from the I vs. q plots: 2.151 $Å^{-1}$ – 2.188 $Å^{-1}$ for Mordenite; 1.220 $Å^{-1}$ – 1.276 $Å^{-1}$ for Na-P (GIS). Sinograms of the integrated intensity values were reconstructed using the simultaneous iterative reconstruction technique (SIRT) with the algorithm provided as part of the ASTRA toolbox[238], with 25 iterations for single slice reconstructions and 50 iterations for the multi-slice reconstruction. A consequence of the correlated imaging and diffraction system was that the rotation centre setting was provided by the Vo-centring[239] plugin reported in the imaging tomography. Note, individual diffraction frames were not corrected for changes in the sample to detector distance, as a function of the rotation angle, though possible using the tomography data, the size of the specimens was sufficiently small to warrant neglecting this for this preliminary study.

Table A.1. Automated and Manual data analysis steps and settings used for data processing.

Automated Imaging Pipeline Implemented in SAVU	1.Apply Dark and flat field correction
	2.Determine centre of rotation using Vo centring using search range
	3. Reconstruct using Filtered Back Projection from the ASTRA toolbox
Automated Diffraction Data Reduction Pipeline	1. Import nearest diffraction geometry description
	2. Mask bad pixels
	3. Reduce to I vs q using the following settings: a. Qmin= 0.97 Å-1 , Qmax = 10 $Å^{-1}$ b. nbins=3500 (dq =0.00258 Å-1) c. Pixel splitting
	4. Integrate regions corresponding to the peak positions of important phases
	5. Convert to I vs 2theta, and export for further analysis.
Manual Diffraction Tomography Pipeline	Pipeline 1. Reconstruct sinograms from D4 above using SIRT algorithm implemented in the ASTRA toolbox[238] using the following settings: a. Number of iterations: 25 (single slice), 50 (long scan) b. Centre of rotation determined from imaging (output of step 2).

A.2 Rietveld Refinements of Powder Composites Generated from Mordenite

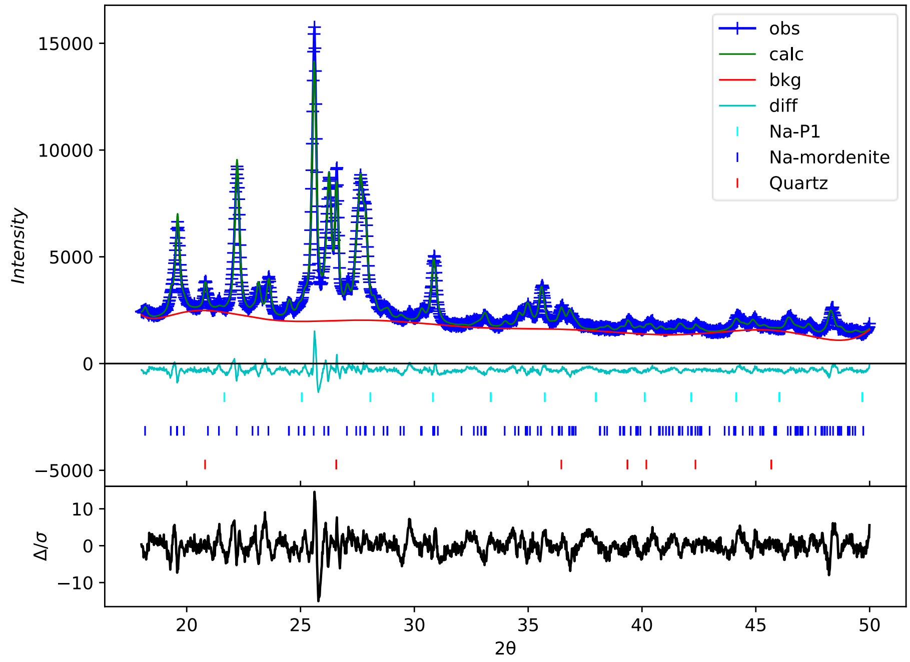

Figure A.1. Rietveld refinement of PXRD data for Na-mordenite.

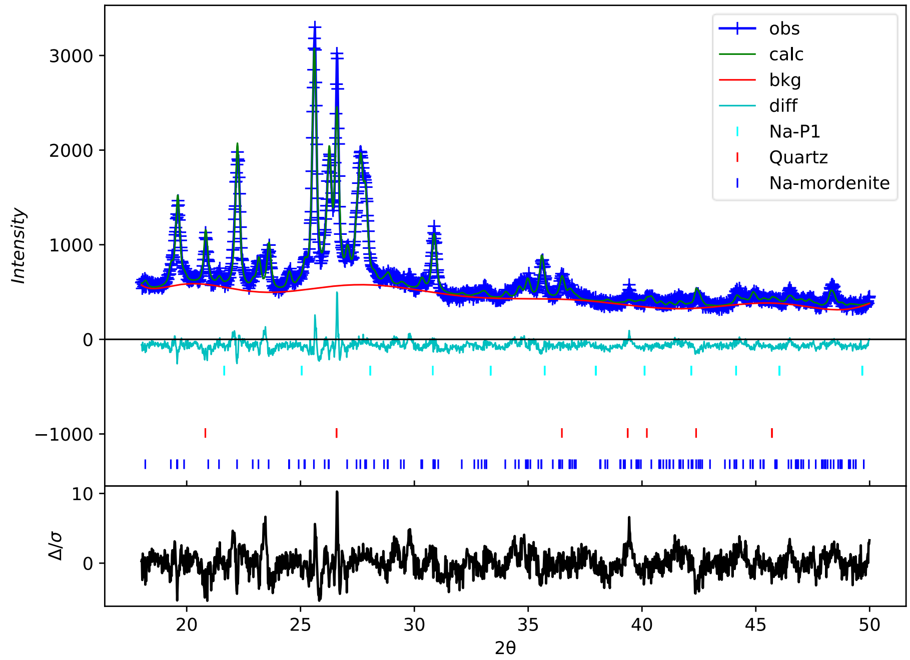

Figure A.2. Rietveld refinement of PXRD data for 0.20 M NaOH treated mordenite.

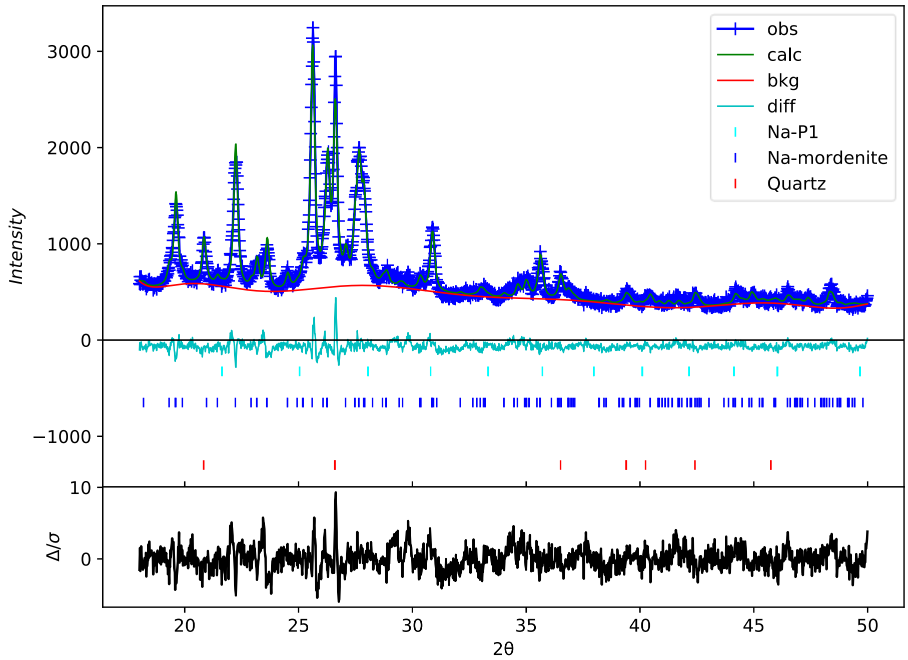

Figure A.3. Rietveld refinement of PXRD data for 0.25 M NaOH treated mordenite.

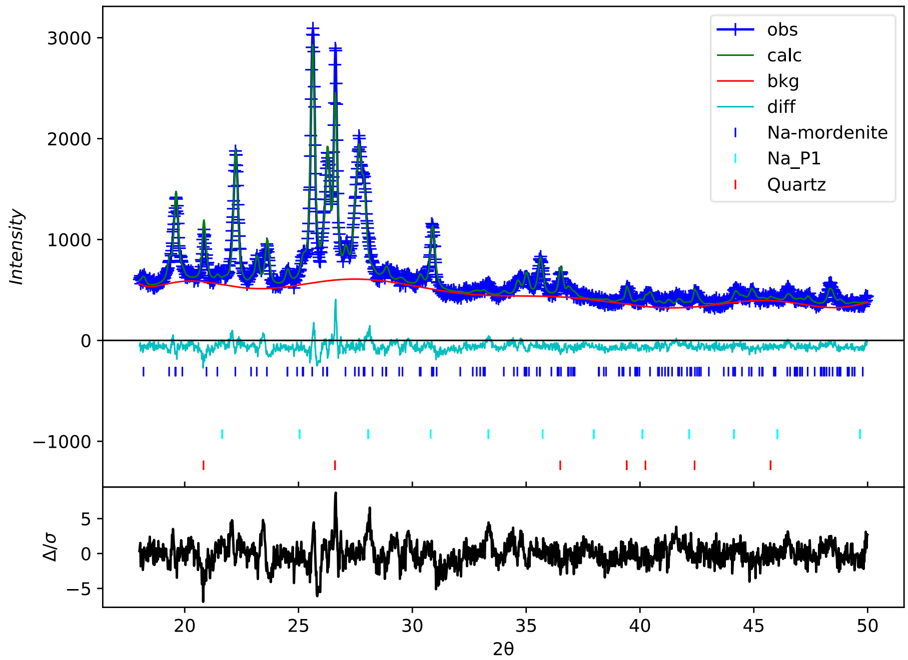

Figure A.4. Rietveld refinement of PXRD data for 0.30 M NaOH treated mordenite.

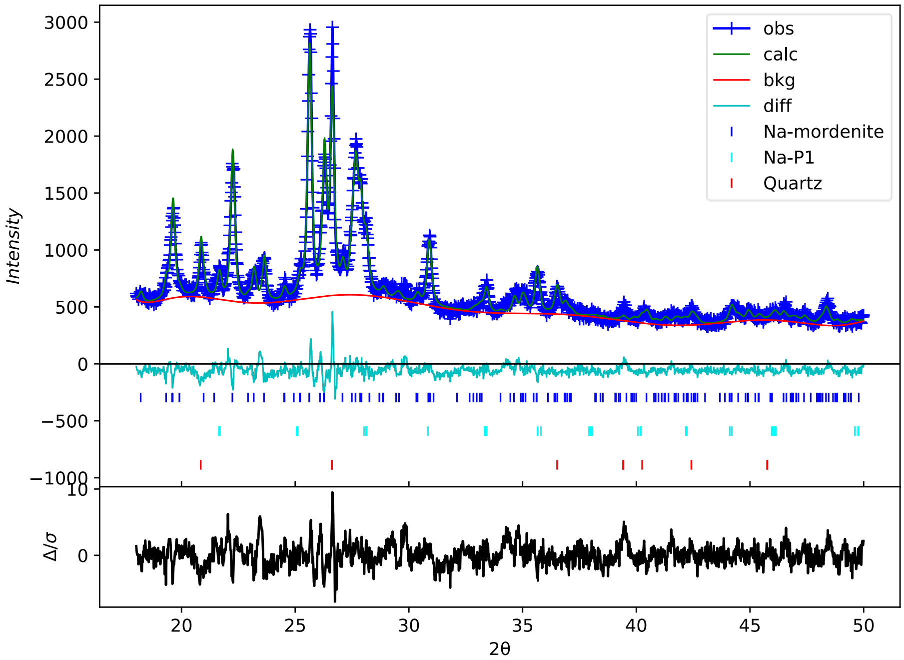

Figure A.5. Rietveld refinement of PXRD data for 0.35 M NaOH treated mordenite.

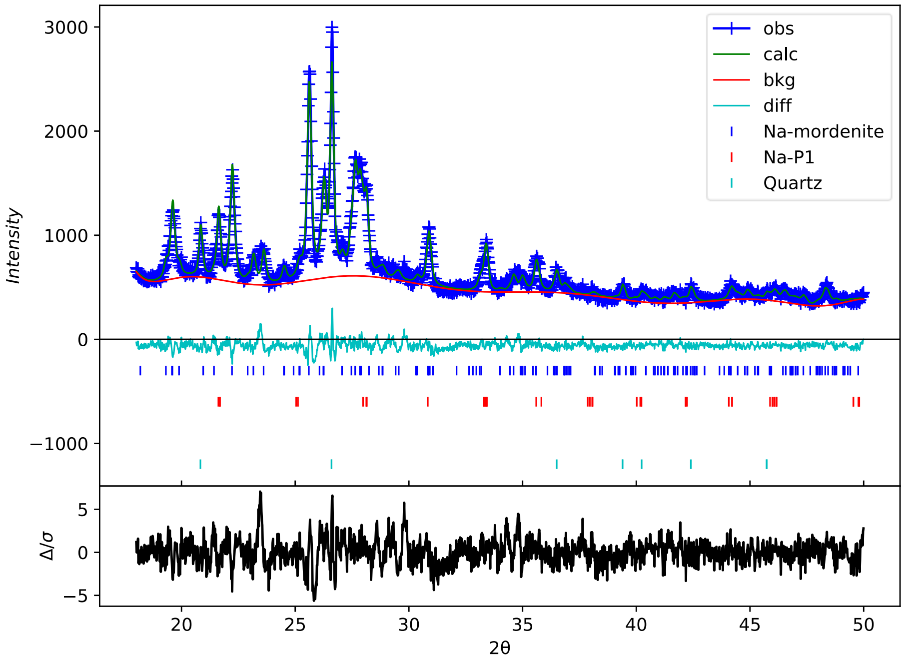

Figure A.6. Rietveld refinement of PXRD data for 0.40 M NaOH treated mordenite.

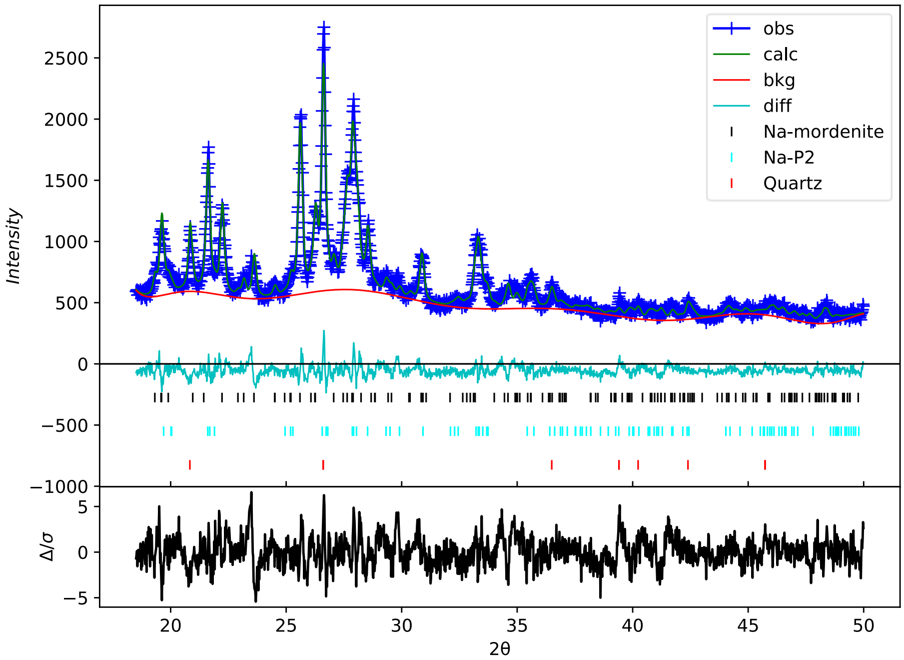

Figure A.7. Rietveld refinement of PXRD data for 0.45 M NaOH treated mordenite.

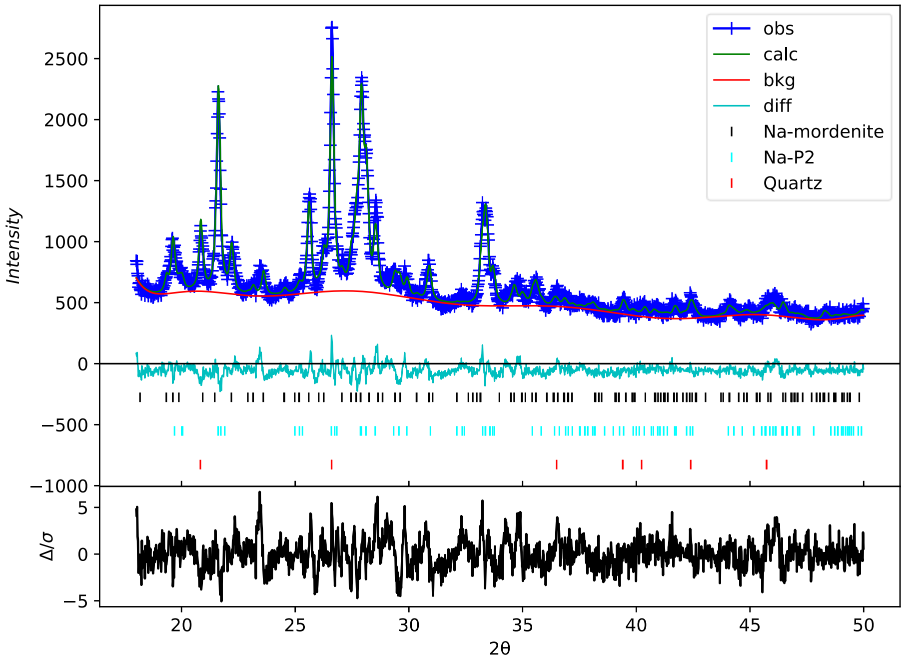

Figure A.8. Rietveld refinement of PXRD data for 0.50 M NaOH treated mordenite.

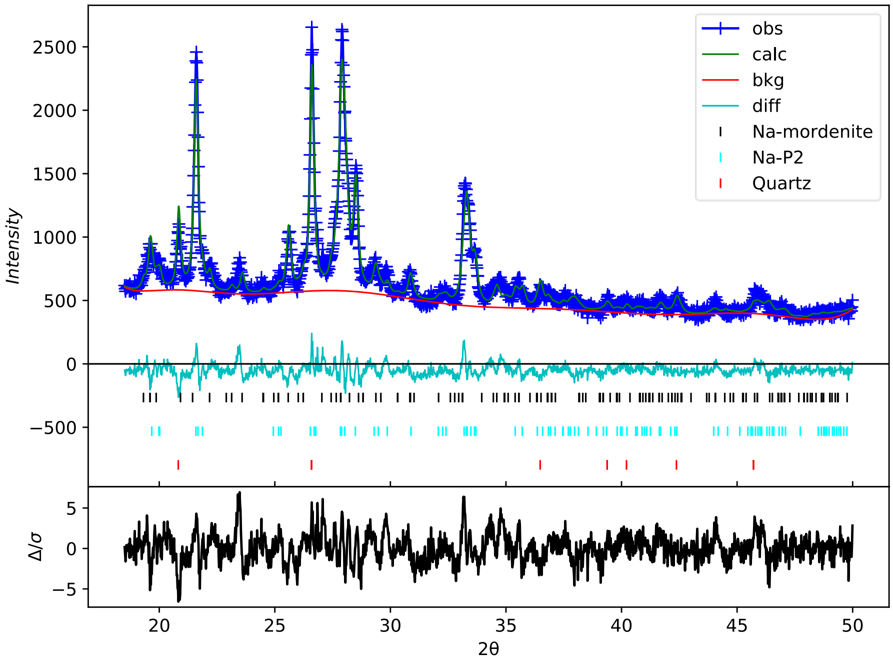

Figure A.9. Rietveld refinement of PXRD data for 0.55 M NaOH treated mordenite.

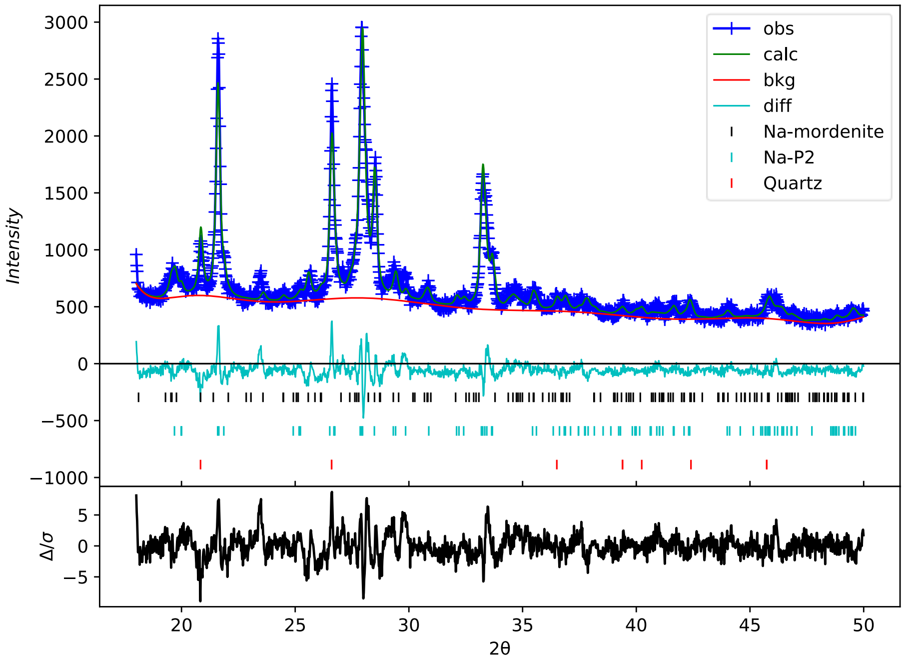

Figure A.10. Rietveld refinement of PXRD data for 0.60 M NaOH treated mordenite.

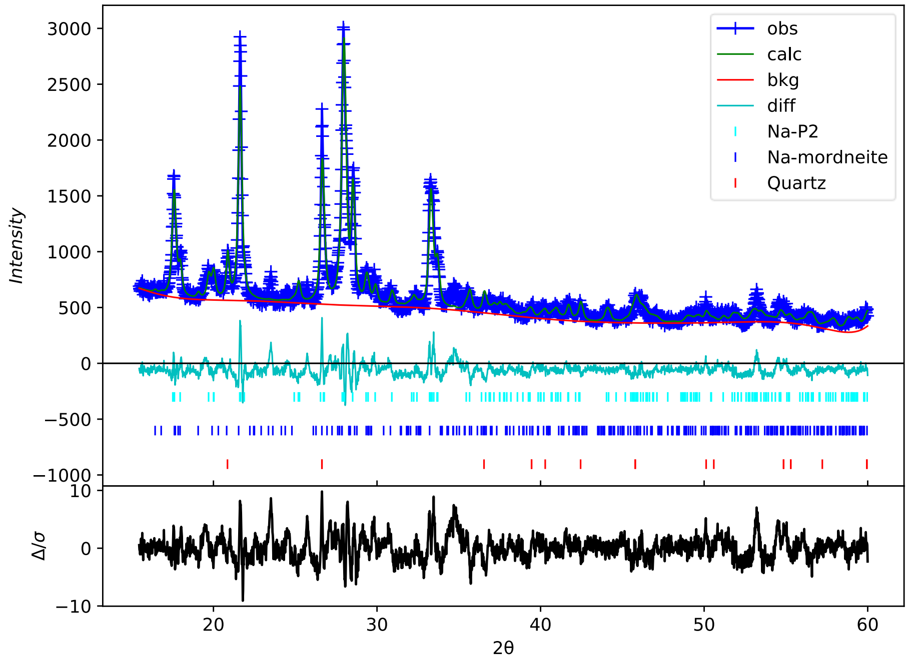

Figure A.11. Rietveld refinement of PXRD data for 0.65 M NaOH treated mordenite.

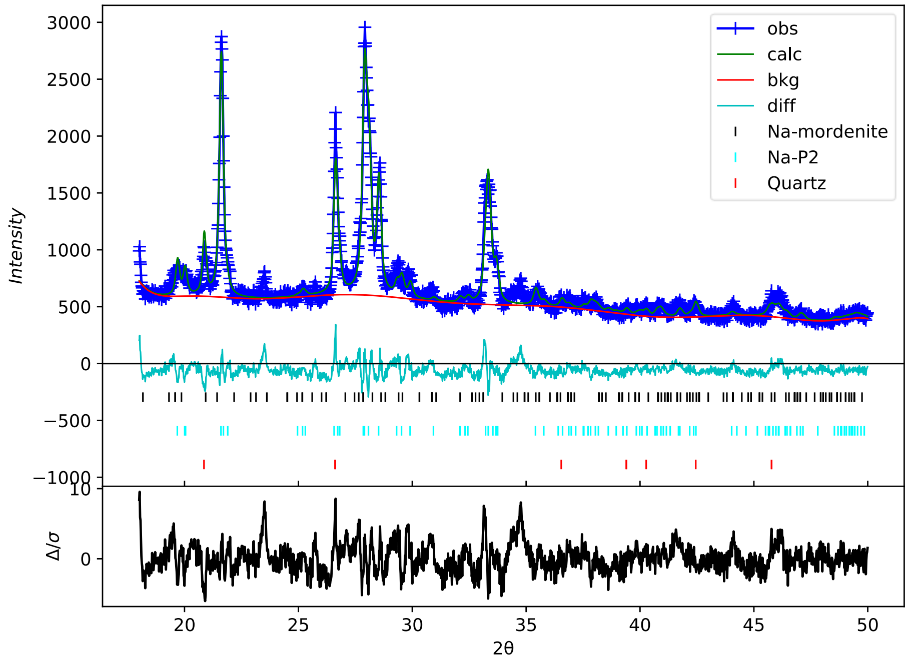

Figure A.12. Rietveld refinement of PXRD data for 0.70 M NaOH treated mordenite.

Table A.2. Summary of refinement results from powdered materials generated from mordenite.

Treatment	wR / %	GOF	MOR W_f	GIS W_f	Quartz W_f
None (Na-mordenite)	4.89	2.51	0.87(2)	0.00(1)	0.13(1)
0.20 M NaOH	6.63	1.65	0.92(1)	0.00(1)	0.08(1)
0.25 M NaOH	6.38	1.60	0.93(1)	0.00(1)	0.07(1)
0.30 M NaOH	6.42	1.61	0.95(1)	0.00(1)	0.05(1)
0.35 M NaOH	6.47	1.63	0.84(1)	0.06(1)	0.10(1)
0.40 M NaOH	5.89	1.48	0.76(1)	0.14(1)	0.11(1)
0.45 M NaOH	6.20	1.57	0.61(1)	0.29(1)	0.10(1)
0.50 M NaOH	6.39	1.61	0.32(1)	0.56(1)	0.12(1)
0.55 M NaOH	6.86	1.72	0.25(1)	0.65(1)	0.11(1)
0.60 M NaOH	7.57	1.92	0.15(1)	0.74(1)	0.11(1)
0.65 M NaOH	8.45	2.07	0.03(1)	0.89(1)	0.08(1)
0.70 M NaOH	7.89	2.00	0.00(1)	0.93(1)	0.07(1)

A.3 Parameters of Equilibrium Fitting Models Fitted to Data from Materials Produced from Mordenite

Table A.3.Parameters of Langmuir, Freundlich and Temkin isotherm models for the adsorption of caesium onto mordenite (Na-exchanged), a MOR/ GIS composite material (32:56 MOR: GIS ratio) and 'fully converted' zeolite P.

	Langmuir			**Freundlich**			**Temkin**		
Material	**q_m / mg g^{-1}**	**b**	**R^2**	**n**	**K_f**	**R^2**	**B_t**	**A_t**	**R^2**
Mordenite	164(3)	2(7)	0.999	0.16(6)	67(2)	0.833	159(29)	148(45)	0.911
Composite	164(3)	0.2(2)	0.998	0.20(3)	51(2)	0.944	129(3)	14(1)	0.978
Zeolite P	189(7)	0.06(2)	0.999	0.24(5)	43(2)	0.946	100(2)	4(1)	0.997

Table A.4. Parameters of Langmuir, Freundlich and Temkin isotherm models for the adsorption of strontium onto mordenite (Na-exchanged), a MOR/ GIS composite material (32:56 MOR: GIS ratio) and 'fully converted' zeolite P.

	Langmuir			**Freundlich**			**Temkin**		
Material	**q_m / mg g^{-1}**	**b**	**R^2**	**n**	**K_f**	**R^2**	**B_t**	**A_t**	**R^2**
Mordenite	41(4)	-0.49(9)	0.996	0.10(3)	25(2)	0.961	886(10)	22000(2000)	0.948
Composite	93(2)	0.090(5)	0.999	0.27(3)	23(2)	0.987	213(5)	8(1)	0.979
Zeolite P	125(5)	0.15(8)	0.993	0.24(3)	35(2)	0.964	176(5)	25(2)	0.984

A.4 Parameters of Kinetic Models Applied to Strontium Adsorption Data from Mordenite-Derived Materials

Table A.5. 2nd order fitting parameters for strontium kinetic isotherms.

Material	q_e / mg g^{-1}	k / g mg^{-1} h^{-1}	R^2
Na mordenite	38(2)	1.23(35)	0.9633
MOR:GIS composite (32:56)	75(4)	0.13(5)	0.9429

Table A.6. Elovich fitting parameters for strontium kinetic isotherms.

Material	α	β	R^2
Fully converted zeolite P	17878(16217)	0.08(2)	0.9421

A.5 Rietveld Refinements of Granular Composites Generated from Mordenite

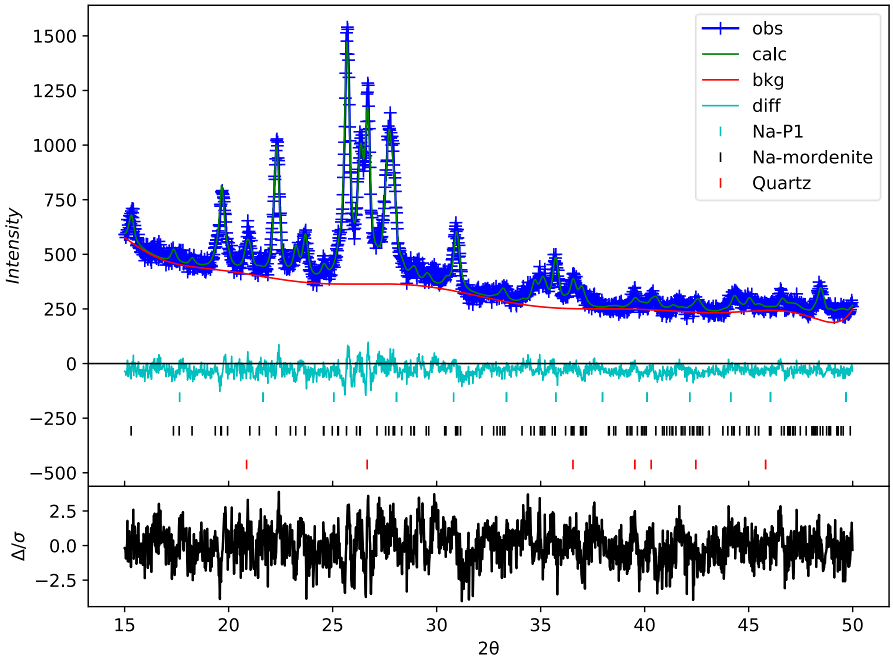

Figure A.13. Rietveld refinement of PXRD data for granular mordenite material (Na-exchanged).

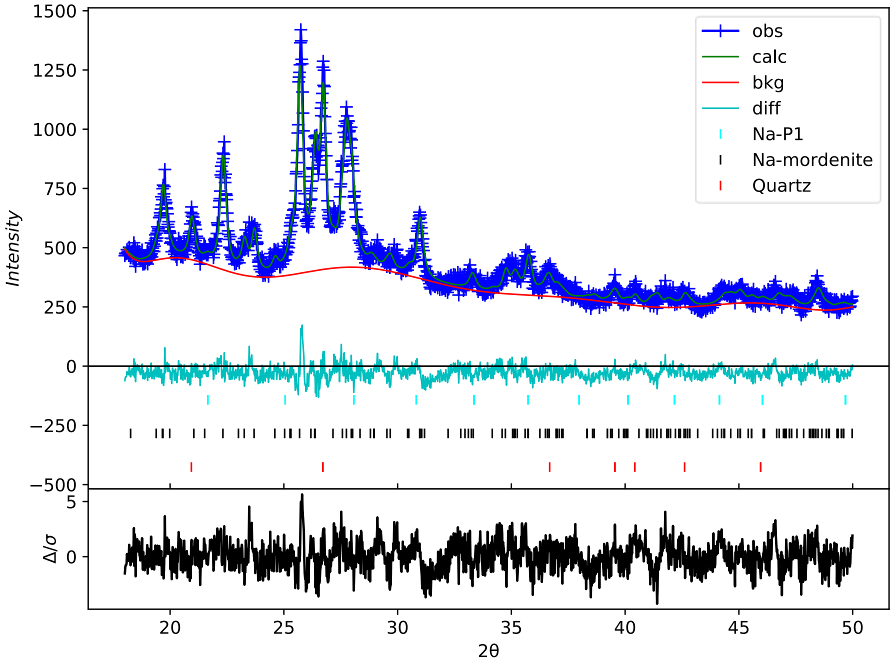

Figure A.14. Rietveld refinement of PXRD data of CG1.

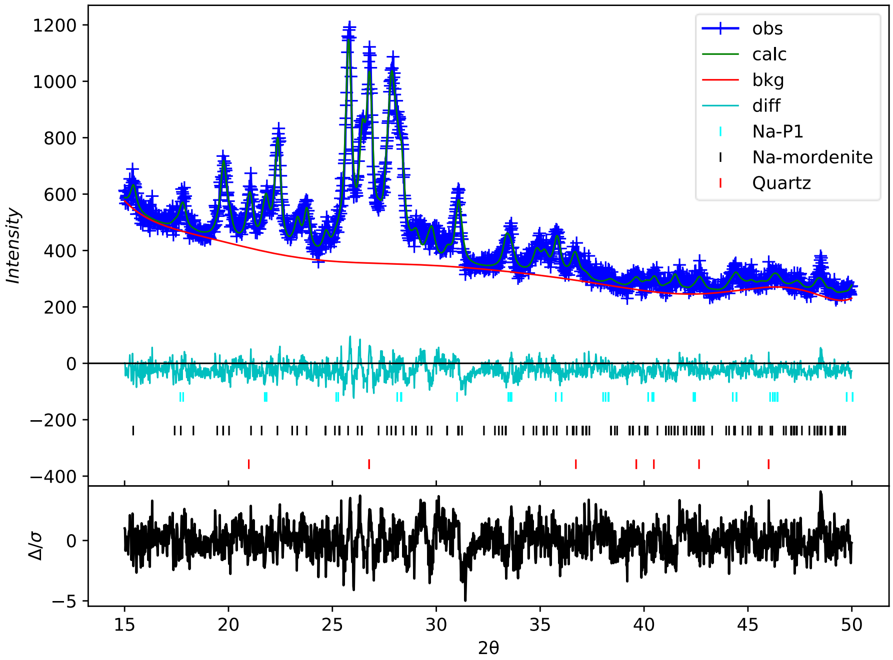

Figure A.15. Rietveld refinement of PXRD data of CG2.

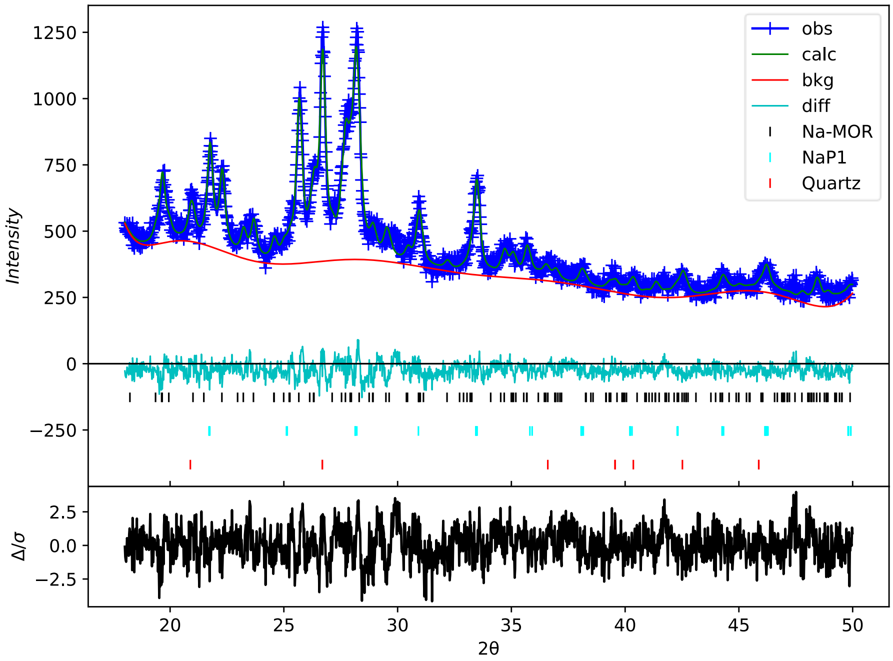

Figure A.16. Rietveld refinement of PXRD data of CG3.

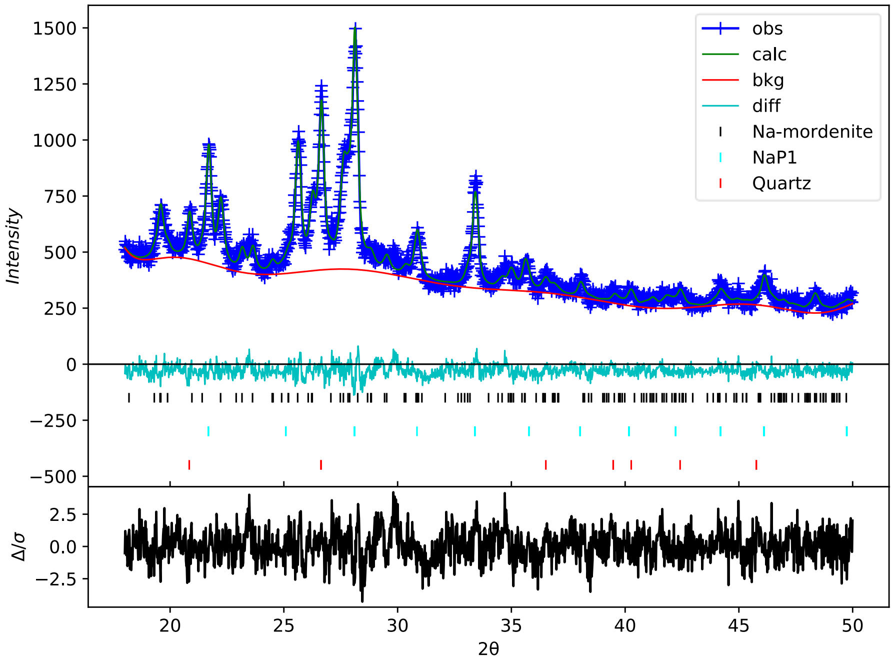

Figure A.17. Rietveld refinement of PXRD data of CG4.

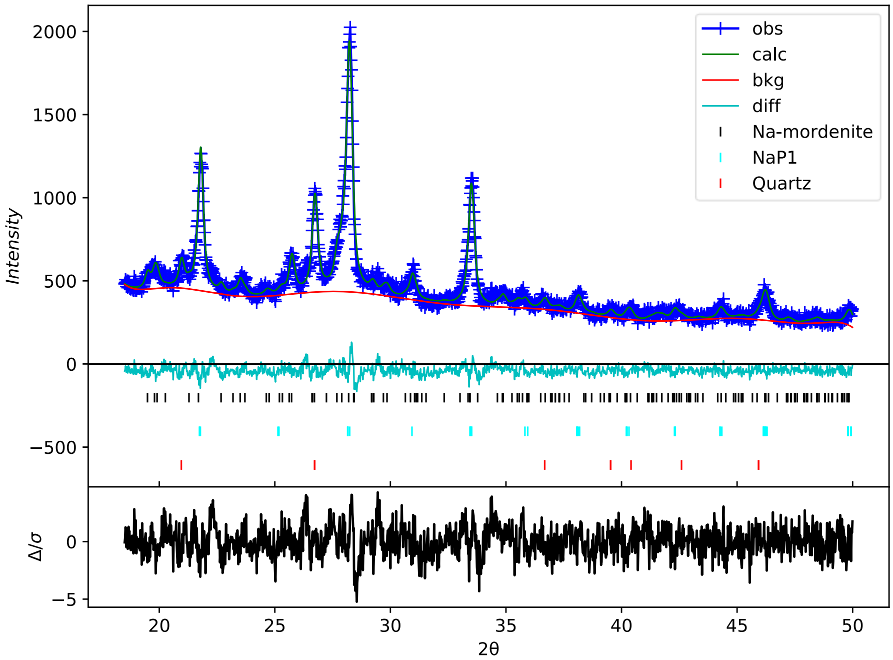

Figure A.18. Rietveld refinement of PXRD data of CG5.

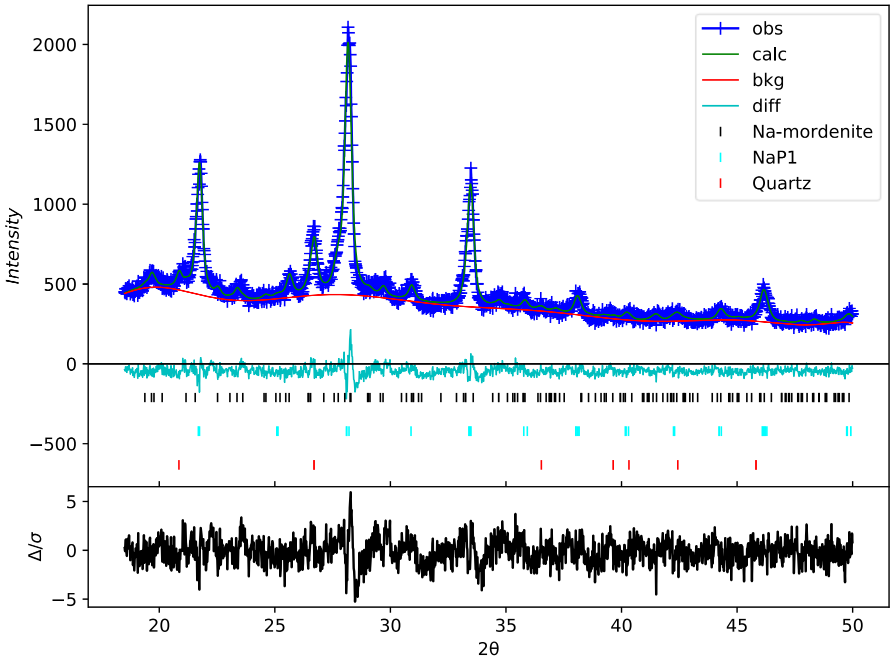

Figure A.19. Rietveld refinement of PXRD data of CG6.

Table A.7. Summary of refinement results of granular materials derived from mordenite.

Material	**wR / %**	**GOF**	**MOR W_f**	**GIS W_f**	**Quartz W_f**
Mordenite	6.12	1.25	0.92(1)	0.00(1)	0.08(1)
CG1	6.30	1.32	0.91(1)	0.01(1)	0.08(1)
CG2	5.89	1.23	0.85(1)	0.09(1)	0.06(1)
CG3	5.89	1.23	0.62(1)	0.28(1)	0.10(1)
CG4	5.64	1.19	0.57(1)	0.34(1)	0.09(1)
CG5	5.99	1.26	0.25(1)	0.67(1)	0.08(1)
CG6	6.22	1.31	0.22(6)	0.73(8)	0.05(2)

A.6 Mordenite and Quartz Reflections in a Local Diffraction Pattern of CG5

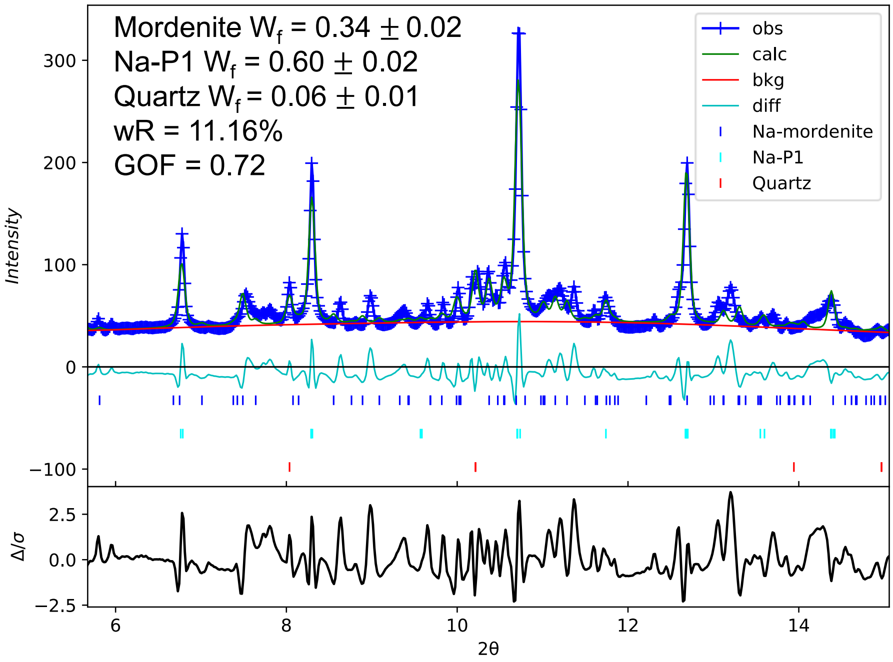

Figure A.20. Rietveld refinement of local diffraction data obtained from CG5.

A.7 Two-Parameter Exponential Decay Fits to RIX Data for Mud Hills Clinoptilolite and Materials Derived from Mordenite

Table A.8. Exponential parameters and R^2 for fits of RIX data to two-parameter exponential decay functions.

Material	Radionuclide	Y_0	A_1	T_1	A_2	T_2	R^2
Mud Hills clinoptilolite	Cs-137	2.18	22.2	55.7	75.7	349	0.993
	Sr-90	-0.84	27.8	51.9	72.3	662	0.987
Mordenite	Cs-137	3.14	32.4	58.0	64.4	366	0.997
	Sr-90	-16.7	32.9	35.3	83.7	1399	0.980
CG2	Cs-137	3.46	48.3	72.1	48.2	429	0.995
	Sr-90	3.39	33.0	32.8	63.6	598	0.991
CG4	Cs-137	4.43	46.3	53.5	49.2	412	0.999
	Sr-90	4.38	44.8	33.3	50.8	650	0.997

A.8 Rietveld Refinements of Powder Composites Generated from Z-HEU

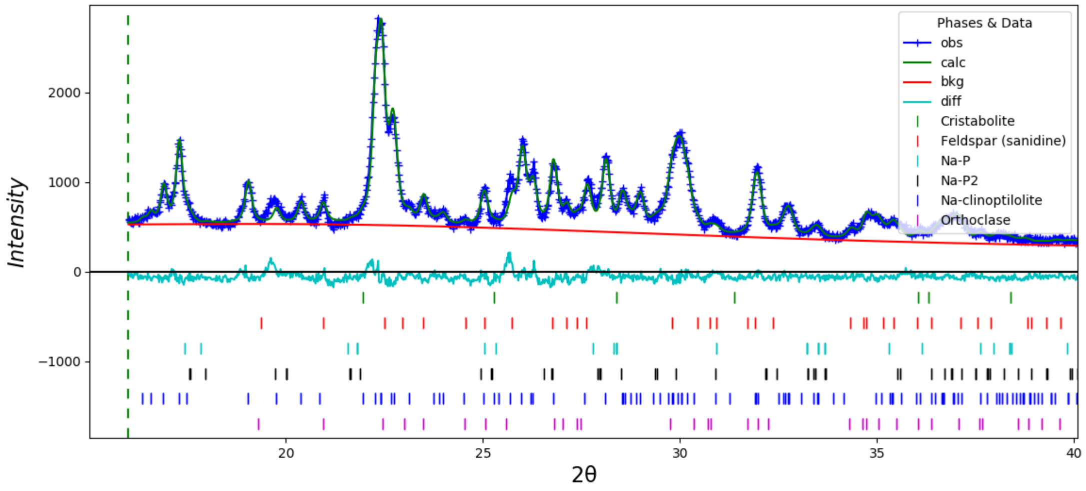

Figure A.21. Rietveld refinement of PXRD data for 0.20 M NaOH treated Z-HEU.

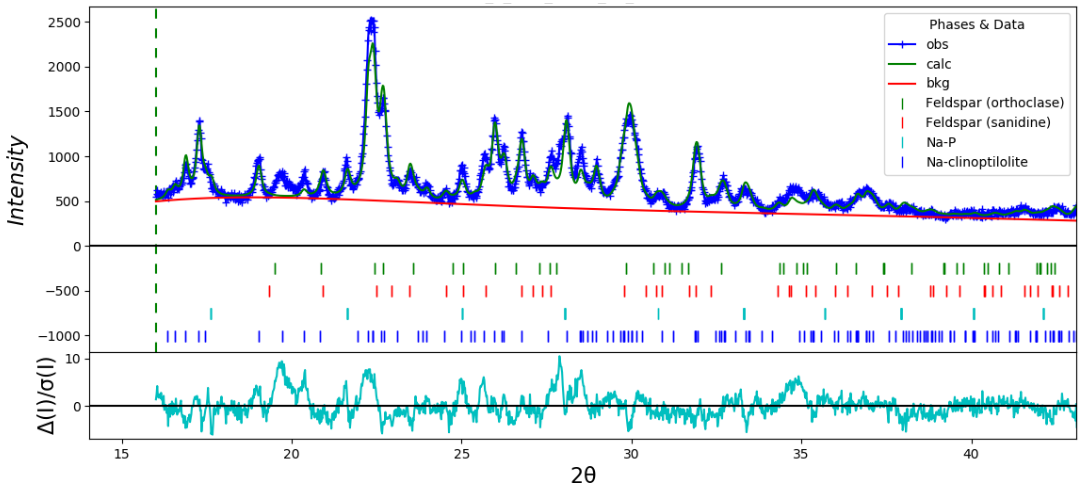

Figure A.22. Rietveld refinement of PXRD data for 0.25 M NaOH treated Z-HEU.

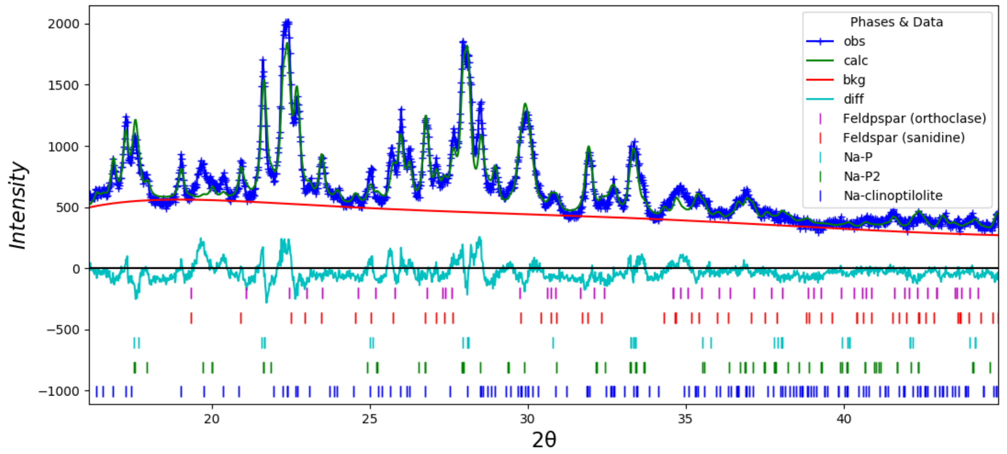

Figure A.23. Rietveld refinement of PXRD data for 0.30 M NaOH treated Z-HEU.

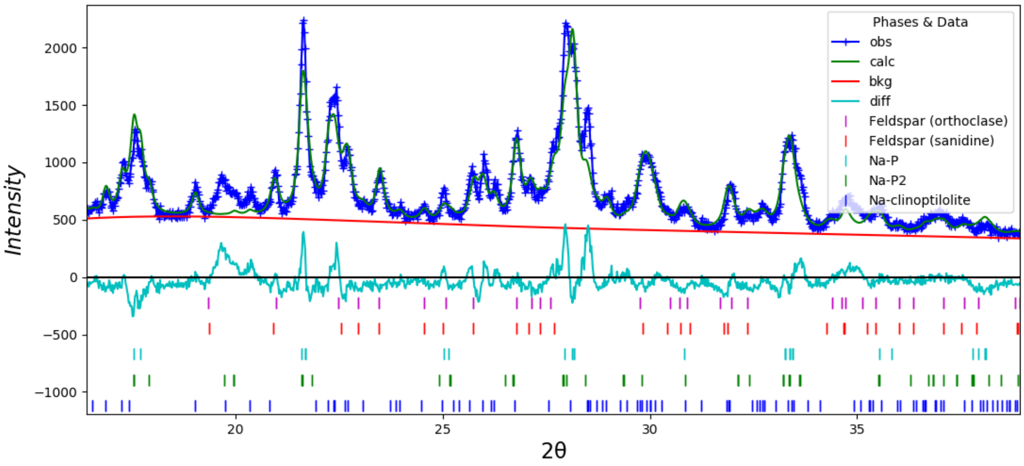

Figure A.24. Rietveld refinement of PXRD data for 0.35 M NaOH treated Z-HEU.

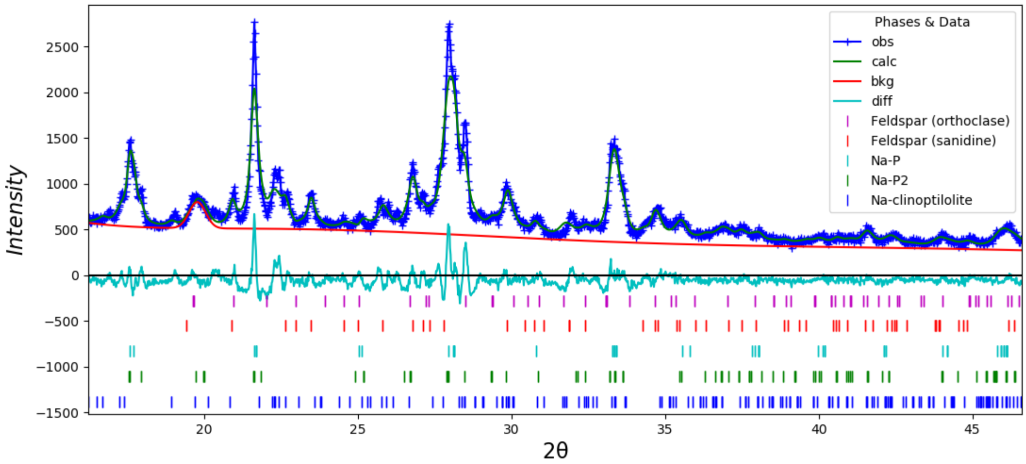

Figure A.25. Rietveld refinement of PXRD data for 0.40 M NaOH treated Z-HEU.

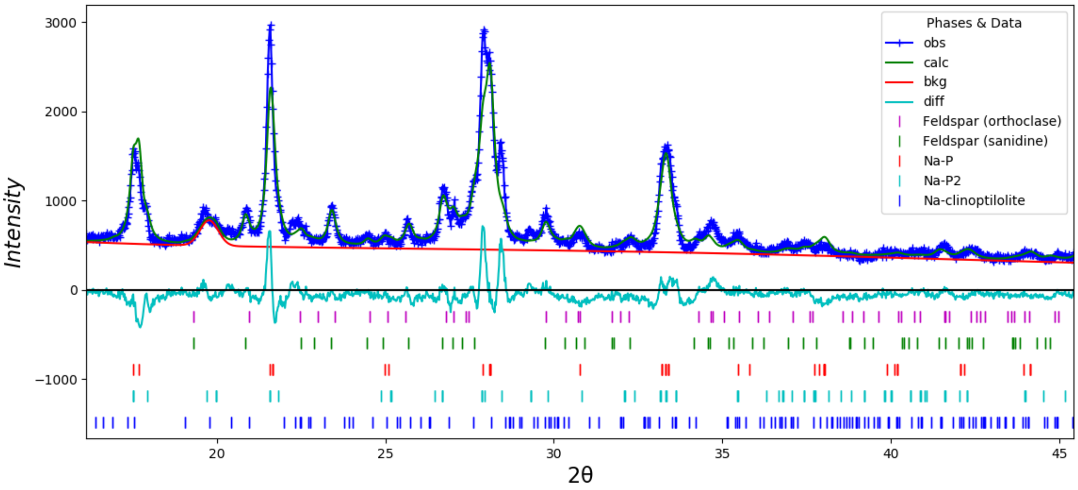

Figure A.26. Rietveld refinement of PXRD data for 0.45 M NaOH treated Z-HEU.

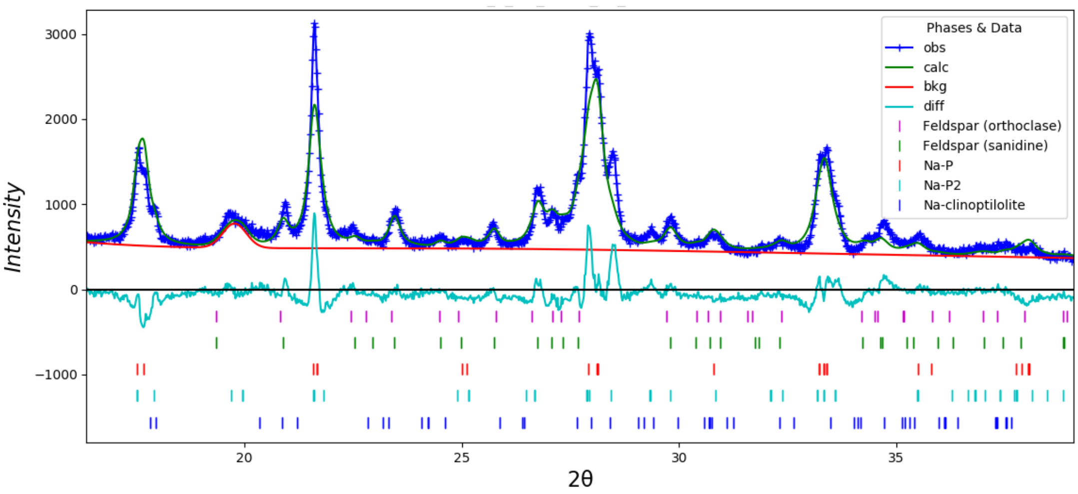

Figure A.27. Rietveld refinement of PXRD data for 0.50 M NaOH treated Z-HEU.

Table A.9. Summary of Rietveld fits for powdered materials produced from Z-HEU. *Sanidine and orthoclase.

Treatment	**wR / %**	**GOF**	**Clinoptilolite W_f**	**Na-P1 W_f**	**Na-P2 W_f**	**Feldspar***
0.20 M NaOH	6.22	1.22	0.81(1)	0.00(1)	0.01(1)	0.18(1)
0.25 M NaOH	9.53	2.21	0.73(1)	0.07(1)	0.00(1)	0.20(1)
0.30 M NaOH	9.03	2.11	0.55(1)	0.09(1)	0.16(1)	0.20(1)
0.35 M NaOH	10.10	2.36	0.37(1)	0.26(1)	0.14(1)	0.23(1)
0.40 M NaOH	8.77	2.07	0.19(1)	0.40(1)	0.23(1)	0.23(1)
0.45 M NaOH	10.20	2.19	0.05(1)	0.52(1)	0.25(1)	0.28(1)
0.50 M NaOH	11.35	2.68	0.00(1)	0.56(1)	0.27(1)	0.29(1)

A.9 Rietveld Refinements of Powder Composites Generated from N-HEU

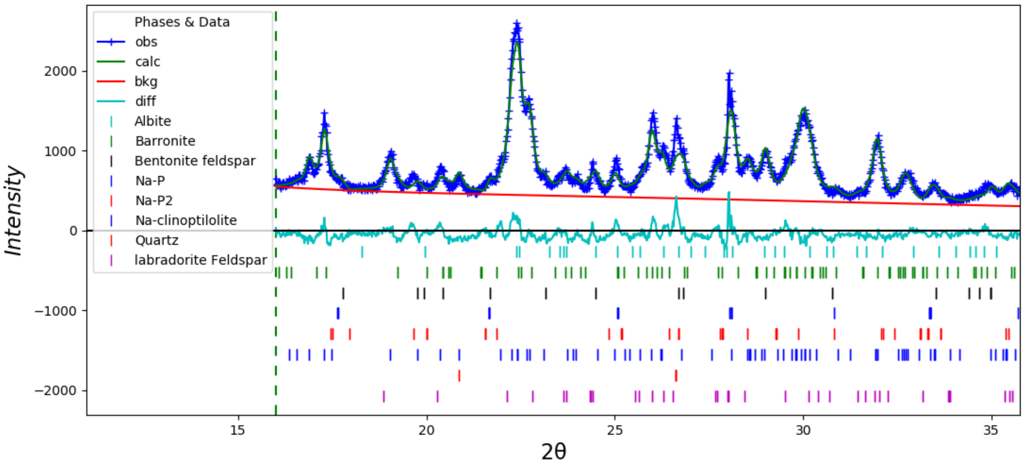

Figure A.28. Rietveld refinement of PXRD data for 0.20 M NaOH treated N-HEU.

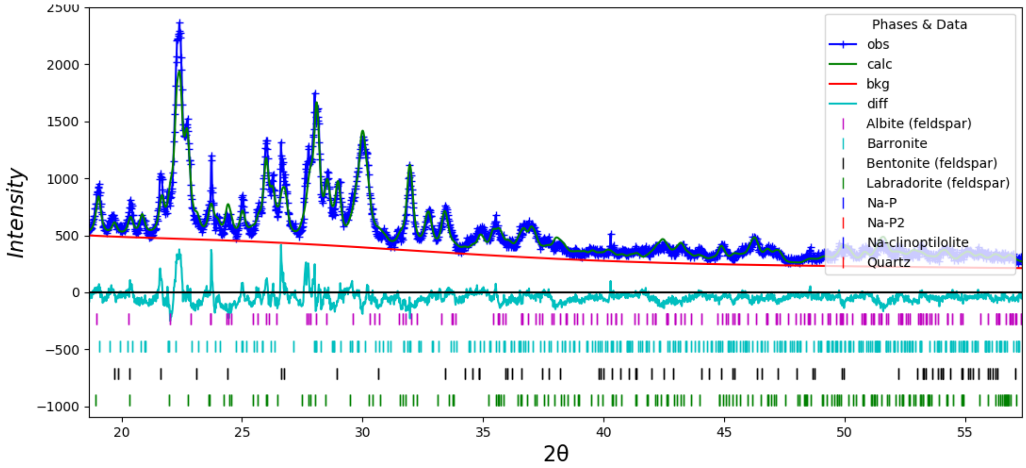

Figure A.29. Rietveld refinement of PXRD data for 0.25 M NaOH treated N-HEU.

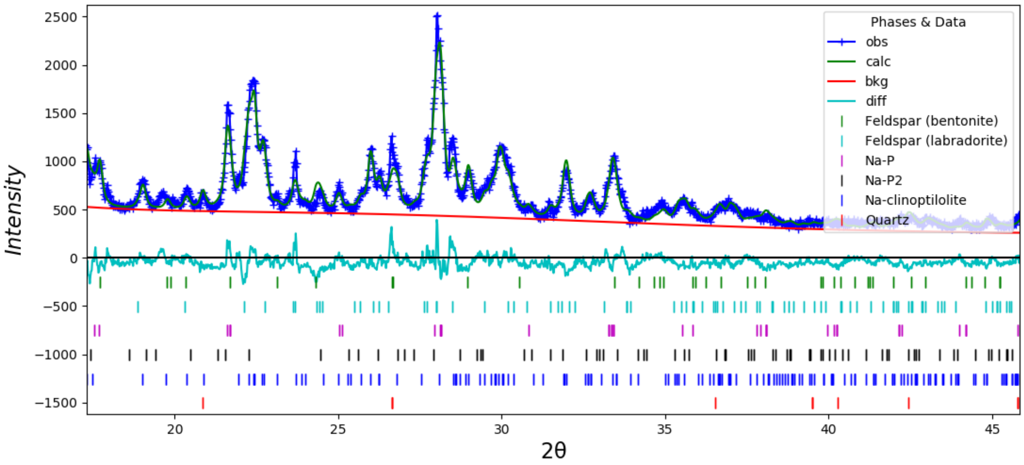

Figure A.30. Rietveld refinement of PXRD data for 0.30 M NaOH treated N-HEU.

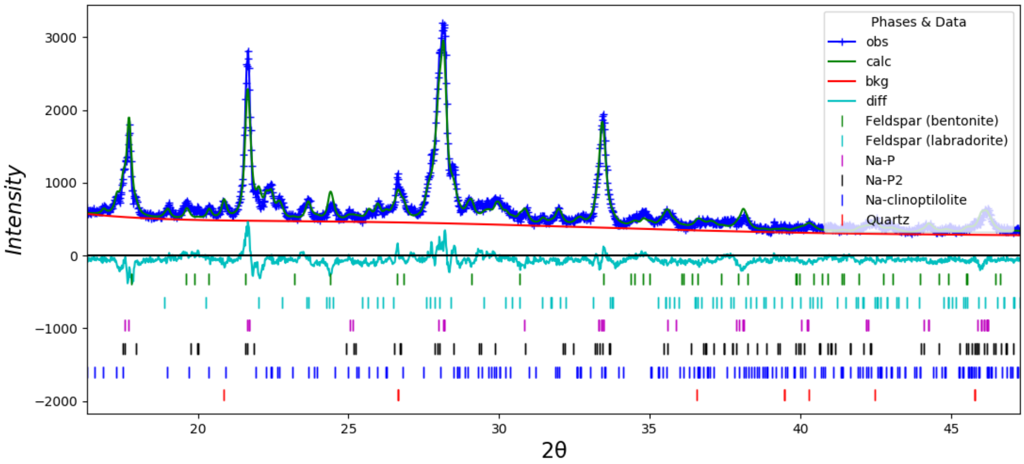

Figure A.31. Rietveld refinement of PXRD data for 0.35 M NaOH treated N-HEU.

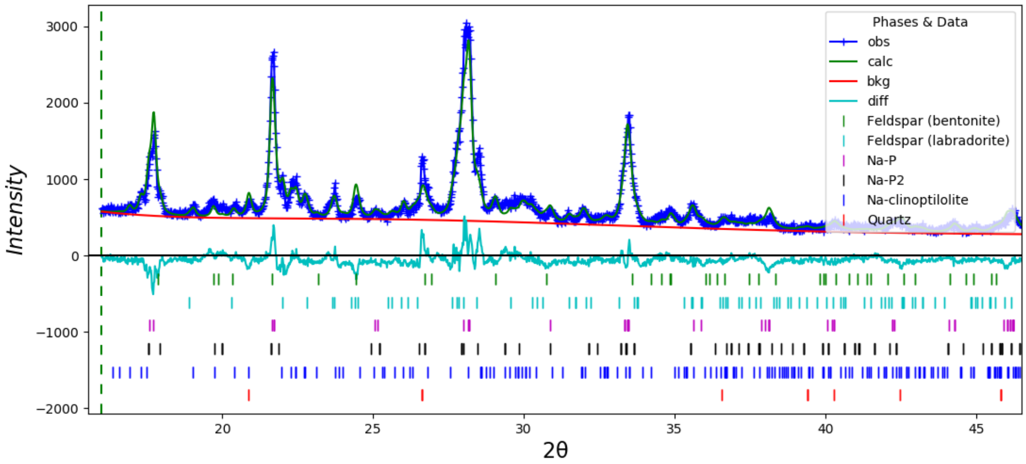

Figure A.32. Rietveld refinement of PXRD data for 0.40 M NaOH treated N-HEU.

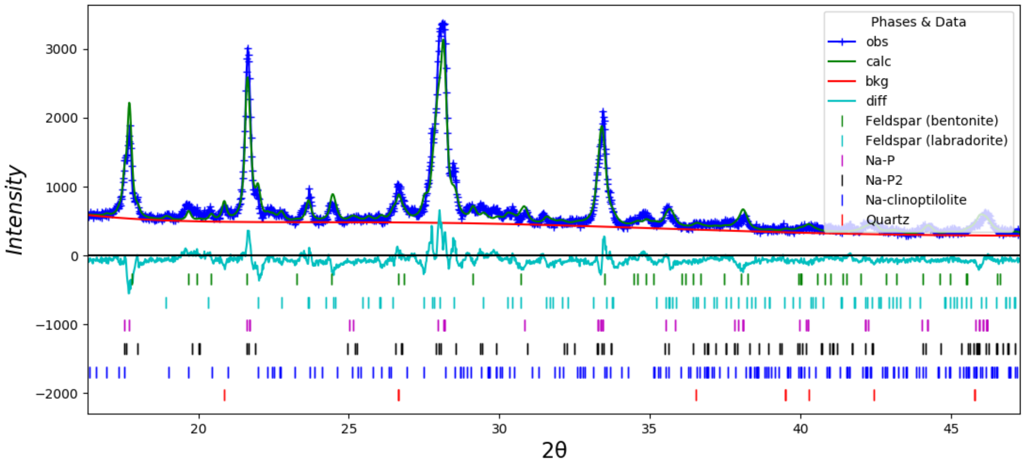

Figure A.33. Rietveld refinement of PXRD data for 0.45 M NaOH treated N-HEU.

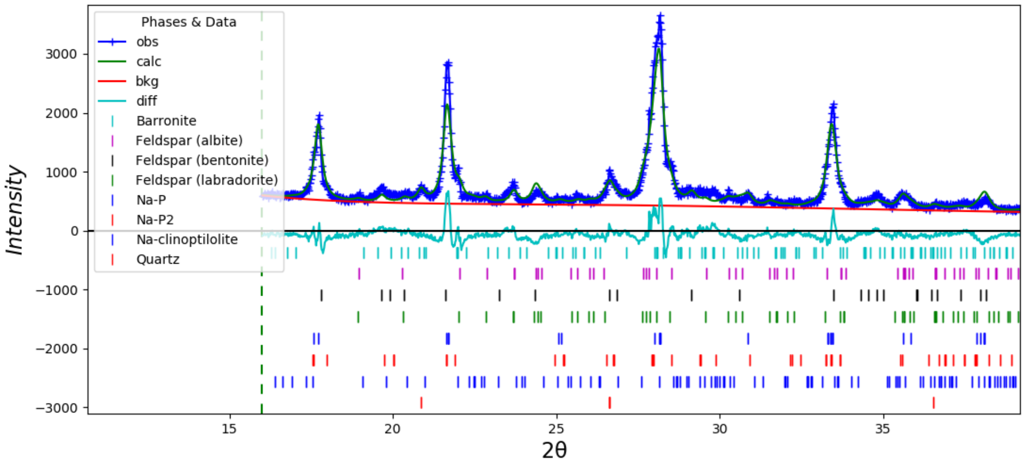

Figure A.34. Rietveld refinement of PXRD data for 0.50 M NaOH treated N-HEU.

Table A.10. Summary of Rietveld fits for powdered materials produced from N-HEU. *Albite, bentonite and labradorite.

Treatment	wR / %	GOF	Clinoptilolite W_f	Na-P1 W_f	Na-P2 W_f	Quartz W_f	Feldspar* W_f
0.20 M NaOH	6.18	1.42	0.72(1)	0.01(1)	0.01(1)	0.04(1)	0.23(1)
0.25 M NaOH	7.00	1.61	0.64(1)	0.05(1)	0.04(1)	0.04(1)	0.27(1)
0.30 M NaOH	7.18	1.65	0.45(1)	0.23(1)	0.02(1)	0.03(1)	0.27(1)
0.35 M NaOH	7.22	1.67	0.18(1)	0.46(1)	0.08(1)	0.03(1)	0.24(1)
0.40 M NaOH	7.27	1.68	0.14(1)	0.49(1)	0.06(1)	0.05(1)	0.26(1)
0.45 M NaOH	6.95	1.62	0.06(1)	0.55(1)	0.06(1)	0.07(1)	0.25(1)
0.50 M NaOH	8.42	1.95	0.02(1)	0.64(1)	0.02(1)	0.05(1)	0.27(1)

A.10 Rietveld Refinements of Powder Composites Generated from S-HEU

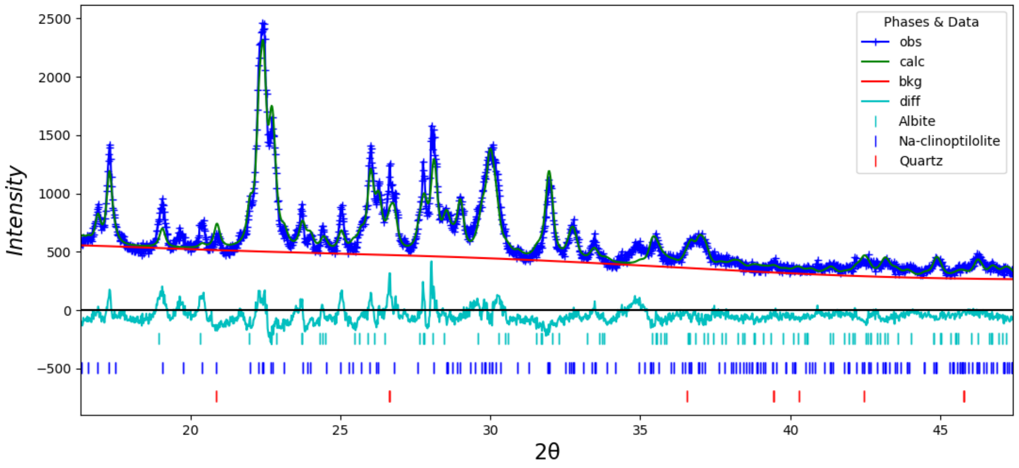

Figure A.35. Rietveld refinement of PXRD data for 0.20 M NaOH treated S-HEU.

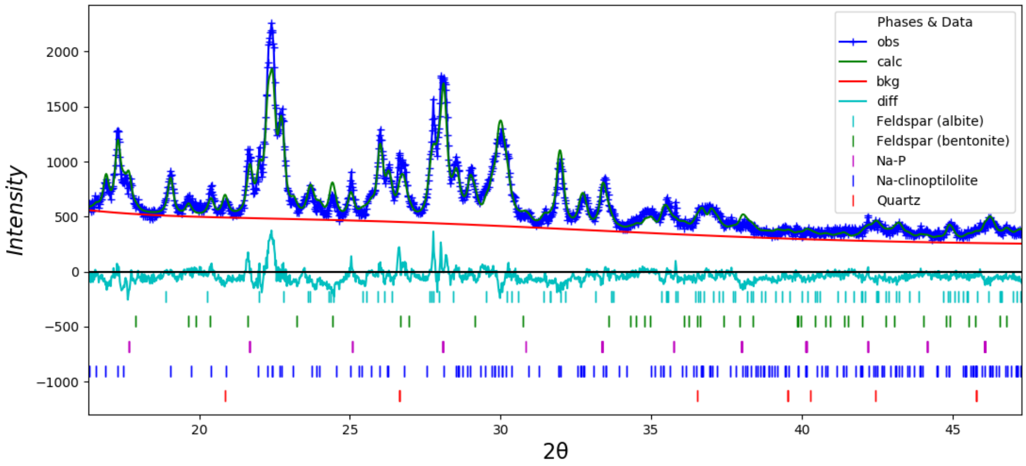

Figure A.36. Rietveld refinement of PXRD data for 0.25 M NaOH treated S-HEU.

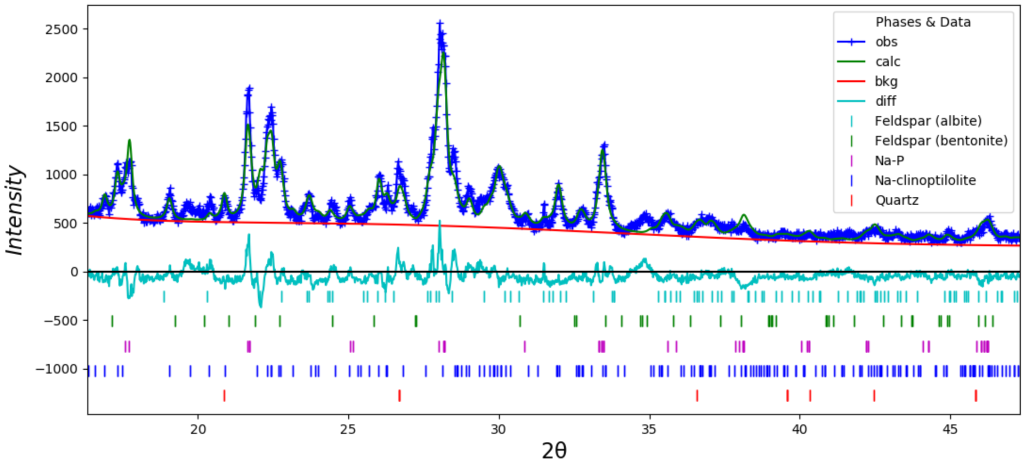

Figure A.37. Rietveld refinement of PXRD data for 0.30 M NaOH treated S-HEU.

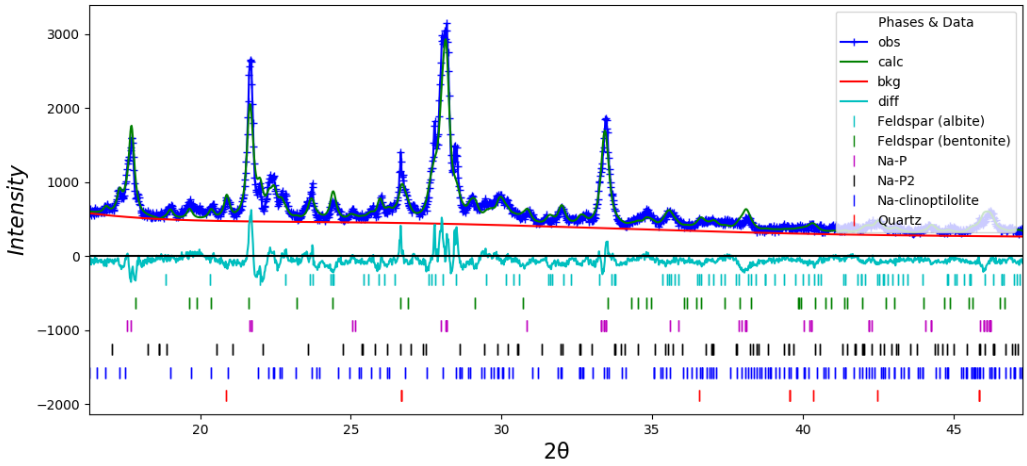

Figure A.38. Rietveld refinement of PXRD data for 0.35 M NaOH treated S-HEU.

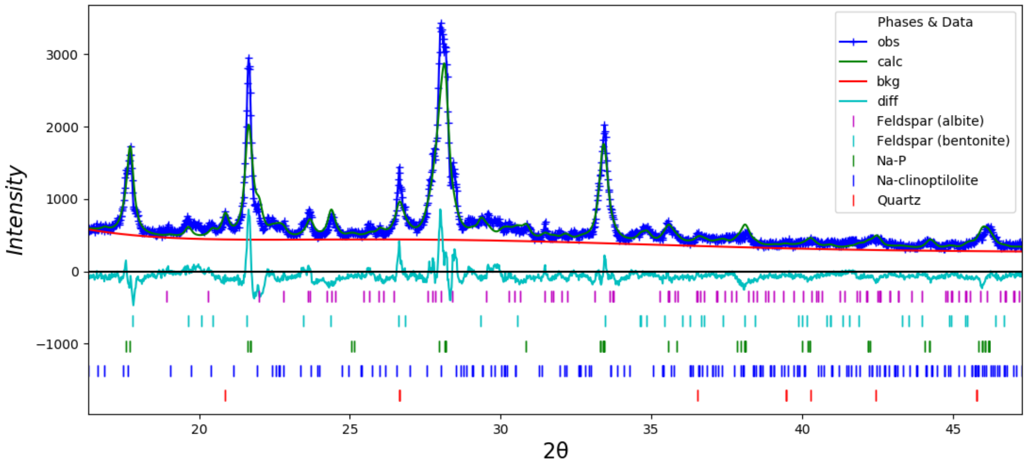

Figure A.39. Rietveld refinement of PXRD data for 0.40 M NaOH treated S-HEU.

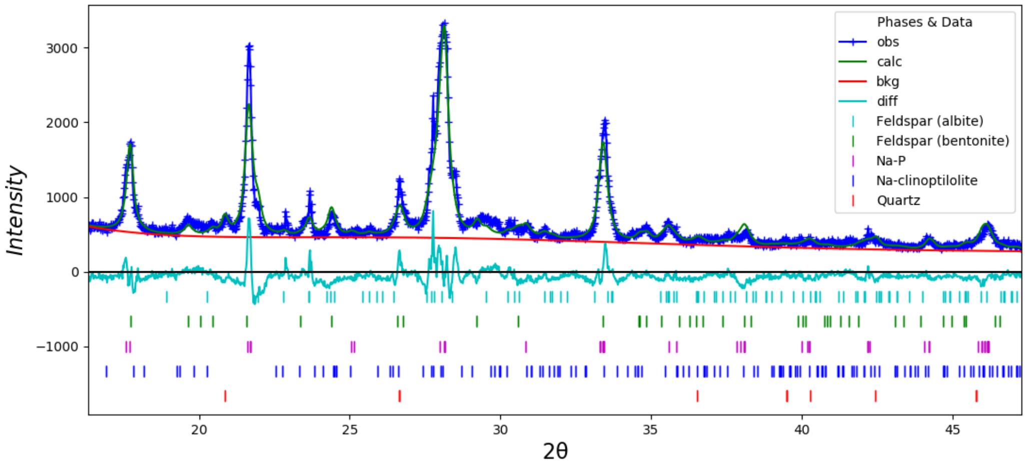

Figure A.40. Rietveld refinement of PXRD data for 0.45 M NaOH treated S-HEU.

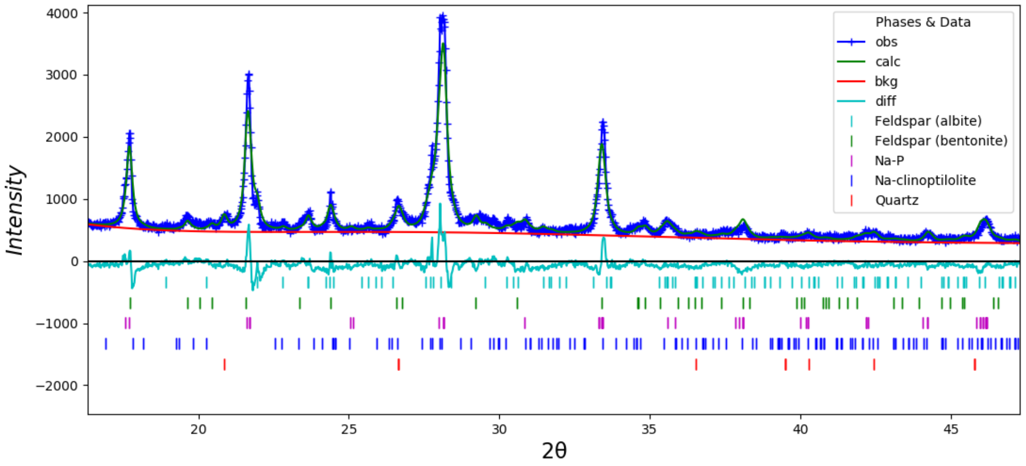

Figure A.41. Rietveld refinement of PXRD data for 0.50 M NaOH treated S-HEU.

Table A.11. Summary of Rietveld fits for powdered materials produced from S-HEU. *Albite and bentonite.

Treatment	**wR / %**	**GOF**	**Clinoptilolite W_f**	**Na-P1 W_f**	**Quartz W_f**	**Feldspar* W_f**
0.20 M NaOH	6.47	1.48	0.80(1)	0.00(1)	0.03(1)	0.17(1)
0.25 M NaOH	5.87	1.35	0.62(1)	0.12(1)	0.03(1)	0.23(1)
0.30 M NaOH	9.25	2.21	0.40(1)	0.34(1)	0.06(1)	0.20(1)
0.35 M NaOH	7.85	1.82	0.19(1)	0.49(1)	0.07(1)	0.26(1)
0.40 M NaOH	9.76	2.35	0.08(1)	0.67(1)	0.06(1)	0.19(1)
0.45 M NaOH	9.16	2.14	0.03(1)	0.67(1)	0.04(1)	0.27(1)
0.50 M NaOH	9.16	2.14	0.02(1)	0.65(1)	0.04(1)	0.28(1)

A.11 Parameters of Equilibrium Fitting Models Fitted to Data from Materials Produced from Z-HEU

Table A.12. Parameters of Langmuir, Freundlich and Temkin isotherm models for the adsorption of caesium onto Z-HEU (Na-exchanged), a HEU/ GIS composite material (37:40 HEU: GIS ratio) and 'fully converted' zeolite P.

	Langmuir			Freundlich			Temkin		
Material	q_m / mg g^{-1}	b	R^2	n	K_f	R^2	B_t	A_t	R^2
Z-HEU	123(7)	0.4(30)	0.990	0.15(3)	52(2)	0.904	210(35)	115(39)	0.902
Composite	185(5)	0.1(1)	0.998	0.15(3)	75(2)	0.936	122(19)	22(9)	0.934
Zeolite P	208(5)	0.1(1)	0.998	0.24(4)	51(2)	0.924	93(7)	6(2)	0.982

Table A.13. Parameters of Langmuir, Freundlich and Temkin isotherm models for the adsorption of strontium onto Z-HEU (Na-exchanged), a HEU/ GIS composite material (37:40 HEU: GIS ratio) and 'fully converted' zeolite P.

	Langmuir			Freundlich			Temkin		
Material	q_m / mg g^{-1}	b	R^2	n	K_f	R^2	B_t	A_t	R^2
Z-HEU	27(2)	-0.1(2)	0.984	0.07(3)	21(2)	0.692	1600(600)	4(2)$\times 10^6$	0.638
Composite	75(4)	-0.5(2)	0.989	0.19(3)	29(2)	0.936	309(41)	86(23)	0.936
Zeolite P	116(2)	0.3(2)	1.000	0.13(2)	57(2)	0.953	215(9)	113(9)	0.996

A.12 Parameters of Kinetic Models Applied to Strontium Adsorption Data Materials Derived from Z-HEU

Table A.14. 2nd order fitting parameters for strontium kinetic isotherms.

Material	**q_e / mg g^{1}**	**k / g mg^{-1}h^{-1}**	**R^2**
Z-HEU	19(2)	0.7(4)	0.876

Table A.15. Elovich fitting parameters for strontium kinetic isotherms.

Material	**α**	**β**	**R^2**
Composite	7(8)×10^4	0.16(2)	0.968
Zeolite P	7(8)×10^4	0.14(3)	0.965

A.13 Rietveld Refinements of Granular Composites Generated from Z-HEU

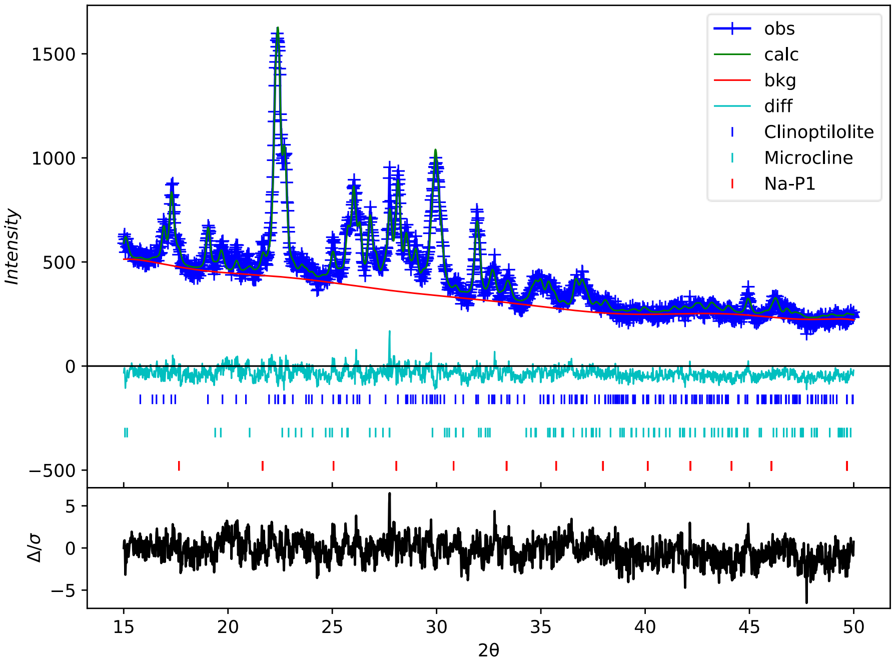

Figure A.42. Rietveld refinement of PXRD data of CG7.

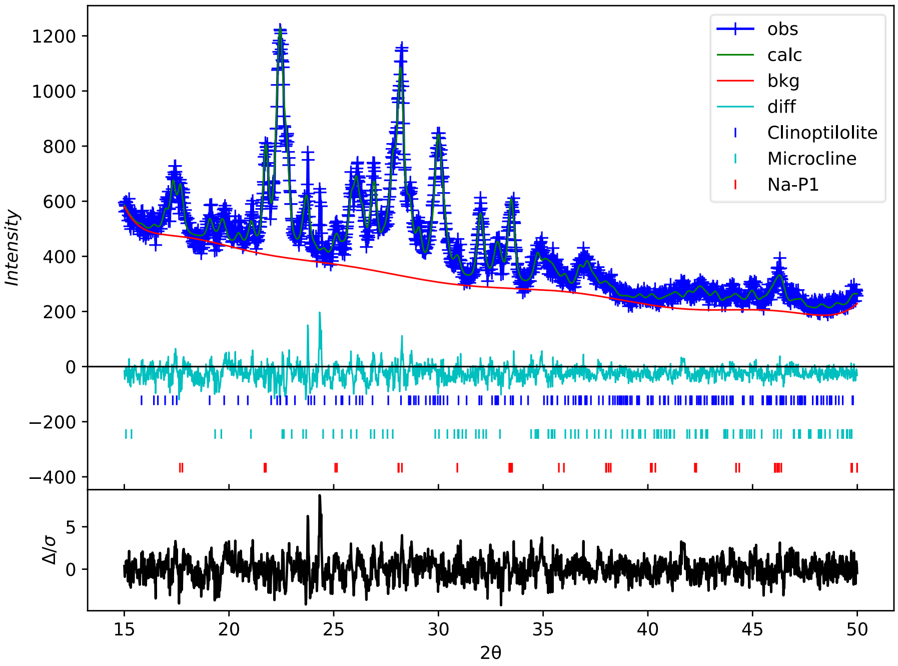

Figure A.43. Rietveld refinement of PXRD data of CG8.

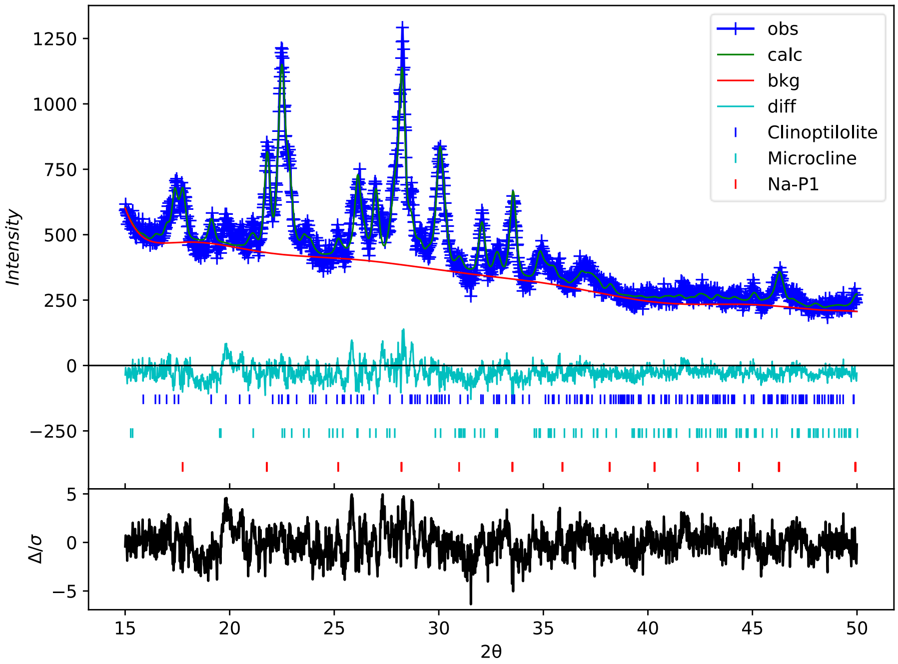

Figure A.44. Rietveld refinement of PXRD data of CG9.

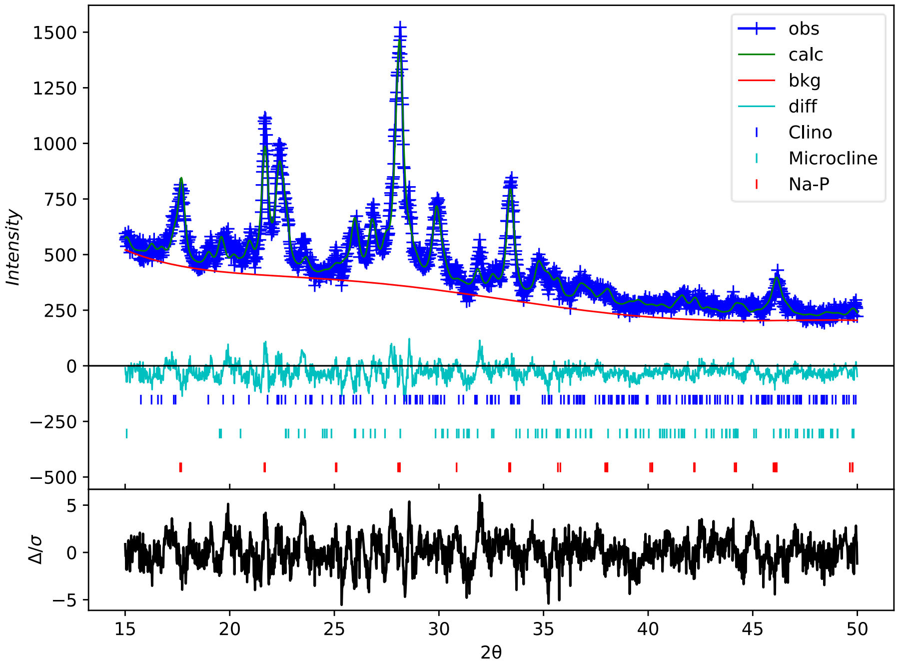

Figure A.45. Rietveld refinement of PXRD data of CG10.

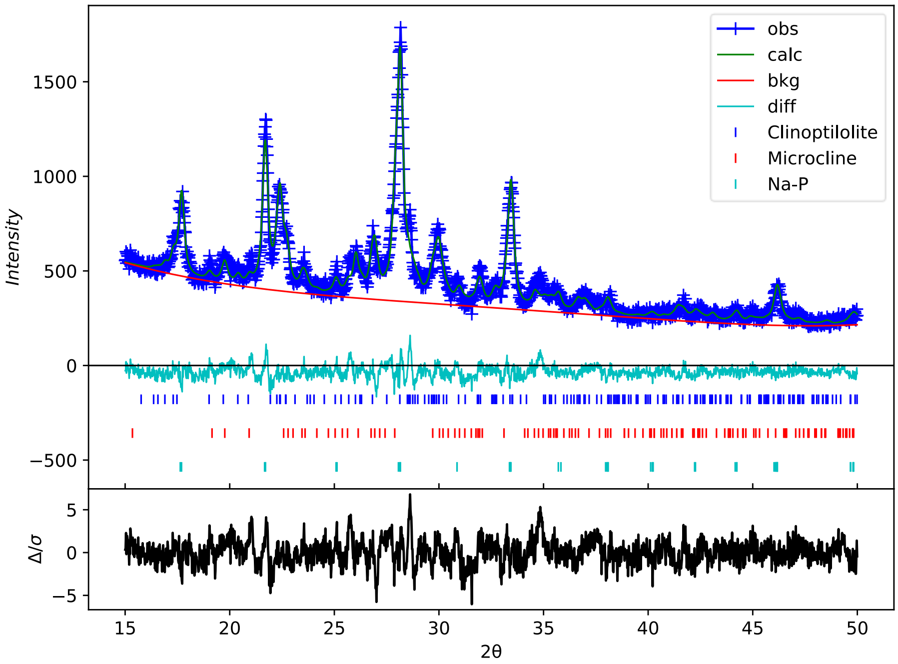

Figure A.46. Rietveld refinement of PXRD data of CG11.

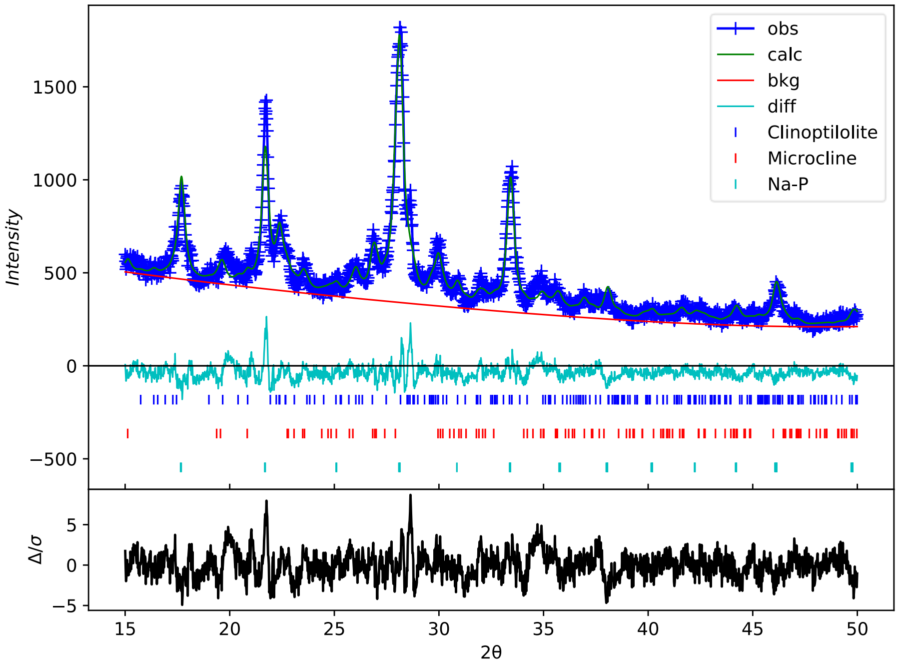

Figure A.47. Rietveld refinement of PXRD data of CG12.

Table A.16. Summary of refinement results of granular materials derived from Z-HEU.

Material	wR / %	GOF	HEU W_f	GIS W_f	Feldspar W_f
CG7	5.98	1.24	0.79(1)	0.05(1)	0.16(1)
CG8	6.41	1.33	0.58(1)	0.17(1)	0.25(1)
CG9	7.38	1.52	0.61(2)	0.22(1)	0.17(2)
CG10	7.49	1.57	0.42(1)	0.37(1)	0.20(1)
CG11	6.99	1.46	0.35(1)	0.45(1)	0.20(1)
CG12	7.44	1.58	0.14(1)	0.57(1)	0.29(1)

A.14 Two-Parameter Exponential Decay Fits to RIX Data for Materials Derived from Z-HEU

Table A.17. Exponential parameters and R^2 for fits of RIX data to two-parameter exponential decay functions.

Material	Radionuclide	Y_0	A_1	T_1	A_2	T_2	R^2
Z-HEU	Cs-137	4.69	36.1	49.1	59.2	389	0.996
	Sr-90	4.06	25.9	14.8	69.1	647	0.988
CG8	Cs-137	4.44	41.0	74.3	54.5	401	0.988
	Sr-90	2.50	11.9	29.1	85.6	506	0.918
CG10	Cs-137	5.67	63.6	71.1	30.6	429	0.998
	Sr-90	5.91	54.2	50.7	39.8	520	0.992

A.15 Acid Treated Z-, N-, and S-HEU PXRD Patterns

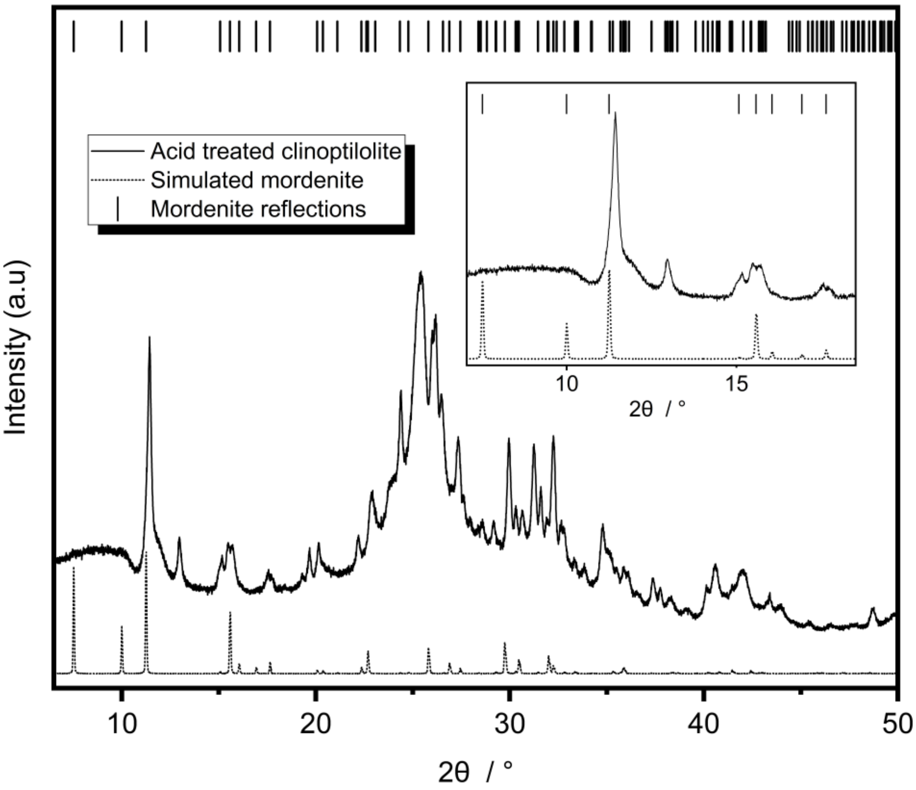

Figure A.48. PXRD pattern of acid-treated Z-HEU. λ = 1.79 Å.

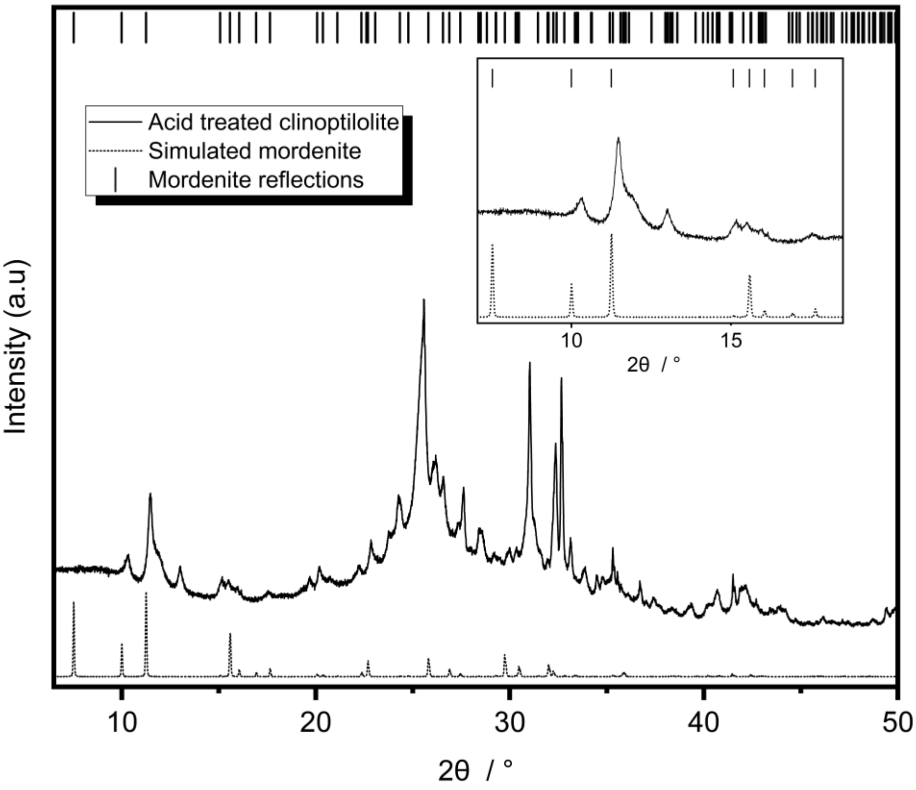

Figure A.49. PXRD pattern of acid-treated N-HEU. λ = 1.79 Å.

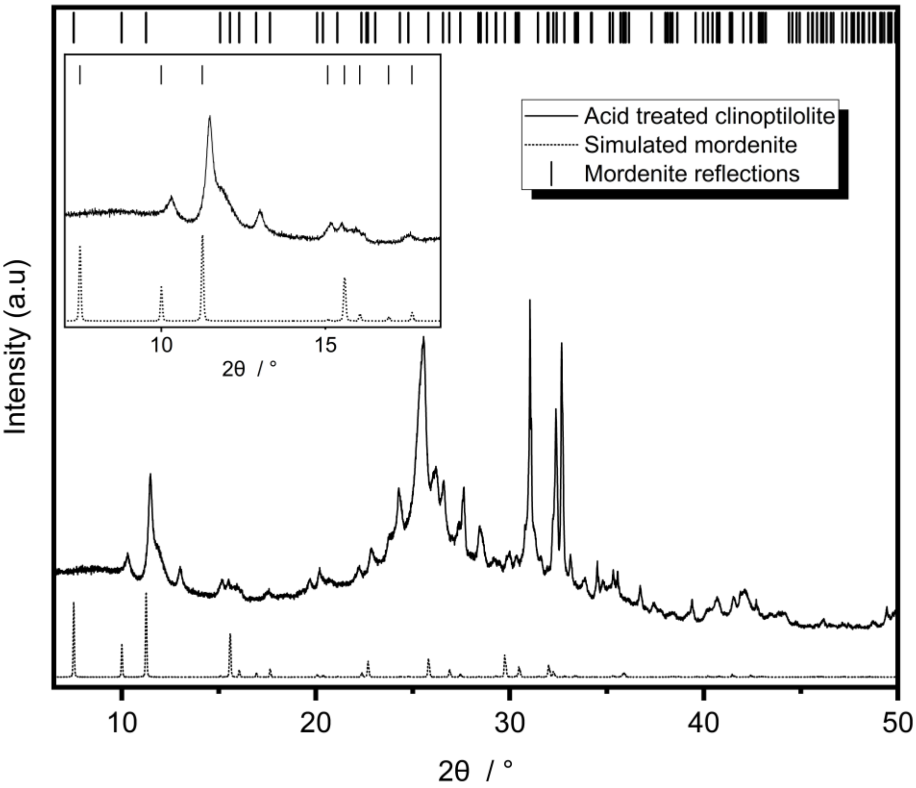

Figure A.50. PXRD pattern of acid-treated S-HEU. λ = 1.79 Å.

A.16 Parameters of Equilibrium Fitting Models Fitted to Data from Various Clinoptilolite Materials

Table A.18. Parameters of Langmuir, Freundlich and Temkin isotherm models for the adsorption of caesium onto four clinoptilolites.

	Langmuir			**Freundlich**			**Temkin**		
Material	q_m / mg g^{-1}	b	R^2	n	K_f	R^2	B_t	A_t	R^2
MH-HEU	192(5)	2(7)	0.999	0.19(5)	65(2)	0.917	123(9)	38(5)	0.982
Z-HEU	123(7)	0.4(30)	0.990	0.15(3)	52(2)	0.904	210(35)	115(39)	0.902
N-HEU	128(7)	0.2(7)	0.989	0.14(3)	54(2)	0.894	211(32)	156(45)	0.920
S-HEU	125(6)	0.1(2)	0.991	0.16(2)	46(2)	0.964	201(18)	45(10)	0.966

Table A.19. Langmuir-Freundlich isotherm parameters for the adsorption of caesium onto four clinoptilolites.

	Langmuir-Freundlich			
Material	q_{max} / mg g^{-1}	K	n	R^2
MH-HEU	203(8)	0.51(6)	0.53(7)	0.996
Z-HEU	136(20)	0.60(23)	0.47(20)	0.933
N-HEU	134(13)	0.68(20)	0.51(17)	0.958
S-HEU	157(39)	0.39(13)	0.34(13)	0.969

Table A.20. Parameters of Langmuir, Freundlich and Temkin isotherm models for the adsorption of strontium onto four clinoptilolites.

	Langmuir			**Freundlich**			**Temkin**		
Material	q_m / mg g^{-1}	b	R^2	n	K_f	R^2	B_t	A_t	R^2
MH-HEU	51(3)	0(1)	0.991	0.11(2)	30(2)	0.887	700(100)	$12(2)\times10^{4}$	0.909
Z-HEU	27(2)	-0.1(2)	0.984	0.07(3)	21(2)	0.692	1600(600)	$4(2)\times10^{6}$	0.638
N-HEU	38(2)	-0.2(3)	0.997	0.10(2)	25(2)	0.901	900(200)	$5(2)\times10^{4}$	0.897
S-HEU	28(3)	-0.1(1)	0.980	0.1(1)	19(2)	0.181	$1(1)\times10^{3}$	$4(8)\times10^{3}$	0.166

Table A.21. Langmuir-Freundlich isotherm parameters for the adsorption of strontium onto four clinoptilolites.

	Langmuir-Freundlich			
Material	q_{max} / mg g^{-1}	K	n	R^2
MH-HEU	56(4)	2(1)	0.42(13)	0.963
Z-HEU	30(2)	20(380)	1(7)	0.827
N-HEU	44(5)	2.3(14)	0.36(15)	0.955
S-HEU	33(5)	1.6(17)	0.69(88)	0.672

A.17 PXRD Patterns of Pre-Treated MH-HEU

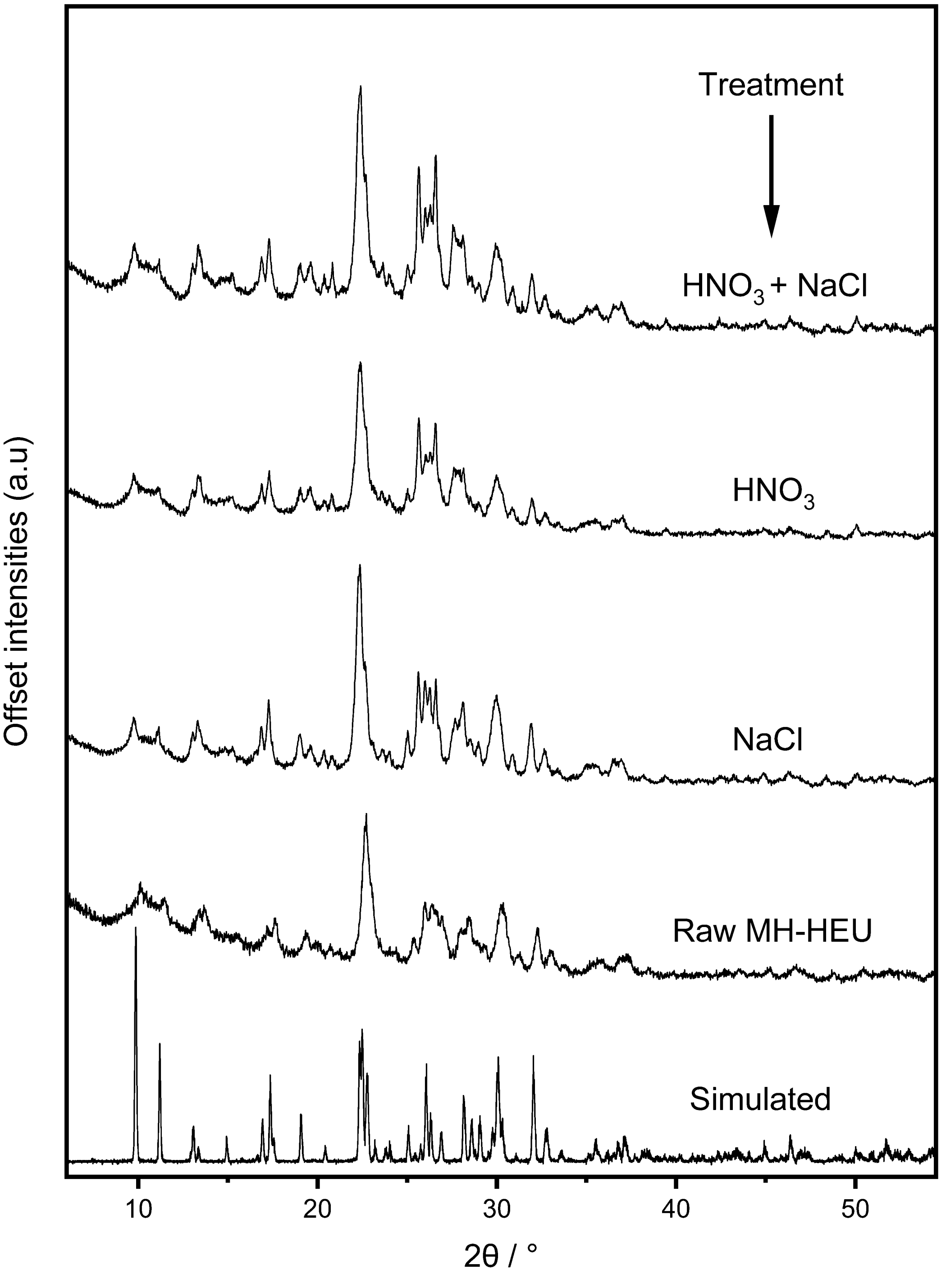

Figure A.51. PXRD patterns of MH-HEU after pre-treatment. Patterns of the raw material and a simulated pattern are also displayed. $\lambda = 1.5406$ Å.

A.18 Chabazite Seeding Experiment

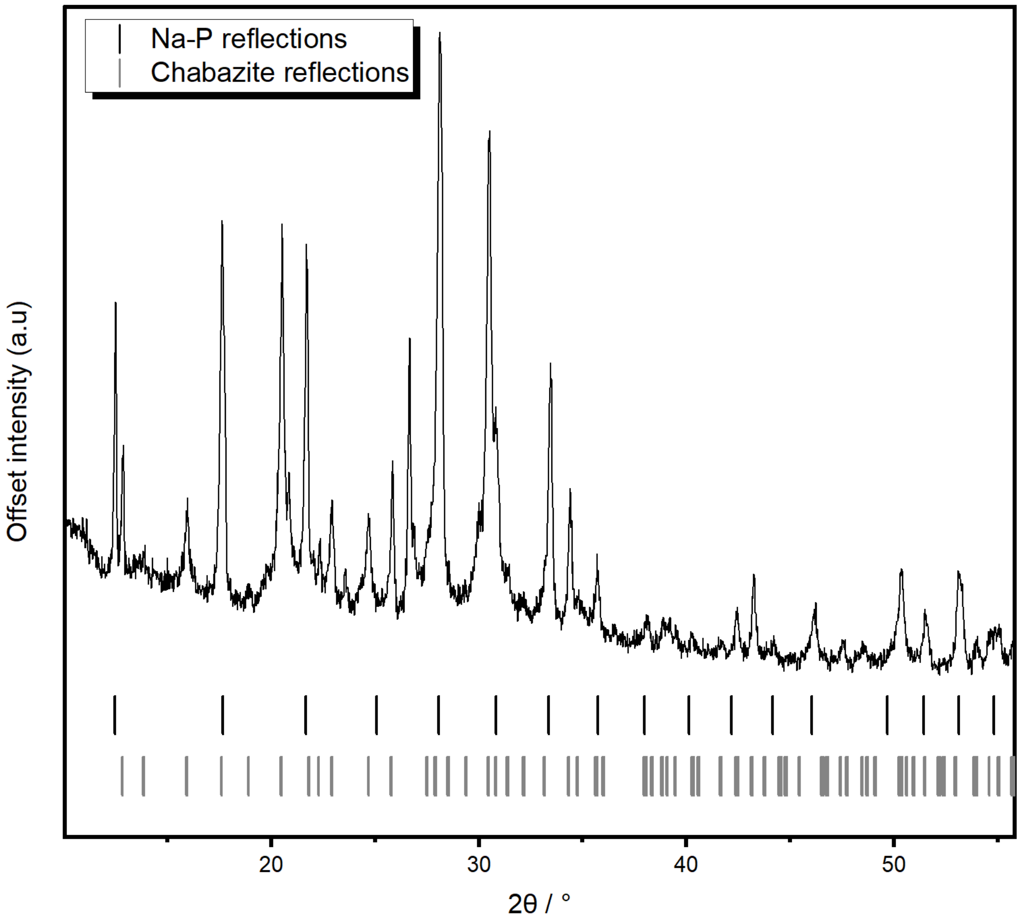

Figure A.52. PXRD pattern of acid-treated, hydrothermally transformed MH-HEU with 10 Wt. % chabazite seeding.

A.19 Pre-Treated Transformations of Z-, N-, and S-HEU

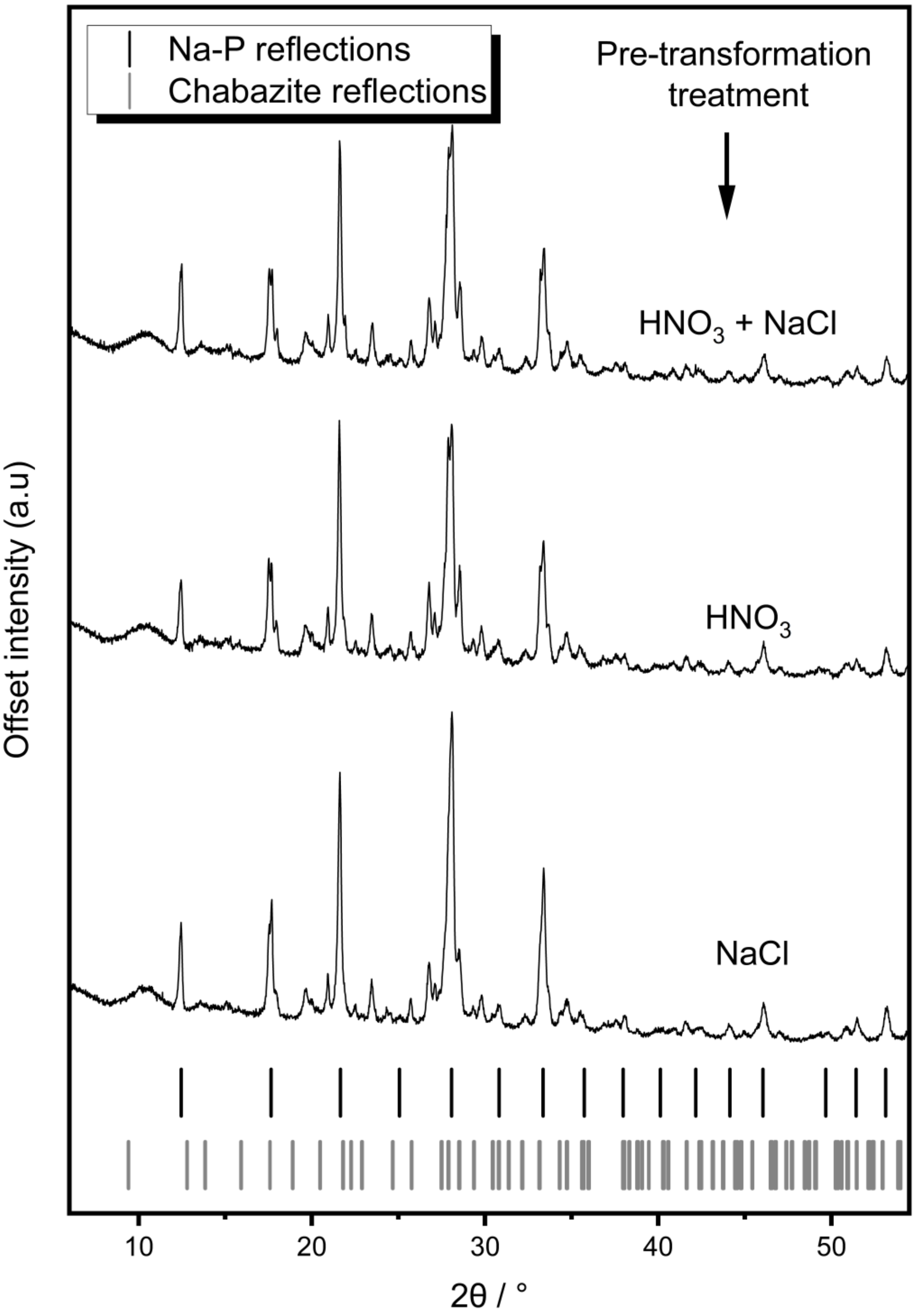

Figure A.53. Pre-treated transformation products of Z-HEU (λ = 1.5406 Å).

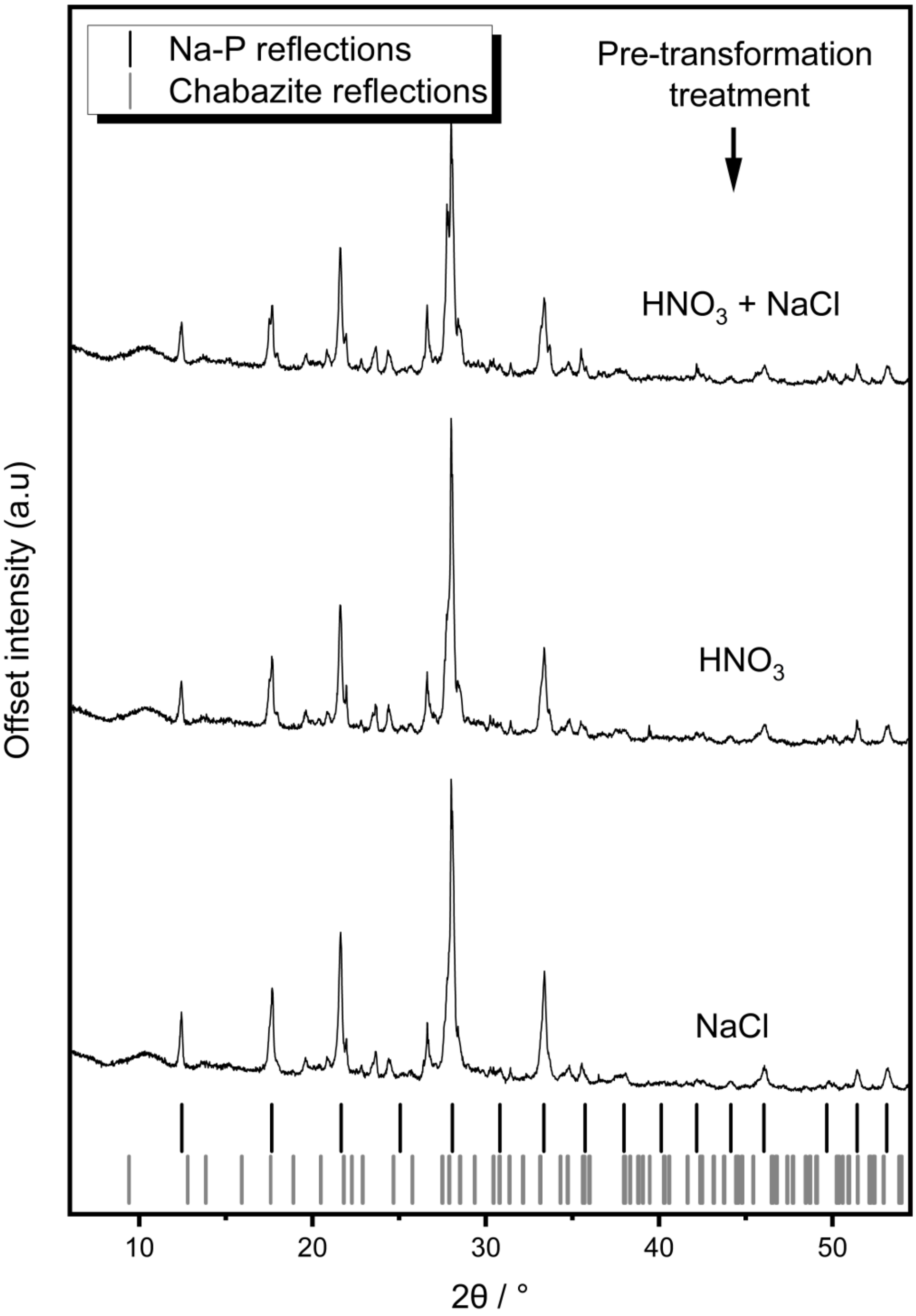

Figure A.54. Pre-treated transformation products of N-HEU (λ = 1.5406 Å).

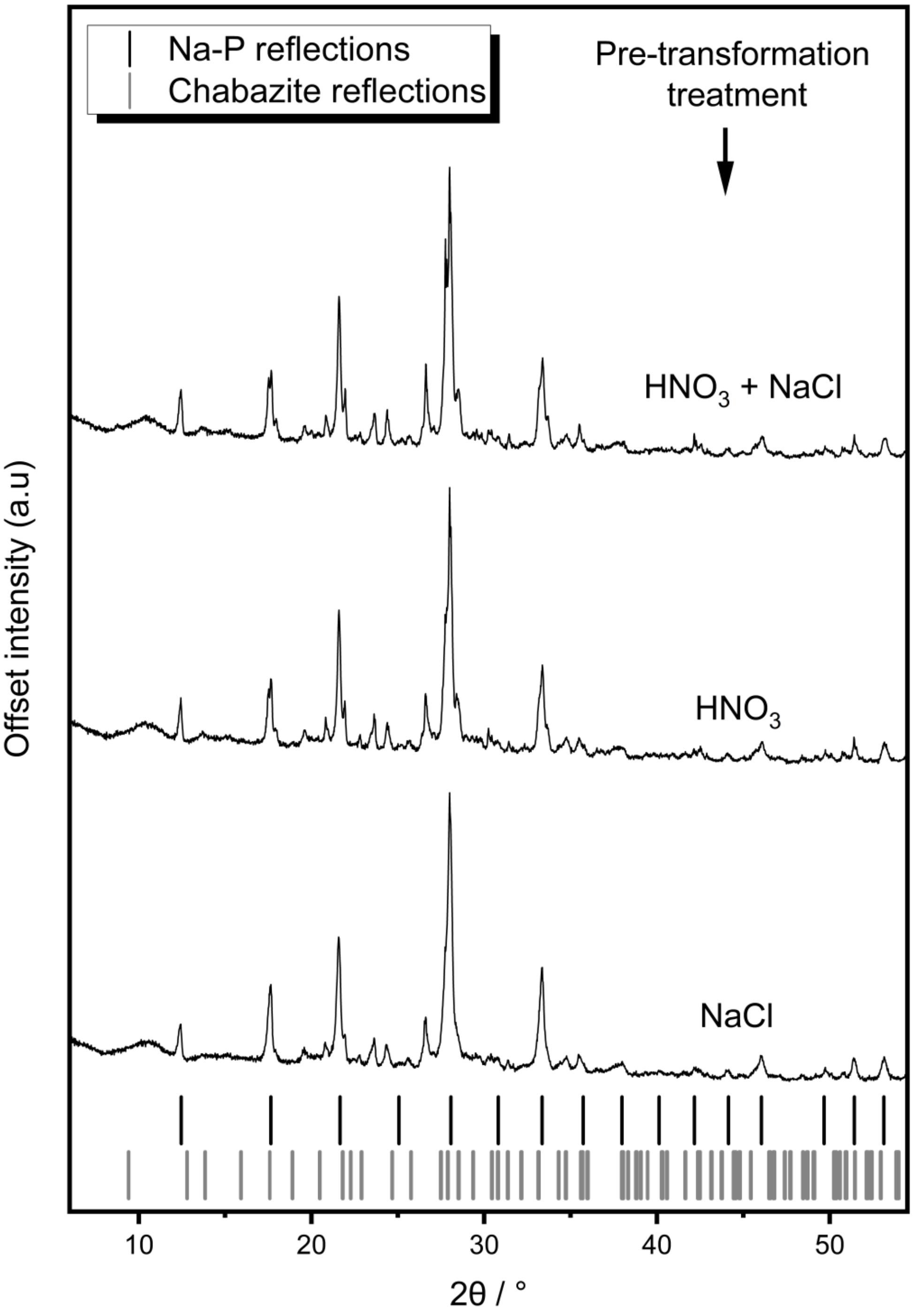

Figure A.55. Pre-treated transformation products of S-HEU (λ = 1.5406 Å).